Thèse de doctorat

de l'Université de Bordeaux

Ecole doctorale n°304, Sciences de l'environnement

Spécialité : **Physique de l'environnement**

Pour obtenir le grade de :

Docteur de l'Université de Bordeaux

Radar backscatter contribution to tropical forest disturbance monitoring

-

Apports de la rétrodiffusion radar au suivi de la déforestation en forêt tropicale

Subtitle: Sentinel-1 contribution to forest disturbance monitoring: a CuSum-based approach

Présentée par Bertrand YGORRA

Soutenue le 14/12/2022

Supervisée par : Frédéric FRAPPART, Jean-Pierre WIGNERON, Serge RIAZANOFF

Unité de recherche : *INRAE, UMR 1391 ISPA Interactions Sol Plante Atmosphère*

Membres du jury :

M.	DARROZES José	Maître de conférences, Université Toulouse III – Paul Sabatier	Rapporteur
M.	MOUGIN Éric	Directeur de recherche CNRS	Rapporteur
M.	BAUP Frédéric	Maître de conférences, Université Toulouse III – Paul Sabatier	Examinateur
M.	CATRY Thibault	Ingénieur de recherche IRD	Examinateur
Mme.	PORTE Annabel	Directrice de recherche INRAE	Examinateur
M.	WIGNERON Jean-Pierre	Directeur de recherche INRAE	Directeur
M.	RIAZANOFF Serge	Directeur de l'entreprise VisioTerra	Co-directeur
M.	FRAPPART Frédéric	Directeur de recherche INRAE	Co-directeur

Résumé : La télédétection spatiale est de plus en plus employée dans la surveillance des problèmes environnementaux. Son intérêt principal réside dans la capacité des capteurs embarqués sur satellites de fournir des informations aux échelles mondiale, régionale et locale. La télédétection optique a montré son potentiel dans le suivi des changements de couvert forestier. Jusqu'à récemment, les systèmes de suivi de la déforestation étaient basés sur l'imagerie satellitaire optique. Dans la bande intertropicale, l'emploi de ce type d'image rencontre des limites liées à la temporalité du couvert nuageux. Ce couvert nuageux, fréquent, entraîne des délais de détection voir des manquements à cause du manque de disponibilité de nouvelles images non-contaminées par les nuages. En effet, des ouvertures d'origine humaine dans la canopée peuvent être refermées par la repousse entre deux images optiques non-contaminées.

Les nouveaux systèmes de Radar à Ouverture Synthétique (RSO, SAR) ont ouvert de nouvelles perspectives dans le domaine de la surveillance des changements de couvert forestier dans les forêts tropicales humides (Sentinel-1, PALSAR-2). Ces capteurs actifs ont la capacité de pénétrer le couvert nuageux. La disponibilité des images Sentinel-1 en bande C à haute résolution spatiale (5x20m) comme temporelle (6 à 12 jours de revisite) en fait un substitut potentiel / complémentaire des systèmes optiques dans le suivi des perturbations du couvert forestier.

Cette thèse s'articule autour de trois parties. La première consiste à développer une nouvelle méthode de détection des changements basée sur le *Cumulative Sum algorithm* (CuSum) combiné avec une analyse de *bootstrap*, appliquée au suivi des changements du couvert forestier. La méthode a été appliquée à des séries temporelles d'images Sentinel-1 *Ground-Range-Detected* (GRD) en polarisation double (VV, VH) obtenues dans une concession forestière légale près de Kisangani, en République Démocratique du Congo. Les améliorations apportées consistent en l'intersection des cartes de résultats de VV et de VH pour créer la carte de résultats VV x VH. Une recombinaison spatiale d'un seuil critique (T_c) haut avec un seuil critique bas a également été réalisée, appelée cross-T_c. Le deuxième axe de la thèse est constitué par le développement de la méthode ReCuSum. Ce développement se traduit par l'application du CuSum cross-T_c de manière itérative pour changer la nature '*single breakpoint'* du CuSum en '*multiple breakpoints'*. Cette amélioration a été réalisée dans l'objectif d'améliorer la capacité du CuSum cross-T_c à détecter et qualifier les changements du couvert forestier. Le développement se base dans la région du Parà, dans la forêt amazonienne brésilienne. Le troisième et dernier axe de cette thèse consiste à développer une version quasi-temp-réelle du CuSum cross-T_c.

Mots clefs : Déforestation, Sentinel-1, Télédétection radar, *Cumulative Sum algorithm*, Détection de changement, Forêts tropicales.

Abstract: Earth Observations are increasingly used to monitor environmental problems. Its interests lie in the ability of sensors aboard satellites to provide information at global, regional and local scales. Optical remote sensing has shown great potential for the monitoring of forest disturbances. Until recently, deforestation monitoring systems were mainly based on remotely sensed optical images. In the intertropical latitudes, such images often face limitations of frequent cloud cover, leading to late detection or misdetections due to the temporal availability of new images uncontaminated by clouds. In tropical humid forests, regrowth can close canopy gaps between two non-cloud-contaminated optical images used for detection.

New SAR (Synthetic Aperture Radar) systems have opened new perspectives for forest disturbance monitoring in tropical humid forests (Sentinel-1, PALSAR-2). These active sensors penetrate the clouds. The availability of Sentinel-1 C-band images at high spatial and temporal resolutions makes it a potential substitute / complementary of optical systems for monitoring disturbances in forest cover.

This work revolves around three parts. The first part consists in the development of a new change detection method for monitoring disturbances in forest cover, based on the Cumulative Sum algorithm (CuSum) combined with a bootstrap analysis. The method was applied to time-series of Sentinel-1 Ground-Range Detected (GRD) dual polarization (VV, VH) images obtained in a legal forest concession near Kisangani in the Democratic Republic of the Congo. The results from VV and VH polarization were intersected in VV x VH result map, and a spatial recombination of a high Critical Threshold (T_c) with a low critical threshold was performed. The second part of this work is to develop a multiple-breakpoints version of the CuSum cross-T_c called ReCuSum to further enhance the ability to monitor changes in forest cover. The development was made by applying the CuSum cross-T_c over a time-series in an iterative manner, in the State of Parà, Brazilian Amazon. The third axis of this thesis is to develop a Near-Real-Time (NRT) version of the CuSum cross-T_c.

Keywords: Deforestation, Sentinel-1, Radar remote sensing, Cumulative Sum algorithm, Change detection, Tropical forests.

Remerciements

Je tiens en tout premier à remercier mon directeur et mes co-directeurs Frédéric, Jean-Pierre et Serge. Sans vous, cette thèse n'aurait jamais vu le jour, et je vous remercie de m'avoir choisi pour ce travail. Je remercie tout particulièrement Serge et la société VisioTerra qui ont financé cette thèse, ainsi que l'Association Nationale Recherche et Technologie.

Un merci tout particulier à Frédéric, qui m'a soutenu contre vents et marées (et mauvaises formulations dans les articles !) et qui n'a cessé de croire en moi. Je te remercie très chaleureusement pour tout ton soutien et encore aujourd'hui.

Je remercie également José Darrozes et Eric Mougin d'avoir accepté d'être mes rapporteurs et de lire mon manuscript dans le détail, ainsi qu'Annabelle Porté, Frédéric Baup et Thibault Catry d'avoir accepté d'examiner mon travail. Désolé Frédéric, promis, mes prochains articles auront moins d'abréviations !

Je souhaite également remercier toutes les personnes qui m'ont aidé, de près ou de loin, à comprendre la technique SAR et les applications sur le suivi de la déforestation (et merci Guillaume pour les illustrations).

Je n'oublie évidemment pas les personnes qui m'ont permis de travailler d'un point de vue informatique. Merci à toi Grégory, Kévin, Alexis, Christophe, Eric et Tovo (linux a à moitié gagné… c'est mieux que rien !).

Mais une thèse, ce n'est pas seulement de l'aide technique ou des discussions scientifiques. Que serait une thèse à inrae la grande ferrade sans son équipe de volley ball du lundi, ou des week-ends de surf / mâtinées de surf ! Merci à Tovo d'être aussi actif (et didactique). Je remercie maintenant également mes collègues doctorants et de bureau Pablo (et ses triples contrepèteries bien trop complexes pour nous), Thomas et ses trombones (à quand la tour Eiffel ?) et Klara pour les discussions, les thés et les petites courses à pied, mais également mon ex-collègue de bureau Tom, parti dans l'autre aile (ou la cuisse ?). Vous m'avez fait passer de très agréables moments au bureau.

Evidemment, je n'oublie pas non plus Xiaojun, Xianghzuo pour les discussions et l'aide sur les présentations.

Je consacre mes derniers remerciements à mes proches. Ma famille, mes parents qui m'ont toujours soutenu en ces périodes difficiles. Mes frères également, particulièrement Virgile, qui a été un soutien énorme dans les périodes les plus rudes de la thèse, au début comme à la fin. Merci à toi.

Enfin, je remercie mon fils Manao, qui m’aura bien entraîné à dormir peu pour me préparer au marathon qu’est une fin de thèse. Et enfin toi, Pauline. On s’est connus deux mois avant le début de la thèse. Puis on s’est mariés… Puis Manao est né… Tu as été mon soutien le plus solide, tu as toujours cru en moi, plus que moi-même je n’y croyais. Merci de tout ce que tu as fait pour moi (et des Lanvins. C’est bon, les Lanvins.).

Thank you for everything.

Aperçu de la thèse :

Les forêts tropicales jouent un rôle primordial dans la régulation globale du climat en recyclant entre ~2.1 Gt $CO_2.y^{-1}$ (Federici et al., 2015; Nunes et al., 2020) et 7.0 Gt $CO_2.y^{-1}$ (Harris et al., 2021), Ces dernières années, le taux de déforestation a continué d'augmenter. Des études récentes ont monté que globalement, les forêts tropicales jouent à la fois un rôle de puit mais aussi de source dans le cycle du carbone avec un bilan global neutre (Fan et al., 2019). En Afrique et en Amazonie, ces déforestations ont diverses causes, comme les 'coupes sélectives' légales ou non, ou des coupes pour parfaire aux besoins des populations locales (Contreras-Hermosilla and others, 2000; Creese et al., 2019; Gatti et al., 2021; Kleinschroth et al., 2019; Lescuyer et al., 2011; Qin et al., 2021; Umunay et al., 2019).

Pour être en mesure de suivre la déforestation et la dégradation des forêts tropicales, il était urgent d'implémenter des systèmes de suivi à grande échelle avec des résolutions spatiale et temporelle fines. La télédétection par satellite a été identifiée comme l'outil principal dans l'initiative sur la lutte contre la déforestation (*Reduced Emissions from Deforestation and Degradation initiative*, REDD+) orchestrée par *l'United Nations Framework Convention on Climate Change* (UNFCCC, Lynch *et al.*, 2013).

Il existe deux catégories principales d'Observation de la Terre employées dans le cadre du suivi de la déforestation : les micro-ondes actives (RADAR) ou passives (télédétection optique). Avec les progrès technologiques, les images optiques ou radar ont pu être acquises avec des résolutions spatiales et temporelles de plus en plus fines. L'amélioration de la résolution a permis d'obtenir des cartes de perturbation du couvert forestier à plus fine échelle, avec des seuils d'aire minimale de détection plus faibles.

Dans un premier temps, l'imagerie satellitaire optique a été communément utilisée dans le suivi des changements de couvert forestier car les méthodes employées produisaient des résultats précis sur plusieurs régions (Bullock et al., 2020; Hansen et al., 2013; Tyukavina et al., 2018). Pourtant, les systèmes de suivi basés sur ce type d'image sont plus à même de produire des informations imprécises dans les régions soumises à un couvert nuageux régulier (Doblas et al., 2020; Hansen et al., 2016; Weisse et al., 2019).

Afin de réduire l'impact du couvert nuageux dans le suivi des perturbations du couvert forestier, le potentiel des capteurs actifs type radar a été exploré. En effet, les capteurs actifs en bande C et L sont connus pour pénétrer le couvert nuageux (Joshi et al., 2015).

Le système de Radar à Synthèse d'Ouverture a permis de produire des images en bande C et L à une résolution moyenne-haute. La rétrodiffusion des micro-ondes est sensible à la

biomasse aérienne (*Above-Ground Biomass, AGB*), et cette sensibilité atteint vite une saturation selon la polarisation et la longueur d'onde utilisée (Thuy Le Toan et al., 1992; Kj. Ranson and Sun, 1994; Rignot et al., 1994). La déforestation cause une diminution importante dans le signal SAR, visible dans le temps (Kellndorfer, 2019).

Actuellement, seuls les deux satellites de la mission Sentinel-1 de l'Agence Européenne de l'Espace sont en cours de fonctionnement avec un capteur SAR en bande C, dont les données sont accessibles gratuitement dans le cadre du programme Copernicus. Ces deux satellites fournissent des données à une résolution spatiale de 5 x 20 m et temporelle de 6 à 12 jours (en mode *Interferometric Wideswath)* depuis 2014 et 2016 respectivement (Torres et al., 2012).

L'objectif principal de cette thèse est d'exploiter le potentiel des images Sentinel-1 pour la détection de changements du couvert forestier. Les résolutions spatiale et temporelle des images Sentinel-1 ont permis de développer des algorithmes de détection de perturbation du couvert forestier en temps quasi-réel et différé pour la réalisation de bilans de déforestation. Le produit temps quasi-réel de détection de changement du couvert forestier dans la bande intertropicale et l'objectif industriel principal de cette thèse pour l'entreprise VisioTerra. Dans ce but, une méthode de détection de changements sur série temporelle, la méthode des sommes cumulées des résidus (CuSum), a été employée, améliorée et pourrait être mise à disposition sur des plateformes en ligne telles que VtWeb ou FlegtWatch.

Les objectifs suivants ont été adressés dans ce manuscrit de thèse :

(i) Proposer une méthode de détection de changement basée sur l'analyse des séries temporelles qui pourrait aussi bien en temps quasi-réel qu'en temps différé à partir des séries d'image Sentinel-1 pour identifier les changements de couvert forestier.

Cet objectif a été atteint par la sélection de l'algorithme *CuSum* qui répond à ces exigences. L'algorithme CuSum se base sur la surface séparant la courbe des coefficients de rétrodiffusion et la moyenne de cette courbe. Lorsque cette surface atteint un maximum, un point de changement potentiel est déclaré et une analyse de *bootstrap* (rééchantillonnage aléatoire de la série temporelle des coefficients de rétrodiffusion) est réalisée pour valider ou invalider le changement, en fonction du critère de sensibilité en entrée de l'algorithme (*Critical Threshold* : T_c). L'analyse de la pertinence des cartes de détection a été réalisée par les statistiques de matrice de confusion entre une carte de référence produite par interprétation visuelle d'images optiques et les cartes de résultat du CuSum.

Les premiers résultats de l'algorithme appliqué aux acquisitions effectuées en polarisations VV et VH indépendamment présentaient des lacunes liées au nombre d'omissions (faux négatifs) ou de commissions (faux positifs). En effet, le nombre d'omissions était trop élevé lorsque le T_c était élevé, alors que le nombre de commissions était trop élevé dans le cadre d'un faible T_c. Il était donc nécessaire d'améliorer l'algorithme pour le rendre plus précis. Les détections basées sur VV ou sur VH présentaient également un trop grand nombre de faux positifs : l'intersection des deux cartes de résultat a produit de meilleurs résultats (VV x VH).

(ii) Améliorer l'algorithme de détection pour réduire le nombre de faux positifs et faux négatifs dégradant les résultats.

Cet objectif a été atteint au moyen de trois améliorations majeures. La première amélioration de l'algorithme consiste en une recombinaison spatiale des résultats de l'analyse temporelle à différents niveaux de seuil critique T_c. Son développement est décrit en plus ample détail dans le chapitre IV et a mené à une publication dans le journal scientifique évalué par des pairs *International Journal of Applied Earth Observation and Geoinformation* et une note de conférence à l'*International Geoscience and Remote Sensing Symposium* édition 2021. Cette recombinaison est réalisée en plusieurs étapes :

- Premièrement, le CuSum doit être lancé avec une valeur T_c élevée et avec une valeur T_c plus basse, dans le cadre de l'étude, T_c = 1.00 et T_c = 0.75 pour obtenir des cartes de polygones de changement.
- Ensuite, l'intersection entre les polygones issus du haut T_c et ceux du bas T_c est analysée : tout polygone du bas T_c ne présentant pas au moins une intersection avec un polygone de haut T_c est supprimé. Ainsi, tout polygone de bas T_c repose sur une base robuste de haut T_c, diminuant le nombre de faux positifs en sortie par rapport à l'ensemble des résultats du bas T_c. Les polygones de bas T_c étant plus larges que ceux de haut T_c, le nombre de faux négatifs est réduit par rapport au haut T_c. A l'issu de cette recombinaison surnommée cross-T_c, les statistiques ont augmenté par rapport au simple T_c pour atteindre une *Precision* de 0.77, une *Accuracy* de 0.91, un *Recall* de 0.55 et un *Kappa coefficient* de 0.59 pour les paramètres suivants : VV x VH cross-T_c 100_75.

La première version de la méthode ne permettait de détecter qu'un seul changement. Dans l'objectif de différencier déforestation et dégradation, une version '*multiple-breakpoints'*, multi-changements, a été proposée et testée sur une nouvelle zone d'étude au Parà, en Amazonie Brésilienne. C'est le développement du ReCuSum, qui produit des cartes de nombre de changements par pixel. Son développement et l'analyse des résultats obtenus sont présentés

dans le chapitre V et font l'objet d'une publication soumise dans L'*International Society for Photogrammetry and Remote Sensing* et d'une note de conférence à l'*International Geoscience and Remote Sensing Symposium* édition 2022. Le ReCuSum se base sur l'application du CuSum de manière récursive : si un point de changement valide est détecté dans une série temporelle, celle-ci est scindée en deux et le CuSum est relancé indépendamment sur chacune des séries. Au cours de l'étude des résultats, il a été mis en évidence que le nombre de changements était lié à la nature de la surface du pixel : les zones de végétation basse / champs d'agriculture / sols nus présentent plus de changements que les zones de coupes ou dégradations situées dans la partie forestière.

Ce changement de nature *Single-breakpoint* en *Multiple-breakpoints* a donc permis de définir un seuil basé sur le nombre de changements, T_{nbc} pour différencier les changements situés sur des pixels de forêt des changements situés sur des pixels de non-forêt (sols nus, végétation secondaire, champs agricoles). Les pixels présentant un nombre de changement dans les polarisations et T_c recommandés supérieur à T_{nbc} sont supprimés de la carte de résultats VV x VH cross-T_c. Réaliser cette étape de seuillage a permis d'augmenter les *Precision, Accuracy, Kappa Coefficient* et *F1-score* par rapport au CuSum cross-T_c VV x VH 100_75 : la Precision augmente à 0.49 (+11%), l'*Accuracy* augmente à 0.89 (+9%), le *Kappa coefficient* à 0.53 (+9%) et le *F1-score* à 0.59 (+7%).

Lors de l'analyse des résultats, il était apparu que le CuSum cross-T_c arrivait à détecter jusqu'à 90% de la surface végétale non-forestière (*Recall* = 90%). La troisième et dernière amélioration en date du CuSum consiste à créer un masque de non-forêt à partir du CuSum cross-T_c lancé sur une période antérieure à la période de suivi (créer une *'forest baseline'* au début de la date de suivi). Cette méthode permettrait d'éliminer 90% des faux positifs liés à la végétation secondaire / agriculture / sol nu. Cette étape d'application d'un masque de non-forêt a été appelé '*rm_hist'* pour '*Remove historic'*. L'application de cette étape a permis d'augmenter sur cette zone la *Precision* à 0.70, l'*Accuracy* à 0.94, le *Kappa coefficient* à 0.70 et le F1-score à 0.74.

L'application conjuguée des deux dernières améliorations a permis d'atteindre des valeurs de *Precision* de 0.81 (+43%), d'*Accuracy* de 0.95 (+11%), de *Kappa coefficient* de 0.72 (+28%) et de *F1-score* de 0.74 (+22%). Cependant, il faut considérer également que le taux d'omission augmente : le *Recall* diminue à 0.68 (-14%). On ne détecte plus que 68% des aires à détecter.

(iii) Développer le CuSum version temps quasi-réel et réaliser une comparaison des différents produits temps-quasi-réels sur une grande zone d'étude en Amazonie.

Cette dernière partie a permis de répondre aux objectifs industriels de la société VisioTerra. Le CuSum temps quasi-réel connaît une contrainte principale : il doit se baser sur un nombre restreint d'images avant / après la date à analyser. Il n'est donc pas possible d'employer le ReCuSum dans ce but. Le CuSum-NRT (*Near-Real-Time*, temps quasi-réel) aura donc les améliorations de cross-T_c et de rm_hist, mais pas de T_{nbc} (voir Figure ci-dessous). De plus, les seuils de sensibilité employés dans les études précédentes ont été définis arbitrairement. Une analyse complète de l'espace des possibilités des 4 paramètres d'entrée du CuSum-NRT (Nombre d'images avant la date à analyser, nombre d'images après la date à analyser, haut T_c, bas T_c) a été réalisée dans la même zone que le chapitre V, dans le but de déterminer les meilleurs paramètres d'entrée. Les paramètres suivants ont produit les meilleurs résultats de l'analyse :

Polarisation	Nombre d'images avant	Nombre d'images après	Valeur du haut T_c	Valeur du bas T_c
VV x VH	11	3	100	92

La *Precision* obtenue est de 0.68, le *Recall* de 0.72, l'*Accuracy* de 0.93, le *Kappa coefficient* de 0.67 et le *F1-score* de 0.71. Ces valeurs sont proches des valeurs obtenues pour le ReCuSum avec application de rm_hist et T_{nbc} (voir tableau ci-après).

	Precision (%)	Recall (%)	Accuracy (%)	F1-score	Kappa coefficient
ReCuSum 100_75	81	68	95	0.74	0.72
CuSum NRT 100_92	68	72	93	0.71	0.67

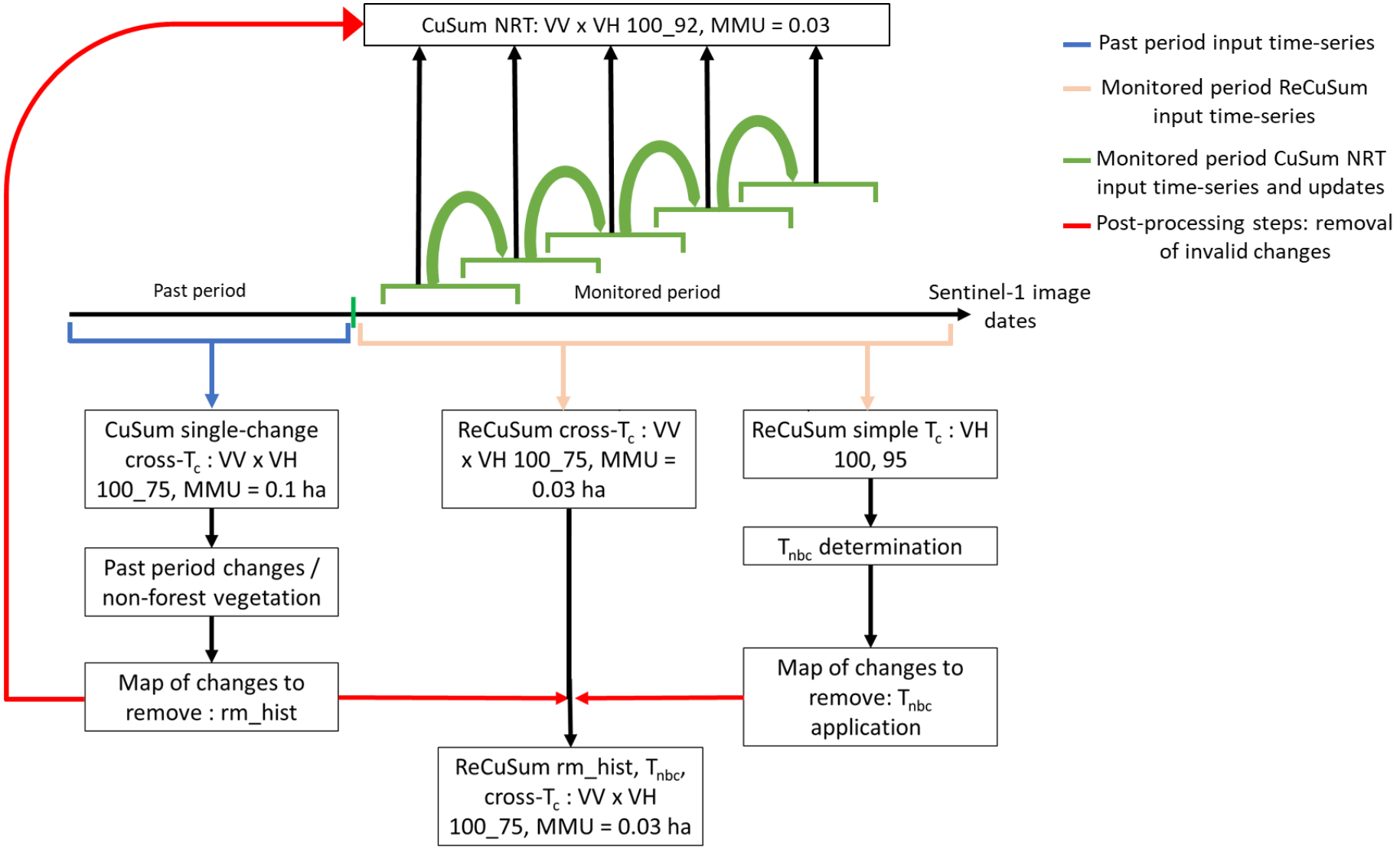

Modes de fonctionnement et étapes de post-traitement du CuSum-NRT et du ReCuSum

Table of Contents

List of Figures

List of tables

Scientific production

Publications

Ygorra, B., Frappart, F., Wigneron, J.P., Moisy, C., Catry, T., Baup, F., Hamunyela, E. and Riazanoff, S., 2021. Monitoring loss of tropical forest cover from Sentinel-1 time-series: A CuSum-based approach. *International Journal of Applied Earth Observation and Geoinformation*, *103*, p.102532.

Ygorra, B., Frappart, F., Wigneron, J.P., Moisy, C., Catry, T., Pillot, B., Kharlanova, A., Riazanoff, S. *ReCuSum: a polyvalent method to monitor tropical forest disturbances.* Submitted in: *International Society for Photogrammetry and Remote Sensing.*

Frappart, F., **Ygorra, B.,** Wigneron, J.P. *Forest cover change from spaceborne SAR sensors: A review.* Work in progress.

Ygorra, B., Frappart, F., Wigneron, J.P., Moisy, C., Catry, T., Pillot, B., Riazanoff, S. *CuSum cross-T_c Near-Real-Time development and comparison for tropical forest disturbance monitoring*. Work in progress.

Conference notes:

Ygorra, B., Frappart, F., Wigneron, J.P., Moisy, C., Catry, T., Baup, F., Hamunyela, E. and Riazanoff, S., 2021, July. Deforestation Monitoring Using Sentinel-1 SAR Images in Humid Tropical Areas. In *2021 IEEE International Geoscience and Remote Sensing Symposium IGARSS* (pp. 5957-5960). IEEE.

Ygorra, B., Frappart, F., Wigneron, J.P., Moisy, C., Pillot, B., Puiseux, J., Riazanoff, S., 2022. Classification and deforestation monitoring using Sentinel-1 C-SAR images in a temperate exploited pine forest. In *2022 IEEE International Geosciences and Remote Sensing Symposium IGARSS.* IEEE.

Other works:

Wigneron, J.P., Li, X., Liu, X., Wang, M., Frappart, F., Fan, L., Al-Yaari, A., Fernandez-Moran, R., Ma, H., **Ygorra, B**. and Xing, Z., 2021, July. Alternate Inrae-Bordeaux VOD indices from SMOS, AMSR2 and ASCAT: Overview of recent developments. In *2021 IEEE International Geoscience and Remote Sensing Symposium IGARSS* (pp. 6210-6213). IEEE.

Frappart, F., Wigneron, J.P., Li, X., Liu, X., Al-Yaari, A., Fan, L., Wang, M., Moisy, C., Le Masson, E., Lafkih, Z.A., Vallé, C., **Ygorra B**. and Baghdadi N. 2020. Global monitoring of the vegetation dynamics from the Vegetation Optical Depth (VOD): A review. *Remote Sensing*, *12*(18), p.2915.

List of abbreviations

AGB	**:**	Above-Ground Biomass
AMI	**:**	Active Microwave Instrument
ALOS	**:**	Advanced Land Observing Satellite
AOD	**:**	Aerosol Optical Depth
ASAR	**:**	Advanced Synthetic Aperture Radar
AVHRR	**:**	Advances Very High Resolution Radiometer
BFAST	**:**	Breaks for Additive Season and Trend
BUDD	**:**	Bayesian Updating Deforestation Detection
CL	**:**	Confidence Level
CuSum	**:**	Cumulative Sum algorithm
CuSu-SMC	**:**	Cumulative Sum – Spatial Mean Corrected
DETER	**:**	Near-Real-Time Deforestation Detection System
DEM	**:**	Digital Elevation Model
DRC	**:**	Democratic Republic of the Congo
DTM	**:**	Digital Terrain Model
ENVISAT	**:**	ENVIronment SATellite
EM	**:**	ElectroMagnetic
EO	**:**	Earth Observation
ERS	**:**	European Remote Satellite
ESA	**:**	European Space Agency
ETM	**:**	Enhanced Thematic Mapper
FN	**:**	False Negative
FP	**:**	False Positive
GCP	**:**	Ground Control Points
GEE	**:**	Google Earth Engine
GFW	**:**	Global Forest Watch

GLAD	**:**	Global Land Analysis and Discovery
GLCM	**:**	Grey Level Co-Occurrence Matrix
GNSS-R	**:**	Global Navigation Satellite System Reflectometry
GRD	**:**	Ground Range Detected
HH	**:**	Horizontal emission – Horizontal reception
HV	**:**	Horizontal Emission – Vertical reception
IFCO	**:**	Industrie Forestière du COngo
IGARSS	**:**	International Geoscience and Remote Sensing Symposium
INPE	**:**	Brazil's National Institute for Space Research
InSAR	**:**	Interferometric Synthetic Aperture Radar
IRD	**:**	Institut de Recherche pour le Développement
IRF	**:**	Impulsion Repetition Frequency
ISPRS	**:**	International Society for Photogrammetry and Remote Sensing
ISRO	**:**	Indian Space Research Organization
IW	**:**	Interferometric Wide Swath
JAXA	**:**	Japan Aerospace Exploration Agency
JERS	**:**	Japanese Earth Remote Sensing Satellite
JICA	**:**	Japan International Cooperation Agency
JJ-FAST	**:**	Jica-Jaxa forest early warning system
LULC	**:**	Land Use Land Cover
MLE	**:**	Maximum Likelihood Estimator
MMU	**:**	Minimum Mapping Unit
MODIS	**:**	MODerate-resolution Imaging Spectroradiometer
MSI	**:**	Multi Spectral Instrument
NASA	**:**	National Aeronautics and Space Administration
NDVI	**:**	Normalised Difference Vegetation Index
NICFI	**:**	Norway's International Climate and Forest Initiative
NIR	**:**	Near-InfraRed
NISAR	**:**	NASA-ISRO SAR mission
NRT	**:**	Near-Real-Time
OA	**:**	Overall Accuracy
OLI	**:**	Operational Land Imager
ONF	**:**	Office National de la Forêt
PALSAR	**:**	Phased-Array L-band Synthetic Aperture Radar
PNCBMCC	**:**	Programa Nacional de Conservacion de los Bosques para la Mitigacion del Cambio Climatico

PRODES : Projeto de Monitoramento do Desmatamento na Amazônia por Satélites
PSE : Programme de Paiement pour Service Environnemental
RADAR : Radio Detection And Ranging
RADD : Radar for Detecting Deforestation
ReCuSum : Recursive Cumulative Sum algorithm
REDD+ : Reduced Emissions from Deforestation and Degradation
RF : Random Forest
RGB : Red Green Blue
RVI : Radar Vegetation Index
SAOCOM : Satélite Argentino de Observaion Con Microondas
SIR-C : Shuttle Imaging Radar C
SLC : Single-Look Complex
SR : Surface Reflectance
TanDEM-L : TerraSAR-X add-on for Digital Elevation Measurement
T_c : Critical Threshold
TCL : Tree Cover Loss
TIRS : Thermal Infrared Sensor
TM : Landsat Thematic Mapper
TN : True Negative
T_{nbc} : Threshold based on the number of changes
TOAR : Top Of Atmosphere Radiance
TP : True Positive
UDM2 : Usable Data Masks
UNFCCC : United Nations Framework Convention on Climate Change
VH : Vertical emission – Horizontal reception
VV : Vertical emission – Vertical reception
VWC : Vegetation Water Content
WOS : Web Of Science
WRI : World Resource Institute

CHAPTER I.

GENERAL INTRODUCTION

Table of content

1.1. Introduction

The tropical forests play a critical role in the global climate regulation by recycling between ~2.1 Gt $CO_2.y^{-1}$ (Federici et al., 2015; Nunes et al., 2020) and 7.0 Gt $CO_2.y^{-1}$ (Harris et al., 2021). These forests are being deforested at increasing rates. Recent studies have shown that tropical rainforests are both a sink / source in the carbon cycle with an overall neutral budget (Fan et al., 2019). Increased global awareness of climate change and degradation of tropical forests has not decreased deforestation rates over time. According to the Global Forest Review published by the World Resources Institute (WRI) in Washington, DC, USA, in 2021, the annual loss of tree cover has increased continuously since the beginning of the monitoring by (Hansen et al., 2013), in the year 2000, reaching 12 million hectares in 2020. In Africa and Amazonia, the forest losses in carbon stocks are driven by multiple factors, including legal or illegal selective logging causing degradations, or cuts to fulfil the agricultural needs of local populations (Contreras-Hermosilla and others, 2000; Creese et al., 2019; Gatti et al., 2021; Kleinschroth et al., 2019; Lescuyer et al., 2011; Qin et al., 2021; Umunay et al., 2019). There was an urgent need for a monitoring system at large scale and with fine temporal and spatial resolutions. Remote sensing has been identified as a key tool for Reduced Emissions from Deforestation and Degradation (REDD+) initiative of the United Nations Framework Convention on Climate Change (UNFCCC, Lynch *et al.*, 2013).

Two main types of Earth Observations are used for deforestation monitoring: active microwave (RADAR) or passive (optical remote sensing). The resolution at which images were acquired by both passive / active methods increased with time, as the resolution went from kilometres to now decametres, metres and even decimetres. This increase, along with the computational capacities / technological evolutions, allowed for monitoring systems to detect ever decreasing size of disturbances.

First, optical remote sensing has been commonly used to monitor changes in forest cover, as the methods provided accurate results on many regions (Bullock et al., 2020; Hansen et al., 2013; Tyukavina et al., 2018). Yet, the monitoring systems based on this kind of images are likely to provide inaccurate information over regions strongly affected by cloud cover (Doblas et al., 2020; Hansen et al., 2016; Weisse et al., 2019). They were also shown to be less robust in regions where forest exhibits strong seasonal variability in the canopy water content (Hamunyela et al., 2017). Nevertheless, several operational systems were developed and are still issuing forest disturbances alerts to this date (Bullock et al., 2020; Diniz et al., 2015; Hansen et al., 2016, 2013). Such systems are an important element in the deforestation rate decrease in Brazil (Assunção et al., 2017).

In order to reduce the impact of the cloud cover, the potential of active sensors was explored for the monitoring of deforestation. Active sensors at C- and L-bands are known to penetrate through the clouds (Joshi et al., 2015). The Synthetic Aperture Radar (SAR) allowed to produce C-band and L-band images at medium high resolution. Microwave backscatter was found to be sensitive to forest total Above-Ground Biomass (AGB). This sensitivity reaches saturation for a certain level of AGB depending on polarization and wavelength (Thuy Le Toan et al., 1992; Kj. Ranson and Sun, 1994; Rignot et al., 1994). The forest backscatter signal is dominated by volume scattering at both L and C-bands (Andersen et al., 2006; Thuy Le Toan et al., 1992; Shakil Ahmad Romshoo et al., 2002). Deforestation affects the SAR signal, causing a backscatter decrease more important than the speckle, visible over time (Kellndorfer, 2019).

Currently, there are two satellite missions providing images at high resolution: Sentinel-1 with a C-SAR sensor onboard, developed by the European Space Agency (ESA) in the framework of the Copernicus program composed of two satellites launched in 2014 and 2016, respectively (Torres et al., 2012). It provides SAR images at C-band at 5 x 20 m spatial resolution in IW mode (see Chap. 2 for more details). Advanced Land Observing Satellite 2 (ALOS-2), launched in 2014, is the second satellite currently operating, with a L-SAR (Phased-Array L-band Synthetic Aperture Radar 2,PALSAR-2) sensor onboard, from the Japan International Cooperation Agency (JICA) – Japan Aerospace Exploration Agency (JAXA), acquiring images at 50 m spatial resolution (Arikawa et al., 2014). The current advantage for ALOS-2 PALSAR-2 is that L-band is less impacted by the presence of raincells and penetrates deeper in vegetation cover compared to C-band. Sentinel-1 has a better spatial and temporal resolution, as the revisit time of a scene ranges from 6 to 12 days compared to 42 days (ALOS-2).

There is only one operational system working Near-Real-Time based on PALSAR-2 imagery at the present time. This system uses the JJ-FAST algorithm. It produces a forest disturbance alert map at a Minimum Mapping Unit of 2 ha (Watanabe et al., 2018, 2017, 2017). More recently, many approaches have been developed using Sentinel-1 SAR images. A new approach is to use the shadow created by a change in forest cover in the opposite side of the satellite (Ballère et al., 2021; Bouvet et al., 2018; Mermoz et al., 2021). (Reiche et al., 2021; Zhao et al., 2022) used machine learning to monitor disturbances in forest cover based on Sentinel-1 time-series. (Doblas et al., 2020; Hoekman et al., 2020; Kellndorfer, 2019; Mistry et al., 2021; Ruiz-Ramos et al., 2020) used time series change point analysis methods to detect disturbances using Sentinel-1.

At the beginning of this PhD, only Kellndorfer and Ruiz-Ramos had developed algorithms detecting changes in mangroves and temperate forest based on Sentinel-1 time-series of image. These processing chains had not been applied as widely as today on tropical rainforests. There was a lack of literature on Sentinel-1 capabilities to monitor accurately tropical forest disturbances, and this field of research needed to be developed.

1.2. Thesis objectives and outline

This PhD was funded by VisioTerra through CIFRE contract managed by ANRT (CIFRE number 2019/0457). VisioTerra is a French independent company specialised in scientific consulting in Earth Observation. VisioTerra provides several services online, including data visualisation, indexes computation, DEM evaluation, oil spill monitoring, … Recently, VisioTerra developed a new program for deforestation monitoring in subtropical Africa. This PhD was funded for this purpose, with the main objective being the development of an algorithm monitoring deforestation near-real-time based on Sentinel-1.

1.2.1. Thesis objectives

In the context of monitoring changes in forest cover in tropical regions, the main scientific objectives of this doctoral thesis were presented in the previous section. Earlier, we emphasized the need for a forest cover change monitoring system based on high resolution radar. Early in my PhD, there was a lack of literature on tropical forest cover change monitoring using Sentinel-1 SAR time-series. The temporal and spatial resolutions of the Sentinel-1 images allowed for the development of both offline and Near-Real-Time algorithms monitoring changes in forest cover. The combination of both features shows potential for improvement for monitoring changes in tropical forest cover. We chose to explore this field to develop a Near-Real-Time algorithm that would be processed on-the-fly as the achievement of the CIFRE industrial objective.

Thus, the overall purpose of this manuscript is to produce a tropical forest cover change NRT monitoring system based on Sentinel-1 time-series of images. In addition, an existing method, the CuSum, has been used and improved for this particular objective and could soon be available on online platforms such as VtWeb or FlegtWatch. The following objectives have been addressed in this doctoral dissertation:

(i) Selection of a change detection algorithm for time-series that could work in both Offline and Near-Real-Time (online) modes and develop it for forest cover change monitoring on Sentinel-1 time series.

(ii) Improvement of the change detection method to reduce the number of false positives and false negatives found to impede the results.

(iii) Development of the Near-Real-Time version of the CuSum

To achieve these objectives, we first selected the Cumulative Sum algorithm as the basis of our approach to monitor changes in forest cover. This algorithm was described in (Kellndorfer, 2019; Manogaran and Lopez, 2018; Ruiz-ramos et al., 2018) and seemed promising in terms of application to Sentinel-1 time-series. I first tried it as an offline product requiring a long time-series. I then focused on the improvements made to this method, as it was initially based only on the temporal aspect of the Sentinel-1 time-series of images. I improved the method by adding a spatial recombination of the result using different various sensitivity levels in the input settings. Then, the 'single breakpoint' feature of the algorithm was improved to become a 'multiple breakpoints' feature. This feature enabled the definition of a threshold that further improved monitoring of changes in forest cover. Using the different results of the Offline version, I then developed the NRT version of the CuSum cross-T_c and compared it with the ReCuSum. The results from the comparison between CuSum-NRT and other NRT operational algorithms (RADD, JJ-FAST, DETER-R, PRODES, DETER-B) will be later added to this manuscript.

1.2.2. Thesis outline

The results of this doctoral project are presented through 7 chapters, each chapter corresponding to a research objective outlined in the preceding section.

Chapter I lists the context and motivation, the research scope and the objectives of this doctoral dissertation.

Chapter II provides background on RADAR technique, including the presentation of the Sentinel-1 mission, whose data were used during this PhD.

The state-of-the-art of forest cover change monitoring using remotely sensed SAR images is described in Chapter III. It includes sensors and methods unused in this manuscript.

The development of the first methodology, CuSum cross-T_c is described in Chapter IV. The methodology of the CuSum algorithm with bootstrap is developed and applied to time-series of Sentinel-1 images. This purpose of this method is to assess changes in forest cover on tropical forest in a forest concession near Kisangani, in the Democratic Republic of the Congo. The addition of the cross-T_c step to the original CuSum method includes the spatial dimension of the data. The results of the different methods and input parameters are described and discussed.

Chapter V presents the development of the new ReCuSum approach for forest cover change assessment. This product is also offline, thus requiring a long time-series to be efficient. This new method enables multiple breakpoints to be found in the time-series, comparatively to the single-breakpoint feature of the original / cross-T_c CuSum. The capability of the CuSum cross-T_c to monitor all types of cover changes was analysed in order to create a non-forest mask through Sentinel-1. New post-processing steps were added, such as the application of a threshold based on the number of changes per pixel (T_{nbc}). The definition and application of a non-forest mask based on Sentinel-1 time series was also done in this chapter.

The development of a new CuSum-based Near-Real-Time method is presented in Chapter VI. A parameters sensitivity analysis was performed using Monte-Carlo's method.

Chapter VII is a summary of the whole doctoral dissertation, including concluding remarks, the limitations of this research, the outlook and insights.

CHAPTER II.

RADAR REMOTE SENSING

Table of content

Chapter 2 – Radar remote sensing

2.1. The RADAR technique

RADAR (Radio Detection And Ranging) is an active technique which can be used for Earth observations. Radar methods present the advantages of being able to penetrate clouds (as it operates in microwaves wavelengths) and to be able to acquire images during the night (as an active remote sensing method). Radar sensors operate in the electromagnetic spectrum microwave frequency domain (300 MHz to 300 GHz). The principle of radar used for Earth observation applications consists in emitting and receiving an electromagnetic wave in a selected configuration (incidence angle, frequency and incidence angle, Figure II.1**Erreur ! Source du renvoi introuvable.**). The electromagnetic wave is emitted at a wavelength $\lambda = \frac{c}{f}$ as an impulsion of τ_p time, from an antenna characterized by a G gain. The distance R to the target is determined from the time t between emission and reception following the equation $R = \frac{ct}{2}$, with c the wave velocity. The wave energy is partly scattered in the direction of the reception antenna (the same as the emission antenna in the case of spaceborne sensors). This backscatter depends on the physical properties of the target (morphology, moisture, nature of the material, …(Flores et al., 2019)).

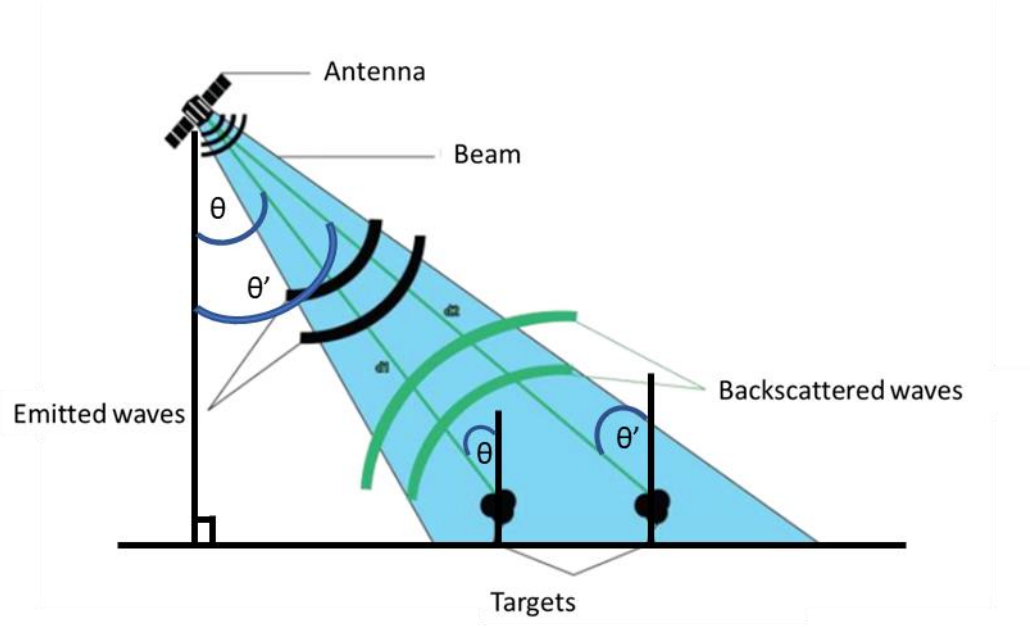

Figure II.1: Imaging radar principle. A signal is emitted from the sensor atop the antenna, the surface receives the signal and interacts with it before backscattering the electromagnetic waves to the antenna. θ and θ' are the incidence angle. Image modified from lucas Ternynck - Satellite from Jose luis Algara and tree image from James Keuning.

The configuration used in satellite radars is mostly the monostatic configuration, with GNSS-R being multistatic. In this configuration, the emission antenna is the same as the reception

antenna. The echo backscatters from objects interacting with the incident wave and are sorted by arrival order.

The radar impulsions are spaced according to Eq.1:

$$P_a = \frac{V}{IRF} \quad \text{Eq.1}$$

where V is the celerity, P_a the distance and IRF the impulsion repetition frequency. The IRF is subjected to two main constraints:

- The minimal frequency is a function of the signal sampling: The sampling needs a record number by time unit at least twice higher than the difference between the minimal and maximal frequency of the signal it contains according to Shannon-Nyquist theorem. For SAR systems, a resolution cell is subjected to two successive impulses. The Doppler effect induces a small frequency shift between the two echoes. This frequency shift constitutes the minimal frequency, determined by the impulsion bandwidth: $B_D = 2\frac{V}{L}$ where V it the satellite movement speed (km/s) and L the antenna length (km).
- The maximal frequency is a function of the echo physical record: the minimal time for the record is δ_t = F / c, where c is the light celerity and F the swath width (Eq.2):

$$F = \frac{\lambda}{W} r \cos\theta_M \quad \text{Eq.2}$$

This leads to the following framing of IRF:

$$\frac{2V}{L} < IRF < \frac{cW}{2\lambda r \cos\theta_M}$$

The electromagnetic wave received by the sensor is characterised by its amplitude A (obtained from its intensity I = A²), its angular frequency $\omega = 2\pi f$ (Rad.s^{-1}) and its phase (Eq.3):

$$\psi(r,t) = A\cos(\omega t + \varphi) \quad \text{Eq.3}$$

The wave intensity I characterises the radar backscatter coefficient σ^0 (m².m^{-2}), which is related to the observed environment characteristics. It is calculated using the simplified radar equation, based on the signals, target characteristics and the system parameters (Eq.4).

$$P_r = \frac{P_t G^2 \lambda^2}{(4\pi)^3 R^4}\sigma^0 \leftrightarrow \sigma^0 = \frac{P_r (4\pi)^3 R^4}{P_t G^2 \lambda^2 S} \quad \text{Eq.4}$$

where P_r is the received power (Watts), P_t is the transmitted power (Watts), S is the effective surface seen by the antenna (m²), λ is the wavelength (m) and G is the antenna gain. σ^0 is influenced by the surface backscatter properties (physical parameters, cover, topography,

roughness, moisture) and by the radar properties (incidence angle, wavelength, polarisation). σ^0 behaves similarly to the bidirectional optical reflectance. It is usually set to decibels (dB, Eq.5, (Massonnet and Souyris, 2008; Ulaby et al., 2014):

$$\sigma^0 = 10.log_{10}(\sigma^0_{lin}) \quad \text{Eq.5.}$$

2.2. Instrumental parameters

2.2.1. Incidence angle

The incidence angle θ is the angle between the normal surface and the incident propagation direction, in the plane of propagation (see Figure II.1). Sensors can be either mono-angular (with a fixed sight / incidence angle) or multi-angular using variable-focus antennas. With these antennas, images can be acquired with different incidence angles ranging from 20° to 46° for Sentinel-1 images.

2.2.2. Polarisation

The polarisation is a property of the electromagnetic wave emitted by the sensor emission/reception modes. The polarisation describes the electric field orientation in the plane orthogonal to the direction of propagation. If the wave is linear and the field is contained in the incident plan (yOz, Figure II.2), the polarisation is vertical. If the electric field is orthogonal to the incident plan, the polarisation is horizontal. In the Earth Observation field, only two directions are used: vertical or horizontal. This leads to multiple emission/reception polarisation possibilities: VV and/or HH for single polarisation and VV, VH, HH, HV for dual polarisations. VH stands for Vertical emission, Horizontal reception.

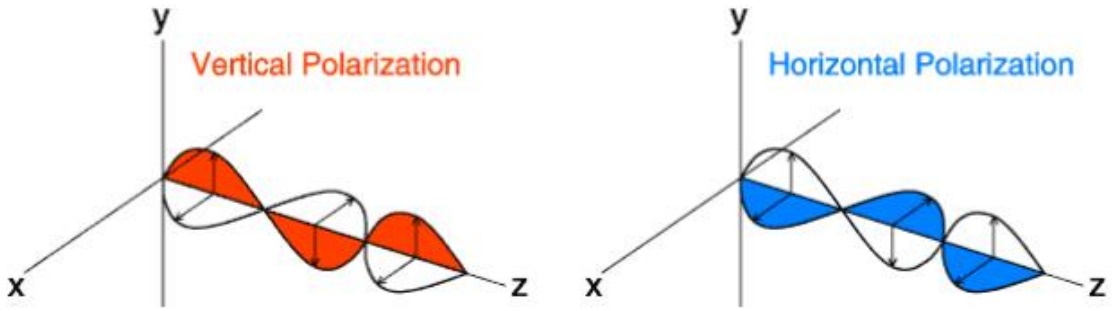

Figure II.2: Polarisation as a function of the electromagnetic field and incidence plane.

2.2.3. Radar frequency

Radar systems operate in the microwave wavelength domain. The frequency of a transmitted signal is the number of waves emitted during the interval of one second, measured in Hertz (Hz). The Table II.1 lists the main bands used by spaceborne Synthetic Aperture Radar (SAR) sensors as Sentinel-1, used in this PhD.

Agency	Satellite / constellation	Sensor	Lifetime	Band	Wavelength (cm)
European Space Agency (ESA)	BIOMASS	/	To be launched	P	70
German Aerospace Center (DLR)	TanDEM-L	SAR-L TandemL	To be launched	L	24.6
National Space Development Agency of Japan (NASDA)	JERS – 1	JERS-1 SAR	1995 - 1998	L	24.6
Japan Aerospace eXploration Agency (JAXA)	ALOS-1	PALSAR	2006-2011	L	24.6
JAXA	ALOS-2	PALSAR-2	2014-	L	24.6
Indian Space Research Organization (ISRO) & National Aeronautics and Space Administration (NASA)	NISAR	/	To be launched	L	24.6
Argentina space agency CONAE	SAOCOM	LBI	2018-	L	24.6

ESA	ENVISAT	ASAR	2002-2012	C	5.6
ESA	ERS-1 & 2	AMI	1991-2001	C	5.6
		AMI	1995-2011	C	5.6
Canadian Space Agency (CSA)	RADARSAT	Radarsat-1	1995-2013	C	5.6
		Radarsat-2	2007-	C	5.6
ESA	SENTINEL-1	Sentinel-1	2014-	C	5.6

Table II.1: List of the available space-sensors for C- and L-bands.

The frequency, linked to the wavelength, is an important factor in vegetation monitoring due to the penetration depth it induces. Different frequencies monitor different parts of trees, as they are able / unable to penetrate the canopy (*Figure II.3*, (Flores et al., 2019; Kellndorfer, 2019)). For example, a C-band signal only penetrates the top layers of the canopy of the forest, scattering mostly on the tree branches. L-band and above all P-band signals much deeper penetrates the canopy as their wavelength is longer than the C-band. For forest monitoring, the C-band scattering is mostly roughness scattering with some volume scattering whereas bands with higher wavelength (lower frequency) can experience volume scattering with double-bounce scattering on tree trunks or natural corner reflector.

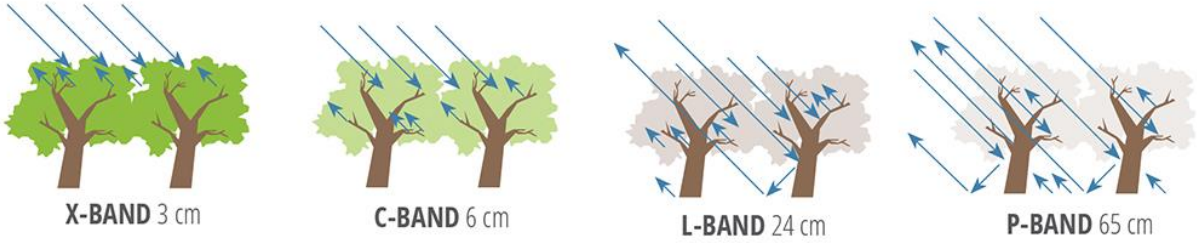

Figure II.3: Signal penetration over a forest according to the band. Image credits: NASA SAR handbook.

2.3. Scattering mechanisms

The backscattered signal carries information about the structure of the imaged surface. There are three main scattering types: double-bounce, surface and volume scattering (*Figure II.4*). Double-bounce scattering is caused by the presence of tree trunks, inundated areas below the vegetation (though simple bounce can also occur on inundated areas) or building. Rough surface scattering is often caused by bare rough soil or water. It is known to be most

sensitive to VV scattering. The volume scattering can be cause by leaves and branches in a forest canopy is most sensitive to cross-polarized data (VH, HV).

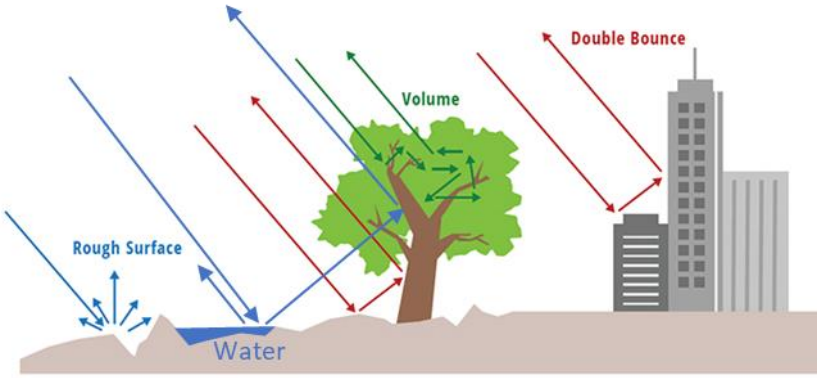

Figure II.4: The 3 scattering mechanisms: rough surface, volume and double bounce on ground, water and buildings. Image credits: NASA SAR Handbook, modified.

2.4. Synthetic Aperture Radar

In Earth Observation, the resolution of the images is coarse in order to be compatible with the applications. With no processing, a spatial radar system has a native resolution of several kilometres. The SAR technique increases the resolution to meters or tenths of meters. The resolution is a function of the antenna length: a longer antenna has a better resolution at the price of increased weight and clutter.

The SAR system consists in simulating a long antenna with ad hoc signal processing (*Figure II.5*). The antenna is simulated by the radar movement along the satellite trajectory, creating observations from several points of view giving information on phase, amplitude. the SAR processing cascade combines those to create an artificial radar signal for the synthetical high-sized antenna. Similarly to the non-SAR techniques, electromagnetic waves are emitted at a given frequency (impulsion frequency, see 2.1). These echoes backscatter from objects interacting with the incident wave and are sorted by arrival order. Images are formed from the distance and azimuth directions: the sampling of these echoes constitutes the output image column (direction called ‘in distance’). The output image rows are constituted by the echoes received from impulsions sent during the satellite movement (direction called ‘in azimuth’).

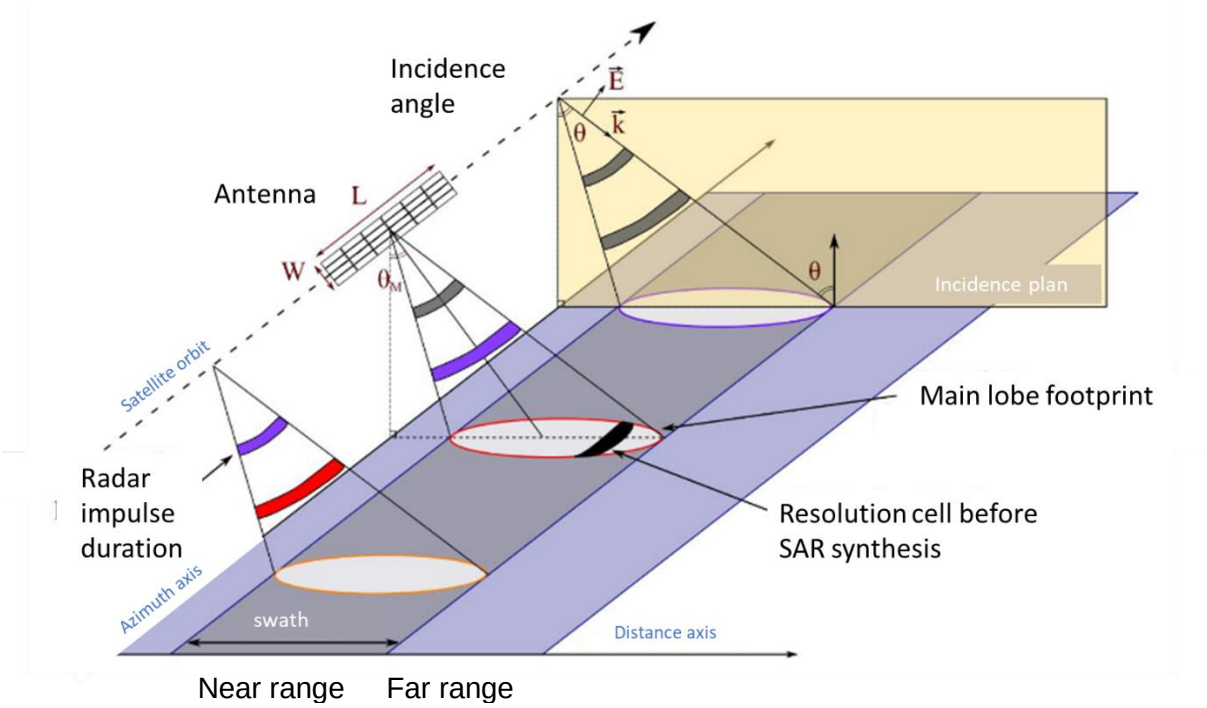

Figure II.5: Radar images acquisition geometry (From Lardeux, 2008, modified).

The targets backscatter coefficients can be presented as an image (azimuth, distance axes). Each measure is presented as a pixel of σ^0 value. SAR images obtained this way can have a high resolution. Each pixel value is the result of the targets physical characteristics within.

The spatial resolution of SAR systems is a factor of two axes: the azimuth and the range axes. In the azimuth direction, multiple echoes are sent. The resolution in azimuth is the shortest distance separating two distinguishable objects. Each axis has its own resolution. The range resolution R_d (km), also called the radar impulsion width τ_p, or the system resolution in radar geometry is defined by the following equation (Eq.6, *Figure II.6*)

$$R_d = \frac{c}{2B} \qquad \text{Eq.6}$$

where B is the bandwidth (Maıtre, 2001) and c the wave propagation celerity ($km.s^{-1}$). A factor ½ is applied due to the two-way travelled distance, result of impulsion compression techniques (generation of an impulsion with a great bandwidth while maintaining a τ_p duration long enough to keep an adequate impulsion power).

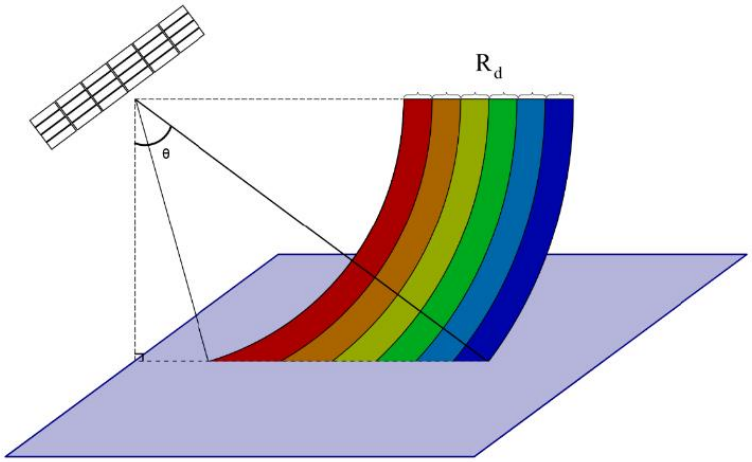

Figure II.6: Resolution in range of a SAR image (Lardeux, 2008)

The effective resolution of the surface image results from the projection of R_d on the ground:

$$R_{d,s} = \frac{R_d}{\sin\theta} = \frac{c}{2B\sin\theta} \quad \text{Eq.7}$$

where θ is the incidence angle defined as the angle between the radar sight direction and the normal to the observed surface.

In the azimuth direction, the first order of the resolution after SAR processing and simplification (as the resolution is a function of all SAR processing parameters) is R_a:

$$R_a = \frac{L}{2} \quad \text{Eq.8}$$

where L is the antenna width.

These two parameters result in the following raw radar pixel size P_d:

$$P_d = \frac{c}{2P_f} \quad \text{Eq.9}$$

Where P_f is the backscattered echo sampling frequency on the distance axis, varying the observed real ground surface within the pixel, due to the incidence angle. A lower angle results in a wider ground area represented by pixel.

Projected to the ground, P_d becomes $P_{d,s}$:

$$P_{d,s} = \frac{P_d}{\sin\theta} = \frac{c}{2P_f\sin\theta} \quad \text{Eq.10}$$

2.4.1. SAR products processing level

Radar images obtained using the aforementioned methods are raw with a part coded in the complex domain. There are 3 main processing levels: 0 (RAW), 1 (SLC) and 1 (GRD

2.4.1.1. RAW products

In the RAW products, the target is part of both l1 and l2 rows backscatter (*Figure II.7*). This effect needs to be accounted for using a deconvolution to SLC images.

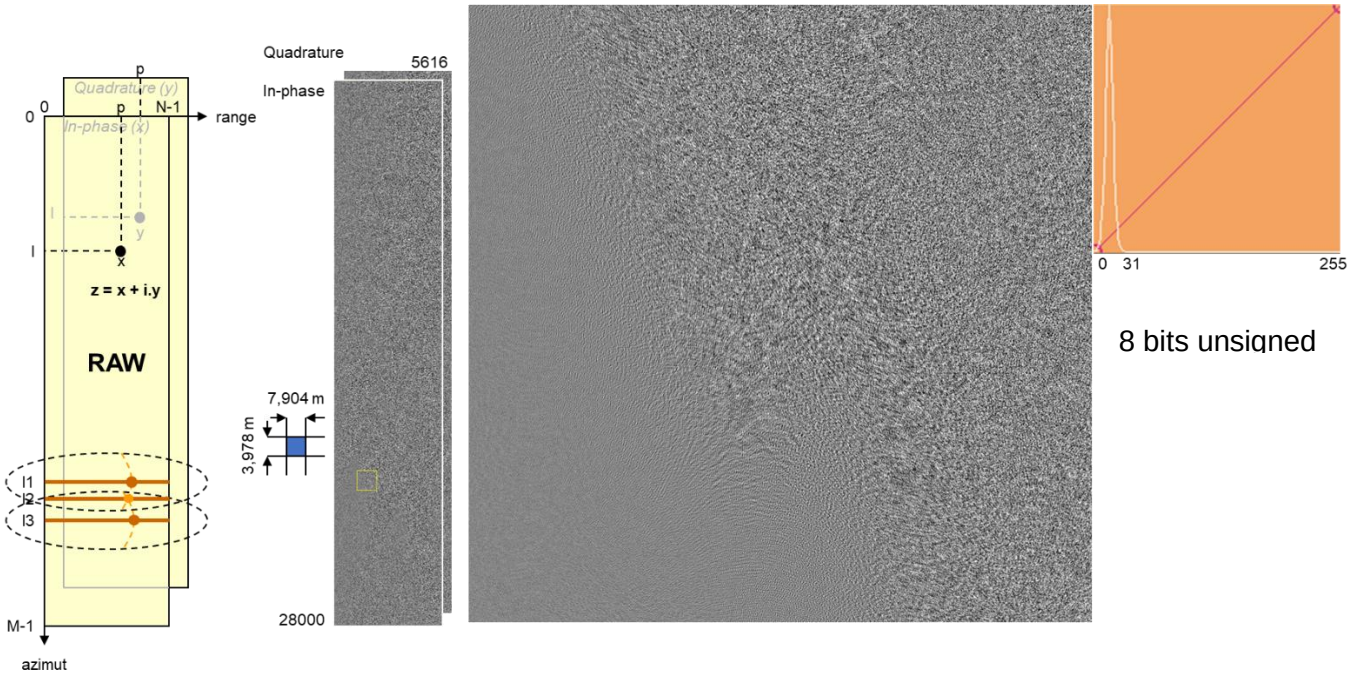

Figure II.7: RAW image from ERS-SAR scene dated 27/02/1999 at Naples (Italy). Image credits: Riazanoff S.

2.4.1.2. Single Look Complex (SLC) images

SLC products are obtained by deconvoluting the RAW images. These images are constituted from a single look, thus conserving their base resolution (*Figure II.8*). They are given in slant-range geometry (radar range observation coordinate), defined as the line-of-sight from the radar to each reflecting object. Each row of pixels represents points along a line perpendicular to the satellite track (Sentinel-1 SAR Copernicus user guide).

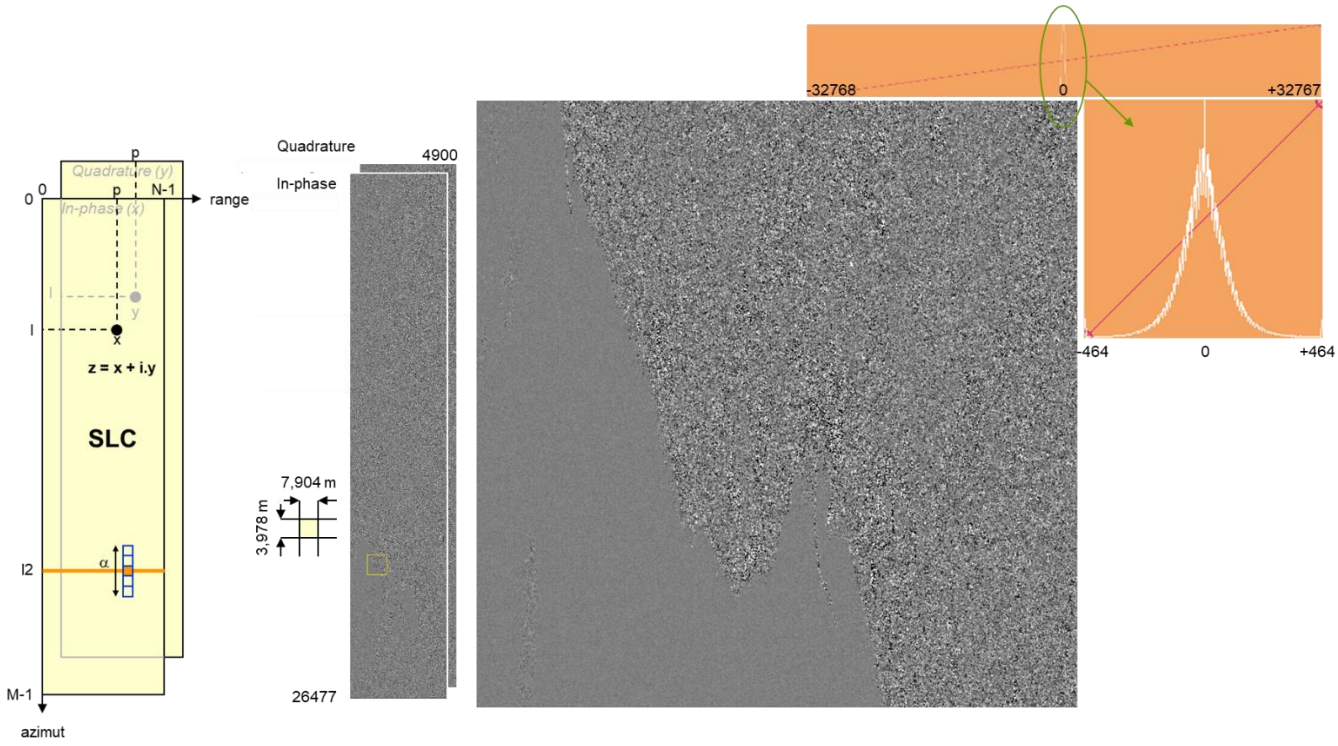

Figure II.8: SLC result image after RAW image deconvolution. Scene from ERS-SAR dated 27/02/1999 at Naples (Italy). Image credits: Riazanoff S.

2.4.1.3. Ground Range Detected (GRD) images

GRD images are obtained by applying 3 processing steps to the SLC images. Firstly (Figure II.9a), the image is compressed in azimuth (factor $\frac{1}{\alpha}$). The result image is then projected slant-to-ground (Figure II.9b). Last, the amplitude is computed to obtain the GRD image (Figure II.9c). These products are multi-looked. It is also corrected using terrain height, varying in azimuth but constant in range. The pixel value is the detected magnitude and the phase information is lost (Sentinel-1 SAR Copernicus user guide).

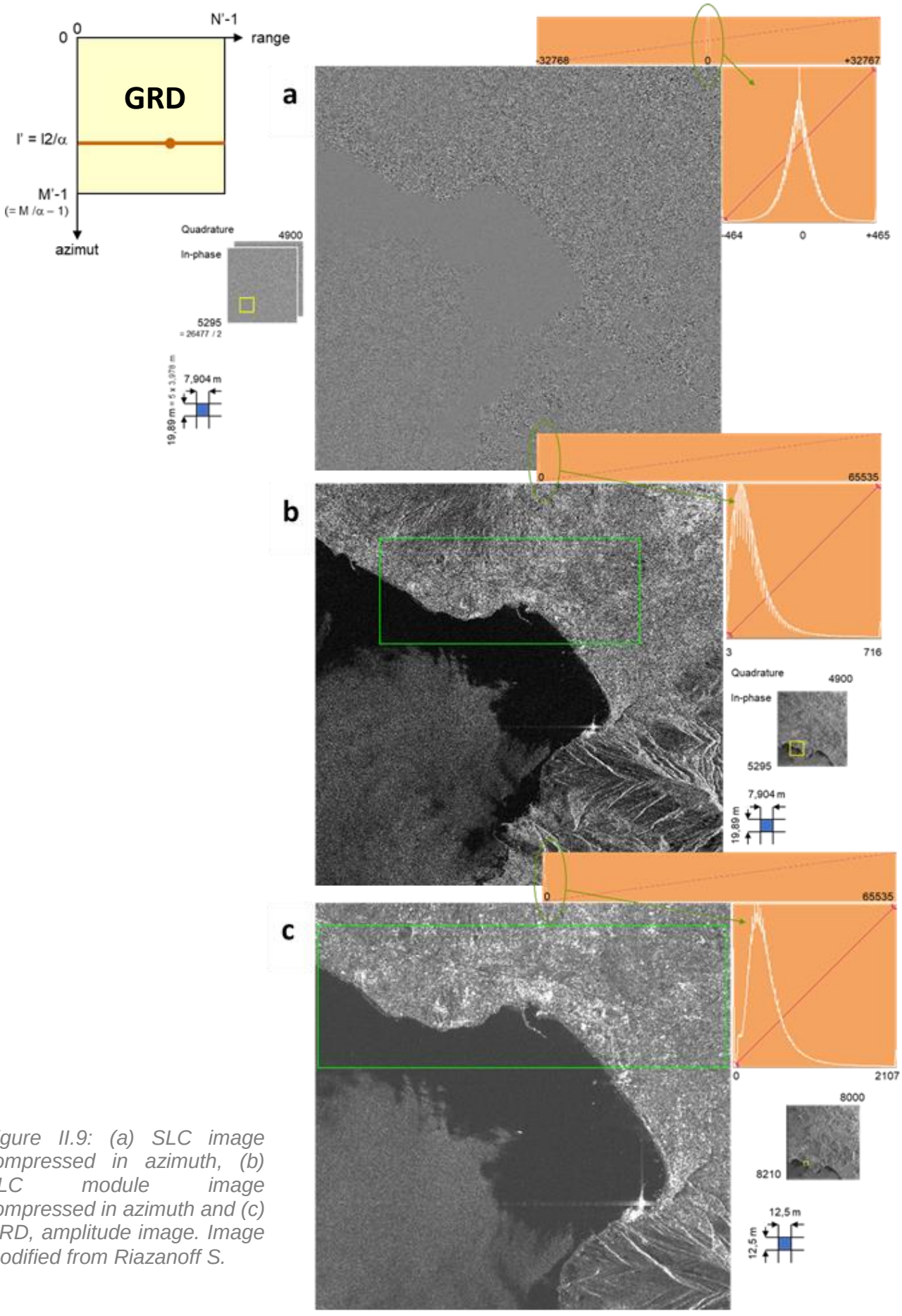

Figure II.9: (a) SLC image compressed in azimuth, (b) SLC module image compressed in azimuth and (c) GRD, amplitude image. Image modified from Riazanoff S.

2.4.2. Speckle effect

SAR images are degraded by the speckle phenomena. The speckle effect is a noise degrading the image information. It is created by the interaction of elementary targets with the signal within the resolution cell limit. It is often modelized as a random multiplicative noise (*Figure II.10*, Goodman, 1975; Elachi, 1988; Ulaby *et al.*, 2014). Each resolution cell will have its own target interactions. This results in a SAR image with a noisy granular aspect. Each elementary scattering element is characterized by a complex response S_{nXY} of module $|S_{nXY}|$ and phase ϕ_{nXY}, where X and Y are the polarisations. The backscatter of a resolution cell results from the following equation:

$$z = i + jq = \sum_{n_{XY}=1}^{N} a_{n_{XY}} . e^{j\phi_{n_{XY}}} \quad \text{Eq.11}$$

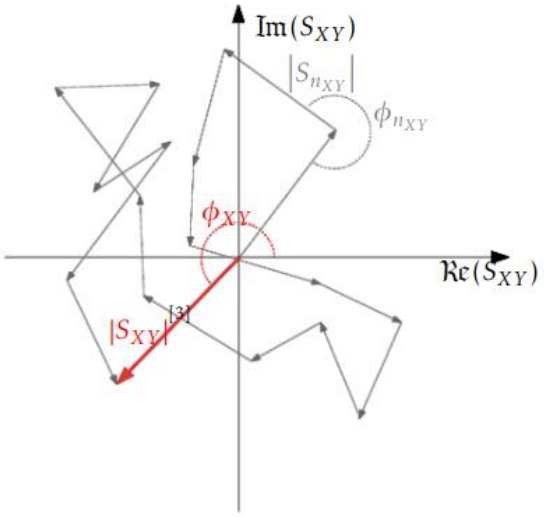

Figure II.10: Representation of the coherent sum of the N = 17 elementary scattering elements within a resolution cell. Grey is the scattering of each scattering element and the coherent sum appears in red. From Giordano, 2015.

The intensity is considered as random with a stable mean according to the presence / absence of speckle. The intensity variance is a function of this noise:

$$V_1 = \sigma^0 S_p \quad \text{Eq.12}$$

Where S_p is the backscatter linked to speckle, equal to $|S_{XY}|$ in *Figure II.10*.

The SAR images are often depicted as hard to interpret due to their granular aspect. Multiple methods have been developed to decrease the impact of speckle on the image. These methods are separated in two groups: image noise filtering (Figure II.11) and multi-look processing. The image noise filtering allows to keep the pixel resolution. They are based on spatial statistics over a fraction of the image surrounding each pixel (Brodu, 2018; Frost et al.,

1982; Kuan et al., 1985; Lee, 1980; Tomasi and Manduchi, 1998) and/or on the temporal statistics of any pixel over a time-series of images (Quegan et al., 2000).

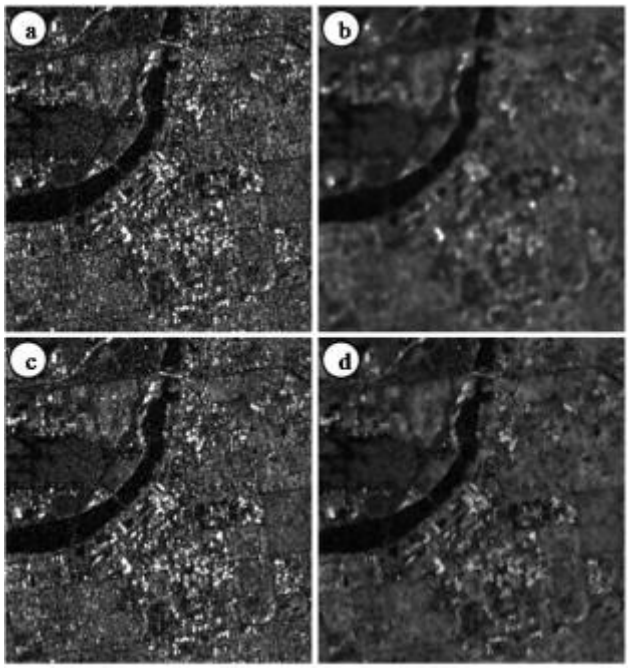

Figure II.11: A detailed image of an urban area; a) the original Radarsat-2 image, and the results of its filtration using b) Median filter, c) Frost filter, d) Lee-sigma filter. From (Kupidura, 2016), modified.

The multi-look processing consists in computing independent measures of a same scene. The mean of the measures is then computed and allows to reduce the variance of the signal, decreasing the effect of the speckle. However, a higher number of looks degrades the resolution. GRD data are often multi-looked whereas SLC data has only one look.

2.4.3. Geometric distortions

As an incidence angle exists between the antenna aperture and the normal to the surface, geometric distortions are bound to appear. Often, the ground surface observed in a SAR image is composed by numerous slope inversions. There are 3 known artefacts: the foreshortening, the layover and the shadow (*Figure II.12*).

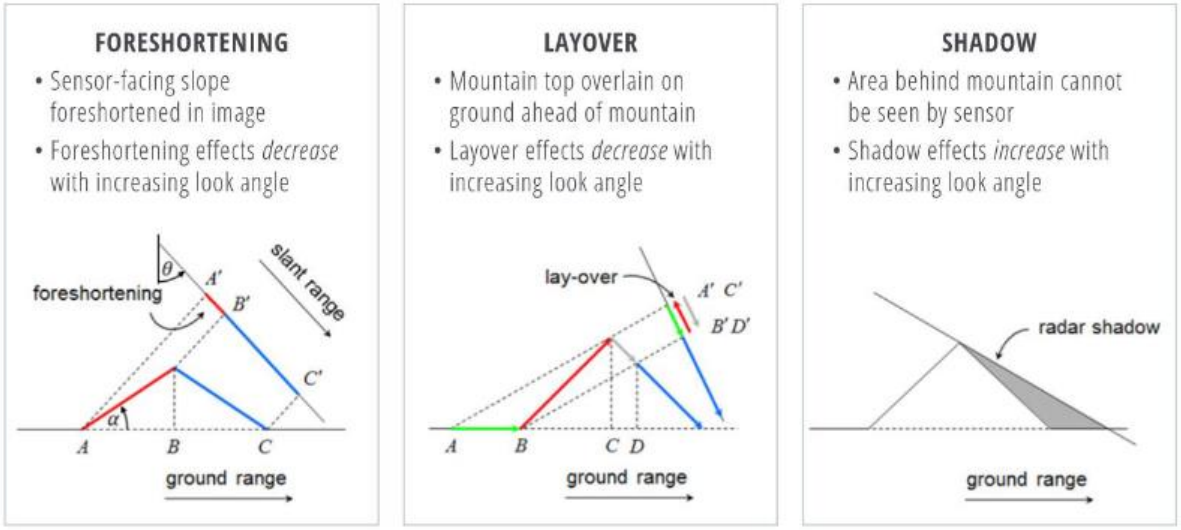

Figure II.12: Geometric distortions appearing in SAR images: (a) foreshortening, (b) layover and (c) shadow. Image from Kellndorfer, 2019*.*

2.4.3.1. Foreshortening

When the slope is lower than the sensor incidence angle, a visual distance compression effect appears in SAR image. This phenomenon is called foreshortening (*Figure II.12*a). The distance between the sensor and the surface is determined using radar echoes, which means that a point located on top of a mountain will be seen as 'nearer' the sensor than a point located at its base. Projected in the image plan, the distance between a and b is seen as shortened.

2.4.3.2. Layover

The layover effect is the opposite of the foreshortening. This artefact appears when the slope is greatly higher than the signal incidence angle *Figure II.12*b). The radar echoes reach the top of the mountain before its base, leading to a layover effect (Inversion of the target points). This phenomenon is visualized as a bright (high backscatter value) pixel in SAR images.

2.4.3.3. SAR Shadow

The third possible artefact is the SAR shadow. The presence of an obstruction or mask between the sensor and its target (e.g. a mountain) disrupts the illumination of the target, causing the SAR shadow (*Figure II.13*, *Figure II.12*c). It is function of the slope 'behind' the obstructing object and the incidence angle. The target area appears as dark pixels in the SAR image due to the signal absence.

2.4.4. SAR processing cascade

In order to perform analyses, corrections to the signal must be performed to extract a performing backscatter coefficient. Multiple stages are necessary and a preprocessing cascade is often done on SAR images (Filipponi, 2019), as original SAR data is distributed in Single-Look Complex (SLC) to keep the original resolution. Ground Range Detected images can also be made available, with the multi-looking process already applied.

2.4.4.1. Radiometric calibration

The images obtained through the SAR method are coded in numerical count. The radiometric calibration changes the pixel numerical counts to backscatter coefficients linked to the targeted surface reflectivity. This step allows to remove the local incidence angle effect between the far-ranged and the near-ranged to obtain γ^0_{lin}, the input to the Terrain Correction by Small, 2011 (*Figure II.13*).

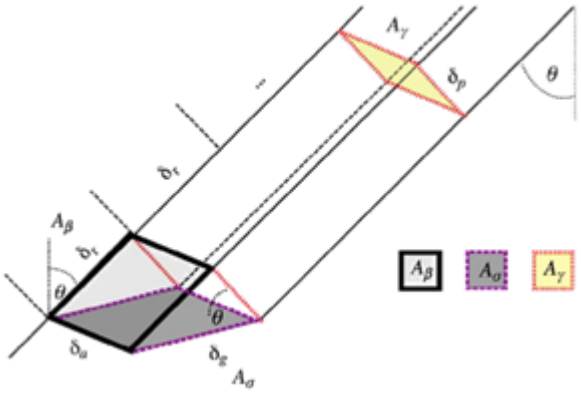

Figure II.13: Normalization areas for SAR backscatter. δ_g is the ground range resolution, δ_r is the slant range resolution. θ is the incidence angle. From (Small, 2011).

2.4.4.2. Range Doppler Terrain Correction

After calibrating the signal, a geometric correction needs to be applied as SAR data are generally acquired with a varying viewing angle greater than 0°. In order to compensate for the aforementioned distortions (layover / foreshortening / shadow), a Digital Elevation Model is often applied in the range doppler terrain correction. The said distortions can then be modelled and accounted for in the image. This step also allows to project the GRD product on the DEM grid to generate a map in the chosen CRS (Small, 2011).

2.4.4.3. Speckle filter

The last preprocessing step applied to the SAR image is the despeckling. which consists in removing the speckle noise (see 2.4.2. Speckle noise). The speckle noise can be removed

efficiently using multilook images, and further image processing noise filtering methods can be applied to GRD images.

2.5. Sentinel-1

2.5.1. Sentinel-1 mission characteristics

Sentinel-1 consists in a satellite constellation composed on two satellites allowing a frequent access to SAR images over the world surface. It is a spatial system with free access to images, developed by the European program Copernicus. Two satellites were launched to constitute the constellation: Sentinel-1a and Sentinel-1b respectively launched on 03/04/2014 and 25/05/2016 (Torres et al., 2012). The satellites are currently orbiting at an altitude of 700 km following a heliosynchronous orbit. The imaging takes place on both ascending and descending orbits. Each satellite has a 12-day revisit period. The phasing of the two revisit periods allows for a revisit period of 6 days mainly for European countries (*Figure II.14*). Each satellite has a C-band SAR imager aboard, producing 5 x 20 m spatial resolution images.

Sentinel-1 has multiple acquisition modes: Strip Map, SpotLight, ScanSAR and Interferometric Wide swath (IW). All Sentinel-1 imagery used in my PhD was obtained using the IW mode.

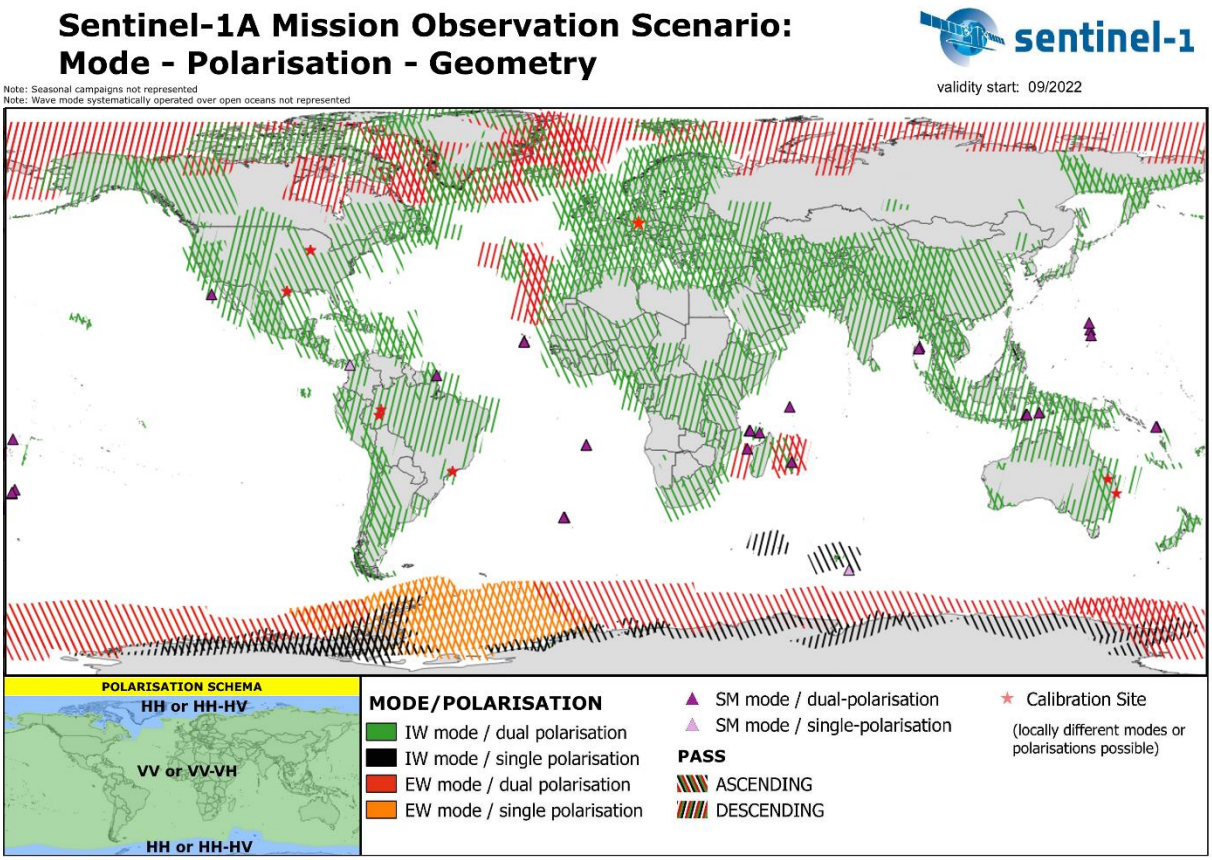

Figure II.14 Worldwide coverage frequency of the Sentinel-1 mission. Source: https://sentinels.copernicus.eu/web/sentinel/missions/sentinel-1/observation-scenario

Sentinel-1 images have a spatial resolution of 5 x 20 m in Interferometric Wide swath mode. The IW mode consists in acquiring large swath images by dividing it into three sub-swaths. The sensor acquires bursts alternatively on each sub-swath (Figure II.*15*). A video describing the process is available on the ESA website at: http://www.esa.int/Our_Activities/Observing_the_Earth/Copernicus/Sentinel-1/Instrument. Sentinel-1 images can be freely accessed at **https://www.copernicus.eu/en/**.

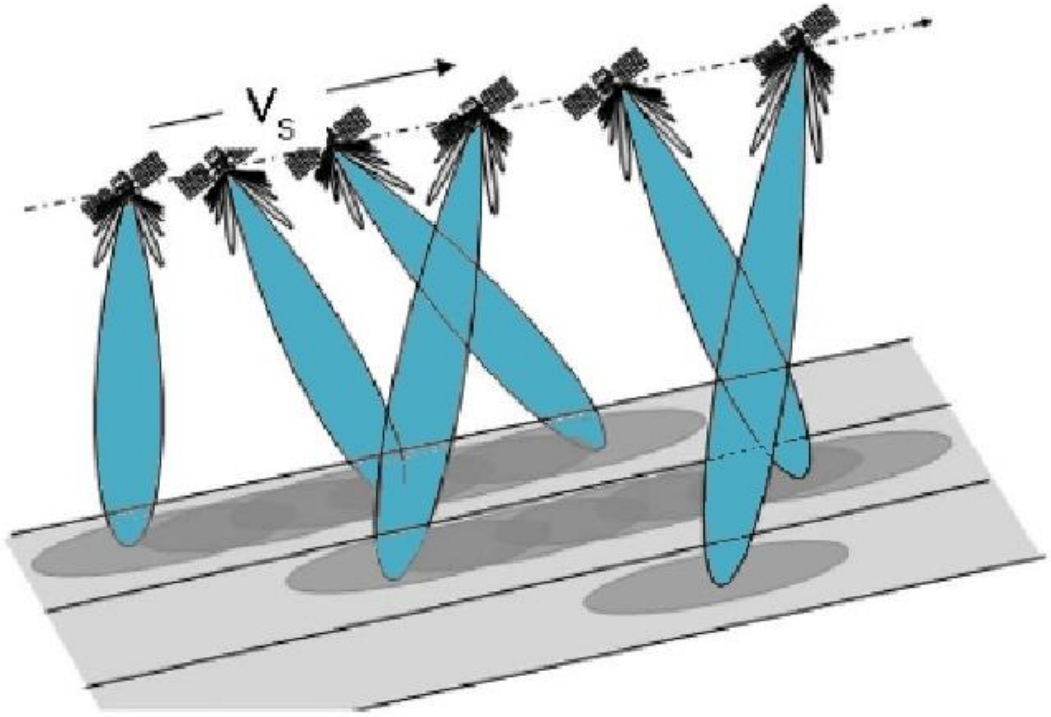

Figure II.15: Interferometric Wide swath acquisition mode (IW). From ESA.

2.5.2. Sentinel-1 preprocessing

In order to perform analyses, corrections to the signal must be performed to extract a useful backscatter coefficient. The preprocessing cascade was described in the previous section. Other preprocessing steps are required to obtain an optimal quality of the Sentinel-1 SAR images. They are described in the following sub-sections.

2.5.2.1. Orbit correction

The metadata information of Sentinel-1 SAR contains orbit state vectors. Those vectors can often be not accurate. The precise orbits are determined several days after the generation of the product and need to be applied to compute the correct orbit of the satellite at the time of the imaging.

2.5.2.2. Thermal noise removal

Sentinel-1 intensity image is disturbed by additive thermal noise. This thermal noise can be particularly found in the cross-polarisation (VH). These effects are reduced by applying routines such as the one described in (Park et al., 2017). The thermal noise is strongly reduced in the inter-sub-swath texture and their removal induces a normalisation of the backscatter signal within the entire Sentinel-1 scene. Discontinuities at the edge are also reduced.

2.5.2.3. Border noise removal

During the generation of level-1 products, in order to compensate for the change of Earth's curvature, the sampling start time needs to be corrected. A compression also takes place at the same time in both azimuth and range, leading to radiometric artefacts at the image borders. The low intensity noise and invalid data can be removed using a border noise removal algorithm (Ali et al., 2018; Luo and Flett, 2018)

.

CHAPTER III. METHODS FOR MONITORING FOREST COVER CHANGE USING SPACEBORNE SAR SENSORS

Table of Contents

Chapter III. Methods for monitoring forest cover change using spaceborne SAR sensors

3.1. Introduction

This section presents the different methods currently existing for monitoring forest cover change using spaceborne SAR sensors. This chapter's content is currently being wrote as a review paper to be submitted to a peer-reviewed scientific journal and is not completed yet. This section summarizes the publication.

According to a search performed on Clarivate Analytics Web of Science (WoS, webofscience.com, last accessed on 25 august 2022), SAR-based forest cover monitoring number of published papers have been increasing since 2008. The number of published papers has risen from 4.1 over 1994-2003 to 7.2 over 2004-2013, reaching 21.6 over the 2014-2021 period (Figure III.1). Over this time, many new methods for forest disturbance detection were developed. It is possible to define three main different categories of methods (detailed in section III.2):

- Thresholds: As SAR-based parameters present a variation higher than the noise level when submitted to cover change, simple thresholds were first developed (Avtar et al., 2012; Rignot et al., 1997; Santoro et al., 2010);
- Classifications: Both unsupervised and supervised classification methods were applied to discriminate forest, non-forest and deforested areas. These methods were applied on InSAR coherence, derived SAR parameters at C, L-bands and directly on SAR backscattering. These methods include Multi-image Segmentation, Maximum Likelihood Estimator, Maximum Bayesian and Decision Tree (Gaveau et al., 2003; Podest and Saatchi, 2002; Saatchi et al., 2000; Servello et al., 2010; Thiel et al., 2006).
- Machine learning methods: These techniques were also employed in forest cover change detection, and include Neural Network, Support Vector Machine and Random Forests methods (Kuplich, 2006; Longepe et al., 2011; Milne et al., 2012; Servello et al., 2010).
- Other statistical approaches: Statistical methods were also applied to detect disturbances in forest cover. These methods include Fuzzy Logic, Bayesian Approach, Adaptative Linear Thresholding and Cumulative Sum (Bujor et al., 2001; Doblas et al., 2020; Durieux et al., 2020, 2021; Manogaran and Lopez, 2018; Reiche et al., 2015, 2018b; Ruiz-Ramos et al., 2020;Ygorra *et al*., 2021b).

This section covers the state-of-the-art change detection algorithms and literature about SAR contributions to deforestation monitoring.

3.2. Publication

Forest cover change from spaceborne SAR sensors: A review

Frédéric Frappart [1,*], Bertrand Ygorra [1,2], Serge Riazanoff[2], Jean-Pierre Wigneron [1]

[1] INRAE, Bordeaux Sciences Agro, UMR 1391 ISPA, 33140 Villenave-d'Ornon, France; frederic.frappart@inrae.fr; bertrand.ygorra@inrae.fr; jean-pierre.wigneron@inrae.fr

[2] VisioTerra, 14 rue Albert Einstein, 77420 Champs-sur-Marne, France; serge.riazanoff@visioterra.fr

* Correspondence: frederic.frappart@inrae.fr

Keywords: deforestation; remote sensing; SAR

3.2.1. Introduction

Forests play a major role in the carbon cycle as they cover more than 60% of the land surfaces and contain 90% of the C in the vegetation and 80% of the C in the soil of the terrestrial ecosystems and take around 60% of the CO_2 removed from the atmosphere (Gower, 2003; Grace et al., 2014). Forests were found to be an overall of -2.1Gt of CO_2 per year between 1990 and 2015, mostly in the tropical and Northern Hemisphere forests (Federici et al., 2015; Mitchard, 2018). Change in Land Use/Land Cover (LULC) represented 12.5% of the anthropogenic emissions over 1990-2010 (Houghton et al., 2012). Deforestation, i.e., the direct, human-induced, conversion of forests to non-forest areas, has been identified as the major factor of change in LULC in temperate regions in the past, and, now, in the tropical areas (Gower, 2003; Hoang and Kanemoto, 2021). From a sink, tropical areas are likely to become a carbon source in the near future (Mitchard, 2018) as the annual forest carbon loss over the tropics doubled between 2001-2005 and 2015-2019 (Feng et al., 2022). Different factors can account for the forest carbon loss including predominantly agriculture activities, especially in Africa and Southeast Asia (Feng et al., 2022), but, also, forest degradation in the Brazilian Amazon (Qin et al., 2021), or logging and public roads in the Congo Basin (Kleinschroth et al., 2019).

Deforestation is the greatest concern in the impact of LULC change, especially in the tropics (Kondo et al., 2022), responsible, among over factors such as overgrazing and inappropriate irrigation practices, for land degradation (e.g., wind and water erosion, changes in vegetation cover, salinization) (Metternicht et al., 2010). The use Earth Observations (EO) images combined with ground measurements is essential for monitoring worldwide, and in particular in remote areas (Achard et al., 2007). EO was identified has a key source of information for Reduced Emissions from Deforestation and Degradation (REDD+) initiative of the United Nations Framework Convention on Climate Change (UNFCCC) (Lynch et al., 2013). First studies on deforestation were based on the use of optical/multispectral images during the 1980s (NELSON et al., 1987; Nelson and Holben, 1986). They lead to the first estimate of deforestation in the Amazon derived from Landsat Thematic Mapper (TM): 162,000 km² of tropical forests were removed between 1978 and 1988 (Skole and Tucker, 1993). Forest monitoring was achieved at coarse resolution (8 km) using Advanced Very High Resolution Radiometer (AVHRR) images at pantropical scale (DeFries et al., 2002) and, later, at medium (250 m using Moderate-resolution Imaging Spectroradiometer - MODIS) and high resolution high resolution (30 m using Landsat) at regional scale (e.g., Brazilian Amazon or Indonesia) (Margono et al., 2012; Morton et al., 2005). These studies paved the way to operational forest cover change product available either globally such as Global Forest Watch (GFW) Tree Cover Loss (TCL) (Hansen et al., 2013) or regionally as in the Project for the Satellite Monitoring of Deforestation (Projeto de Monitoramento do Desmatamento na Amazônia por Satélites - PRODES) in the Brazilian Amazon (Valeriano et al., 2004) or in the GeoBosques platform of the National Forest Conservation Program for Climate Change Mitigation (Programa Nacional de Conservacion de los Bosques para la Mitigacion del Cambio Climatico - PNCBMCC) of the Peruvian Environment Ministry (Ministerio del Ambiente – MINAM) based on the Global Land Analysis and Discovery (GLAD) system (Potapov et al., 2014), for instance. Two main factors limiting the use of optical images for deforestation alert systems were identified:

The persistent cloud cover which can strongly affect the availability of the observations, especially in the intertropical zone (e.g., (Hansen et al., 2016)). The cautious use of multiple EO sensors (optical images from different sources or optical and SAR images) is a solution to overcome this issue (Hansen et al., 2008; Reiche et al., 2015);

The strong seasonal variations in canopy water content and photosynthetic activity of the forest (Hamunyela, 2017).

The potential of satellite Synthetic Aperture Radar (SAR) images in mapping land cover types and monitoring deforestation was early identified, in the mid-1990s, over tropical areas (Grover and Quegan, 1995; Keil et al., 1995; Saatchi et al., 1997), including mangroves (Lucas

et al., 2007), as radar (i.e., active microwave) images offer day and night and all weather observations of the Earth surface (except in presence of rain cells at C (4-8 GHz) and X (8-12 GHz) bands (Marzano et al., 2010; Melshelmer et al., 1996)) contrary to optical images which use is limited due to the presence of clouds, especially in tropical areas during the rainy season or at temperate latitude during winter. The synergy between optical and SAR images was first brought to the forth (Ranson et al., 2003; Rosenqvist et al., 2003; Shimabukuro et al., 2007). Optical images were used to detect deforestation while SAR images provided reliable information of the vegetation regrowth (da C.F. Yanasse et al., 1997; Rignot et al., 1997; Saatchi et al., 1997; Salas and Skole, 1998). The huge interest of SAR acquisitions for monitoring deforestation was also noticed analysing either the observations at the different polarizations (Kuntz and Siegert, 1999; Rignot, 2000; Souyris et al., 1996) or the Interferometry SAR (InSAR) mode (Ribbes et al., 1997; Suga and Takeuchi, 2000). From the first identification of the potential of SAR acquisitions from the Shuttle Imaging Radar C (SIR-C), European Remote Sensing satellite (ERS-1&2), and Japanese Earth Remote Sensing Satellite (JERS-1) (da C.F. Yanasse et al., 1997; Grover and Quegan, 1995; Hoekman, 2000; Keil et al., 1995; Lawrence et al., 1995) for deforestation monitoring to the current operational approaches used to derive early waring/near real-time forest cover loss based on Phased Array L-band Synthetic Aperture Radar-2 (PALSAR-2) and Sentinel-1 images (Ballère et al., 2021; Reiche et al., 2021; Watanabe et al., 2021), improvements in both technical and theoretical aspects of the radar domains were achieved and new methodologies were developed or adapted to be able to monitor the deforestation using active microwave images. This review proposes to synthetize the major advances achieved in this field.

This review has the following outline. Section 2 describes the method used to select the studies included in the review. Section 3 presents the signatures of the forest in SAR images and InSAR data. Section 4 summarizes the different types of approaches to identify the change in forest cover from SAR and InSAR data.

3.2.2. Literature Review on deforestation from SAR remote sensing

To provide the more exhaustive analysis on the topics of the use of remotely-sensed SAR images for the monitoring of deforestation, a systematic literature review was performed. For this purpose, a search was performed on Clarivate Analytics Web of Science (WoS, webofscience.com, last accessed on 25 August 2022) to identify the scientific articles published between January 1991 and August 2022 on this topic using the keywords: “remote sensing” and “deforestation”. The query link is given in Appendix A. A total of 292 scientific articles, conference proceedings, book were found considering the results from “All

Databases". Not relevant publications including airborne SAR acquisitions, land use/land cover (LULC) classifications, … were removed. The results exhibit a clear increase in the number of studies against time over the last 30 years (Figure III.1). The number of publications per decade rose from 4.1 over 1994-2003 (1994 being the year of the first record of our bibliographic search) to 7.2 over 2004-2013, and is currently reaching 21.6 over 2014-2021 (not taking into account 2022 as all the publications are not referred in WOS for the current year yet). The number of references per year on deforestation from SAR RS is above 20 after 2018, and peaking at 34 and 30 in 2020 and 2018, respectively.

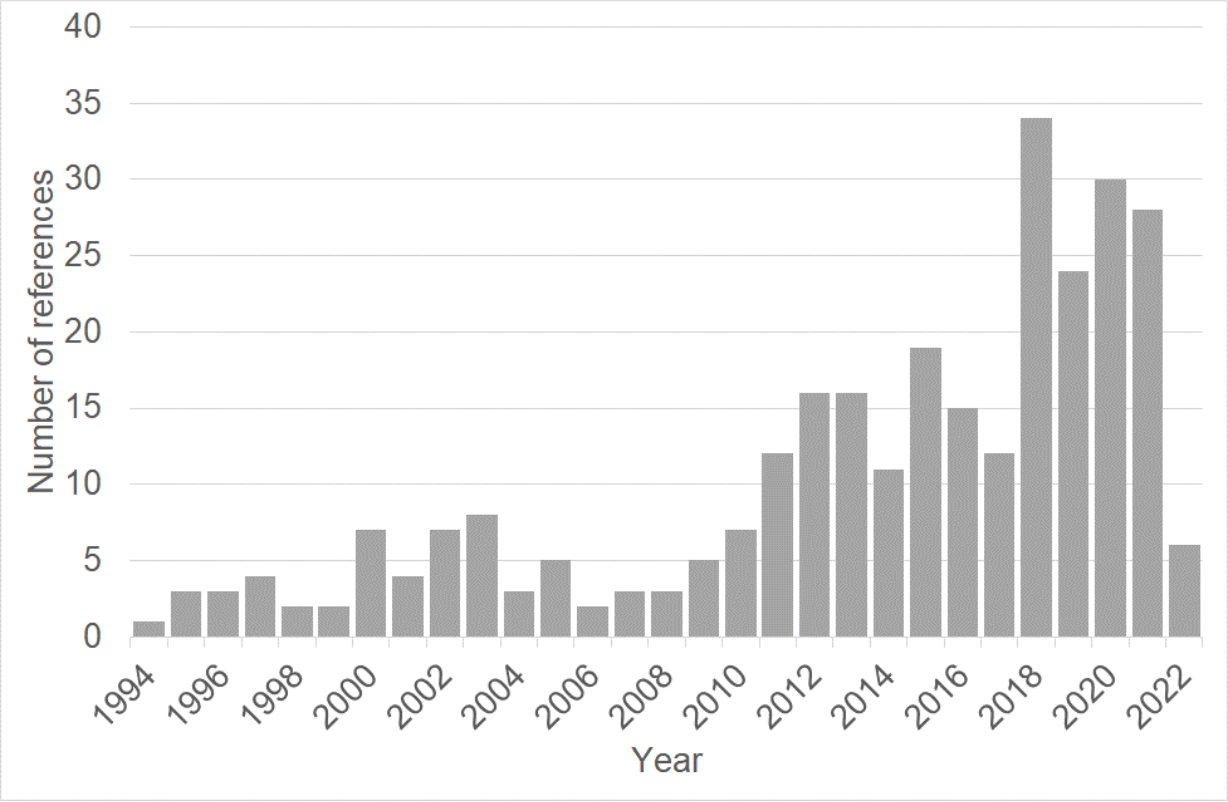

Figure III.1: Temporal evolution of the number of publications per year related to deforestation using SAR RS based on WOS over 1994-2022.

3.2.3. Forest signatures in SAR observations

This section will remind the principles of interaction between the radar wave and the forests.

3.2.3.1. Forest signatures in SAR observations

Microwave backscatter was found to be sensitive to total above-ground biomass (AGB) of forests. This sensitivity is function of the radar wavelength (the lower the frequency, the higher the penetration in the vegetation) and of its polarization and reaches saturation for a certain level of AGB (T. Le Toan et al., 1992; K. J. Ranson and Sun, 1994; Rignot et al., 1994).

Volume scattering dominates the backscatter signal by the forest at both L (1-2 GHz) and C (4-8 GHz) bands while surface scattering is dominating at X (8-12 GHz) band (Andersen et al., 2006; T. Le Toan et al., 1992; S.A. Romshoo et al., 2002). Surface scattering is related to small components of the canopy (i.e., small branches and foliage) which interact with an electromagnetic wave of wavelength between 2.5 and 3.75 cm at X band, while volume scattering is caused by the interactions of the radar of longer wavelength (between 3.75 and 7.5 cm at C band and 15 and 30 cm at L band, and eventually P band between 30 and 100 cm) (Andersen et al., 2006). All microwave frequencies are sensitive to vegetation water content (VWC), and for the ones able to reach the surface underneath the vegetation (especially L and P (0.3 – 1 GHz) bands for forest cover, soil water content (SWC), as well as the vegetation horizontal (row plantations, canopy density) and vertical (crown depth, trunk, branching and leaf structure) structure (Lucas et al., 2011; Rignot et al., 1997). Polarization also plays an important role through its ability to discriminate between forest and non-forest surfaces. The backscatter from the co-polarization (HH and VV) is associated to surface scattering while the backscatter from cross-polarization (HV and VH) is associated with volume scattering. HV (related to volume scattering) polarization was found to be related to forest biomass (Almeida-Filho et al., 2005; da C.F. Yanasse et al., 1997; Green, 1998) and useful for detecting new deforestation fronts (Almeida- Filho et al., 2009), especially at L band. The SAR backscatter exhibits higher values over mature and regrowing forests than over clear-felled areas as the contribution of the volume scattering is greater than the direct scattering component from the ground (Santoro et al., 2010).

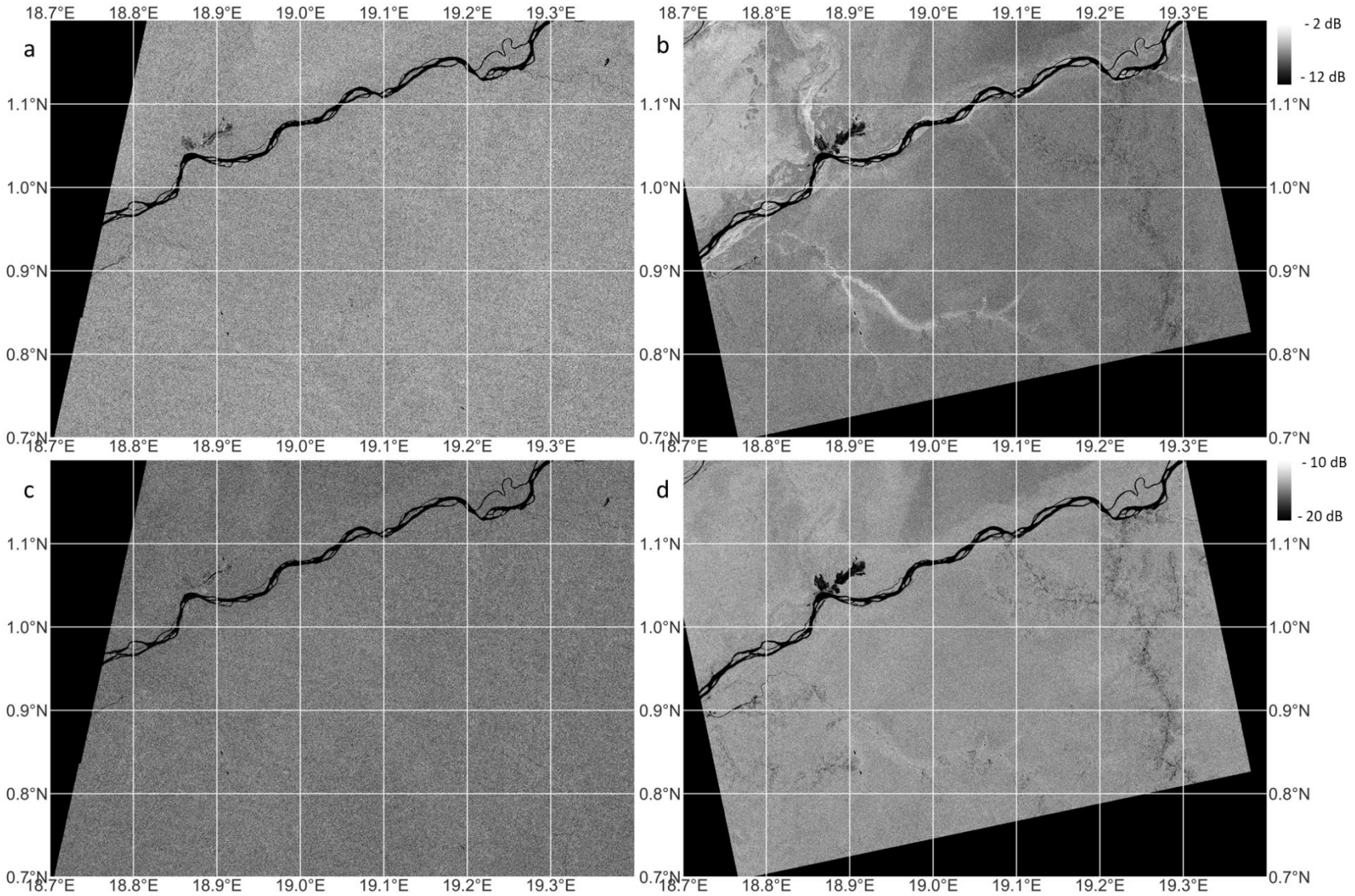

Figure III.2: Comparison between the ASAR image dated 10/07/2010 at VV (a) and VH (c) polarisations with the PALSAR image dated 19/07/2010 at HH (b) and HV (d) polarisations. The area is located in the Democratic Republic of the Congo.

3.2.3.2. Forest characteristics from InSAR

InSAR was also found to be useful for LULC classification. This technique is based on the acquisition of two images under slightly different geometrical configuration. The degree of coherence or coherence (γ), which represents the correlation between the two aforementioned images is defined as (Bamler and Hartl, 1998; Hanssen, 2001; S. Takeuchi et al., 2001):

$$\gamma = \frac{E(s_1 s_2^*)}{\sqrt{E(s_1 s_1^*)E(s_2 s_2^*)}} \quad (1)$$

where s_1 and s_2 are two complex SAR images, and E is the expectation value.*is the conjugate.

Sources of decorrelation, which degrade the coherence, have multiple origins, related to the acquisition system (γ_{syst}), environment properties with both surface (γ_{surf}) and volume (γ_{vol}) interactions, temporal variations (effects of the wind on the branches and the leaves and vegetation growth) (Balzter, 2001; Ribbes et al., 1997):

$$\gamma = \gamma_{syst} \cdot \gamma_{spat} \cdot \gamma_{temp} = \gamma_{syst} \cdot \gamma_{surf} \cdot \gamma_{vol} \cdot \gamma_{temp} \quad (2)$$

The degree of coherence is lower on forest compared to non-forest due to the move of the scattering elements in forest (Le Toan et al., 2004; Takeuchi and Yamada, 2002). The degree of coherence at HH and VV polarizations at C band was also found to be the most suited for discriminating between forest and non-forest pixels (Souyris et al., 1996).

The volume component of the coherence can be related to the vertical profile of the vegetation and, hence, to the vegetation height, structure, and biomass, through (Neumann et al., 2010; Treuhaft et al., 2015, 2009):

$$\gamma_{vol} = \frac{\int_0^{+\infty} g(z) e^{i\alpha_z z} dz}{\int_0^{+\infty} g(z) dz} \quad (3)$$

with

$$\alpha_z = \frac{2\pi B_\perp}{\lambda r \sin(\theta)} \quad (4)$$

Where α_z is the vertical interferometric frequency, g(z) is the normalized Fourier transform of the radar power profile in the vertical direction z, $B_\perp$ is the component of the baseline perpendicular to the sensor line of sight, λ is the wavelength of the electromagnetic wave emitted by the radar, r is the range (i.e., the distance from the sensor to the ground location), and θ is the incidence angle.

Most of the estimates were achieved using P (airborne), L and C bands (Le Toan et al., 2004). Recent studies demonstrated the feasibility of biomass estimates over tropical forests using X-band InSAR from Tandem-X (Treuhaft et al., 2015). The degree of coherence was found to be more sensitive to the changes in woody biomass than the backscatter at C and L bands (Gaveau et al., 2003).

3.2.4. Deforestation from SAR images: Methods

This section will summarize the main approaches used to detect deforestation in the SAR images, and present the main products for forest cover change based on radar observations. When available, information on band and polarization is mentioned. This latter information is sometimes omitted in a few articles, and, hence, cannot be reported in this review.

3.2.4.1. Thresholds

Change detection methods applied to SAR images are based on the evidence that one or a combination of SAR-based parameters are presenting a variation higher than the noise level to be detected when the land cover change from forest to non-forest from one pixel to another or from one acquisition to another (e.g., the backscatter at HV polarization at L-band (Fransson et al., 2007; Santoro et al., 2010) or at C-band (Zhang et al., 2011)). Based on this observation, simple thresholds were first applied to backscatter and/or SAR-derived parameters such as the image texture or the Radar Vegetation Index (RVI) defined as the ration between linear combinations of cross and co-polarization backscatters (Kim and van Zyl, 2009), to discriminate between forest and non-forest areas. For example, forests were reported to be characterized by:

- higher values of the HV backscatter (~8 dB) at L band compared to clear-cut areas in Rondonia (Brazil) (Rignot et al., 1997);
- higher values of the HV backscatter (~10 dB) at L band and RVI (~0.8) than no-forest areas, in Cambodia among others (Avtar et al., 2012);
- higher backscatters at HH polarization ranging from 4 to 7 dB compared to clear-felled areas in Malaysia (Igarashi et al., 2003) and Sumatra (Takeuchi et al., 2000);
- higher backscatter values at HH polarization (~1.5 dB) in comparison to clear-cuts in a British forest (Thiel et al., 2006);

- higher backscatter at HV polarization, between 2 and 3 dB, at L band in a Swedish boreal forest (Santoro et al., 2010);
- higher backscatter values up to 5 dB at X band and HV polarization compared to clear-cuts in a boreal forest in Canada (Ranson and Sun, 2000);
- higher backscatter values at HH polarization at L and VV polarization at C band (2-3 dB) compared to forests that experienced a disturbance due to logging or fires in Siberia (Ranson et al., 2003);
- higher values of backscatter of 1-2 dB at VV polarization under frozen conditions at C band, as well as of 2-4 dB at HH polarization and a change in coherence of 0.4-0.6 (0.3-0.4) at C(L) band, respectively, compared to deforested areas in Siberia (Gaveau et al., 2003; Santoro and Schmullius, 2004).

But, in many cases, simple thresholds are not sufficient enough to distinguish between forests, disturbed forests and logged areas depending on the frequency and the polarizations available (e.g., HH polarization at C band over Siberia (Ranson et al., 2003), limited utility of C band and multiple polarizations required over most of the equatorial forests (Rignot et al., 1997)). The threshold value is often determined empirically as there are difficulties to define the threshold automatically in certain regions.

3.2.4.2. Classification techniques

Classification techniques (supervised and unsupervised) were widely applied to discriminate between forest, non-forest, and deforested areas (Gaveau et al., 2003; Podest and Saatchi, 2002; Saatchi et al., 2000, p. 200; Servello et al., 2010; Thiel et al., 2006). These techniques were applied on SAR backscattering or on InSAR coherence, or other derived parameters, at both C and L bands, and on a wide range of forest types, from the equatorial areas to the boreal regions, including temperate forests. Among the different classification techniques were used:

Multi-image segmentation. This technique was applied to the mean SAR backscattering coefficients of a series of images acquired at L-band between 1992 and 1998 over temperate and boreal forests located in United Kingdom (UK), Germany, Sweden and Siberia. These sites are characterized with high forest cover but different forest management practices. Detection of forest, non-forest and deforested areas has an overall accuracy (OA) ~90% (Thiel et al., 2006) ;

Maximum likelihood estimator (MLE). This approach was applied either on backscatter images and their texture or on coherence. MLE was used on a multi-scale on SAR images acquired at L-band during low and high water stages in three test sites in the Amazon,

characterized by deforestation, presence of savannas and inundated vegetation, on both their backscatter and their textural features defined by (Robert M. Haralick et al., 1973) on 2 x 2, 4 x 4, and 8 x 8 pixel boxes. Discrimination between forest and no-forest has an OA higher than 90% (Podest and Saatchi, 2002). It was also applied on a time-series of INSAR coherence at C-band over Central Siberia to classify forest woody biomass in terms of growing stock volume. An OA of 80% was obtained (Gaveau et al., 2003). To improve the results, MLE was also used on a combination of backscattering at C and L bands and coherence at C band. OA above 70% were obtained over forests in UK, Sweden, and Siberia (Tansey et al., 2004; Wagner et al., 2003). MLE was tested on SAR backscattering at C band for Near Real-Time (NRT) deforestation in Brazilian Amazonia. Tested on ~6,000 locations in 2019, an OA of 94.4% was obtained (Doblas et al., 2020);

Maximum Bayesian. A two-stage approach was applied to a mosaic of SAR images at L-band acquired during low water stage over the Amazon on 10 x 10 pixel boxes. The Bayesian approach allowed to identify 5 general land categories, and, then textural features were used to refine into 14 subcategory classes, including deforested areas. The OA was estimated to reach 78% (Saatchi et al., 2000);

Decision tree. SAR backscattering and coherence at L-band were also included in a multi-sensor (along with medium resolution multi-spectral images and low resolution radar scatterometer) decision tree classification approach for mapping biomass distribution as they provide useful information on biomass, structure and cover type which allowed to detect, among others, logging and forest degradation with an OA higher than 80% (Saatchi et al., 2007).

3.2.4.3. Machine learning techniques

Machine learning classification techniques were also used to characterize changes in forest cover. Among others, the following techniques were applied:

Neural network (NN). A NN approach was applied on L, C and X bands SAR images at various polarizations (H, HV and VV for L and C bands, and only VV for X band) and multi-spectral images to classify the regenerating forest stages in Amazonia. The use of SAR images allowed to discriminate regenerating from mature forests (0A=80%) but cannot differentiate the different regenerating stages (OA=30%). When adding multi-spectral bands, 5 classes of regenerating forests were determined with an 0A of 87% (Kuplich, 2006);

Support Vector Machine (SVM). This method was applied on L band SAR images acquired at HH and HV polarizations in 2007 in Sumatra. An OA of 70% was reached for LC, including clear-cuts and of 87% for natural forest mapping (Longepe et al., 2011). It was also used on

multi-spectral and L-band backscattering to map land cover change in Tasmania between 2007 and 2009, and on L and X backscattering to identify forest degradation and deforestation in West Columbia between 2007 and 2008. OA was found to reach 98% in the forest/non-forest discrimination (Milne et al., 2012);

Random Forests (RF). Extremely Random Clustering Forests, an extension of classifical RF, was applied on full polarimetric (HH, HV, VH, VV) C band SAR backscattering and associated phase acquired in 2008 and 2009 to discriminate forest and non-forest areas in Brazilian Amazonia. OA were 71% and 89% in 2008 and 2009, respectively, allowing to accurately estimate deforestation during this period (Servello et al., 2010).

3.2.4.4. Other statistical approaches

Other statistical approaches were also applied to detect forest cover changes. Among them, the followings were used to determine forest cover changes:

Fuzzy logic. A two-step approach based on fuzzy subset theory was applied to two C band SAR images acquired before and after a deforestation event that occurred in French Guiana. The first step corresponds to the extraction of the changes and the second consists in to the information of the first step to build a rule to attribute pixels to forest and deforested areas using a probability density function (Bujor et al., 2001);

Bayesian approach. Bayesian approach was developed to update the conditional probability of deforestation using previous and future observations of one or several sensors (Reiche et al., 2015). This method was initially applied to merge Normalized Difference Vegetative Index (NDVI) from multi-spectral images and L band SAR backscatter at HH and HV polarizations for NRT deforestation monitoring. This approach was adapted to combine information from backscatter at L band and HV polarization, C band at VV polarization, and NDVI or SAR backscatter at C band in VH and VV polarizations (Reiche et al., 2018a). OA of 87.4% in evergreen forest plantation in Fiji, 99.8% in Bolivia for tropical dry forests, and above 90% in Sumatra were obtained, respectively. A similar Bayesian approach was also developed to update deforestation using the ratio between the acquisition at VV and VH polarizations at C band, their coherence, and NDVI from multi-spectral images. The Bayesian updating deforestation detection (BUDD) showed that better results were obtained combining NDVI, backscatter and coherence or NDVI and backscatter than backscatter and coherence in the Amazonas and Para states of Brazil over 2018-2019 (Durieux et al., 2020). BUDD was also applied on C band VH backscatter and coherence in Sumatra over 2018-2019. An OA of 99% was obtained (Durieux et al., 2021);

Adaptative linear thresholding. This approach is a statistical method based on the difference between the average and the minimum value of the time-series of the SAR backscatter at C band under the assumption the backscattering is constant over forest. The threshold to differentiate a pixel covered with forest from a pixel non-covered with forest is defined using training samples over forest and non-forest areas. It was tested on the same ~6,000 locations in the Brazilian Amazonia in 2019 as the MLE presented above. A slightly better OA of 95.9% was obtained than for MLE (Doblas et al., 2020);

Cumulative sum (CUSUM). CUSUM is a statistical method used to detect both abrupt and slow variations of a variable measured during a certain time period, based on the cumulative sum between the variable values and its temporal average (Manogaran and Lopez, 2018). After being widely used in the financial sector, its application for monitoring deforestation and forest degradation was proposed by [90]. It was applied on time-series of C band SAR backscatter images at VH and VV polarizations acquired i) in Scotland in 2019, with the addition of a spatial averaging to account for the effect of seasonality at temperate latitudes CUSU-SMC (cumulative sum-spatial mean corrected) (Ruiz-Ramos et al., 2020), in Congo over 2018-2020, with a cross threshold recombination (Ygorra *et al*., 2021a; Ygorra et al., 2021b). Over these areas, OA were 77% and 91%, respectively.

3.2.5. References

1. Gower, S.T. Patterns and Mechanisms of the Forest Carbon Cycle. 2003.

2. Grace, J.; Mitchard, E.; Gloor, E. Perturbations in the Carbon Budget of the Tropics. Global Change Biology 2014, 20, 3238–3255, doi:10.1111/gcb.12600.

3. Federici, S.; Tubiello, F.N.; Salvatore, M.; Jacobs, H.; Schmidhuber, J. New Estimates of CO2 Forest Emissions and Removals: 1990-2015. Forest Ecology and Management 2015, 352, 89–98, doi:10.1016/j.foreco.2015.04.022.

4. Mitchard, E.T.A. The Tropical Forest Carbon Cycle and Climate Change. Nature 2018, 559, 527–534, doi:10.1038/s41586-018-0300-2.

5. Houghton, R.A.; House, J.I.; Pongratz, J.; van der Werf, G.R.; DeFries, R.S.; Hansen, M.C.; Le Quéré, C.; Ramankutty, N. Carbon Emissions from Land Use and Land-Cover Change. Biogeosciences 2012, 9, 5125–5142, doi:10.5194/bg-9-5125-2012.

6. Hoang, N.T.; Kanemoto, K. Mapping the Deforestation Footprint of Nations Reveals Growing Threat to Tropical Forests. Nat Ecol Evol 2021, 5, 845–853, doi:10.1038/s41559-021-01417-z.

7. Feng, Y.; Zeng, Z.; Searchinger, T.D.; Ziegler, A.D.; Wu, J.; Wang, D.; He, X.; Elsen, P.R.; Ciais, P.; Xu, R.; et al. Doubling of Annual Forest Carbon Loss over the Tropics during the Early Twenty-First Century. Nat Sustain 2022, 5, 444–451, doi:10.1038/s41893-022-00854-3.

8. Qin, Y.; Xiao, X.; Wigneron, J.P.; Ciais, P.; Brandt, M.; Fan, L.; Li, X.; Crowell, S.; Wu, X.; Doughty, R.; et al. Carbon Loss from Forest Degradation Exceeds That from Deforestation in the Brazilian Amazon. Nature Climate Change 2021, 11, 442–448, doi:10.1038/s41558-021-01026-5.

9. Kleinschroth, F.; Laporte, N.; Laurance, W.F.; Goetz, S.J.; Ghazoul, J. Road Expansion and Persistence in Forests of the Congo Basin. Nat Sustain 2019, 2, 628–634, doi:10.1038/s41893-019-0310-6.

10. Kondo, M.; Birdsey, R.; Pugh, T.A.M.; Lauerwald, R.; Raymond, P.A.; Niu, S.; Naudts, K. Chapter 7 - State of Science in Carbon Budget Assessments for Temperate Forests and Grasslands. In Balancing Greenhouse Gas Budgets; Poulter, B., Canadell, J.G., Hayes, D.J., Thompson, R.L., Eds.; Elsevier, 2022; pp. 237–270 ISBN 978-0-12-814952-2.

11. Metternicht, G.; Zinck, J.A.; Blanco, P.D.; del Valle, H.F. Remote Sensing of Land Degradation: Experiences from Latin America and the Caribbean. Journal of Environmental Quality 2010, 39, 42–61, doi:10.2134/jeq2009.0127.

12. Achard, F.; DeFries, R.; Eva, H.; Hansen, M.; Mayaux, P.; Stibig, H.-J. Pan-Tropical Monitoring of Deforestation. Environ. Res. Lett. 2007, 2, 045022, doi:10.1088/1748-9326/2/4/045022.

13. Lynch, J.; Maslin, M.; Balzter, H.; Sweeting, M. Choose Satellites to Monitor Deforestation. Nature 2013, 496, 293–294, doi:10.1038/496293a.

14. Nelson, R.; Holben, B. Identifying Deforestation in Brazil Using Multiresolution Satellite Data. International Journal of Remote Sensing 1986, 7, 429–448, doi:10.1080/01431168608954696.

15. NELSON, R.; HORNING, N.; STONE, T.A. Determining the Rate of Forest Conversion in Mato Grosso, Brazil, Using Landsat MSS and AVHRR Data. International Journal of Remote Sensing 1987, 8, 1767–1784, doi:10.1080/01431168708954815.

16. Skole, D.; Tucker, C. Tropical Deforestation and Habitat Fragmentation in the Amazon: Satellite Data from 1978 to 1988. Science 1993, 260, 1905–1910, doi:10.1126/science.260.5116.1905.

17. DeFries, R.S.; Houghton, R.A.; Hansen, M.C.; Field, C.B.; Skole, D.; Townshend, J. Carbon Emissions from Tropical Deforestation and Regrowth Based on Satellite Observations for the 1980s and 1990s. Proceedings of the National Academy of Sciences 2002, 99, 14256–14261, doi:10.1073/pnas.182560099.

18. Morton, D.C.; DeFries, R.S.; Shimabukuro, Y.E.; Anderson, L.O.; Espírito-Santo, F.D.B.; Hansen, M.; Carroll, M. Rapid Assessment of Annual Deforestation in the Brazilian Amazon Using MODIS Data. Earth Interactions 2005, 9, 1–22, doi:10.1175/EI139.1.

19. Margono, B.A.; Turubanova, S.; Zhuravleva, I.; Potapov, P.; Tyukavina, A.; Baccini, A.; Goetz, S.; Hansen, M.C. Mapping and Monitoring Deforestation and Forest Degradation in Sumatra (Indonesia) Using Landsat Time Series Data Sets from 1990 to 2010. Environ. Res. Lett. 2012, 7, 034010, doi:10.1088/1748-9326/7/3/034010.

20. Hansen, M.C.; Potapov, P.V.; Moore, R.; Hancher, M.; Turubanova, S.A.; Tyukavina, A.; Thau, D.; Stehman, S.V.; Goetz, S.J.; Loveland, T.R.; et al. High-Resolution Global Maps of 21st-Century Forest Cover Change. Science 2013, 342, 850–853, doi:10.1126/science.1244693.

21. Valeriano, D.M.; Mello, E.M.; Moreira, J.C.; Shimabukuro, Y.E.; Duarte, V.; Souza, I.; Santos, J.; Barbosa, C.C.; Souza, R. Monitoring Tropical Forest from Space: The PRODES Digital Project. International Archives of Photogrammetry Remote Sensing and Spatial Information Sciences 2004, 35, 272–274.

22. Potapov, P.V.; Dempewolf, J.; Talero, Y.; Hansen, M.C.; Stehman, S.V.; Vargas, C.; Rojas, E.J.; Castillo, D.; Mendoza, E.; Calderón, A.; et al. National Satellite-Based Humid Tropical Forest Change Assessment in Peru in Support of REDD$\mathplus$ Implementation. Environ. Res. Lett. 2014, 9, 124012, doi:10.1088/1748-9326/9/12/124012.

23. Hansen, M.C.; Krylov, A.; Tyukavina, A.; Potapov, P.V.; Turubanova, S.; Zutta, B.; Ifo, S.; Margono, B.; Stolle, F.; Moore, R. Humid Tropical Forest Disturbance Alerts Using Landsat Data. Environ. Res. Lett. 2016, 11, 034008, doi:10.1088/1748-9326/11/3/034008.

24. Reiche, J.; De Bruin, S.; Hoekman, D.; Verbesselt, J.; Herold, M. A Bayesian Approach to Combine Landsat and ALOS PALSAR Time Series for Near Real-Time Deforestation Detection. Remote Sensing 2015, 7, 4973–4996, doi:10.3390/rs70504973.

25. Hansen, M.C.; Roy, D.P.; Lindquist, E.; Adusei, B.; Justice, C.O.; Altstatt, A. A Method for Integrating MODIS and Landsat Data for Systematic Monitoring of Forest Cover and Change in the Congo Basin. Remote Sensing of Environment 2008, 112, 2495–2513, doi:10.1016/j.rse.2007.11.012.

26. Hamunyela, E. Space-Time Monitoring of Tropical Forest Changes Using Observations from Multiple Satellites. 2017, doi:10.18174/420048.

27. Saatchi, S.S.; Soares, J.V.; Alves, D.S. Mapping Deforestation and Land Use in Amazon Rainforest by Using SIR-C Imagery. Remote Sensing of Environment 1997, 59, 191–202, doi:10.1016/S0034-4257(96)00153-8.

28. Keil, M.; Scales, D.; Winter, R. Investigation of Forest Areas in Germany and Brazil Using SAR Data of the SIR-C/X-SAR and Other SAR Missions. In Proceedings of the 1995 International Geoscience and Remote Sensing Symposium, IGARSS '95. Quantitative Remote Sensing for Science and Applications; July 1995; Vol. 2, pp. 997–999 vol.2.

29. Grover, K.D.; Quegan, S. ERS-1 Observations and Potential for Use in Tropical Forest Monitoring. In Proceedings of the 1995 International Geoscience and Remote Sensing Symposium, IGARSS '95. Quantitative Remote Sensing for Science and Applications; July 1995; Vol. 2, pp. 1210–1212 vol.2.

30. Lucas, R.M.; Mitchell, A.L.; Rosenqvist, A.; Proisy, C.; Melius, A.; Ticehurst, C. The Potential of L-Band SAR for Quantifying Mangrove Characteristics and Change: Case Studies from the Tropics. Aquatic Conserv: Mar. Freshw. Ecosyst. 2007, 17, 245–264, doi:10.1002/aqc.833.

31. Melshelmer, C.; Alpers, W.; Gade, M. Investigation of Multifrequency/Multipolarization Radar Signatures of Rain Cells, Derived from SIR-C/X-SAR Data. In Proceedings of the IGARSS '96. 1996 International Geoscience and Remote Sensing Symposium; May 1996; Vol. 2, pp. 1370–1372 vol.2.

32. Marzano, F.S.; Mori, S.; Weinman, J.A. Evidence of Rainfall Signatures on X-Band Synthetic Aperture Radar Imagery Over Land. IEEE Transactions on Geoscience and Remote Sensing 2010, 48, 950–964, doi:10.1109/TGRS.2009.2034843.

33. Rosenqvist, Å.; Milne, A.; Lucas, R.; Imhoff, M.; Dobson, C. A Review of Remote Sensing Technology in Support of the Kyoto Protocol. Environmental Science & Policy 2003, 6, 441–455, doi:10.1016/S1462-9011(03)00070-4.

34. Ranson, K.J.; Kovacs, K.; Sun, G.; Kharuk, V.I. Disturbance Recognition in the Boreal Forest Using Radar and Landsat-7. Canadian Journal of Remote Sensing 2003, 29, 271–285, doi:10.5589/m02-096.

35. Shimabukuro, Y.E.; Almeida-Filho, R.; Kuplich, T.M.; de Freitas, R.M. Quantifying Optical and SAR Image Relationships for Tropical Landscape Features in the Amazônia. International Journal of Remote Sensing 2007, 28, 3831–3840, doi:10.1080/01431160701236829.

36. da C.F. Yanasse, C.; J.S. Sant'Anna, S.; Frery, A.C.; Rennó, C.D.; Soares, J.V.; Luckman, A.J. Exploratory Study of the Relationship between Tropical Forest Regeneration Stages and SIR-C L and C Data. Remote Sensing of Environment 1997, 59, 180–190, doi:10.1016/S0034-4257(96)00149-6.

37. Salas, W.A.; Skole, D. Remote Sensing of Land Cover Change: Secondary Growth Dynamics in Rondonia, Brazil. In Proceedings of the IGARSS '98. Sensing and Managing the Environment. 1998 IEEE International Geoscience and Remote Sensing. Symposium Proceedings. (Cat. No.98CH36174); July 1998; Vol. 5, pp. 2515–2517 vol.5.

38. Rignot, E.; Salas, W.A.; Skole, D.L. Mapping Deforestation and Secondary Growth in Rondonia, Brazil, Using Imaging Radar and Thematic Mapper Data. Remote Sensing of Environment 1997, 59, 167–179, doi:10.1016/S0034-4257(96)00150-2.

39. Souyris, J.-C.; Le Toan, T.; Floury, N.; Thomasson, L.; Hsu, C.-C.; Kong, J.A. Use of Polarisation Synthesis for Deforestation Studies Based on SIR-C/XSAR Data Analysis. In Proceedings of the IGARSS '96. 1996 International Geoscience and Remote Sensing Symposium; May 1996; Vol. 2, pp. 836–838 vol.2.

40. Kuntz, S.; Siegert, F. Monitoring of Deforestation and Land Use in Indonesia with Multitemporal ERS Data. International Journal of Remote Sensing 1999, 20, 2835–2853, doi:10.1080/014311699211822.

41. Rignot, E.J.M. Effect of Faraday Rotation on L-Band Interferometric and Polarimetric Synthetic-Aperture Radar Data. IEEE Transactions on Geoscience and Remote Sensing 2000, 38, 383–390, doi:10.1109/36.823934.

42. Ribbes, F.; Le Toan, T.L.; Bruniquel, J.; Floury, N.; Stussi, N.; Liew, S.C.; Wasrin, U.R. Deforestation Monitoring in Tropical Regions Using Multitemporal ERS/JERS SAR and INSAR Data. In Proceedings of the IGARSS'97. 1997 IEEE International Geoscience and Remote Sensing Symposium Proceedings. Remote Sensing - A Scientific Vision for Sustainable Development; August 1997; Vol. 4, pp. 1560–1562 vol.4.

43. Suga, Y.; Takeuchi, S. Application of JERS-1 InSAR for Monitoring Deforestation of Tropical Rain Forest. In Proceedings of the IGARSS 2000. IEEE 2000 International Geoscience and Remote Sensing Symposium. Taking the Pulse of the Planet: The Role of Remote Sensing in Managing the Environment. Proceedings (Cat. No.00CH37120); July 2000; Vol. 1, pp. 432–434 vol.1.

44. Lawrence, W.; Saatchi, S.; DeFries, R.; Dietz, J.; Rice, R.; Dietz, L.A.; Siquiera De Araujo, M.; Alger, K. Utilization of SAR and Optical Remote Sensing Data for Habitat Conservation in the Tropical Forest of Brazil. In Proceedings of the 1995 International Geoscience and Remote Sensing Symposium, IGARSS '95. Quantitative Remote Sensing for Science and Applications; July 1995; Vol. 2, pp. 1480–1482 vol.2.

45. Hoekman, D. Monitoring Tropical Forests Using Synthetic Aperture Radar. In Proceedings of the INDREX (Indonesian Radar Experiment) Final Results Workshop; 2000; Vol. 489, p. 11.

46. Reiche, J.; Mullissa, A.; Slagter, B.; Gou, Y.; Tsendbazar, N.E.; Odongo-Braun, C.; Vollrath, A.; Weisse, M.J.; Stolle, F.; Pickens, A.; et al. Forest Disturbance Alerts for the Congo Basin Using Sentinel-1. Environmental Research Letters 2021, 16, 024005, doi:10.1088/1748-9326/abd0a8.

47. Watanabe, M.; Koyama, C.N.; Hayashi, M.; Nagatani, I.; Tadono, T.; Shimada, M. Refined Algorithm for Forest Early Warning System with ALOS-2/PALSAR-2 ScanSAR Data in Tropical Forest Regions. Remote Sensing of Environment 2021, 265, 112643, doi:10.1016/j.rse.2021.112643.

48. Ballère, M.; Bouvet, A.; Mermoz, S.; Le Toan, T.; Koleck, T.; Bedeau, C.; André, M.; Forestier, E.; Frison, P.-L.; Lardeux, C. SAR Data for Tropical Forest Disturbance Alerts in French Guiana: Benefit over Optical Imagery. Remote Sensing of Environment 2021, 252, 112159, doi:10.1016/j.rse.2020.112159.

49. Le Toan, T.; Beaudoin, A.; Riom, J.; Guyon, D. Relating Forest Biomass to SAR Data. IEEE Transactions on Geoscience and Remote Sensing 1992, 30, 403–411, doi:10.1109/36.134089.

50. Ranson, K.J.; Sun, G. Northern Forest Classification Using Temporal Multifrequency and Multipolarimetric SAR Images. Remote Sensing of Environment 1994, 47, 142–153, doi:10.1016/0034-4257(94)90151-1.

51. Rignot, E.; Williams, C.; Viereck, L. Radar Estimates of Aboveground Biomass in Boreal Forests of Interior Alaska. IEEE Transactions on Geoscience and Remote Sensing 1994, 32, 1117–1124, doi:10.1109/36.312903.

52. Romshoo, S.A.; Shimada, M.; Igarashi, T. Peatland Ecosystem Characterization Employing L-Band SAR. In Proceedings of the IEEE International Geoscience and Remote Sensing Symposium; June 2002; Vol. 3, pp. 1795–1797 vol.3.

53. Andersen, H.-E.; Reutebuch, S.; Mcgaughey, R. Active Remote Sensing. In; 2006; pp. 43–66 ISBN 978-1-4020-4305-5.

54. Lucas, R.; Armston, J.; Fairfax, R.; Fensham, R.; Accad, A.; Carreiras, J.; Kelley, J.; Bunting, P.; Clewley, D.; Bray, S.; et al. An Evaluation of the ALOS PALSAR L-Band Backscatter—Above Ground Biomass Relationship Queensland, Australia: Impacts of Surface Moisture Condition and Vegetation Structure. Selected Topics in Applied Earth Observations and Remote Sensing, IEEE Journal of 2011, 3, 576–593, doi:10.1109/JSTARS.2010.2086436.

55. Green, R.M. Relationships between Polarimetric SAR Backscatter and Forest Canopy and Sub-Canopy Biophysical Properties. International Journal of Remote Sensing 1998, 19, 2395–2412, doi:10.1080/014311698214794.

56. Almeida-Filho, R.; Rosenqvist, A.; Shimabukuro, Y.E.; dos Santos, J.R. Evaluation and Perspectives of Using Multitemporal L-Band SAR Data to Monitor Deforestation in the Brazilian Amazo/Spl Circ/Nia. IEEE Geoscience and Remote Sensing Letters 2005, 2, 409–412, doi:10.1109/LGRS.2005.856679.

57. Almeida-Filho, R.; Shimabukuro, Y.E.; Rosenqvist, A.; Sánchez, G.A. Using Dual-polarized ALOS PALSAR Data for Detecting New Fronts of Deforestation in the Brazilian Amazônia. International Journal of Remote Sensing 2009, 30, 3735–3743, doi:10.1080/01431160902777175.

58. Santoro, M.; Fransson, J.E.S.; Eriksson, L.E.B.; Ulander, L.M.H. Clear-Cut Detection in Swedish Boreal Forest Using Multi-Temporal ALOS PALSAR Backscatter Data. IEEE Journal of Selected Topics in Applied Earth Observations and Remote Sensing 2010, 3, 618–631, doi:10.1109/JSTARS.2010.2048201.

59. Bamler, R.; Hartl, P. Synthetic Aperture Radar Interferometry. Inverse Problems 1998, 14, R1–R54, doi:10.1088/0266-5611/14/4/001.

60. Hanssen, R.F. Radar Interferometry: Data Interpretation and Error Analysis; Springer Science & Business Media, 2001; Vol. 2;.

61. Takeuchi, S.; Suga, Y.; Yoshimura, M. A Comparative Study of Coherence Information by L-Band and C-Band SAR for Detecting Deforestation in Tropical Rain Forest. In Proceedings of the IGARSS 2001. Scanning the Present and Resolving the Future. Proceedings. IEEE 2001 International Geoscience and Remote Sensing Symposium (Cat. No.01CH37217); July 2001; Vol. 5, pp. 2259–2261 vol.5.

62. Balzter, H. Forest Mapping and Monitoring with Interferometric Synthetic Aperture Radar (InSAR). Progress in Physical Geography: Earth and Environment 2001, 25, 159–177, doi:10.1177/030913330102500201.

63. Takeuchi, S.; Yamada, S. Monitoring of Forest Fire Damage by Using JERS-1 InSAR. In Proceedings of the IEEE International Geoscience and Remote Sensing Symposium; June 2002; Vol. 6, pp. 3290–3292 vol.6.

64. Le Toan, T.; Quegan, S.; Woodward, I.; Lomas, M.; Delbart, N.; Picard, G. Relating Radar Remote Sensing of Biomass to Modelling of Forest Carbon Budgets. Climatic Change 2004, 67, 379–402, doi:10.1007/s10584-004-3155-5.

65. Treuhaft, R.N.; Chapman, B.D.; dos Santos, J.R.; Gonçalves, F.G.; Dutra, L.V.; Graça, P.M.L.A.; Drake, J.B. Vegetation Profiles in Tropical Forests from Multibaseline Interferometric Synthetic Aperture Radar, Field, and Lidar Measurements. Journal of Geophysical Research: Atmospheres 2009, 114, doi:10.1029/2008JD011674.

66. Neumann, M.; Ferro-Famil, L.; Reigber, A. Estimation of Forest Structure, Ground, and Canopy Layer Characteristics From Multibaseline Polarimetric Interferometric SAR Data. IEEE Transactions on Geoscience and Remote Sensing 2010, 48, 1086–1104, doi:10.1109/TGRS.2009.2031101.

67. Treuhaft, R.; Gonçalves, F.; dos Santos, J.R.; Keller, M.; Palace, M.; Madsen, S.N.; Sullivan, F.; Graça, P.M.L.A. Tropical-Forest Biomass Estimation at X-Band From the Spaceborne TanDEM-X Interferometer. IEEE Geoscience and Remote Sensing Letters 2015, 12, 239–243, doi:10.1109/LGRS.2014.2334140.

68. Gaveau, D.L.A.; Balzter, H.; Plummer, S. Forest Woody Biomass Classification with Satellite-Based Radar Coherence over 900 000 Km2 in Central Siberia. Forest Ecology and Management 2003, 174, 65–75, doi:10.1016/S0378-1127(02)00028-2.

69. Fransson, J.E.S.; Magnusson, M.; Olsson, H.; Eriksson, L.E.B.; Sandberg, G.; Smith-Jonforsen, G.; Ulander, L.M.H. Detection of Forest Changes Using ALOS PALSAR Satellite Images. In Proceedings of the 2007 IEEE International Geoscience and Remote Sensing Symposium; July 2007; pp. 2330–2333.

70. Zhang, F.; Xu, M.; Xie, C.; Xia, Z.; Li, K.; Cai, A.; Shao, Y.; Wang, X.; Touzi, R. Polarimetric Signature and the Temporal Variation Analysis for Deforestation Mapping in Southwest China. 2011, 5.

71. Kim, Y.; van Zyl, J.J. A Time-Series Approach to Estimate Soil Moisture Using Polarimetric Radar Data. IEEE Transactions on Geoscience and Remote Sensing 2009, 47, 2519–2527, doi:10.1109/TGRS.2009.2014944.

72. Avtar, R.; Sawada, H.; Takeuchi, W.; Singh, G. Characterization of Forests and Deforestation in Cambodia Using ALOS/PALSAR Observation. Geocarto International 2012, 27, 119–137, doi:10.1080/10106049.2011.626081.

73. Igarashi, T.; Shimada, M.; Rosenqvist, A.; Hashimoto, T.; Tadono, T.; Matsuoka, M.; Yamamoto, H. Preliminary Study on Data Sets of ADEOS-II and ALOS Dedicated to Terrestrial Carbon Observation. Advances in Space Research 2003, 32, 2147–2152, doi:10.1016/S0273-1177(03)90536-9.

74. Takeuchi, S.; Suga, Y.; Oguro, Y.; Konishi, T. Monitoring of New Plantation Development in Tropical Rain Forests Using JERS-1 SAR Data. Advances in Space Research 2000, 26, 1151–1154, doi:10.1016/S0273-1177(99)01134-5.

75. Thiel, C.; Drezet, P.; Weise, C.; Quegan, S.; Schmullius, C. Radar Remote Sensing for the Delineation of Forest Cover Maps and the Detection of Deforestation. Forestry: An International Journal of Forest Research 2006, 79, 589–597, doi:10.1093/forestry/cpl036.

76. Ranson, K.J.; Sun, G. Effects of Environmental Conditions on Boreal Forest Classification and Biomass Estimates with SAR. IEEE Transactions on Geoscience and Remote Sensing 2000, 38, 1242–1252, doi:10.1109/36.843016.

77. Santoro, M.; Schmullius, C. Investigations on ARD Monitoring in Siberian Forest Using Spaceborne SAR. In Proceedings of the IGARSS 2004. 2004 IEEE International Geoscience and Remote Sensing Symposium; September 2004; Vol. 2, pp. 1029–1032 vol.2.

78. Saatchi, S.S.; Nelson, B.; Podest, E.; Holt, J. Mapping Land Cover Types in the Amazon Basin Using 1 Km JERS-1 Mosaic. International Journal of Remote Sensing 2000, 21, 1201–1234, doi:10.1080/014311600210146.

79. Podest, E.; Saatchi, S. Application of Multiscale Texture in Classifying JERS-1 Radar Data over Tropical Vegetation. International Journal of Remote Sensing 2002, 23, 1487–1506, doi:10.1080/01431160110093000.

80. Servello, E.L.; Kuplich, T.M.; Edemir Shimabukuro, Y. Tropical Land Cover Change Detection with Polarimetric SAR Data. In Proceedings of the 2010 IEEE International Geoscience and Remote Sensing Symposium; July 2010; pp. 1477–1480.

81. Haralick, R.M.; Shanmugam, K.; Dinstein, I. Textural Features for Image Classification. IEEE Transactions on Systems, Man, and Cybernetics 1973, SMC-3, 610–621, doi:10.1109/TSMC.1973.4309314.

82. Wagner, W.; Luckman, A.; Vietmeier, J.; Tansey, K.; Balzter, H.; Schmullius, C.; Davidson, M.; Gaveau, D.; Gluck, M.; Le Toan, T.; et al. Large-Scale Mapping of Boreal Forest in SIBERIA Using ERS Tandem Coherence and JERS Backscatter Data. Remote Sensing of Environment 2003, 85, 125–144, doi:10.1016/S0034-4257(02)00198-0.

83. Tansey, K.J.; Luckman, A.J.; Skinner, L.; Balzter, H.; Strozzi, T.; Wagner, W. Classification of Forest Volume Resources Using ERS Tandem Coherence and JERS Backscatter Data. International Journal of Remote Sensing 2004, 25, 751–768, doi:10.1080/0143116031000149970.

84. Doblas, J.; Shimabukuro, Y.; Sant'Anna, S.; Carneiro, A.; Aragão, L.; Almeida, C. Optimizing Near Real-Time Detection of Deforestation on Tropical Rainforests Using Sentinel-1 Data. Remote Sensing 2020, 12, 3922, doi:10.3390/rs12233922.

85. Saatchi, S.S.; Houghton, R.A.; Dos Santos Alvalá, R.C.; Soares, J.V.; Yu, Y. Distribution of Aboveground Live Biomass in the Amazon Basin. Global Change Biology 2007, 13, 816–837, doi:10.1111/j.1365-2486.2007.01323.x.

86. Kuplich, T.M. Classifying Regenerating Forest Stages in Amazônia Using Remotely Sensed Images and a Neural Network. Forest Ecology and Management 2006, 234, 1–9, doi:10.1016/j.foreco.2006.05.066.

87. Longepe, N.; Rakwatin, P.; Isoguchi, O.; Shimada, M.; Uryu, Y.; Yulianto, K. Assessment of ALOS PALSAR 50 m Orthorectified FBD Data for Regional Land Cover Classification by Support Vector Machines. IEEE Transactions on Geoscience and Remote Sensing 2011, 49, 2135–2150, doi:10.1109/TGRS.2010.2102041.

88. Milne, A.K.; Mitchell, A.L.; Williams, M.; Tapley, I.; Kuntz, S. Sensor Capabilities for Deforestation and Forest Degradation. In Proceedings of the 2012 IEEE International Geoscience and Remote Sensing Symposium; July 2012; pp. 3154–3157.

89. Bujor, F.T.; Valet, L.; Trouvw, E.; Mauris, G.; Classeau, N.; Rudant, J.P. Data Fusion Approach for Change Detection in Multi-Temporal ERS-SAR Images. In Proceedings of the IGARSS 2001. Scanning the Present and Resolving the Future. Proceedings. IEEE 2001

International Geoscience and Remote Sensing Symposium (Cat. No.01CH37217); July 2001; Vol. 6, pp. 2590–2592 vol.6.

90. Reiche, J.; Hamunyela, E.; Verbesselt, J.; Hoekman, D.; Herold, M. Improving Near-Real Time Deforestation Monitoring in Tropical Dry Forests by Combining Dense Sentinel-1 Time Series with Landsat and ALOS-2 PALSAR-2. Remote Sensing of Environment 2018, 204, 147–161, doi:10.1016/j.rse.2017.10.034.

91. Reiche, J.; Verhoeven, R.; Verbesselt, J.; Hamunyela, E.; Wielaard, N.; Herold, M. Characterizing Tropical Forest Cover Loss Using Dense Sentinel-1 Data and Active Fire Alerts. Remote Sensing 2018, 10, 777, doi:10.3390/rs10050777.

92. Durieux, A.M.S.; Ren, C.X.; Calef, M.T.; Chartrand, R.; Warren, M.S. BUDD: Multi-Modal Bayesian Updating Deforestation Detections. In Proceedings of the IGARSS 2020 - 2020 IEEE International Geoscience and Remote Sensing Symposium; September 2020; pp. 6638–6641.

93. Durieux, A.M.S.; Rustowicz, R.; Sharma, N.; Schatz, J.; Calef, M.T.; Ren, C.X. Expanding SAR-Based Probabilistic Deforestation Detections Using Deep Learning. In Proceedings of the Applications of Machine Learning 2021; SPIE, August 1 2021; Vol. 11843, pp. 24–31.

94. Manogaran, G.; Lopez, D. Spatial Cumulative Sum Algorithm with Big Data Analytics for Climate Change Detection. Computers & Electrical Engineering 2018, 65, 207–221, doi:10.1016/j.compeleceng.2017.04.006.

95. Ruiz-Ramos, J.; Marino, A.; Boardman, C.; Suarez, J. Continuous Forest Monitoring Using Cumulative Sums of Sentinel-1 Timeseries. Remote Sensing 2020, 12, 3061, doi:10.3390/rs12183061.

96. Ygorra, B.; Frappart, F.; Wigneron, J.P.; Moisy, C.; Catry, T.; Baup, F.; Hamunyela, E.; Riazanoff, S. Monitoring Loss of Tropical Forest Cover from Sentinel-1 Time-Series: A CuSum-Based Approach. International Journal of Applied Earth Observation and Geoinformation 2021, 103, 102532, doi:10.1016/j.jag.2021.102532.

97. Ygorra, B.; Frappart, F.; Wigneron, J.; Moisy, C.; Catry, T.; Baup, F.; Hamunyela, E.; Riazanoff, S. Deforestation Monitoring Using Sentinel-1 SAR Images in Humid Tropical Areas. In Proceedings of the 2021 IEEE International Geoscience and Remote Sensing Symposium IGARSS; July 2021; pp. 5957–5960.

98. Langner, A.; Nakayama, M.; Liew, S.C. Integrated-Use-of-Multi-Mode-and-Multi-Angle-SAR-Data-for-Land-Cover-Identification-in-Tropics.Pdf. In Proceedings of the The Second Joint PI symposium of ALOS Data Nodes for ALOS Science Program; 2008.

99. Koch, B. Status and Future of Laser Scanning, Synthetic Aperture Radar and Hyperspectral Remote Sensing Data for Forest Biomass Assessment. ISPRS Journal of Photogrammetry and Remote Sensing 2010, 65, 581–590, doi:10.1016/j.isprsjprs.2010.09.001.

3.3. Contribution and perspectives

In this chapter, we described the interaction of C- and L-band SAR signal with forest. We also described the main methods used to monitor forest cover change. We selected the CuSum as a basis for cover change monitoring for both near-real-time and offline monitoring, as described in the following chapters.

CHAPTER IV. MONITORING FOREST DISTURBANCES FROM SENTINEL-1 TIME-SERIES: A CUSUM-BASED APPROACH

Table of contents

Chapter IV. Monitoring forest disturbances from Sentinel-1 time-series: a CuSum-based approach

4.1. Introduction

This section presents the results of the first part of my PhD, published in the International Journal of Applied Earth Observation and Geoinformation in August 2021. When I started my PhD, several physical-based change detection algorithms based on SAR time-series for deforestation monitoring were available online and quickly applicable.

The study area was defined with *VisioTerra*. It is located in the *Alibuku* IFCO concession, near Kisangani, Democratic Republic of Congo (DRC). We had the great opportunity to explore the performance of Cumulative Sum (CuSum)-based method on tropical forests using Sentinel-1 data.

After comparing the results of the CuSum with the industrial algorithm over a small area, the Cumulative Sum Algorithm was chosen for its high potential in tropical deforestation monitoring (Manogaran and Lopez, 2018; Ruiz-ramos et al., 2018). This algorithm was chosen for its dual ability to produce offline products (use of a long time-series to establish a deforestation rate over a period) and near-real-time products (shorter time-series to be updated at each new image acquired, to establish the deforestation localisation in the fastest way available,(Kellndorfer, 2019).

CuSum is an algorithm that can be applied on a time-series of any variable. It is characterized by a single input parameter: the critical threshold (T_C), computed as a threshold based on the confidence level (CL) obtained doing a bootstrap analysis. A high T_c (> 0.9) resulted systematically in a low number of commissions but in a high number of omissions, whereas a low T_c (< 0.9) resulted systematically in a high number of commissions but a low number of omissions. The CuSum method was applied to every pixel of the Sentinel-1 images on both VH and VV polarizations.

As I realised that the CuSum based on the temporal dimension alone would not produce sufficiently accurate results in terms of statistics, I decided to take into account the spatial dimension of the results in the monitoring. First, I applied a known spatial filter – the Minimum Mapping Unit, set at 300m². Then, I removed all low-T_c polygons which do not have any intersection with a high-T_c polygon. This spatial recombination was then named cross-T_c recombination, and represents the main innovation in this article, as the numbers of omission / commission decreased compared to their high or low T_c counterparts. The ability of the CuSum cross-T_c to monitor deforestation caused by small clearances was validated using a couple multi-spectral images. Another sub-study area was defined, where roads made by loggers within the concession could be accurately seen using Sentinel-1. This result was presented at the IGARSS 2021 (Ygorra *et al*., 2021a).

Several articles using Sentinel-1 data for tropical deforestation monitoring (Ballère et al., 2021; Doblas et al., 2022, 2020; Mermoz et al., 2021; Mistry et al., 2021; Reiche et al., 2021; Ruiz-Ramos et al., 2020), some based on the CuSum (Mistry et al., 2021; Ruiz-Ramos et al., 2020) were published during the writing of this publication.

Data acquisition and processing, methods, findings and discussion of this work are presented in the following publication. Following a brief commentary on these results, the perspectives of this work in the PhD plan will be presented.

4.2. Publication

Monitoring loss of tropical forest cover from Sentinel-1 time-series: a CuSum-based approach

Ygorra B.[1,2,3], Frappart F.[1,4], Wigneron J-P.[1], Moisy C.[1], Catry T.[5], Baup F.[6], Hamunyela E.[7], Riazanoff S.[2]

[1] INRAE, UMR1391 ISPA, 33140, Villenave d'Ornon, France

[2] VisioTerra,77420, Champs-sur-Marne, France

[3] Université de Bordeaux, 33400, Talence, France

[4] LEGOS, Université de Toulouse, UMR CNES/CNRS/IRD/UPS 31400, Toulouse, France

[5] ESPACE-DEV, Univ Montpellier, IRD, Univ Antilles, Univ Guyane, Univ Réunion, Montpellier, France

[6] CESBIO, 31400, Toulouse, France

[7] University of Namibia, Private Bag 13301, Windhoek, Namibia

Corresponding author: Ygorra Bertrand, bertrand.ygorra@gmail.com.

Abstract

The forest decline in tropical areas is one of the largest global environmental threats as the growth of both global population and its needs have put an increasing pressure on these ecosystems. Efforts are ongoing to reduce tropical deforestation rates. Earth observations are increasingly used to monitor deforestation over the whole equatorial area. Change detection methods are mainly applied to satellite optical images which face limitations in humid tropical areas. For instance, due to frequent cloud cover in the tropics, there are often long delays in the detection of deforestation events. Recently, detection methods applied to Synthetic Aperture Radar (SAR) have been developed to address the limitations related to cloud cover. In this study, we present an application of a recently developed change detection method for monitoring forest cover loss from SAR time-series data in tropical zone. The method is based on the Cumulative Sum algorithm (CuSum) combined with a bootstrap analysis. The method

was applied to time-series of Sentinel-1 ground range detected (GRD) dual polarization (VV, VH) images forming a dataset of 60 images to monitor forest cover loss in a legal forest concession of the Democratic Republic of Congo during the 2018-2020 period. A cross-threshold recombination was then conducted on the computed maps. Evaluated against reference forest cut maps, an overall accuracy up to 91% and a precision up to 75% in forest clear cut detection was obtained. Our results show that more than 60% of forest disturbances were detected before the PlanetScope-based estimated date of cut, which may suggest the capacity of our method to detect forest degradation.

Keywords: Deforestation, Remote Sensing; Sentinel-1; Cumulative Sum Algorithm; Tropical Forest; Change Detection.

4.2.1. Introduction

The tropical forests, which play a critical role in the global climate regulation by recycling ~2.1 Gt CO_2 per year (Federici et al., 2015; Nunes et al., 2020), are being deforested at increasing rates. In Africa, the forest losses in carbon stocks are driven by multiple factors, including legal or illegal selective logging causing degradations, or cuts to fulfil the agricultural needs of local populations (Contreras-Hermosilla and others, 2000). Optical satellite remote sensing is commonly used to monitor forest cover changes (e.g., Global Forest Watch (Bullock et al., 2020; Hansen et al., 2013; Tyukavina et al., 2018)). Yet, the monitoring systems based on this kind of images are likely to provide inaccurate information over regions strongly affected by cloud cover (Hansen et al., 2016). They were also shown to be less robust in regions where forest exhibits strong seasonal variability in the canopy water content (Hamunyela et al., 2017)**.** Studies based on the merging of optical and Synthetic Aperture Radar (SAR) datasets, showed a better temporal accuracy in the detection of forest cuts by accounting for the seasonal changes in the vegetation structure but at the costs of a high computational complexity (Hamunyela et al., 2020). With the advances in the spatial and temporal resolutions of the satellite observations, the application of change detection algorithms to satellite data requires increasing computational platform performances. Some change detection algorithms such as the RADD and JJFAST alerts (Watanabe et al., 2021) are currently operational on powerful platforms such as Google Earth Engine, (see (Reiche et al., 2021) for instance). As the revisit time of the satellite observations decreases, change detection algorithms based on temporal analysis are increasingly used (Duveiller et al., 2008; Hamunyela et al., 2016; Souza et al., 2013). Among them, a change detection algorithm analysing the temporal stability of the signal through the deviation of a variable to its mean – the cumulative Sum (CuSum) – has been used in environmental studies, including for forest monitoring: (Kucera et al., 2007; Manogaran and Lopez, 2018; Ruiz-Ramos et al., 2020).The CuSum is a change detection method based on statistics to analyse multi-temporal processes, as it allows the detection of any type of variation (slow, abrupt) as long as it has an impact on the trend of the time-series. This method has been found to be less affected by the seasonal variability of vegetation and thus more performant to detect abrupt changes in the vegetation structure due to forest cut (Ruiz-Ramos et al., 2020).

To monitor forest cover changes, many studies have used pairwise or single epoque image comparison or multi-temporal averages for detecting changes between two dates (Antropov et al., 2016; Bouvet et al., 2018; Joshi et al., 2015; Lievens et al., 2017; Reiche et al., 2018b; Rüetschi et al., 2019; Tanase et al., 2015, 2010). These methods have known limits: there is

often a delay between a change in the vegetation structure and/or cover and a change in the SAR backscattering. Due to the SAR sensitivity to changes in the vegetation/soil moisture content and surface roughness, vegetation change is difficult to detect or may be detected with a delay (Belenguer-Plomer et al., 2019; Reiche et al., 2018a; Ruiz-ramos et al., 2018; Watanabe et al., 2018). Moreover, if the revisit time of the satellite is too low, vegetation may partially recover after being cut, hindering the detection of the cut (Numbisi and Van Coillie, 2020; Reiche et al., 2021). Though L-band SAR images can be used for an accurate monitoring of the deforestation in tropical environments e.g.,(S Takeuchi et al., 2001; Whittle et al., 2012), they are not easily available and often have a lower temporal resolution. The use of time-series with a high temporal resolution such as Sentinel-1 allows early detection and permits to detect changes at different time scales and to reduce the noise in the backscatter signal due to speckle or temporary changes.

In this study, C-band SAR observations from Sentinel-1 A satellite were used to monitor deforestation and other forest cover changes in the living area of a legal forest concession of the Democratic Republic of Congo (DRC). This satellite, launched in 2014, has a 12-day revisit period over the DRC and a spatial resolution of 20 m x 22 m, allowing to monitor changes in vegetation with a high resolution in both space and time. We evaluated the use of the CuSum algorithm (Manogaran and Lopez, 2018) applied to dual polarization VV-VH observations, taking advantage of the high capability of CuSum to detect vegetation cover change (Ruiz-Ramos et al., 2020)**.** Results based on the combination of different configurations of the CuSum approach are analysed and optimal configurations are presented and discussed.

4.2.2. Study site and data

4.2.2.1. Study Site

For the investigation of forest change in the Congo Basin by developing using our approach, we chose to monitor the forest near the living area of a forest concession where degradation and deforestation are likely to occur. The concession is the Industrie Forestière du Congo (IFCO) COD 018/11 forest concession (Alibuku), located within the North-Eastern region of Kisangani in the Democratic Republic of Congo (DRC), in central equatorial Africa (Figure IV.1). The climate of the region is characterised by two wet seasons, reaching their peaks in terms of rainfall respectively at the end of March / early April and end of September / early October and two dry seasons per year. The maps of the forest concessions are available at the DRC forest atlas (https://cod.forest-atlas.org/). This concession is formed of yearly allowed cut zones where trees are extracted and in a living area for the logger community. The study

site was specifically selected based on the nature/typology of the expected forest change. Since most of the forest changes were expected to be made by logger communities (over-exploitation for timber and firewood, agricultural activities (Contreras-Hermosilla and others, 2000)) instead of commercial logging clear-cuts, the study site was located near the populated area of the Alibuku concession. The study site (area = 22.57 km²) is located between 25.4122° and 25.4657° E, and 0.9033° and 0.9376° N, in the north-western part of a living area.

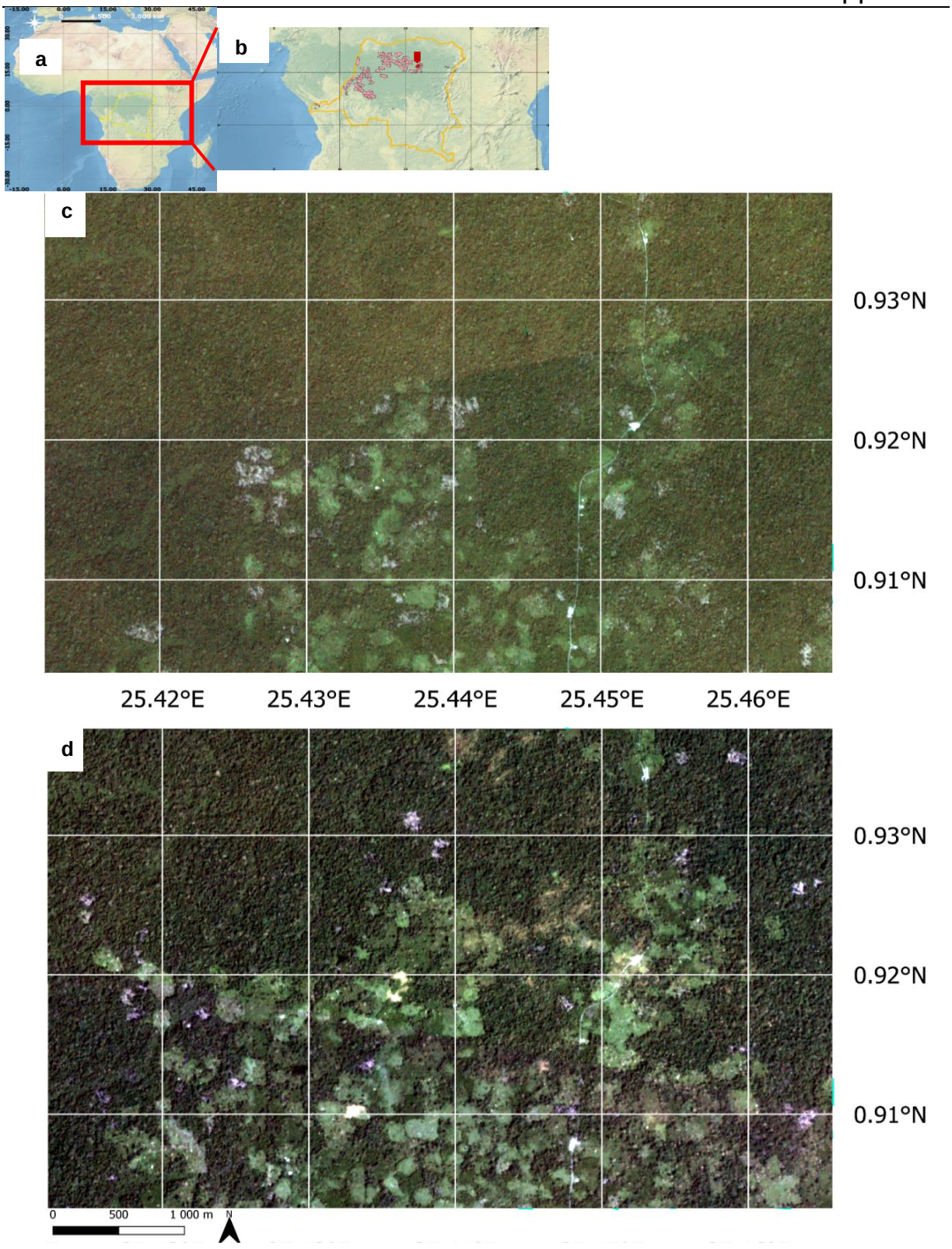

Figure IV.1: Study site: (a) global view including DRC borders, (b) global view including DRC borders with its forest concessions. The study zone is indicated by the red pinpoint. PlanetScope 3m surface reflectance image over the study site dated from (c) 2018-01-06 and (d) 2019-11-29.

4.2.2.2. Data

4.2.2.2.1. Sentinel-1 SAR images

The Sentinel-1 mission, developed by the European Space Agency (ESA) in the framework of the Copernicus programme, is a constellation composed of 2 satellites positioned on the same reference orbit plane with a 180° orbital phasing difference at an altitude of 693 km (Torres et al., 2012). The sun-synchronous orbit is near polar, presenting an inclination of 98.18°. The repeat cycle of each satellite is 12 days over the study site. Sentinel-1A was launched on April 3rd of 2014, while Sentinel-1B was launched on April 25th 2016. The main instrument onboard both Sentinel-1 satellites is a C-band Synthetic Aperture Radar (SAR) referenced as C-SAR. It is operating at a frequency of 5.405 GHz in 4 different modes, of which the Interferometric Wide-swath (IW) with a ground resolution of 20m x 22m, at the VV and VH polarizations was selected in this study. The images are available in several formats: Slant Range, Single Look Complex (SLC), Ground Range, and Multi-Look Detected (GRD). The data used in this study are the GRD products in IW mode at the VV and VH polarizations. The images used in this study were only acquired from Sentinel-1 A on a single descending orbit at the sampling period of 12 days as no Sentinel-1 B images were available on the study area. The resulting pixel size is 10 m x 10 m. This product was chosen instead of the SLC as it is a good compromise in terms of possible speckle noise reduction and volume of data to get accurate data but not increasing too much the computational time. A total of 60 images that formed our time-series on the study site between 01/01/2018 and 01/01/2020 were provided by the European Space Agency (ESA) at https://scihub.copernicus.eu and downloaded using VtWeb (https://visioterra.org/VtWeb/).

4.2.2.2.2. PlanetScope optical images

To evaluate our Sentinel 1 detection algorithm, a reference map of the forest changes was created using high-resolution PlanetScope images. We used the level 3B product of PlanetScope Ortho Scene obtained from a multispectral Cubesat constellation. This product is a 4-band (Red: 605 - 695 nm**,** Green: 515 - 595 nm, Blue: 450 - 515 nm, NIR: 740 – 900 nm) Surface Reflectance (SR) image, orthorectified and scaled, with a pixel resolution of 3 meters. The PlanetScope images available during the period ranging from 06/01/2018 to 30/12/2019 were selected upon the following criteria: (i) Images on which the visual interpretation was not possible because of large cloud cover were removed. No strict threshold on cloud cover could be used as the visualization depends on the thickness of the clouds. For instance, it was possible to perform visual interpretation if the cloud cover corresponds to a thin cloud veil covering the whole scene. (ii) Images partially covering the scene and images separated by a day or less from one another were removed. After this selection step, only twenty-four images

were kept. Among the kept images, some of them were still affected by the presence of a few clouds that did not prevent to perform a visual interpretation. The images were downloaded from Planet Explorer at https://www.planet.com.

4.2.2.2.3. Tree Cover Loss map from Global Forest Watch

To compare with the results obtained from the CuSum change detection algorithm applied to Sentinel-1 SAR images, the performances of the Global Forest Watch (GFW) Tree Cover Loss (TCL) map (Hansen et al., 2013) were also evaluated against the visual interpretation of the PlanetScope images. Results obtained from this forest change cover analysis were subsequently used for assessing the performance of our detector. The TCL map is a dataset developed for monitoring forest cover loss worldwide based on Landsat-5 TM, Landsat 7 ETM+, Landsat 8 OLI/TIRS and MODIS data with a pixel resolution of 30 m (Potapov et al., 2020). The TCL map over the study site is made freely available at https://data.globalforestwatch.org/ (Dataset: 'Granule 10N 20E' on GFW website). According to the TCL map, the study zone lost about 204 ha of tree cover (Figure IV.2) between 2018 and early 2020.

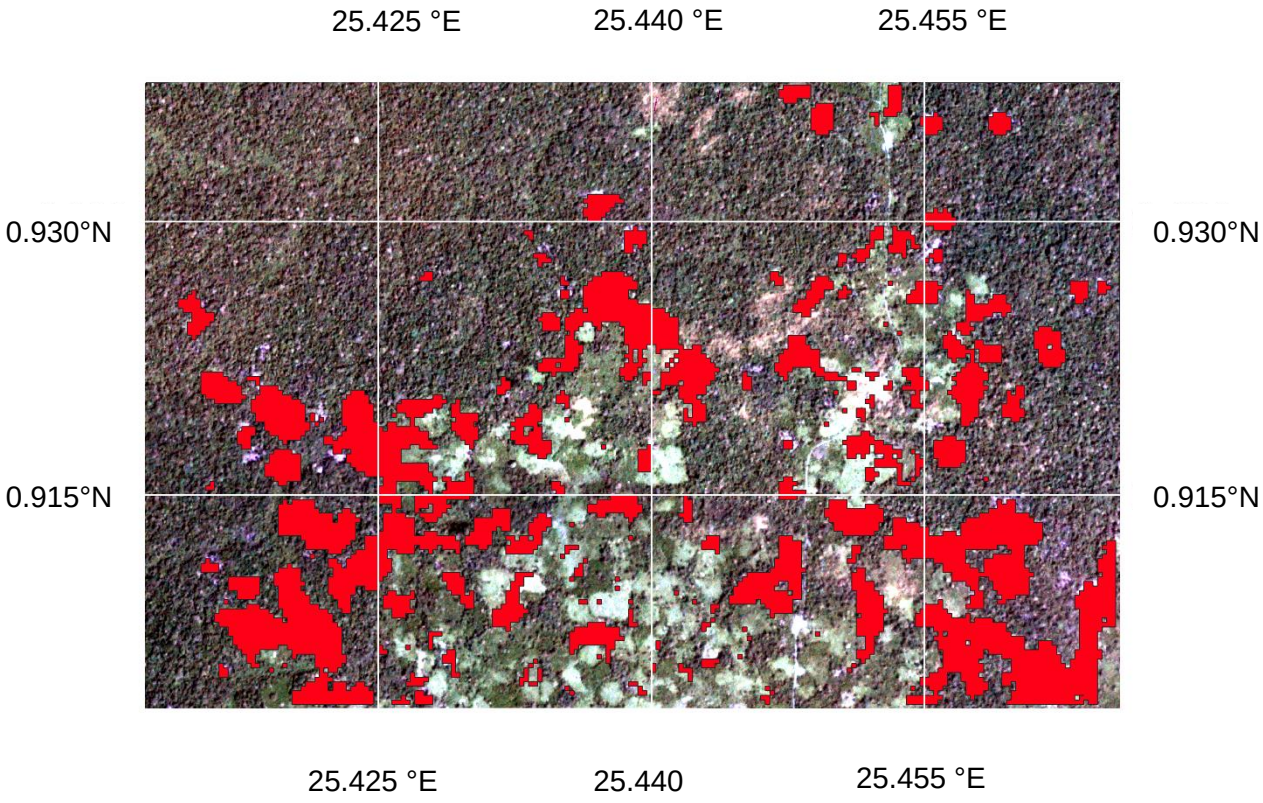

Figure IV.2: Tree Cover Loss map (Hansen, 2018-2019) on the PlanetScope 2019-11-29 RGB image background.

4.2.3. Methods

4.2.3.1. Pre-processing

The Sentinel-1 SAR images were pre-processed using VtWeb. VtWeb is an online platform enabling users to easily browse free Earth observation data, display it in 2D/3D and process it on-the-fly (https://visioterra.org/VtWeb/). The pre-processing performed by VtWeb to obtain geo-corrected backscatter images (resulting in γ^0 terrain corrected data) consisted in the 3 following steps (Figure IV.3):

- Orbit correction
- thermal noise removal (Piantanida and Miranda, 2017),
- terrain flattening as terrain correction to remove topological and incidence effects (Small, 2011).

The speckle was filtered using the bilateral filter made available in the python PyRAT Toolbox (Reigber et al., 2019) with a kernel window size of 7x7. This filter is a spatial filter presenting the advantage of preserving edges in the images. Its filtering principle relies on the replacement of a pixel value with the weighted pixel value average in the kernel (Tomasi and Manduchi, 1998).

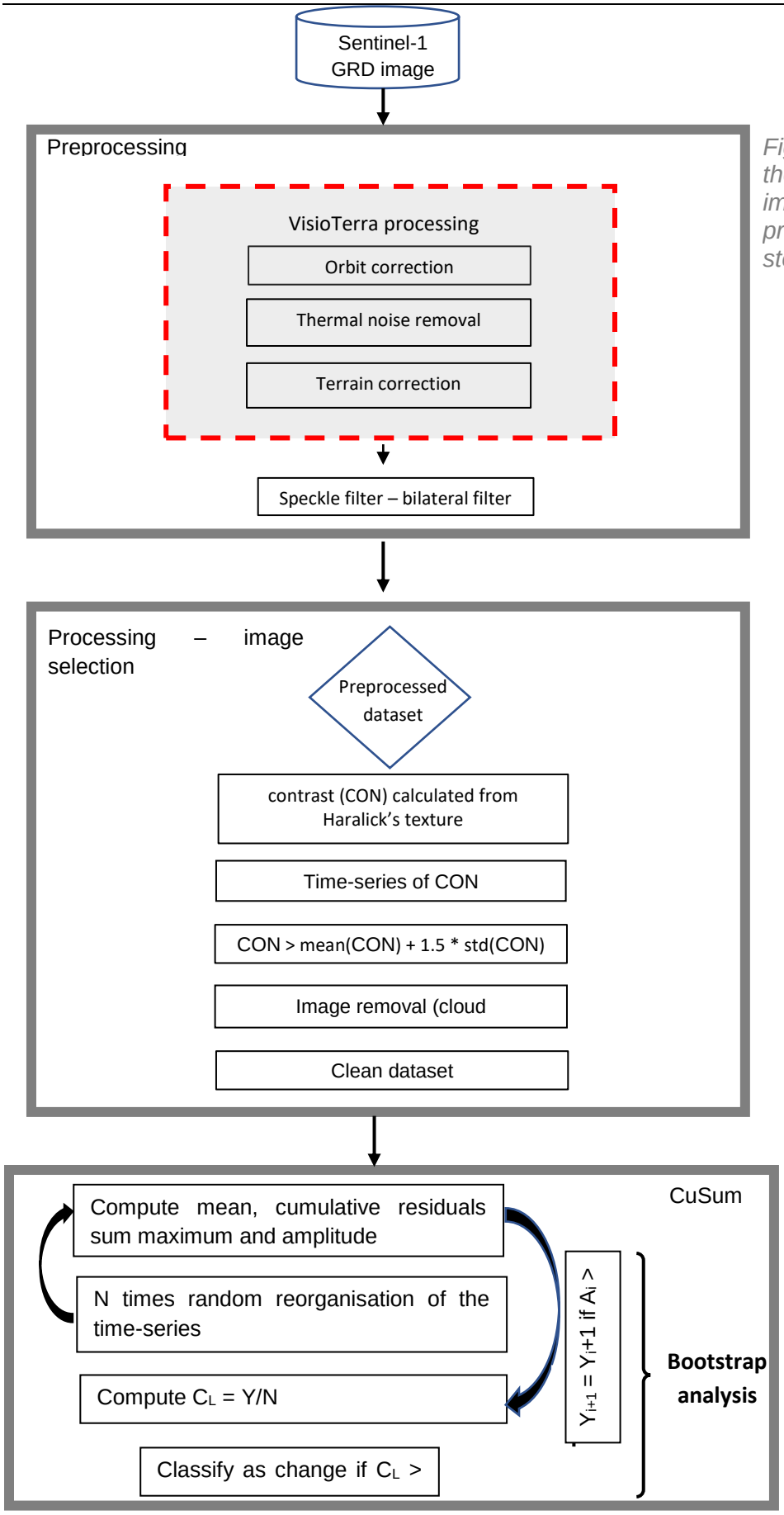

Figure IV.3: Workflow of the Sentinel-1 C-SAR image preprocessing, processing and CuSum steps.

4.2.3.2. Haralick textures and image selection

VtWeb provides different levels of aggregation of the Sentinel-1 SAR images ranging from the highest pixel resolution (10 m) to a very low pixel resolution (40960 m). The Contrast (CON) from Haralick textures (Coelho, 2013; Robert M Haralick et al., 1973) was computed on aggregated images with a resulting pixel resolution of 1,280 m to monitor changes in the SAR backscatter at a larger scale than that of S1 (10m x 10m) as follows:

$$CON = \sum_i \sum_j p(i,j) * (i-j)^2 \quad (1)$$

where *p(i,j)* is the frequency of the elements in Grey Level Co-Occurrence Matrix (GLCM),(i,j) is the cell index.

The study zone is located in a region characterized by a high cloud cover during the entire year. The presence of raincells has been confirmed on this area. Raincells are known to cause either an enhancement and/or a darkening of the SAR images (see an example of this latter effect on Figure IV.4). These two opposite effects are due to the presence of hydrometeors which interact with the EM waves emitted by the SAR sensor, causing dark and bright areas, on the SAR images, especially at C and X-bands (Alpers and Melsheimer, 2004; Kellndorfer, 2019). To detect the presence of large raincells in the SAR images, the Haralick texture features were used. The presence of raincell strongly modifies the CON parameter as defined in Eq. (1).

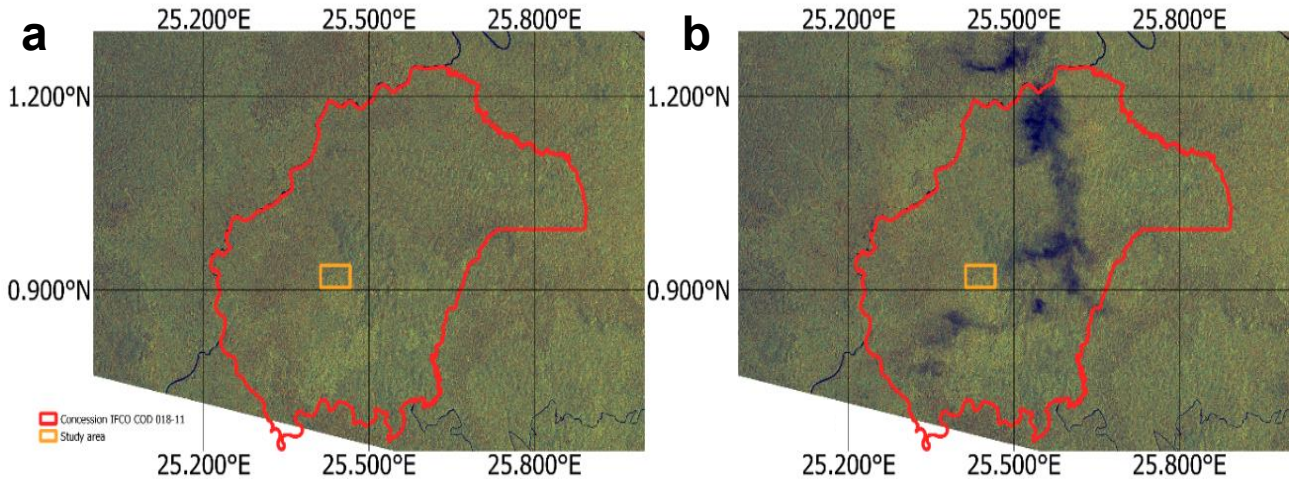

Figure IV.4: Sentinel-1 SAR images dated from (a) 20/10/2018 and (b) 13/11/2018 displayed in RGB : VV, VH, NDI(VV,VH). The raincell effect is visible on the second image.

The removal of raincell-contaminated images was automatized using a threshold (τ) defined using the temporal dynamics of CON in both the VV and VH polarizations:

$$\tau = K * (\sigma_{CON} + \overline{CON}) \quad (2)$$

where $\overline{CON}$ and σ_{CON} are respectively the average and the standard deviation (std) of CON during the observation period, and K a constant empirically set equal at 2 in this study. If *CON* is greater than t in a Sentinel-1 images for both the VV and VH polarizations, the S1 image is removed from the analysis. A large raincell was observed on the image acquired on 13/11/2018. This image was removed from the analysis (Figure IV.5).

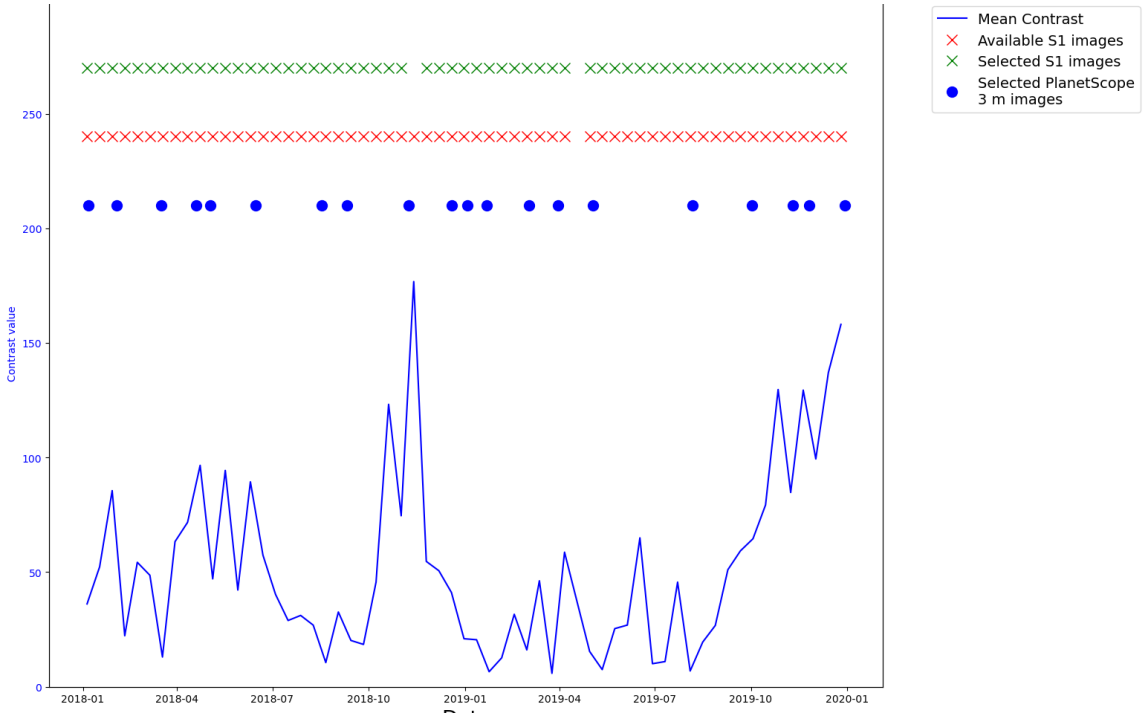

Figure IV.5: Temporal availability of Sentinel-1 C-SAR IW dual polarization and PlanetScope 3 meters images. The 13/11/2018 Sentinel-1 image was removed due to partial raincell contamination. The Contrast is computed from Haralick's texture (see 3.2), showed on VV polarisation. The Mean Contrast is the average contrast of a Sentinel-1 image with a pixel resolution of 1 280 m over the study area.

4.2.3.3. Change detection algorithm

4.2.3.3.1. CuSum algorithm

The Cumulative Sum (CuSum) algorithm is a change point detection method based on time-series analysis. It has been initially used in the financial sector (Manogaran and Lopez, 2018) and pioneer studies have applied it for mangrove and temperate forest monitoring (Kellndorfer, 2019; Ruiz-Ramos et al., 2020). Previous studies showed better performances in deforestation detection when this method was applied to filtered and smoothed time-series (Kellndorfer, 2019). The C-band SAR backscatter signal tends to decrease after a forest cut, according to

literature (Kellndorfer, 2019). The CuSum method is able to detect such changes in the signal (Manogaran and Lopez, 2018). The CuSum method consists in 5 steps including the bootstrap analysis.

The first step is to compute the VV and VH backscatter time-series of each pixel of the Sentinel-1 image in the study area over a given period. Then, the mean of the time-series ($\overline{\gamma^0}$ (j), over each pixel j) is determined at both the VV and VH polarizations and used in the computation of the cumulative sum of the residuals, R_{sumj}:

$$R_{sumj} = \sum_{i=1}^{n_{images}} R_{ij} \quad (3)$$

Where $R_{ij} = \gamma_{ij}^0 - \overline{\gamma_j^0}$, n_{images} is the number of images and j the pixel index.

The third step consists in determining the maximum and minimum value of the cumulative sum of the residuals to compute the amplitude A_{sumj} over the period:

$$A_{sumj} = R_{sum\_maxj} - R_{sum\_minj} \quad (4)$$

Where R_{sum_maxj} is the maximum value of R_{sumj} and R_{sum_minj} is the minimum value of R_{sumj}. The date of change in the vegetation over the pixel j is assumed to happen at the date when R_{sumj} reaches a maximum. A bootstrap analysis based on A_{sumj} is then conducted to validate or invalidate the change. There is no global threshold over the magnitude of the change. A threshold is computed individually over each pixel, as the mean value of the time series may change from one pixel to another.

4.2.3.3.2. Bootstrap analysis

A bootstrap analysis is conducted on the CuSum result. The bootstrap analysis is a mean to check the validity of the change detected through an indirect measure of the impact of the order sequence on the timeseries. The bootstrap consists in conducting CuSum on a randomly modified backscatter timeseries $n_{bootstraps}$ times and check if the generated amplitude of the residuals is greater than the original amplitude of the residuals. $n_{bootstraps}$ is the number of bootstraps. It depends on the length of the time-series (Kellndorfer, 2019). Firstly, the original backscatter time-series is randomly reorganized, thus modifying the temporal order. Then, the CuSum method is applied to the newly reorganized series to compute $R_{sum\_randj\_i}$ and $A_{sum\_randj\_i}$ (with i the index of the bootstrap). The next step is to compute the difference of amplitude between A_{sumj} and $A_{sum\_randj\_i}$ (Eq.6)

$$n_{bootstraps} = \begin{cases} n_{images}\,!\,(\,if\ n_{images}\,! < 1500) \\ 1500\ (if\ n_{images} \geq 1500) \end{cases} \quad (5)$$

Where $n_{images}!$ is the factorial of the number of images.

$$A_{diffj_i} = A_{sumj} - A_{sum\_randj_i} \quad (6)$$

If $A_{diffj\_i} > 0$, the residual amplitude of the randomly generated reorganized time-series ($A_{sum\_rand\_i}$) is lower than its original value (before reorganization). This means the original residual amplitude (A_{sumj}) is affected by the temporal dimension. The number of times the original residual time-series presents a A_{sumj} value greater than the randomly reorganised one is estimated and referred to as the index N_{gj} (Eq. 7). This index is incremented by 1 each time $A_{diffj\_i} > 0$. It is an indirect measure of the sequence effect in the backscatter time-series and a sensitivity parameter that intervenes in the computation of the Confidence Level (CL_j, Eq. 8).

$$N_{Gj} = \sum_{i=1}^{n_{bootstraps}} Index_{Gji} \quad (7)$$

With $Index_{Gji} = \begin{cases} 1\ if\ A_{diffj_i} > 0 \\ 0\ if\ A_{diffj_i} \leq 0 \end{cases}$

$$CL_j = \left(\frac{N_{Gj}}{n_{bootstraps}}\right) \quad (8)$$

CL represents the ratio of bootstraps in which the original backscatter time-series presents the amplitude $A_{sumj} > A_{randj}$ in comparison to the total number of bootstraps. A critical threshold value (T_c) can be set as a CL over which the change point is considered as valid by the bootstrap analysis.

4.2.3.3.3. Sensitivity to input parameter

The Confidence Level (CL) is a criterion related to the algorithm's sensitivity. In this study, we evaluated four different critical thresholds T_c based on the Confidence Level over which we consider the change as valid: T_c = 0.25, 0.50, 0.75 and 1.00. Higher T_c values resulted generally in a lesser number of pixels detected as "change" since only "change" pixel with high confidence level will reach the specific threshold, whereas lower T_c values resulted generally in a higher number of pixels detected as "change" because the lower specific threshold will be crossed on many pixels.

4.2.3.3.4. Spatial operations over the CuSum results

The two maps resulting from application of the CuSum algorithm to the VV and VH SAR images were intersected to form the "VV intersect VH" dataset. In that case, a pixel is considered to be subject to a change when it is classified as 'change' at both the VV and VH polarizations. This dataset was made in order to assess if changes affect both volume and surface components. As the SAR backscatter is affected by the dominant scattering mechanism resulting from the signal/target interaction, the impact on polarisation channels can vary. A dominant surface or double-bounce scattering mechanism generally display a higher intensity on the VV channel, while a dominant volume scattering will greatly influence the VH backscatter signals. The changes affecting an area can modify these interactions, resulting in changes being more detected by a polarisation than by the other.

The maps based on the VV and VH results were joined to form the "VV union VH" dataset. In that case, a pixel is considered to be subject to a change when it is classified as "change" from at least one of the polarizations (either VV or VH). Our objective with these "intersection" and "union" maps were to check the consistency / difference of the results based on both the VV and VH polarizations and to evaluate their complementarity.

High threshold values of T_c (T_c = 1.00) were found to be the most robust values in terms of accuracy from preliminary tests. In order to reduce the number of false positives obtained from low T_c values in the form of small clusters of change, a spatial recombination of T_c thresholds was applied. Results obtained from high T_c values were combined with those obtained from low T_c values. The raster images were first converted to vector images containing changes as polygons by using a 4-pixel connexion. Secondly, the areas corresponding to "high T_c" polygons (polygons to computed from high T_C values) were selected and only polygons of area > 300 m² were kept. They composed the base on which the following filter was applied. A filter was then applied using lower T_c values. Only the "low T_c" polygons including a "high T_c" polygon were kept in the analysis (Annexe 2). This resulted in the cross-T_c results, also referred to as 100_25 (base: T_c = 1.00, low T_c = 0.25), 100_50 (base: T_c = 1.00, low T_c = 0.5) and 100_75 (base: T_c = 1.00, low T_c = 0.75).

4.2.3.4. Validation steps

4.2.3.4.1. Reference map composition

The resulting maps of the date of forest change occurrence obtained in this study were evaluated using the PlanetScope optical images as no in-situ information was available. The GFW maps were not used as the visual inspection showed they missed newly deforested areas compared to the ones observed on the PlanetScope images, and hence, were considered to

be less reliable over the study zone. Eventually, all the areas visually determined as newly deforested from the consecutive PlanetScope images over the 2018-2019 period were assembled to form the PlanetScope 2018-2019 cover change image. This image was used as a reference to assess the accuracy of the change detection method based on the CuSum algorithm applied to the Sentinel 1 images. The 'deforestation' considered in the following parts of this study was the visual interpretation of change from forest to non-forest. The 'degradation' considered in the following parts of this study was estimated from the visual interpretation of PlanetScope images. It corresponds to the changes in the radiance of forested areas before their deforestation.

4.2.3.4.2. Statistics

There are two types of errors when comparing two binary spatial datasets: i) the false positive, which corresponds to the reference map detecting no change while the algorithm detects a change, ii) the false negative, which occurs when the reference map detects a change whereas the algorithm does not detect it. In order to describe the quality of the matching between our S1-based retrieved change map and the reference PlanetScope change map, the following classical statistical indicators (Overall Accuracy as Accuracy, Recall, Precision, F-score and Kappa Coefficient) derived from the confusion matrix were used. Due to class imbalance between Change and No Change, the overall accuracy, recall and precision should be studied along with F-score and Kappa coefficient for interpretation. The overall accuracy is shown here as an indicative statistic and should not be interpreted by itself, as explained in (Olofsson et al., 2014)) which provides exhaustive information about good practices for land cover change estimates. The overall accuracy is the ratio between the number of correctly classified pixels and the total number of pixels.

$$Accuracy = \frac{TP+TN}{TP+TN+FP+FN} \quad (9)$$

where TP are the True Positive (pixels classified by both the reference map and the algorithm as 'cover change'), TN are the True Negative (pixels classified by both the reference map and the algorithm as 'no cover change'), FP are the False Positive errors and FN are the False Negative errors. The precision corresponds to the ratio between the number of pixels correctly classified as 'cover change' and the total number of pixels classified as 'cover change' by the algorithm.

$$Precision = \frac{TP}{TP+FP} \quad (10)$$

The recall corresponds to the ratio between the number of pixels correctly classified as 'cover change' and the total number of pixels classified as 'cover change' by the reference map.

$$Recall = \frac{TP}{TP+FN} \quad (11)$$

The F1-score is the weighted average of precision and recall. This score is used when the classes are unevenly distributed.

$$F1 = 2\frac{recall\ .precision}{recall+\ precision} \quad (11)$$

The Kappa Coefficient is a measure quantifying how better the algorithm performs compared to a random classification according to the frequency of each class.

$$\kappa = \frac{P_0-P_e}{1-P_e} \quad (12)$$

Where P_o is the Observed Accuracy (Eq.9) and P_e the expected accuracy.

$$P_e = \frac{TP+FP}{Total}.\frac{TP+FN}{Total} + \frac{TN+FN}{Total}.\frac{TN+FP}{Total} \quad (13)$$

4.2.4. Results

Results obtained from the investigation of the PlanetScope data revealed a cover change area estimated at 341.5 ha (15.1% of the total study area) over the 06/01/2018 – 26/11/2019 period.

4.2.4.1. Spatiotemporal distribution of the changes

The CuSum algorithm was applied on the time-series of backscattering coefficients from the Sentinel-1 SAR images acquired at C-band in both the VH and the VV polarisations, for T_c values of 0.25, 0.5, 0.75 and 1.00. Cover changes detected by the CuSum approach are presented in Figure IV.6-a to d, and Figure IV.7-a to d, respectively for VH and VV. Change pixels are developed in continuous and consistent spatial patterns. For all mapping configurations (in terms of polarisation and T_c values), the number of pixels affected by a change decreases as T_c increases: the total area presenting a change ranges from a minimum value of 113.2 ha (VV intersect VH, T_c = 1) to a maximum value of 1333.6 ha (VV union VH,

T_c = 0.25). Smaller clusters affected by changes are generally detected for lower values of T_c than for higher values. Besides, the cluster size is also greater for lower values of T_c than for higher T_c values. The use of higher T_c values lowers the number of these clusters, but also reduces the size of the larger clusters. The latter are most often connected whereas the small clusters are not.

The results of the change detection method were compared with the PlanetScope reference map. Results obtained for a lower T_c value of 0.25 show a better detection of the cut areas with lower false negatives (True Positives = 273.7 ha / False Negatives = 67.8 ha for VV union VH) than for higher T_c values of 1 (True Positives = 160.5 ha / False Negatives = 181.1 ha for VV union VH). However, results obtained for lower T_c values (T_c = 0.25) present a large number of false positives (1060.0 ha for VV union VH) compared to higher T_c values of 1 (327.7 ha for VV union VH, Table IV.1). It is worth noticing that the larger clusters of change detected for any VV and VH combinations and for any T_c values correspond to the areas detected as cut in the PlanetScope reference map.

When comparing the results of the CuSum algorithm applied to the polarization channels, the VV channel detects more small clusters of change compared to the results obtained at VH. Similar results were obtained when comparing VV with VV union VH results. The area of the largest clusters was lower for VV (True Positives = 230.9 ha and False Negatives = 110.6 ha for T_c = 0.25, True Positives = 136.6 ha and False Negatives = 205.0 ha for T_c = 1.00). The clusters based on the VV polarization are more isolated than those obtained at VH polarization. For low Tc values (high sensitivity to changes), less changes are detected using VV than using VH, but it is the opposite for a higher T_c value.

Base	T_c	TP (ha)	TN (ha)	FP (ha)	FN (ha)
VV	0.25	230.9	1426.1	488.9	110.6
	0.50	227.5	1501.6	413.5	114.0
	0.75	217.8	1641.2	273.9	123.8
	1.00	136.6	1895.4	19.7	205.0
	100_25	219.9	1719.6	195.5	121.7
	100_50	217.1	1764.6	150.5	124.5
	100_75	208.6	1810.5	104.6	133.0
VH	0.25	261.3	1029.8	885.2	80.3
	0.50	253.8	1193.9	721.2	87.8
	0.75	239.7	1453.0	462.1	101.9
	1.00	128.2	1893.8	21.3	213.4
	100_25	259.5	1153.3	761.8	82.0
	100_50	249.1	1491.1	424.0	92.4
	100_75	231.6	1718.7	196.4	109.9
VV union VH	0.25	273.7	855.1	1060.0	67.9
	0.50	269.7	1007.8	907.3	71.9
	0.75	258.4	1296.1	618.9	83.1
	1.00	160.5	1882.3	32.8	181.1
	100_25	273.0	895.9	1019.2	68.5
	100_50	267.7	1257.5	657.6	73.8
	100_75	252.8	1614.6	300.5	88.7
VV intersect VH	0.25	218.9	1599.4	315.6	122.7
	0.50	212.2	1686.5	228.5	129.4
	0.75	199.2	1797.5	117.6	142.3
	1.00	104.9	1906.9	8.2	236.6
	100_25	200.4	1806.2	108.9	141.2
	100_50	196.4	1829.7	85.3	145.2
	100_75	187.4	1858.4	56.7	154.1
		Legend	Legend	Legend	Legend
		<85 (<25% c)	<479 (<25% nc)	>256 (>75% c)	>256 (>75% c)
		85-171 (25-50%)	479-958 (25-50%)	256-171 (75-50%)	256-171 (75-50%)

171-256 (50-75%)	958-1436 (50-75%)	171-85 (50-25%)	171-85 (50-25%)
>256 (>75%)	>1436 (>75%)	<85 (<25%)	<85 (<25%)

Table IV.1: Comparison between the CuSum results and the reference map. Change area of reference (from PlanetScope images) = 341.5 ha, non-change area of reference = 6581.1 ha. c = change area, nc = non-change area, TP: True Positives, TN: True Negative, FP: False Positive, FN: False Negative. The colour legend is qualitative: red is considered as "poor", orange as "relatively poor", yellow as "relatively good" and green as "good".

According to Table IV.2, the number of separated clusters of change is not proportional to the threshold. This could be explained as the bigger clusters can often be dissociated at higher T_c, but smaller T_c clusters can disappear at higher T_c. The cross-threshold operations result in increasing mean and median areas compared to their simple T_c equivalent.

Base	T_c	Number	mean area (ha)	median (ha)
VV	0.25	1711	0,4207	0,0544
	0.50	2054	0,3121	0,0453
	0.75	1972	0,2493	0,0453
	1.00	453	0,3449	0,0272
	100_25	122	3,4043	1,65
	100_50	122	3,013	1,4505
	100_75	138	2,2695	1,1785
VH	0.25	583	1,9666	0,0453
	0.50	1077	0,9053	0,0635
	0.75	1522	0,4611	0,0725
	1.00	525	0,2847	0,0181
	100_25	41	24,9114	3,6535
	100_50	77	8,7425	2,7016
	100_75	115	3,7219	2,1486
VV union VH	0.25	574	2,3235	0,0181
	0.50	1041	1,1307	0,0272
	0.75	1953	0,4492	0,0453
	1.00	586	0,3297	0,0181
	100_25	29	44,561	0,5802

	100_50	55	16,8254	2,9645
	100_75	117	4,7293	2,1576
VV intersect VH	0.25	1609	0,3322	0,0544
	0.50	1703	0,2587	0,0363
	0.75	1160	0,2731	0,0363
	1.00	240	0,4715	0,0725
	100_25	92	3,3616	2,0229
	100_50	97	2,9045	1,7973
	100_75	101	2,417	1,514

Table IV.2: Spatial comparison between the CuSum clusters of change detected.

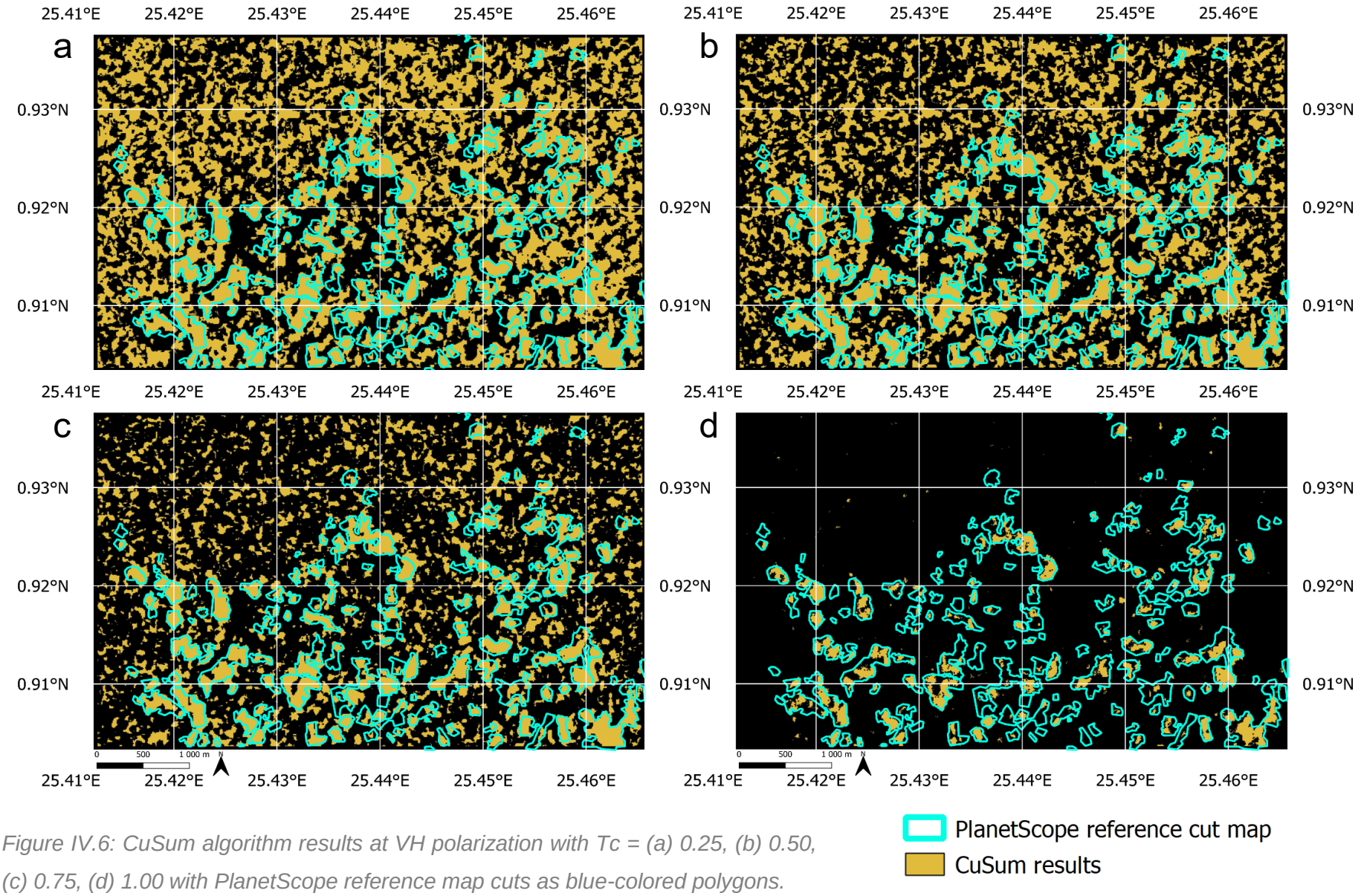

Figure IV.6: CuSum algorithm results at VH polarization with Tc = (a) 0.25, (b) 0.50, (c) 0.75, (d) 1.00 with PlanetScope reference map cuts as blue-colored polygons.

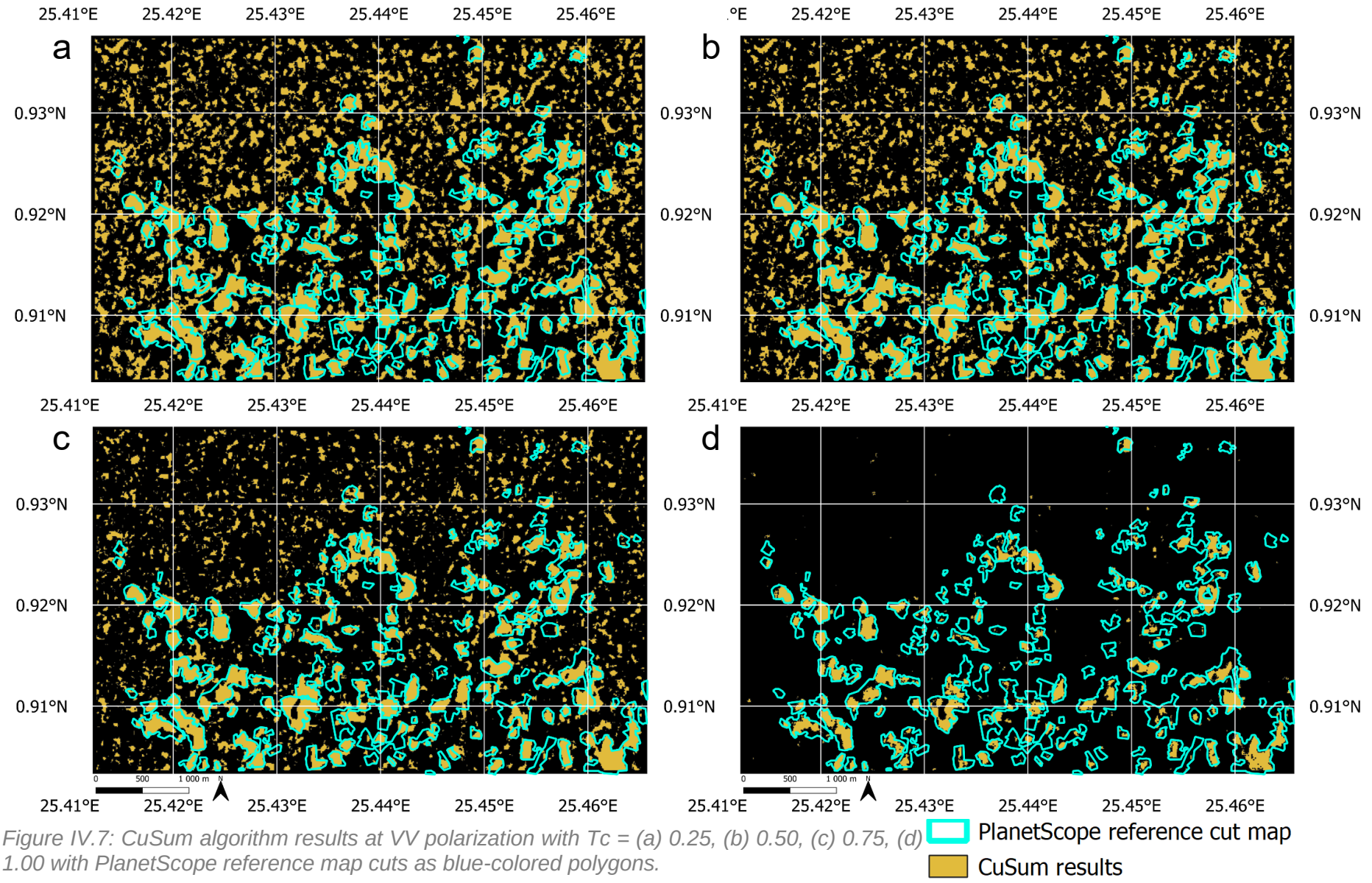

Figure IV.7: CuSum algorithm results at VV polarization with Tc = (a) 0.25, (b) 0.50, (c) 0.75, (d) 1.00 with PlanetScope reference map cuts as blue-colored polygons.

4.2.4.2. Cross comparison against external datasets using confusion-matrix derived statistics

When comparing results obtained for all mapping configurations based on VV, VH and their combinations (intersection and union) and for any T_c value (0.25, 0.5, 0.75, 1 and 100_25, 100_50 and 100_75), the precision ranges from very low (0.21 for VV union VH for T_c=0.25) to high (0.93 for VV intersect VH for T_c=1.00). Precision is very similar for all mapping configurations for T_c = 1.00 (0.87 to 0.90). The results of the different mapping configurations are very scattered for T_c ranging from 0.25 to 0.75. The cross-Tc combination generally increases the precision (compared to the simple T_c configuration), for instance the precision increased by 11.0% for VH (compared to T_c = 0.5 against 100_50) or by 23.8% for VV intersect VH (compared to T_c = 0.25 against 100_25, Table IV.3, Figure IV.8). However, the use of cross-Tc does not significantly increase the precision for VV union VH (for T_c = {0.25; 0.50} against {100_25; 100_50}) and for VH (T_c = 0.25 against 100_25). Whatever the T_c values, the VV intersect VH presents a better precision, followed by simple VV with a difference in precision of 0.11 (Table IV.3).

The accuracy results range from acceptable (50% for VV union VH at T_c = 0.25) to very accurate (91% for VV intersect VH at 100_75). The range of results is larger for lower T_c values than for higher ones. The use of cross-T_c leads to a narrower range of the accuracy values, increasing the accuracy from 2% to 10%. The most stable accuracy values were observed for VV intersect VH, with accuracy ranging from 81% to 91%. For VV intersect VH, the accuracy results obtained for T_c = 1.00 are similar to those obtained for cross-Tc = 0.75.

Lower recall values were obtained for higher T_c values (Table IV.3, Figure IV.8). The range of the Recall values is 0.34 - 0.78 considering all combinations of polarisations. This range is larger for T_c = 0.75 than for T_c = 0.25, 0.50 or 1.00 considering all possible combinations of VV and/or VH. The best recall values at all T_c and cross-T_c were obtained with VV union VH, increasing up to 0.78 for cross-T_c = 100_25.

The Kappa coefficient values range from very low (0.12) to acceptable (0.59) considering all VV and/or VH combinations. The range of the Kappa coefficient values is larger for lower T_c values. Use of cross-Tc configurations increases the Kappa coefficient by 13.5%. Overall, the higher value of the kappa coefficient is obtained using VV intersect VH.

The F1-score results range from relatively low (0.33) to acceptable (0.64) considering all VV and/or VH combinations. Use of cross-Tc configurations increases the F1-score by 4% up to 15%. Overall, the higher value of the F1-score is obtained using VV intersect VH.

Base	T_c	Precision	Accuracy	Recall	Kappa coefficient	F1-score
VV	0.25	0.32	0.73	0.68	0.29	0.44
	0.50	0.35	0.77	0.67	0.33	0.46
	0.75	0.44	0.82	0.64	0.42	0.52
	1.00	0.87	0.90	0.40	0.50	0.55
	100_25	0.53	0.86	0.64	0.50	0.58
	100_50	0.59	0.88	0.64	0.54	0.61
	100_75	0.67	0.89	0.61	0.57	0.64
VH	0.25	0.23	0.57	0.76	0.15	0.35
	0.50	0.26	0.64	0.74	0.21	0.38
	0.75	0.34	0.75	0.70	0.32	0.46
	1.00	0.86	0.89	0.38	0.47	0.53
	100_25	0.25	0.63	0.76	0.20	0.38
	100_50	0.37	0.77	0.73	0.36	0.49
	100_75	0.54	0.86	0.68	0.52	0.60
VV union VH	0.25	0.21	0.50	0.80	0.11	0.33
	0.50	0.23	0.57	0.79	0.16	0.36
	0.75	0.29	0.69	0.76	0.26	0.42
	1.00	0.83	0.91	0.47	0.55	0.60
	100_25	0.21	0.52	0.80	0.12	0.33
	100_50	0.29	0.68	0.78	0.26	0.42
	100_75	0.46	0.83	0.74	0.47	0.57
VV intersect VH	0.25	0.41	0.81	0.64	0.39	0.50
	0.50	0.48	0.84	0.62	0.45	0.54
	0.75	0.63	0.88	0.58	0.54	0.60
	1.00	0.93	0.89	0.31	0.42	0.47
	100_25	0.65	0.89	0.59	0.55	0.62
	100_50	0.70	0.90	0.57	0.57	0.63
	100_75	0.77	0.91	0.55	0.59	0.64
legend	0 – 0.25	0.25 – 0.50	0.50 – 0.75	0.75 - 1		

Table IV.3: Confusion matrix - derived statistics obtained by comparing the CuSum results to the PlanetScope reference map.

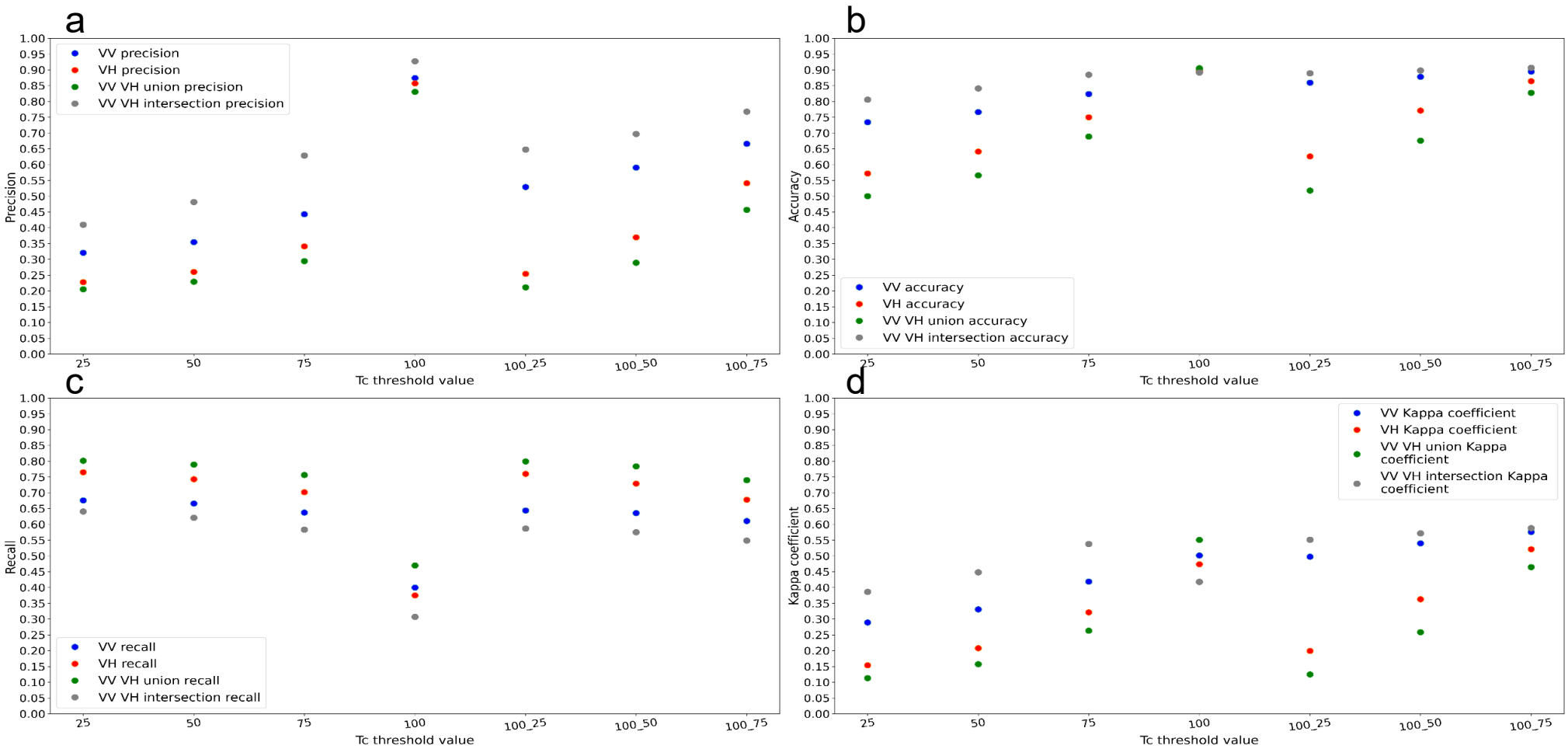

Figure IV.8: CuSum results statistics based on Planet cut map of reference. (a) Precision, (b) Accuracy, (c) Recall, (d) Kappa coefficient.

4.2.5. Discussion

Raincells are a large source of contamination of the backscatter coefficient over tropical forests. When applying the CuSum algorithm, we noted that it is crucial to filter out the images affected by the presence of raincells. If not, the inclusion of a contaminated pixel in the temporal average of the backscatter is likely to impact the results of the change detection method. In the present study, we found that the Contrast parameter from the Haralick's textures provided an efficient way to detect the contaminated images.

The lack of in-situ data complicates the validation process of the surfaces identified as presenting a cover change. By using visual interpretation of PlanetScope high resolution (3 m) images, clear cuts, field cuts and field cover changes could be clearly identified. The visual interpretation permitted to clearly separate forest and non-forest areas, and the changes occurring over these two types of covers. The validation of the method presented above was limited to clear cuts from forest areas, but changes over non-forest areas could be also detected using our approach, showing that this technique is able to detect forest cuts and forest degradation but also crop field cuts and soil cover changes.

High precision (0.93), recall (0.80), accuracy (91%), were obtained by evaluating the results of different parameterizations of the CuSum algorithm against PlanetScope, used as a reference, but the value of the Kappa coefficient remains relatively average (0.59 for the best configuration). The statistics of the comparison between the GFW map and the PlanetScope reference map show that, over the study area, the GFW map presents high accuracy (86%), but average precision (0.54), recall (0.57) and Kappa coefficient (0.48). The Tree Cover Loss area estimated from GFW dataset was 204 ha (9.0 % of the study area) *vs* 341.5 ha (15.1 % of the study area) for the PlanetScope-based reference map. The results of our method applied to Sentinel-1 SAR images has a higher Kappa coefficient than GFW in spite of being impacted by large false positives. Several clusters detected using the CuSum approach to the Sentinel-1 SAR images did not correspond to cuts based on the PlanetScope visual interpretation. As it can be seen in Figure IV.9, several zones were detected "as cover changes" by applying CuSum before the zones were visually seen as deforested. The PlanetScope images exhibited a change in radiance in these zones but this change is much lower than that due to clear-cut. Later on (from a few days to 3 weeks later generally), most of these zones were cut. We assumed that the change in radiance in the PlanetScope images corresponds to degradation prior to deforestation. As the PlanetScope reference map we made does not consider "degradation" but only "deforestation", the value of the Kappa coefficient and precision may be

impacted by the “degradation” events detected by CuSum but unconsidered by the reference map, thus remaining relatively low in comparison to the other (recall, accuracy) criteria.

According to the results some changes are well detected from only one polarization configuration (either VV or VH). This means both polarizations are affected differently by changes. But, overall, most big clusters of deforestation (showing a wide area labelled as deforestation on the reference map) are detected from both polarizations. The detection of a change by a polarization seems to be affected by (1) the nature of the change and (2) the magnitude of the change.

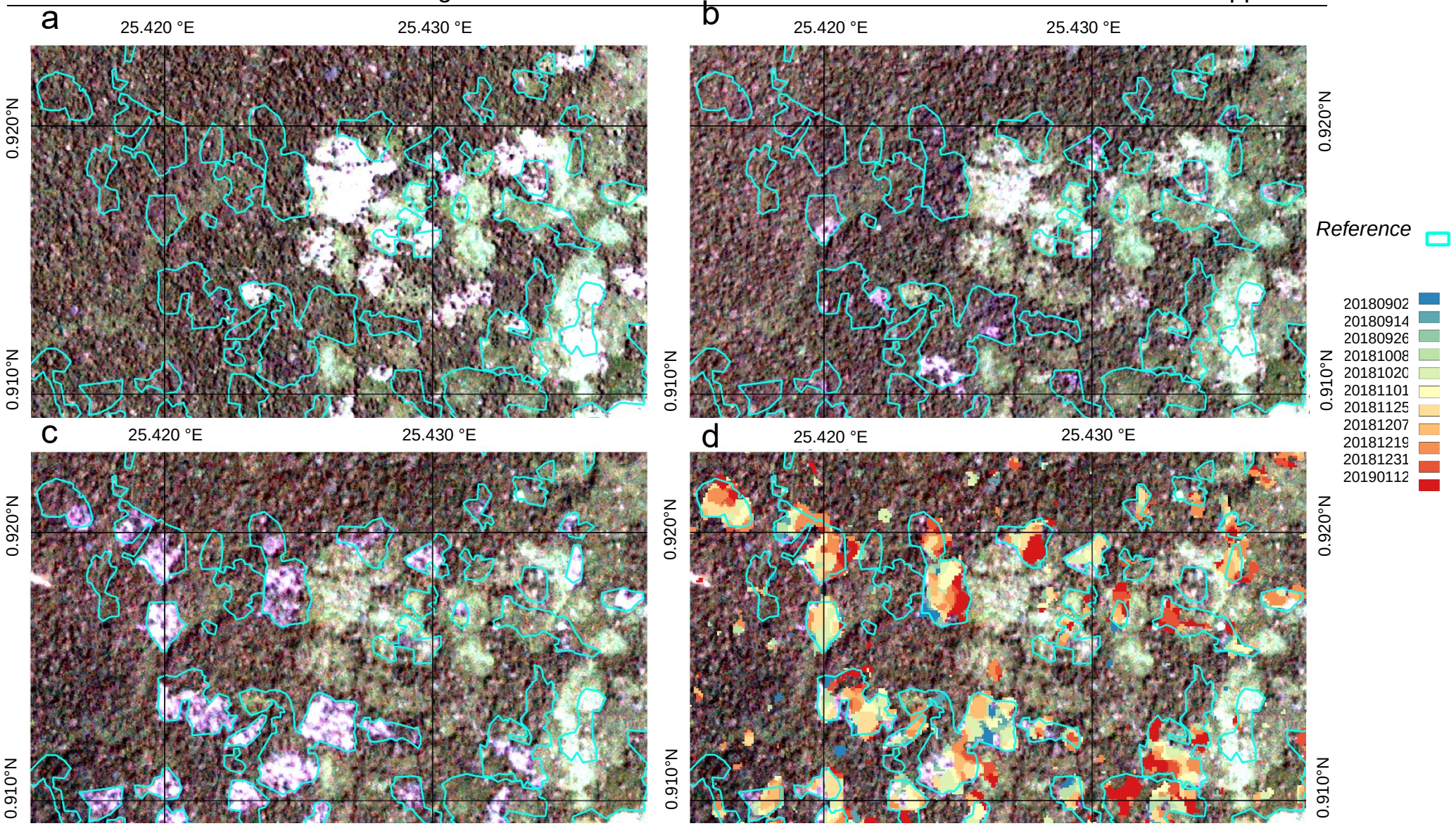

Figure IV.9: (a) 10/09/2018 PlanetScope image, (b) 08/11/2018 PlanetScope image, (c) 03/01/2019 PlanetScope image, (d) CuSum results based on VV with Tc = 0.75. Blue polygons correspond to PlanetScope cut map.

CuSum detected changes in many zones before their estimated dates of cut (64%, 167.3 ha, Table IV.4, Annex 1). This is consistent with the detection of degradations which occur before the reference dates of cut. Due to the relatively low availability of non-cloud-contaminated Planet images and the difficulty to monitor all degradations using this source, a precise estimate of the time-lag between degradation and cut could not be evaluated in this study, so that any change corresponding to a cut detected between the two nearest PlanetScope images is considered as a good detection.

Using two PlanetScope images separated by a long period would be suboptimal. Indeed, both degradation resulting in canopy gaps and canopy recovery may happen during a long period and the PlanetScope visual interpretation would then miss the degradation events that happened during that period. The use of a PlanetScope image temporally too close to the forest change detected by applying CuSum to Sentinel-1 SAR images can also miss the change. Indeed, this image may not be able to detect the forest degradation that was detected on the SAR images (as this change may not affect the canopy enough to be visible on the image). In both cases (small degradation and recovery), changes detected by the SAR images may not be detected by the Planet images. This effect may explain some false positives.

Note that the date pre-emptively detected is mostly detected within two weeks before the actual dates of cut. Nearly no detection of cuts was made later than the dates of cut seen through PlanetScope visual interpretation (5.93 % of the study area, corresponding to 15.49 ha), suggesting that some of the false positives made by applying CuSum are mainly due to degradation just before forest cut, and not by false detection of cut forests. Recent studies using Sentinel-1 images found that tropical canopy gaps and degraded canopy can be partially monitored using High Resolution SAR images ((Numbisi and Van Coillie, 2020; Reiche et al., 2021). It seems that our results confirm these findings over our study area.

Time period monitored	Total TP Cut area (m^2)	TP change area detected in time (m^2)	TP change area detected early (m^2)	TP change area detected early (%)	TP change area detected late (m^2)	TP change area detected late (%)
2018/01/06 - 2019/11/26	2613700	782500	1676300	64,14%	154900	5,93%

Table IV.4: Temporal evaluation of the CuSum results based on VV with Tc = 0.75.

The sensitivity threshold (T_c) plays a crucial role for the precision and recall criteria of the algorithm. A high T_c value provides a robust result with many false negatives and very few false positives whereas a low T_c value provides results reducing vastly the false negatives but

greatly increasing the false positives. The combination of the results based on VV and VH and the use of cross-threshold T_c values seems to be a good compromise to optimize both accuracy and precision. The number of false positives is relatively large for all configurations, but as explained earlier, the reference map is not ground truth as no in-situ data was available and it did not account for forest degradation before forest cut. Despite this lack of in situ data, spatially & temporally consistent results were obtained in this study, making us confident in our evaluation. For instance, a spatial coherence of the cross-threshold results was found (Figure IV.10): it seems the detected cuts form clusters which are dis-connected for high T_c values and the connection between clusters increase for decreasing T_c values, which could be interpreted by the fact roads or forest paths make connection between the different clusters of cut forests. It seems that small areas detected with a low T_c threshold and which are disconnected from the big clusters disappear for higher T_c values and are less reliable than those estimated with the “cross-threshold” clusters. The generalisation of this algorithm to dry forests and deciduous forest showing strong seasonal variability needs to be further tested, and the method probably adapted, as in (Ruiz-Ramos et al., 2020).

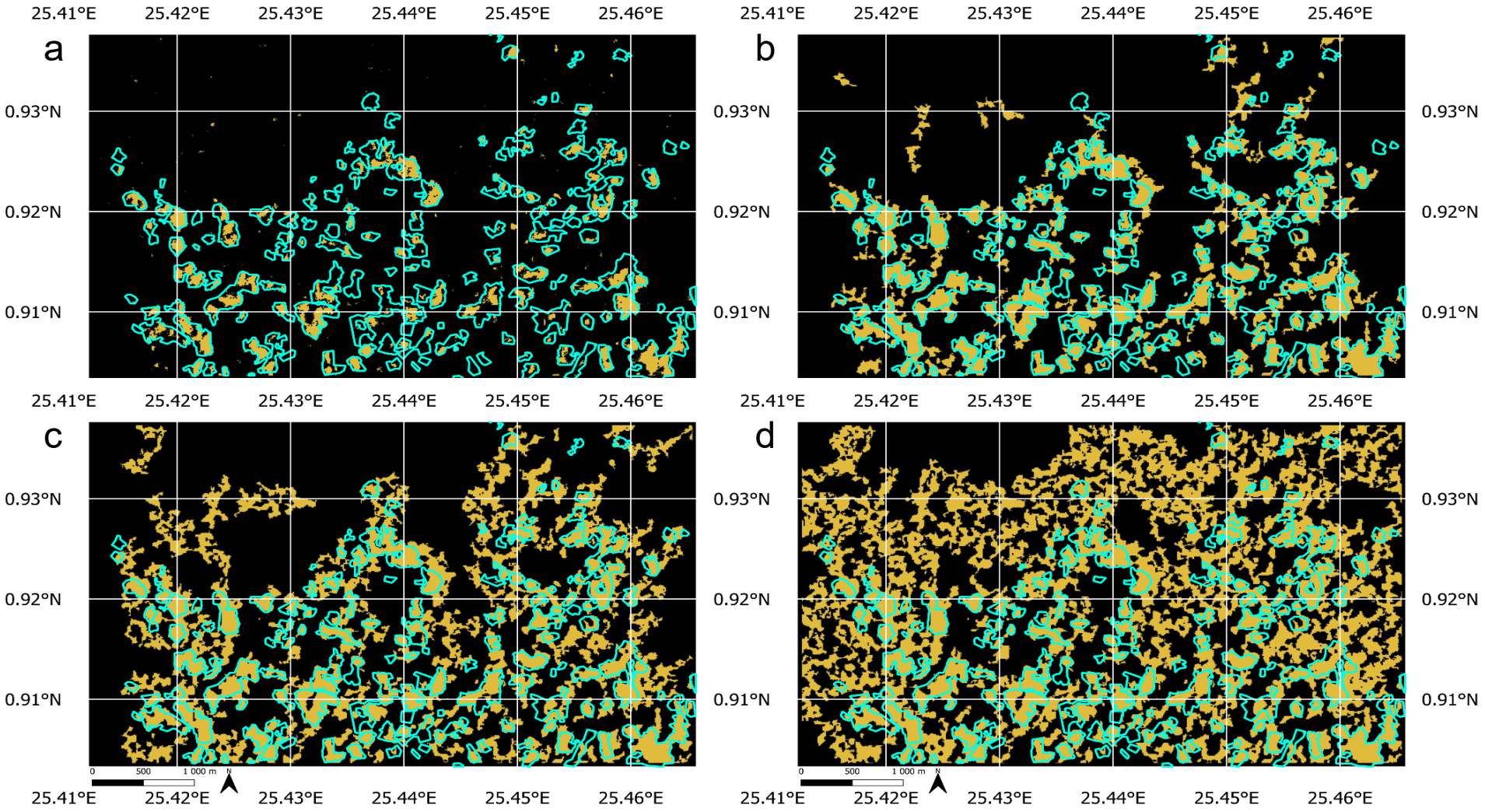

Figure IV.10: Map of the CuSum spatial results for VH with (a) simple Tc = 100, (b) cross Tc =100 and 75, (c) cross Tc = 100 and 50, (d) cross Tc = 100 and 25.

4.2.6. Conclusion

Cover change in tropical forests is difficult to monitor due to the lack of in-situ data and the large-scale extent of deforestation. Using Sentinel-1 C-SAR dual polarisation images, we were able to monitor cover changes in a Democratic Republic of Congo forest concession applying the CuSum approach to the Sentinel-1 SAR images.

According to accuracy assessment derived from the confusion matrix, CuSum applied to VV polarisation Sentinel-1 SAR images provides better results than using the VH polarization in terms of accuracy (minimal difference between VV and VH results of 1% for T_c = 1.00 up to 16% for T_c = 0.25), precision (minimal difference between VV and VH results of 0.01 for T_c = 1.00 up to 0.28 for 100_25) and Kappa coefficient (minimal difference between VV and VH results of 0.03 for T_c = 1.00 up to 0.30 for 100_25). The highest precision, related to the lowest False Negative ratio, was obtained using the intersection of VV with VH, with a minimal difference of 0.06 when comparing VV intersect VH T_c = 1.00 with VV T_c = 1.00 and a maximal difference of 0.33 when comparing VV intersect VH 100_50 with VH 100_50.

It is important to note that large differences of forest cut were found between our reference map based on PlanetScope (341.5 ha) and the GWF Cover Loss map (204 ha) in this area. It is probably due to the fact the tropical forest of DRC is often affected by cloud cover, and the better revisit time and resolution provided by PlanetScope OrthoScene led to improved detections. Our approach based on Sentinel-1 images is less affected by cloud cover, and the 12-day revisit time allows a good temporal monitoring. GFW Cover Loss map presents lower accuracy, precision, recall and kappa coefficient than the modified CuSum algorithm with a cross-Tc of 100_50. It also detects less true change area (189 ha) than the modified CuSum algorithm (up to 231.6 ha for VH 100_75).

The combination of the algorithm presenting the least false positives (high T_c value) with algorithms presenting more false positives (low T_c value) contributes to reduce the false positive errors obtained for low T_c values (minimum difference of 60.9 ha when comparing VV intersect VH T_c = 0.75 to VV intersect VH 100_75 to a maximum difference of 297.2 ha when comparing VH T_c = 0.5 to VH 100_50). It also contributes to reduce the false negative errors obtained for high T_c value (minimum difference of 72 ha when comparing VV T_c = 1.00 to VV 100_75 to a maximum difference of 131.4 ha when comparing VH T_c = 1.00 to VH 100_25). Overall, the CuSum parameters that provided the best detection of vegetation

cover change amongst the different polarisations and T_c configurations is VV intersect VH, cross-Tc 100_75 (Kappa coefficient: 0.59, Precision: 0.77, Accuracy: 0.91, Recall: 0.55).

The lack of in-situ data led us to use a PlanetScope-based reference map of the cover changes which is only based on remotely sensed optical observations and which present many limitations. In particular, degradation effects preceding deforestation were not monitored in this reference map, and canopy gaps can recover between two images. This could partially explain why our results, based on Sentinel-1 SAR images, exhibit more changes than detected in the reference map. This could also explain the lower scores obtained at VH than at VV when applying CuSum to Sentinel-1 images as observations at the VH polarisation are more sensitive to the degradation effects than at the VV polarisation (Kellndorfer, 2019). This could affect the false positives detected using VH: they are more numerous compared to using VV. In conclusion, some of the false positives can be attributed to degradation detected using Sentinel-1 SAR images that cannot be identified using optical images as previously noted by Numbisi and van Collie (2020) and Reiche et al. (2021).

The major drawback of our approach is its limitation to the detection of only one change against time. Once a pixel is affected by a change, its status does not evolve against time. We are currently working on a multi-temporal detection change approach that will be helpful to characterize the evolution of the forest cover from degradation to deforestation and then the possible recovery and could also be applied for the monitoring of lower vegetation canopy types.

4.2.7. Acknowledgement

This work was supported by VisioTerra. We also thank the reviewers for helping us improving the manuscript.

4.2.8. Reference

Alpers, W., Melsheimer, C., 2004. Rainfall. Synth. Aperture Radar Mar. user's Man. 355–371.

Antropov, O., Rauste, Y., Väänänen, A., Mutanen, T., Häme, T., 2016. Mapping forest disturbance using long time series of Sentinel-1 data: Case studies over boreal and tropical forests, in: 2016 IEEE International Geoscience and Remote Sensing Symposium (IGARSS). pp. 3906–3909. https://doi.org/10.1109/IGARSS.2016.7730014

Belenguer-Plomer, M.A., Chuvieco, E., Tanase, M.A., 2019. Temporal decorrelation of c-band backscatter coefficient in mediterranean burned areas. Remote Sens. 11, 1–19. https://doi.org/10.3390/rs11222661

Bouvet, A., Mermoz, S., Ballère, M., Koleck, T., Le Toan, T., 2018. Use of the SAR shadowing effect for deforestation detection with Sentinel-1 time series. Remote Sens. 10, 1–19. https://doi.org/10.3390/rs10081250

Bullock, E.L., Woodcock, C.E., Souza Jr, C., Olofsson, P., 2020. Satellite-based estimates reveal widespread forest degradation in the Amazon. Glob. Chang. Biol. 26, 2956–2969.

Coelho, L.P., 2013. Mahotas: Open source software for scriptable computer vision. J. Open Res. Softw. 1, e3. https://doi.org/10.5334/jors.ac

Contreras-Hermosilla, A., others, 2000. The underlying causes of forest decline. JSTOR.

Duveiller, G., Defourny, P., Desclée, B., Mayaux, P., 2008. Deforestation in Central Africa: Estimates at regional, national and landscape levels by advanced processing of systematically-distributed Landsat extracts. Remote Sens. Environ. 112, 1969–1981. https://doi.org/10.1016/j.rse.2007.07.026

Federici, S., Tubiello, F.N., Salvatore, M., Jacobs, H., Schmidhuber, J., 2015. New estimates of CO2 forest emissions and removals: 1990-2015. For. Ecol. Manage. 352, 89–98. https://doi.org/10.1016/j.foreco.2015.04.022

Hamunyela, E., Herold, M., Verbesselt, J., 2017. Space-time monitoring of tropical forest changes using observations from multiple satellites. Ph.D. Thesis, Wageningen University & Research, Laboratory of Geo-information Science and Remote Sensing, Wageningen, The Netherlands.

Hamunyela, E., Rosca, S., Mirt, A., Engle, E., Herold, M., Gieseke, F., Verbesselt, J., 2020. Implementation of BFASTmonitor Algorithm on Google Earth Engine to support large-area and sub-annual change monitoring using earth observation data. Remote Sens. 12. https://doi.org/10.3390/RS12182953

Hamunyela, E., Verbesselt, J., Herold, M., 2016. Using spatial context to improve early detection of deforestation from Landsat time series. Remote Sens. Environ. 172, 126–138. https://doi.org/https://doi.org/10.1016/j.rse.2015.11.006

Hansen, M.C., Krylov, A., Tyukavina, A., Potapov, P. V., Turubanova, S., Zutta, B., Ifo, S., Margono, B., Stolle, F., Moore, R., 2016. Humid tropical forest disturbance alerts using Landsat data. Environ. Res. Lett. 11. https://doi.org/10.1088/1748-9326/11/3/034008

Hansen, M.C., Potapov, P. V., Moore, R., Hancher, M., Turubanova, S.A., Tyukavina, A., Thau, D., Stehman, S. V., Goetz, S.J., Loveland, T.R., Kommareddy, A., Egorov, A., Chini, L., Justice, C.O., Townshend, J.R.G., 2013. High-resolution global maps of 21st-century forest cover change. Science (80-.). 342, 850–853. https://doi.org/10.1126/science.1244693

Haralick, R.M., Shanmugam, K., Dinstein, I.H., 1973. Textural features for image classification. IEEE Trans. Syst. Man. Cybern. 610–621.

Joshi, N., Mitchard, E.T.A., Woo, N., Torres, J., Moll-Rocek, J., Ehammer, A., Collins, M., Jepsen, M.R., Fensholt, R., 2015. Mapping dynamics of deforestation and forest degradation in tropical forests using radar satellite data. Environ. Res. Lett. 10. https://doi.org/10.1088/1748-9326/10/3/034014

Kellndorfer, J., 2019. Using SAR data for mapping deforestation and forest degradation, in: THE SAR HANDBOOK Comprehensive Methodologies for Forest Monitoring and Biomass Estimation. ServirGlobal : Huntsville, AL, pp. 65–79.

Kucera, J., Barbosa, P., Strobl, P., 2007. Cumulative Sum Charts - A Novel Technique for Processing Daily Time Series of MODIS Data for Burnt Area Mapping in Portugal, in: 2007 International Workshop on the Analysis of Multi-Temporal Remote Sensing Images. pp. 1–6. https://doi.org/10.1109/MULTITEMP.2007.4293051

Lievens, H., Martens, B., Verhoest, N.E.C., Hahn, S., Reichle, R.H., Miralles, D.G., 2017. Assimilation of global radar backscatter and radiometer brightness temperature observations to improve soil moisture and land evaporation estimates. Remote Sens. Environ. 189, 194–210. https://doi.org/https://doi.org/10.1016/j.rse.2016.11.022

Manogaran, G., Lopez, D., 2018. Spatial cumulative sum algorithm with big data analytics for climate change detection. Comput. Electr. Eng. 65, 207–221. https://doi.org/10.1016/j.compeleceng.2017.04.006

Numbisi, F.N., Van Coillie, F., 2020. Does sentinel-1A backscatter capture the spatial variability in canopy gaps of tropical agroforests? A proof-of-concept in cocoa landscapes in Cameroon. Remote Sens. 12, 1–29. https://doi.org/10.3390/rs12244163

Nunes, L.J.R., Meireles, C.I.R., Gomes, C.J.P., Ribeiro, N.M.C.A., 2020. Forest contribution to climate change mitigation: Management oriented to carbon capture and storage. Climate 8. https://doi.org/10.3390/cli8020021

Olofsson, P., Foody, G.M., Herold, M., Stehman, S. V., Woodcock, C.E., Wulder, M.A., 2014. Good practices for estimating area and assessing accuracy of land change. Remote Sens. Environ. 148, 42–57. https://doi.org/10.1016/j.rse.2014.02.015

Piantanida, R., Miranda, N., 2017. Thermal Denoising of Products Generated by the S-1 IPF.

Potapov, P., Hansen, M.C., Kommareddy, I., Kommareddy, A., Turubanova, S., Pickens, A., Adusei, B., Tyukavina, A., Ying, Q., 2020. Landsat analysis ready data for global land cover and land cover change mapping. Remote Sens. 12. https://doi.org/10.3390/rs12030426

Reiche, J., Hamunyela, E., Verbesselt, J., Hoekman, D., Herold, M., 2018. Improving near-real time deforestation monitoring in tropical dry forests by combining dense Sentinel-1 time series with Landsat and ALOS-2 PALSAR-2. Remote Sens. Environ. 204, 147–161. https://doi.org/https://doi.org/10.1016/j.rse.2017.10.034

Reiche, J., Mullissa, A., Slagter, B., Gou, Y., Tsendbazar, N.-E., Odongo-Braun, C., Vollrath, A., Weisse, M.J., Stolle, F., Pickens, A., Donchyts, G., Clinton, N., Gorelick, N., Herold, M., 2021. Forest disturbance alerts for the Congo Basin using Sentinel-1. Environ. Res. Lett. 16, 024005. https://doi.org/10.1088/1748-9326/abd0a8

Reiche, J., Verhoeven, R., Verbesselt, J., Hamunyela, E., Wielaard, N., Herold, M., 2018. Characterizing tropical forest cover loss using dense Sentinel-1 data and active fire alerts. Remote Sens. 10, 1–18. https://doi.org/10.3390/rs10050777

Reigber, A., del Campo Becerra, G.M., Jäger, M., 2019. PyRAT: A Flexible SAR Postprocessing Toolbox, in: ESA POLinSAR Workshop.

Rüetschi, M., Small, D., Waser, L.T., 2019. Rapid detection of windthrows using Sentinel-1 C-band SAR data. Remote Sens. 11, 1–23. https://doi.org/10.3390/rs11020115

Ruiz-Ramos, J., Marino, A., Boardman, C., Suarez, J., 2020. Continuous forest monitoring using cumulative sums of sentinel-1 timeseries. Remote Sens. 12. https://doi.org/10.3390/RS12183061

Ruiz-ramos, J., Marino, A., Boardman, C.P., 2018. USING SENTINEL 1-SAR FOR MONITORING LONG TERM VARIATION IN BURNT FOREST AREAS Javier Ruiz-Ramos ; Armando Marino ; Carl P . Boardman. IGARSS 2018 - 2018 IEEE Int. Geosci. Remote Sens. Symp. 4901–4904.

Small, D., 2011. Flattening gamma: Radiometric terrain correction for SAR imagery. IEEE Trans. Geosci. Remote Sens. 49, 3081–3093. https://doi.org/10.1109/TGRS.2011.2120616

Souza, C.M., Siqueira, J. V., Sales, M.H., Fonseca, A. V., Ribeiro, J.G., Numata, I., Cochrane, M.A., Barber, C.P., Roberts, D.A., Barlow, J., 2013. Ten-year landsat classification of deforestation and forest degradation in the brazilian amazon. Remote Sens. 5, 5493–5513. https://doi.org/10.3390/rs5115493

Takeuchi, S., Suga, Y., Yoshimura, M., 2001. A comparative study of coherence information by L-band and C-band SAR for detecting deforestation in tropical rain forest, in: IGARSS 2001. Scanning the Present and Resolving the Future. Proceedings. IEEE 2001 International Geoscience and Remote Sensing Symposium (Cat. No.01CH37217). pp. 2259–2261 vol.5. https://doi.org/10.1109/IGARSS.2001.977968

Tanase, M.A., Kennedy, R., Aponte, C., 2015. Radar Burn Ratio for fire severity estimation at canopy level: An example for temperate forests. Remote Sens. Environ. 170, 14–31. https://doi.org/https://doi.org/10.1016/j.rse.2015.08.025

Tanase, M.A., Perez-Cabello, F., de la Riva, J., Santoro, M., 2010. TerraSAR-X Data for Burn Severity Evaluation in Mediterranean Forests on Sloped Terrain. IEEE Trans. Geosci. Remote Sens. 48, 917–929. https://doi.org/10.1109/TGRS.2009.2025943

Tomasi, C., Manduchi, R., 1998. Bilateral filtering for gray and color images. Proc. IEEE Int. Conf. Comput. Vis. 839–846. https://doi.org/10.1109/iccv.1998.710815

Tyukavina, A., Hansen, M.C., Potapov, P., Parker, D., Okpa, C., Stehman, S. V., Kommareddy, I., Turubanova, S., 2018. Congo Basin forest loss dominated by increasing smallholder clearing. Sci. Adv. 4. https://doi.org/10.1126/sciadv.aat2993

Watanabe, M., Koyama, C.N., Hayashi, M., Nagatani, I., Shimada, M., 2018. Early-stage deforestation detection in the tropics with L-band SAR. IEEE J. Sel. Top. Appl. Earth Obs. Remote Sens. 11, 2127–2133. https://doi.org/10.1109/JSTARS.2018.2810857

Watanabe, M., Koyama, C.N., Hayashi, M., Nagatani, I., Tadono, T., Shimada, M., 2021. Refined algorithm for forest early warning system with ALOS-2/PALSAR-2 ScanSAR data in tropical forest regions. Remote Sens. Environ. 265, 112643. https://doi.org/https://doi.org/10.1016/j.rse.2021.112643

Whittle, M., Quegan, S., Uryu, Y., Stüewe, M., Yulianto, K., 2012. Detection of tropical deforestation using ALOS-PALSAR: A Sumatran case study. Remote Sens. Environ. 124, 83–98. https://doi.org/https://doi.org/10.1016/j.rse.2012.04.027

4.2.9. Website reference

COD Forest Atlas, 2016. https://cod.forest-atlas.org/ accessed December, 2019.

COPERNICUS, 2015. https://scihub.copernicus.eu accessed January, 2020.

Global Forest Watch, 2015. https://data.globalforestwatch.org/ accessed March, 2020.

Planet, 1996. https://www.planet.com accessed June, 2020.

SAR Users Manuals from NOAA, http://ww.w.sarusersmanual.com accessed June, 2021.

VtWeb, 2015. https://visioterra.org/VtWeb/ accessed November, 2020.

JJ-FAST, http://www.eorc.jaxa.jp/jjfast/jj_index.html, Accessed June 16,2021

4.3. Conference note: IGARSS 2021

Deforestation monitoring using Sentinel-1 SAR images in tropical areas

Ygorra B.[1,2,3], Frappart F.[1,4], Wigneron J-P.[1], Moisy C.[1], Catry T.[5], Baup F.[6], Hamunyela E.[7], Riazanoff S.[2]

[1] INRAE, UMR1391 ISPA, 33140, Villenave d'Ornon, France

[2] VisioTerra,77420, Champs-sur-Marne, France

[3] Université de Bordeaux, 33400, Talence, France

[4] LEGOS, 31400, Toulouse, France

[5] ESPACE-DEV, Univ Montpellier, IRD, Univ Antilles, Univ Guyane, Univ Réunion, Montpellier, France

[6] CESBIO, 31400, Toulouse, France

[7] University of Namibia, Private Bag 13301, Windhoek, Namibia

Chapter IV
Monitoring forest disturbances from Sentinel-1 time-series: a CuSum-based approach

Abstract

Tropical forests are vulnerable to deforestation, and various monitoring techniques have been developed based on remotely sensed data to map deforestation, but are facing multiple problems in the tropical areas. For instance, the techniques based optical data, which are widely used to monitor deforestation, face severe limitations in the humid tropical forest due to high cloud cover. Sentinel-1 C-SAR dense time series can be used for a temporally more accurate monitoring. In this study, a change detection algorithm commonly used in the financial domain, the Cumulative Sum (CuSum) algorithm, was modified to be applied on time-series of Sentinel-1 images in a forest concession of Democratic Republic of Congo (DRC) near Kisangani. The validation was made through the visual interpretation of PlanetScope OrthoScene images as it missed in-situ data. The results show a precision up to 0.75, an accuracy up to 0.95 and a kappa coefficient up to 0.40 for clear cut detection. The algorithm is able to detect forest degradation activities before the clear cuts.

Index Terms— CuSum, Sentinel-1, C-SAR, vegetation cover change, tropical forest, deforestation, degradation

4.3.1. Introduction

The tropical forests play a major role in the global climate regulation as they can recycle about 2.1 Gt CO2 yearly (Ruiz-ramos et al., 2018). In Africa, deforestation occur for multiple reasons, including illegal operations for commercial logging, selective logging causing degradations, or even cuts to fulfil the growing needs of local populations (Tyukavina et al., 2018). Coarse scale satellite observations allowed to quantify the impact of deforestation in terms of carbon losses (Fan et al., 2019; Wigneron et al., 2020). At a much higher spatial resolution change detection methods based on satellite remotely sensed data have been developed in order to monitor such changes (Hansen et al., 2013; Tyukavina et al., 2018) but encounter limitations over the tropical areas as they rely on optical data, which are very often contaminated by clouds. Another study uses SAR shadows to monitor deforestation areas (Bouvet et al., 2018). Other studies showed a better temporal accuracy in change detection (Hamunyela et al., 2020; Reiche et al., 2018a) merging optical and SAR images to account for the sub-annual variability. Yet, such methods increase the computational complexity and costs. These state-of-the-art change detection algorithms need increasing computational power as the satellite remotely sensed images spatial and temporal resolutions continue to increase.

The method developed in this study is based on the analysis of dense Sentinel-1 C-SAR image time series using a CuSum (Kucera et al., 2007; Manogaran and Lopez, 2018; Ruiz-Ramos et al., 2020) that we modified. The modified CuSum allows for the detection of any structural change in the time series, overlooking most seasonal variability.

4.3.2. Data and Methods

4.3.2.1. Data and study site

Two Earth Observation (EO) datasets were used in this study: Sentinel-1 Ground Range Detected (GRD) for the analysis and an optical dataset, PlanetScope Ortho Scene 3 m pixel resolution for the validation. Sixty Sentinel-1 IW GRD VV and VH images, provided by the European Space Agency (ESA) at https://scihub.copernicus.eu, and two PlanetScope images acquired on 08/01/2018 and 29/12/2019, available at https://www.planet.com were downloaded over our study site, located between 25.4122° and 25.4657° E, 0.9033° and 0.9376° N (Figure IV.11).

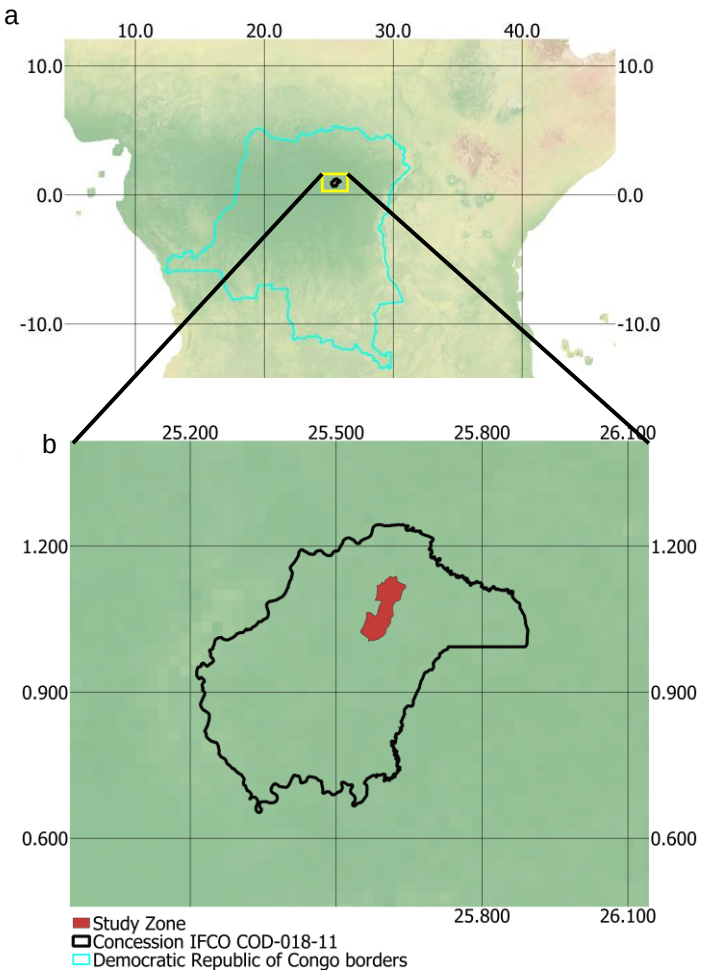

Figure IV.11: Location of the study area with (a) Borders of the Democratic Republic of Congo (in cyan) and (b)The study area (in red) within the IFCO COD-018-11 forest concession (in black), with Natural Earth II in background.

4.3.2.2. Methods

4.3.2.2.1. Preprocessing and processing

Sentinel-1 SAR images were pre-processed using the VtWeb preprocessing routine (https://visioterra.org/VtWeb/) consisting of orbit correction, orthorectification, thermal noise removal, radiometric correction and terrain correction. PyRAT Toolbox's bilateral filter (Reigber et al., 2019) was then applied to reduce the speckle. The VV and VH images contaminated by the presence of dense tropical clouds were removed automatically using a threshold based on the Haralick's Contrast texture (Robert M. Haralick, K. Shanmugam, 1973). The 13/11/2018 image was then removed.

4.3.2.2.2. CuSum algorithm

The Cumulative Sum (CuSum) algorithm is a change point detection method based on time series analysis. It stems from financial science (Flores et al., 2019; Manogaran and Lopez, 2018). The method is based on analysing, over each pixel, the deviation of the measurements from their mean values (= the residual time-series R_{sum}) considering the temporal sequence of the measurements.

$$R_{sum} = \sum_{i=1}^{n_{images}} R_i \quad (1)$$

where $R_i = \gamma_i^0 - \overline{\gamma^0}$ (2)

Extrema are then determined to compute the amplitude A_{sum}:

$$A_{sum} = R_{sum\_max} - R_{sum\_min} \quad (3)$$

where R_{sum_max} is the maximum value of R_{sum} and R_{sum_min} the minimum over each pixel.

The date of change is estimated at the date of R_{sum_max}.

A bootstrap analysis is recommended to "validate" the change, *i.e.*, to assess if the change results from randomness or from the sequel of values in the time series. It consists in reorganizing randomly the backscatter time series $n_{bootstrap}$ times, losing the temporal information then computing the amplitude of residuals of the newly arranged series. Its amplitude was computed as well as the Confidence Level (C_L), a sensitivity criterion, which is the ratio of the number of times the reorganized series amplitude is lower than the original amplitude divided by the total number of bootstraps.

We computed four different critical thresholds Tc over which the change is considered as 'valid': 0.25, 0.50, 0.75, and 1.00. Lower T_c should result in a high detection level with a lot of commissions and few omissions whereas higher T_c should result in a very accurate detection: few commissions but many omissions.

Intersections between the polygons of lower T_c and that of higher T_c were selected if their area is higher than 200 m². These formed the datasets 100_25; 100_50 and 100_75.

The VV by VH product results from the intersection between VV and VH.

4.3.2.3. Validation method

PlanetScope OrthoScene images acquired on 08/01/2018 and 29/12/2019 were used to visually assess the changes and clear cuts over the study area and build a reference map of cover changes. This reference map was used to compute the statistics derived from confusion matrix analysis: Accuracy, Precision, Recall and Cohen's Kappa coefficient. According to this reference map, 190.5 ha were cut over the period 2018-2020.

4.3.3. Results

4.3.3.1. Spatial patterns of changes

Results of the application of the CuSum method applied to the time-series of VH and VV Sentinel-1 SAR images for different T_c and their combination show linear patterns forming a network throughout the map. The changes are mostly located at the roads that were built during the monitoring period, as seen on PlanetScope reference map (Figure IV.12) and their vicinity. The log storage areas were detected on the road sideways. Numerous clusters of change can be detected outside the roads, most of which seem to be connected to the roads. The VV by VH cross-threshold 100_75 detected 364.23 ha as change areas. Results obtained for a lower T_c value show a higher number of commissions compared to higher T_c value. The VH results map shows a higher area detected as change than the VV results map. The algorithm presents few omissions at low T_c (10.92 %).

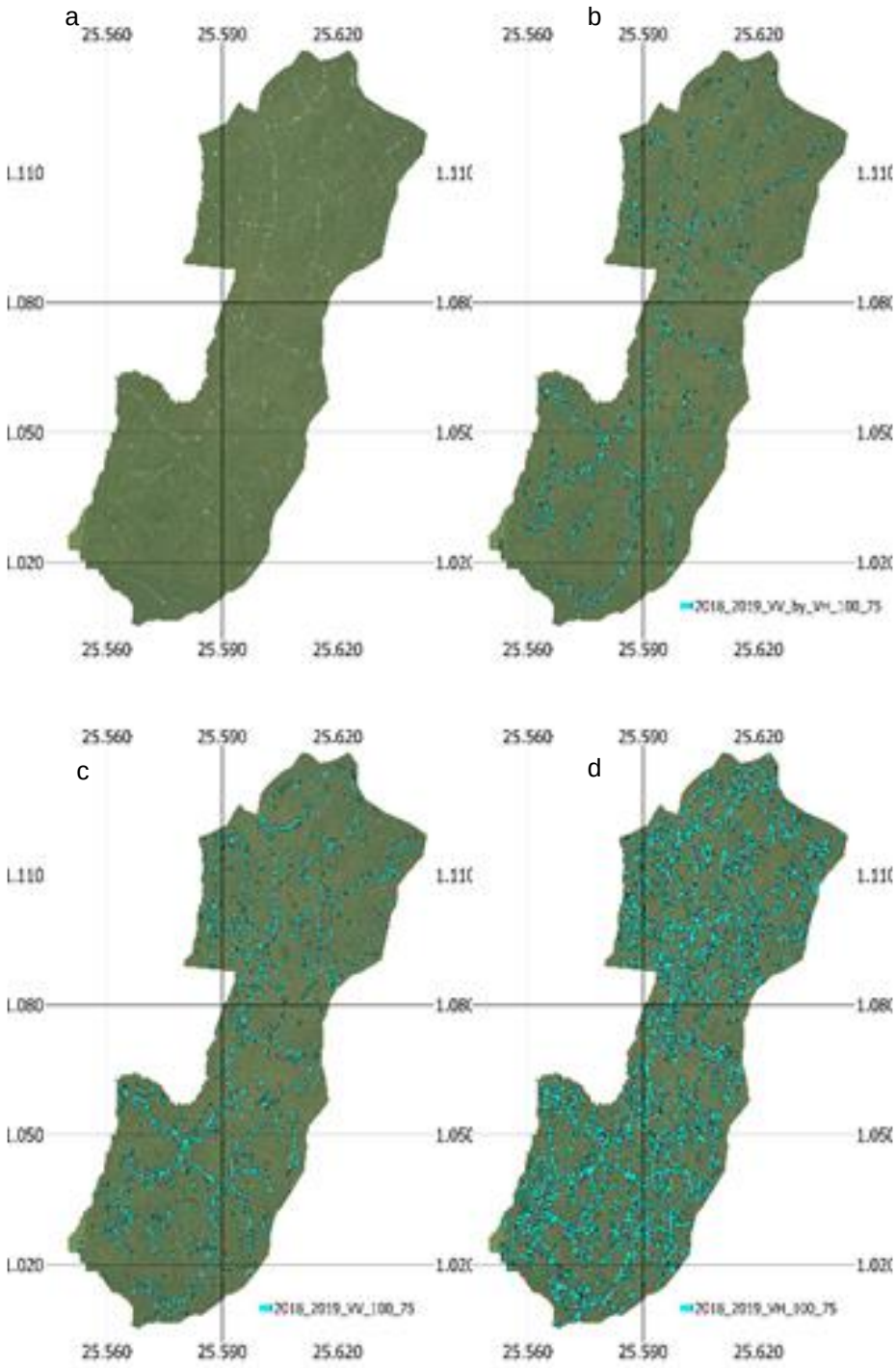

Figure IV.12: (a) PlanetScope image from 29/12/2019, cross-threshold 100-75 results map from (b) VV by VH, (c) VV and (d) VH.

4.3.3.2. Comparison against external datasets

As shown in Figure IV.13, the overall accuracy is very high (up to 97.3 %) for the VV by VH result map for Tc = 1.00. The precision is medium (53.4 %), but the recall is lower (26.4 %) as well as the kappa coefficient (34.1 %). When comparing the different critical thresholds and combinations, it is possible to see that the VH results are overall less performant than the VV results. The use of simple T_c thresholds led to overall lower statistical scores than the spatial combination of thresholds. The highest Kappa coefficient (40.0 %) is obtained using the VV by VH cross threshold 100_75 with medium precision (32.1 %), high accuracy (95.3 %) and good recall (61.4 %).

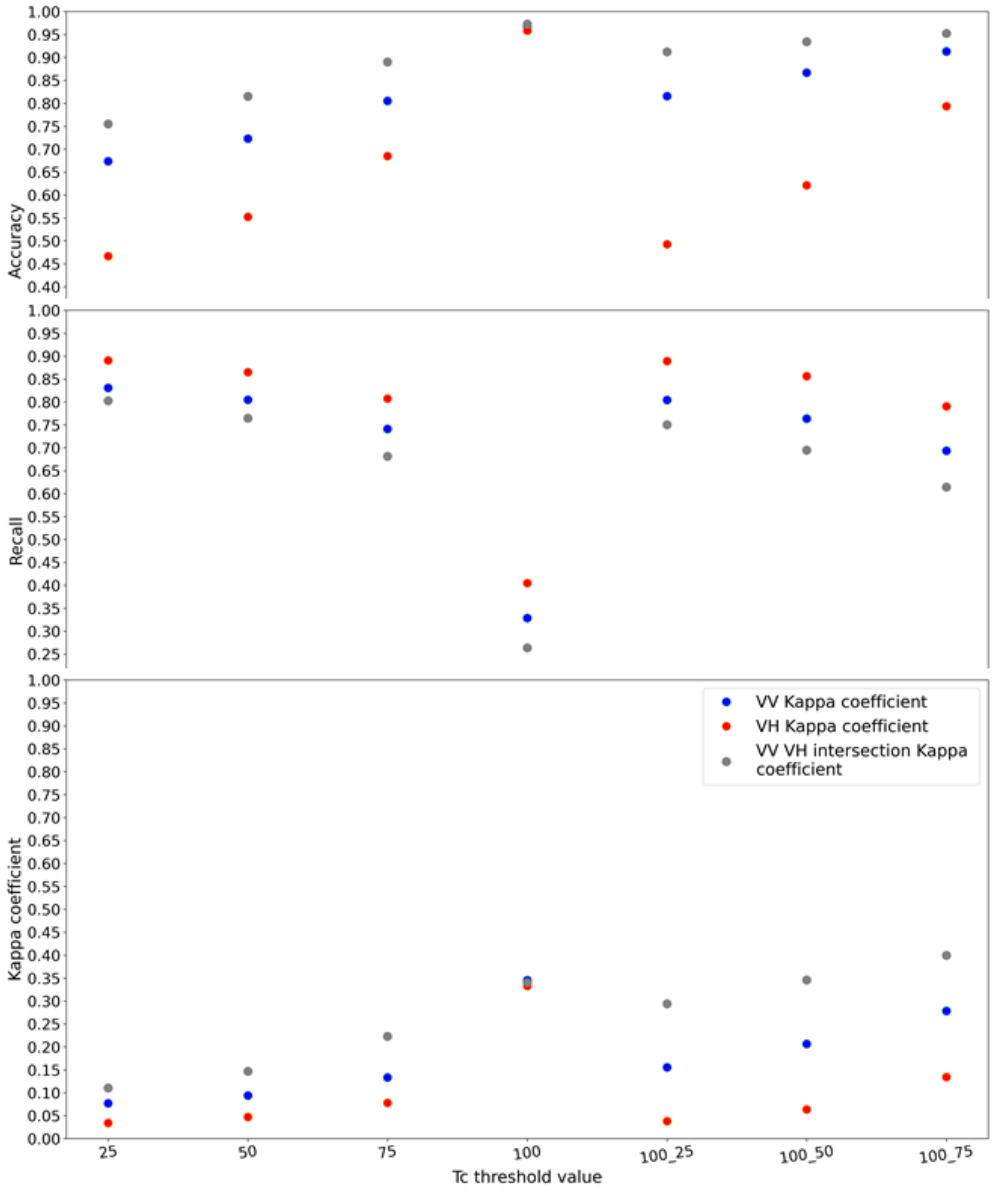

Figure IV.13: Statistics derived from the confusion matrix used in the comparison between the reference map and the results change map based on VV, VH and VV by VH with different thresholds and cross-thresholds. (a) Accuracy, (b) Recall, (c) Kappa coefficient.

4.3.4. Discussion

The CuSum algorithm can be applied to a high number of SAR images to detect changes to limit its sensitivity to the vegetation seasonal changes and their monitoring depending on the available images. The lower precision score can be explained by different factors: the high number of commissions compared to the small cut area detected in the reference map, but we can also make the hypothesis that

the algorithm is able to detect degradation activities under the canopy that optical dataset cannot monitor, thus creating false commissions. This is also what causes the Kappa coefficient low score.

The CuSum algorithm is able to detect the clear cuts in the tropical forest. The clusters connected to the road and unseen from the optical-based reference map exhibit well-organized patterns and can be interpreted as forest degradations beneath the canopy. The choice of the C_L sensitivity parameter through the selection of different T_c thresholds is found to be critical to ensure the best possible detection of the changes affecting the forest cover. We also found the combination of several T_c thresholds to improve the quality of the results.

This could explain the high number of commissions between the changes detected by the CuSum and those visually interpreted through PlanetScope images: the results based on S1 suggest that the reference deforested/degraded area estimated from PlanetScope may be strongly under-estimated.

The high temporal frequency of the Sentinel-1 images seems to be palliating to the average capability of C-SAR for monitoring deforestation in tropical areas.

4.3.5. Conclusion

The CuSum algorithm was found to be a very interesting algorithm for change detection in dense backscatter time series over tropical forests. CuSum is less sensible to seasonal change in vegetation as it is able to detect abrupt changes in the observed time series. The spatial combination of high and low T_c thresholds provides better results than simply keeping results for high T_c values. The combination of both the VV and VH detection results also enhanced the Kappa coefficient by reducing the number of commissions. The results showed an overall accuracy up to 97%.

4.3.6. References

[1] J. Ruiz-ramos, A. Marino, and C. P. Boardman, “USING SENTINEL 1-SAR FOR MONITORING LONG TERM VARIATION IN BURNT FOREST AREAS Javier Ruiz-Ramos ; Armando Marino ; Carl P . Boardman,” IGARSS 2018 - 2018 IEEE Int. Geosci. Remote Sens. Symp., no. July 2017, pp. 4901–4904, 2018.

[2] A. Tyukavina et al., “Congo Basin forest loss dominated by increasing smallholder clearing,” Sci. Adv., vol. 4, no. 11, 2018.

[3] J. P. Wigneron et al., “Tropical forests did not recover from the strong 2015–2016 El Niño event,” Sci. Adv., vol. 6, no. 6, pp. 1–11, 2020.

[4] L. Fan et al., “Satellite-observed pantropical carbon dynamics,” Nat. Plants, vol. 5, no. 9, pp. 944–951, 2019.

[5] M. C. Hansen et al., “High-resolution global maps of 21st-century forest cover change,” Science (80-.)., vol. 342, no. 6160, pp. 850–853, 2013.

[6] A. Bouvet, S. Mermoz, M. Ballère, T. Koleck, and T. Le Toan, “Use of the SAR shadowing effect for deforestation detection with Sentinel-1 time series,” Remote Sens., vol. 10, no. 8, pp. 1–19, 2018.

[7] E. Hamunyela et al., “Implementation of BFASTmonitor Algorithm on Google Earth Engine to support large-area and sub-annual change monitoring using earth observation data,” Remote Sens., vol. 12, no. 18, 2020.

[8] J. Reiche, E. Hamunyela, J. Verbesselt, D. Hoekman, and M. Herold, “Improving near-real time deforestation monitoring in tropical dry forests by combining dense Sentinel-1 time series with Landsat and ALOS-2 PALSAR-2,” Remote Sens. Environ., vol. 204, pp. 147–161, 2018.

[9] J. Kucera, P. Barbosa, and P. Strobl, “Cumulative Sum Charts - A Novel Technique for Processing Daily Time Series of MODIS Data for Burnt Area Mapping in Portugal,” in 2007 International Workshop on the Analysis of Multi-temporal Remote Sensing Images, 2007, pp. 1–6.

[10] G. Manogaran and D. Lopez, “Spatial cumulative sum algorithm with big data analytics for climate change detection,” Comput. Electr. Eng., vol. 65, pp. 207–221, 2018.

[11] J. Ruiz-Ramos, A. Marino, C. Boardman, and J. Suarez, “Continuous forest monitoring using cumulative sums of sentinel-1 timeseries,” Remote Sens., vol. 12, no. 18, 2020.

[12] A. Reigber, G. M. del Campo Becerra, and M. Jäger, “PyRAT: A Flexible SAR Postprocessing Toolbox,” in ESA POLinSAR Workshop, 2019.

[13] I. D. Robert M. Haralick, K. Shanmugam, “Textural Features for Image Classification,” 1973.

[14] A. Flores, K. Herndon, R. Thapa, and E. Cherrington, “SAR Handbook: Comprehensive Methodologies for Forest Monitoring and Biomass Estimation,” SAR Handb. Compr. Methodol. For. Monit. Biomass Estim., pp. 1–307, 2019.

4.4. Contribution to this work and perspectives in the PhD course

This work brings to light the potential of the CuSum algorithm, previously deemed too imprecise in comparison with recent algorithms. The implementation of spatial-temporal CuSum cross-T_c recombination has allowed the CuSum to be very effective for monitoring tropical deforestation.

In this work, changes to forest cover were detected before actual deforestation (viewed via remotely sensed optical images) and during what was deemed to be 'degradation', with no in-situ data for further validation. This assumption would lead to a very important hypothesis, namely that in tropical forests, the Sentinel-1 SAR images were able to detect degradation under the canopy that would be invisible to any optical monitoring systems.

The CuSum cross-T_c could detect only one change over a whole time-series, and not differentiate between different states if multiple changes occurred. This feature led to the following thinking: would it be possible to detect both degradation and deforestation using the CuSum on tropical areas by modifying the 'single point detection' method inherent to the CuSum?

This interrogation was the basis of the second part of my PhD, still focused on offline methods to produce deforestation assessments over a period of time: the multi-change detection CuSum cross-T_c development.

Chapter IV
Monitoring forest disturbances from Sentinel-1 time-series: a CuSum-based approach

CHAPTER V.

MULTIPLE BREAKPOINTS EVOLUTION OF THE CROSS-T_C CUSUM: RECUSUM

Table of contents

Chapter V – Multiple Breakpoints evolution of the CuSum cross-T_c: ReCuSum

5.1. Introduction

This chapter presents the work developed in the second part of my PhD, the implementation of the multi-detection CuSum cross-T_c for deforestation and degradation monitoring, called ReCuSum. The development of this algorithm was originally made in order to differentiate the degradation phase from the clear-cut phase in the IFCO concession near Kisangani, DRC, but the motive shifted to forest cover change monitoring due to the lack of validation data to differentiate degradation from deforestation. The area was also moved from DRC to the Amazon Forest in the Para state in Brazil. This study area is a test site for the Payment Program for Environmental Services (PSE).

The development of the method was quite fast, as it was an iterative CuSum method with time-series separation at every valid change date found. However, this method was time-consuming and needed to be optimized before being used in large areas. The outputs are a map of the number of changes per pixel and a raster file containing the maps of date of change.

The early results further shifted this study object from differentiating degradation and deforestation phases to a dual objective. The first objective consists in fine scale forest cover change monitoring, whereas the second objective consists of the classification in forest or non-forest, which might be differentiated on the number of changes occurrence. The binary classification goal was added because the test area had a larger variety of land cover than the study area in the first article.

Given the results of the binary classification, the capability of the single-change CuSum cross-T_c to monitor all changes occurring in an area (forest and non-forest) was assessed. As most changes occurring on both covers are correctly monitored, I decided to create a non-forest mask by applying the single-change CuSum cross-T_c on an earlier period. This period ends at the starting date of the monitoring period.

An article presenting the results obtained in the Para Sate has been submitted to the International Society for Photogrammetry and Remote Sensing (ISPRS). ReCuSum's capabilities were also evaluated on a temperate maritime pine forest in Aquitaine, north of the Arcachon Basin, Aquitaine, France. The results were presented at IGARSS 2022 (Ygorra et al., 2022)**.**

5.2. Publication

ReCuSum, a polyvalent method to monitor tropical forest disturbances

Ygorra Bertrand[1,2,3], Frappart Frederic[1], Wigneron Jean-Pierre[1], Moisy Christophe[1], Catry Thibault[4], Pillot Benjamin[4], Kharlanova Anna[4], Riazanoff Serge[2]

[1] INRAE, UMR1391 ISPA, 33140, Villenave d'Ornon, France

[2] VisioTerra,77420, Champs-sur-Marne, France

[3] Université de Bordeaux, 33400, Talence, France

[4] ESPACE-DEV, Univ Montpellier, IRD, Univ Antilles, Univ Guyane, Univ Réunion, Montpellier, France

Corresponding author: Ygorra Bertrand, bertrand.ygorra@gmail.com.

Abstract

Change detection methods based on Earth Observations are increasingly used to monitor rainforest in the intertropical band. Until recently, deforestation monitoring was mainly based on remotely sensed optical images which often face limitations in humid tropical areas due to frequent cloud cover, leading to late detections of disturbance events. After the launch of Sentinel-1, Synthetic Aperture Radar (SAR) images have been increasingly used to monitor deforestation owing to the high spatial and temporal resolutions offered by this mission composed of two identical satellites. In this study, we propose a multi-temporal version of the CuSum algorithm, a change detection method we previously applied to time-series of Sentinel-1 SAR images, to monitor deforestation/degradation in the Congo rainforest. CuSum is based on a Cumulative Sum method combined with a spatial recombination of Critical Thresholds (CuSum cross-T_c). The new multitemporal CuSum method (ReCuSum) we developed was applied to a time-series of 82 Sentinel-1 dual polarization (VH, VV) Ground Range Detected (GRD) images acquired in the Parà State, in the Brazilian Amazonia, over the 29/09/2016 - 01/07/2019 period. The ReCuSum method consists in iteratively applying the CuSum cross-T_c to monitor multiple changes in a time-series by splitting the time-series at each date of change detected and by independently iterating over the time periods resulting from the splits. The number of changes in the time-series was then analysed according to the vegetation type and showed a difference between non-forest vegetation and forested areas. A threshold based on the number of changes (T_{nbc}) was then developed to differentiate the vegetation type. The ability to monitor non-forest vegetation was analysed: the CuSum cross-T_c detected up to 90% of the total non-forest vegetation area over the study region in the past period. The non-forest vegetation and older disturbances were then removed from the monitored area. After removing past disturbances and removing the pixels covered with non-forest vegetations based on T_{nbc}, the application of the multitemporal CuSum led to a precision of 81%, a recall of 68%, a kappa coefficient of 0.72 and a F1-score of 0.74 in forest disturbance monitoring.

Keywords: SAR Remote Sensing; Sentinel-1; Cumulative Sum Algorithm; Tropical Deforestation; Multiple Change Detection, Forest Benchmark.

5.2.1. Introduction

Tropical rainforests are both a sink and a source in the carbon cycle with an overall neutral budget (Fan et al., 2019). These forests are vulnerable to anthropogenic activities, including selective logging or clear-cuts and burnings to fulfil the needs of local populations (Contreras-Hermosilla, 2000; Turubanova et al., 2018). Recently, the anthropogenic pressure increased, mainly through increased deforestation and degradations (Creese et al., 2019; Kleinschroth et al., 2019; Qin et al., 2021). Due to the unsustainable or illegal natures of these activities in these regions (Kleinschroth et al., 2019; Lescuyer et al., 2011; Umunay et al., 2019), there is an urgent need for a monitoring system at large-scale and with fine spatial and temporal resolutions. Remote sensing is a key tool to meet these requirements.

Remote sensing has been identified as a major tool for monitoring deforestation (Lynch et al., 2013). Several global operational systems producing near real-time forest disturbance alerts have been developed using optical remote sensing datasets since early 2000s (Hamunyela et al., 2020; Hansen et al., 2013; Vargas et al., 2019). In the inter-tropical band, several national-level systems are now operational (Diniz et al., 2015; Wheeler et al., 2014). As the tropical regions are strongly affected by clouds, such monitoring systems based on optical observations may provide temporally and spatially inaccurate information due to the scarcity of non-cloud-contaminated images over some specific regions/periods (Hansen et al., 2016; Reiche et al., 2018a).

The potential of the Synthetic Aperture Radar (SAR) systems for deforestation monitoring owing to cloud penetration ability of the microwaves observations has recently been highlighted (Joshi et al., 2015). There are currently two main sensors providing SAR images with a sufficient temporal resolution (~ weekly or monthly) which can be used for this purpose: Phased-Array L-band Synthetic Aperture Radar-2 (PALSAR-2) onboard the Japan Aerospace Exploration Agency (JAXA) satellite Advanced Land Observing Satellite-2 (ALOS-2) operating at L-band (Arikawa et al., 2014) and Sentinel-1, developed by the European Space Agency (ESA) in the framework of the Copernicus program and operating at C-band (Torres et al., 2012). Their respective advantages are for PALSAR-2, the use of L-band, less impacted by the presence of raincells and which penetrates deeper in the vegetation cover, and, for Sentinel 1, a free access to the data and better spatial and temporal resolutions (respectively, 6 to 12 days and 5 m x 20 m for Sentinel-1 against 1.5 month and 50 m for PALSAR-2 (Torres et al., 2012; Watanabe et al., 2021, 2018, 2017). The PALSAR-2 images are used by JAXA to produce a forest disturbance alert with a 1.5 month update and with a minimum mapping unit (MMU) of 2 ha, thus missing small-scale changes.

The Sentinel-1 A and B images, offering high spatial and temporal resolutions, allows a better detection of forest disturbances compared to optical and PALSAR-2 images (Reiche et al., 2018a).

Many approaches have been developed to monitor deforestation using C-band images from Sentinel-1. One approach is to use the shadow created by a change in forest cover in the opposite side of the satellite (Ballère et al., 2021; Bouvet et al., 2018). (Doblas et al., 2020; Hoekman et al., 2020; Mistry et al., 2021; Ruiz-Ramos et al., 2020; Ygorra et al., 2021a, 2021b) used time series change point analysis. (Nicolau et al., 2021) used classification based on data time-series to build a decision tree. Recently, machine learning was used to monitor disturbances occurring in tropical rainforests (Reiche et al., 2021; Zhao et al., 2022). Operational alert systems such as JJFAST and RADD, based on the aforementioned techniques, were also developed based on L- and C-band images (Reiche et al., 2021; Watanabe et al., 2018).

According to Ballère *et al.*, 2021, the algorithms used for deforestation monitoring should use a baseline forest benchmark to filter the detected changes, thus removing false alarms due to changes in other land use classes, such as agricultural activities in crop fields or pastures. For this purpose, many studies have used forest/non-forest masks developed from either optical (Hansen et al., 2013; Turubanova et al., 2018), radar (Martone et al., 2018; Watanabe et al., 2021) or lidar sensors (Verhelst et al., 2021). For the RADD alerts, multiple Land Use/Land Cover (LULC) products were used to produce a benchmark forest map (Reiche et al., 2021). The Global Forest Watch (GFW) canopy cover map in year 2000, excluding changes found in the 2000-2018 annual tree cover loss (Hansen et al., 2013), was used as a basis for forest benchmark from which they removed the dry tropical forests using the evergreen layer of Collection 2 Copernicus Global Land Cover dataset (Buchhorn et al., 2020). The produced map was then further refined using the forest benchmark map from Martone *et al.*, 2018**.** The need for a baseline forest benchmark is particularly important for deforestation monitoring algorithms based on Sentinel-1 data. Disturbances affecting different covers (agriculture, inundations, urbanization) may be wrongly labelled as disturbances affecting forest.

In this study, we present a change detection method developed for identifying forest disturbances based on time-series of Sentinel-1 C-band SAR images. The method is based on the Cumulative Sum algorithm (CuSum, Manogaran and Lopez, 2018), that identifies a change in a time-series based on both residual cumulative sum and bootstrap analysis. It has been used to monitor forest disturbances in tropical regions (Mistry et al., 2021; Ygorra *et al*., 2021a; Ygorra *et al*., 2021b).

Following (Reiche et al., 2021) and (Ygorra *et al.*, 2021b), we assumed that C-band SAR images are sensitive to both forest degradation patches and clear-cuts. Based on this assumption, the recursive application of the CuSum approach on different parts of a time-series for the same pixel would allow monitoring land cover changes, including the detection of the degradation or clear-cut dates. The application of such a recursive CuSum approach (referred as ReCuSum in the followings) was developed and is evaluated in the present study. The evaluation was made in a forest area located in the Para state in the Amazonian rainforest of Brazil.

The capability of the ReCuSum method to monitor disturbances occurring on both forests and other land cover types was evaluated. The number of changes computed from ReCuSum was analysed to compare the number of changes due to non-forest vegetation and forest disturbances. Then, we evaluated the possibility to generate a non-forest vegetation benchmark mask from the number of changes estimated over forest and non-forest using a long time-series of C-band SAR images.

5.2.2. Data and study areas

5.2.2.1. Study area

In several states of the Brazilian Amazonia, a payment system is already in place for maintaining ecosystem services, biodiversity conservation, watershed services, carbon sequestration or landscape conservation (Ruggiero et al., 2019; Wunder, 2015) . The selected area in the present study is a test site for the Payment Program for Environmental Services (PSE) evaluation located in Amazon, East of Altamira in the Parà State. Multiple remotely sensed image datasets are available on this test site (Sentinel-1, Sentinel-2, PlanetScope ortho-scene images, PlanetScope monthly mosaic). The study area is equal to ~ 97.2 km² mainly composed of agricultural fields, tropical rainforest, small villages, rivers and roads (Figure V.1). We focused the study on the 2017/2019 time period.

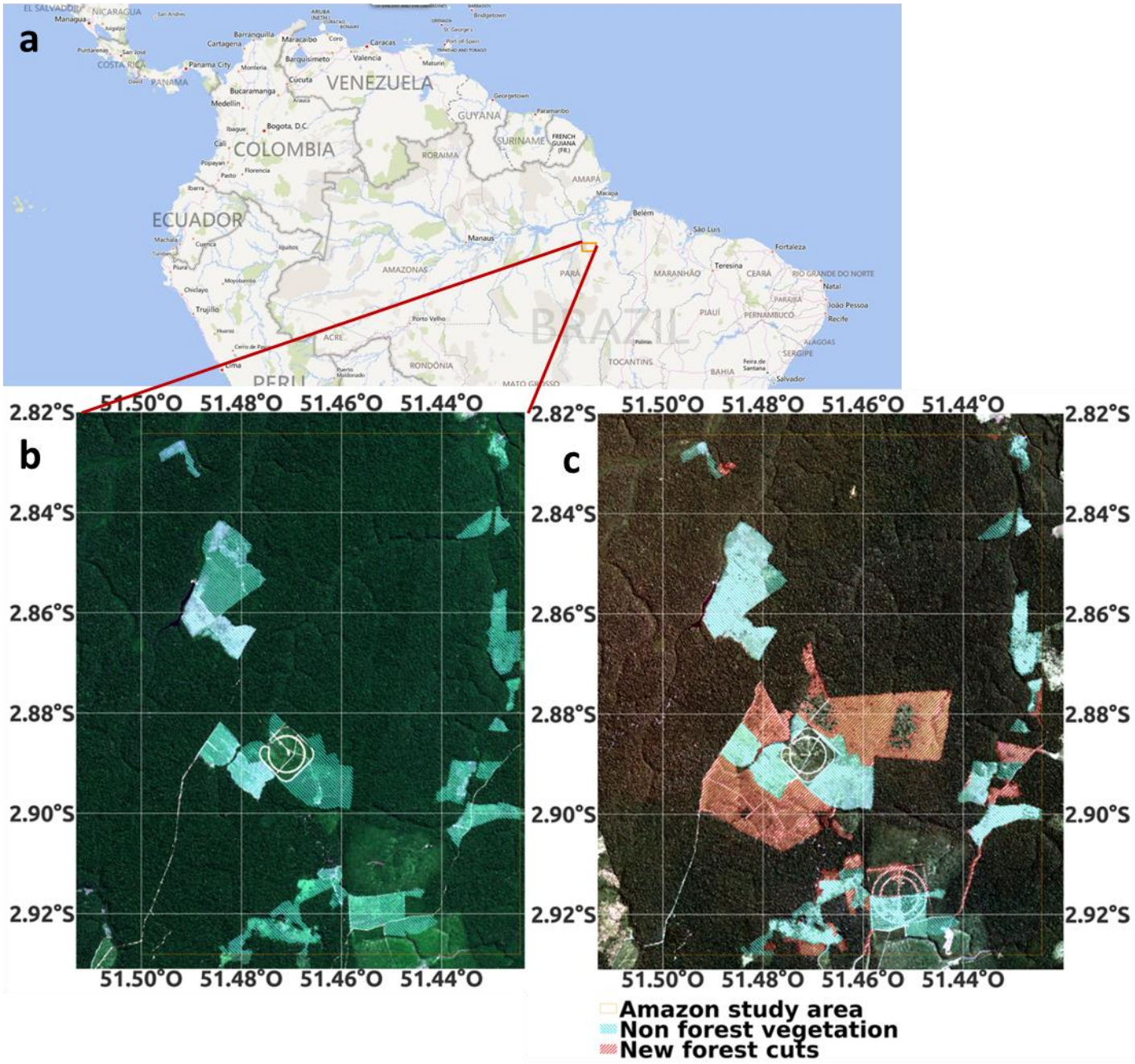

Figure V.1: Amazon study area seen from (a) Sentinel-2 image acquired on 28/07/2017 at the beginning of the monitoring period and (b) from PlanetScope image from June 2019 monthly mosaic, at the end of the monitoring period. The red striped polygons correspond to new forest cuts and the blue striped polygons correspond to non-forest low vegetation.

5.2.2.2. Data

5.2.2.2.1. Sentinel-1 SAR images

Deforestation detection was based on time-series of Sentinel-1 images. The Sentinel-1 mission was developed in the framework of the Copernicus program by ESA. It is a constellation composed of two satellites positioned on the same orbit plane at an altitude of 693 km, with an orbital phasing difference of 180°. The repeat cycle of each satellite is 12 days over the Amazon sites of the present study.

The data used in this study correspond to the Multi-Look Detected (GRD) products. They were acquired in Interferometric Wide-Swath (IW) mode at VV and VH polarizations. The resulting pixel size is 5 m x 20 m. The images were made available by ESA at https://scihub.copernicus.eu and downloaded using VtWeb (https://visioterra.org/VtWeb/). The downloaded images were preprocessed, including orbit correction, thermal noise removal, terrain correction, speckle removal and raincell-contaminated images removal (see (Ygorra *et al.*, 2021b) for more details on these preprocessings performed by VtWeb). A total of 82 images were used on the study area during a period of almost 3 years ranging from 29/09/2016 to 01/07/2019. Among the 82 images, during the first year of the study period ranging from 29/09/2016 to 01/09/2017, 29 images were used to define a forest benchmark (referred as 'past period'). Then during the two following years (01/08/2017-01/07/2019) of the study period, 56 images were used for monitoring the changes occurring over the study area (referred as "monitoring period"). Note that a few (three) images were common to the two periods. As a delay is usually noted for SAR forest disturbance detection, if no images were common to both periods, there would be a lack of detection in the ~first three weeks before the start of the monitoring period (Hamunyela et al., 2017).

5.2.2.2.2. Multispectral Optical datasets: Sentinel-2 images and PlanetScope monthly mosaic

The level 3B products from PlanetScope Ortho-Scene, obtained from CubeSat constellation, were used to produce a mosaic which was used to build a validation dataset for evaluation and validation.

The processing of Level 3B PlanetScope images includes conversion of radiance to top of atmospheric reflectance, geolocation, atmospheric correction, and cloud masking. The data are atmospherically corrected to surface reflectance using the 6S model combined to the spatially and temporally closest available MODIS aerosol optical depth (AOD) data (Levy et al., 2013). Per-pixel unusable data masks are derived indicating if a pixel is missing, clear, cloudy, shadowed, hazy, or snow covered, using a convolutional neural network. Geolocation is based on the matching of the sensed frame data with a globally distributed set of Ground Control Points (GCPs) derived from Landsat-8. A DTM is also used in the geolocation to remove relief distortion effects (Roy et al., 2021).

These images consist in 4-band Surface Reflectance (SR) images, scaled and orthorectified with a pixel resolution of 5 meters (Red: 605 - 695 nm, Green: 515 - 595 nm, Blue: 450 – 515 nm, Near-InfraRed: 740 – 900 nm). Those mosaics are produced following a 4 steps procedure:

- scene selection: the “best” scenes, i.e minimum cloud coverage allowing the maximum amount of GCPs to be available for orthorectification, are selected;
- atmospheric correction: based on seasonal models of Landsat data by applying normalization and harmonization of TOAR scene data to SR corrected Landsat data;
- cloud masking using the UDM2 classification for clouds and cloud shadows (https://developers.planet.com/docs/data/udm-2/);
- radiometric normalization: standard Landsat based reference datasets were updated to create tropics optimized normalization targets.

They are made available through the NICFI program (https://www.planet.com/nicfi/). A PlanetScope monthly mosaic was accessed over the study area in June 2019, at the end of the monitoring period to validate the detections of changes. A multi-spectral Sentinel-2 image (10 m resolution) acquired on 28/07/2017 was also used to determine non-forest vegetation areas at the beginning of the monitoring period as no PlanetScope monthly mosaic was available.

5.2.3. Methods

The ReCuSum method we developed and that we evaluate in this study consists in recursively applying the single-change CuSum detection proposed by Manogaran and Lopez, 2018 to segment a time-series in several sub-periods until no more change is detected. We present successively the two methods in this section**.**

5.2.3.1 Single-change CuSum detection

Before describing the multi-change CuSum detection (ReCuSum), the main aspects of the single detection CuSum approach, that is the basis of the ReCuSum, are summarized. The CuSum change detection method is composed of several steps, performed after the preprocessing of the SAR images using VtWeb (see subsection 2.2.2), including implementation of the CuSum method and several post-processing steps. The CuSum algorithm is based on the detection of the maximum of the Cumulative residual Sum series. It is accompanied by a bootstrap analysis based on the number of times the

cumulative residual sum series is higher than the cumulative residual sum series obtained from randomizing the original backscatter time-series (bootstrap). The number of times the original amplitude is higher than the amplitude obtained on the randomized time-series is then normalized by the number of iterations in the bootstrap to obtain the Confidence Level (CL). The critical threshold T_c is a threshold based on the confidence level.

A change detected by the CuSum is considered valid if the bootstrap analysis shows a Confidence Level (CL) greater than a critical threshold (T_c) previously set. A flowchart of the different post-processing steps is given in Figure V.2. The main objective in the post-processing consists in lowering both the number of false positives in low T_c map (i.e. maps computed with a low Tc value of 75) and the number of false negatives in high T_c map (i.e. maps computed with a high Tc value of 100).

The initial post-processing steps are composed of (1) dilatation and erosion (closing) of the result maps, (2) combination of the results computed from observations at the VV polarization with those computed from observations at the VH polarization, keeping only changes happening in both images, (3) application of a Minimum Mapping Unit of 0.03 ha and (4) the cross-T_c spatial recombination. The cross-T_c recombination consists in keeping all low T_c polygons intersecting with at least one high T_c polygon. The cross-T_c step was determined to be a step greatly increasing the quality of the resulting change detection compared to either low or high simple T_c.

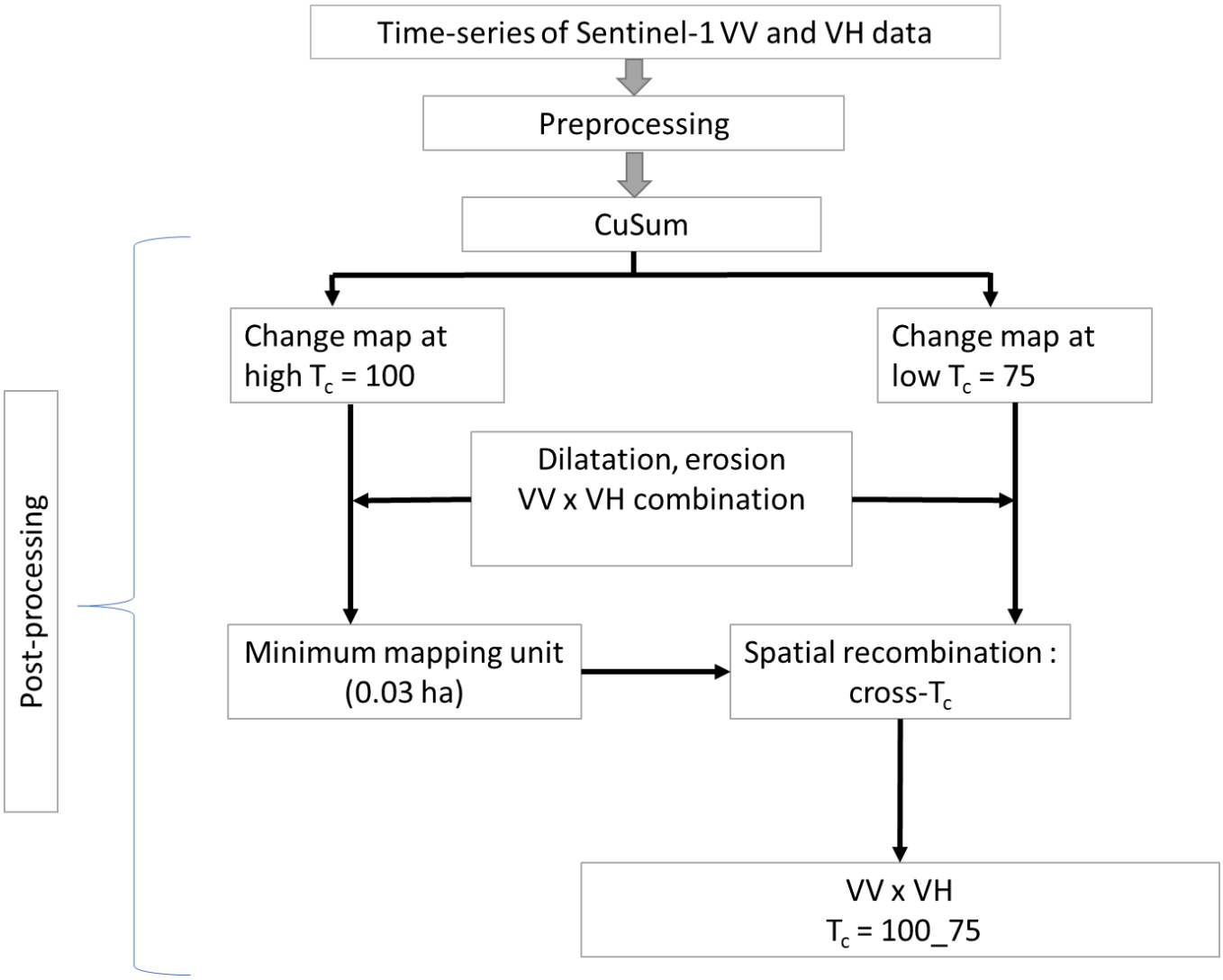

Figure V.2: Commune post-processing cascade for the CuSum and ReCuSum versions. VV x VH is the combination of the VV-based result map with the VH-based result map. T_c is the critical threshold, and the cross-T_c is the spatial recombination between a high T_c map and a low T_c map.

5.2.3.2. Recursive CuSum multi-detection

5.2.3.2.1. ReCuSum algorithm

The ReCuSum method consists in applying the CuSum single change detection adapted for the processing of Sentinel-1 images (Ygorra *et al*., 2021b) in a recursive manner to segment a time-series in several sub-periods until no more change is detected (Figure V.3). At each iteration, the CuSum algorithm is applied on a time-series of satellite images, along with a bootstrap analysis to obtain a single change detection image.

The first input for the ReCuSum method is composed by the same parameters as the CuSum cross-T_c. For each pixel, if a change is detected, then the time-series is divided into two periods from the detected date of change. The single change CuSum is then separately applied over the two newly formed time-series in a recursive manner. If a change is detected in any of these two new periods, the resulting time-series is further split and analysed between the new dates of change. This process is recursively repeated until the original time-series is split into independent time-series in which the CuSum does not detect changes anymore. This approach is independently applied to each pixel of the study area.

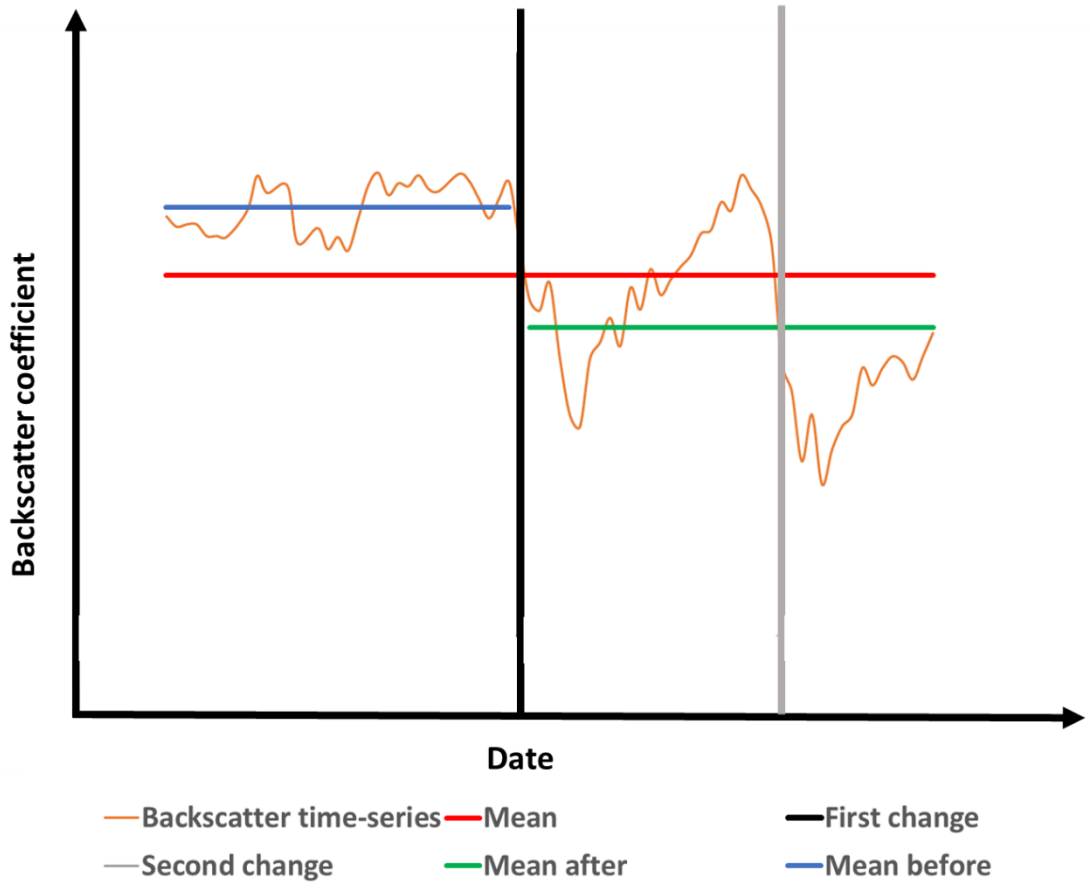

Figure V.3: Application of ReCuSum on a backscatter coefficient time-series. The vertical black line is the date of change found by the first iteration of the CuSum, the vertical grey line is the date of change found by the second iteration of the CuSum. The backscatter time-series is symbolized by an orange line, and its mean is symbolized in red (mean over the entire time-series), blue (mean before the first change) and green (mean after the first change).

5.2.3.2.2. Post-processing steps of the ReCuSum method

5.2.3.2.2.1. Threshold based on the number of changes: T_{nbc}

The application of the ReCuSum approach resulted in maps of the total number of changes which occur during the observation period. These maps of number of changes were obtained using multiple input parameters: different T_c (100, 95, 75) along with different sensor polarization combinations (VV, VH, VV x VH). Classical descriptive statistics (i.e., mean, standard, deviation and 25/75 quartiles) were used to describe the pixel populations of both non-forest vegetation and forest classes based on the

number of changes found in the ReCuSum result map (boxplots). The maps of the number of changes were also visually assessed for spatial consistency.

We compared the results obtained from the different input parameters (Tc, polarization) to determine which combination results in the best forest / non-forest vegetation separability based on the number of changes.

5.2.3.2.2.2. Removal of past changes: determination of radar-active non-forest vegetation areas

The application of the CuSum to a period before the monitoring period was performed. All changes found in this past period were considered as non-forest vegetation areas for the monitoring period and was excluded from our analysis. The application of this removal is referred to as 'rm_past' in the following. Different minimum mapping units were tested.

5.2.3.3. Validation

A reference map was estimated from visual interpretation of the Sentinel-2 and PlanetScope mosaic and was used to distinguish 3 main classes (Figure V.4): 1) non-forest vegetation at the beginning of the monitoring period, 2) disturbed forest during the monitoring period and 3) undisturbed forest. A pixel-based validation was performed using these 3 "reference" classes. A pixel from the CuSum outputs was considered as representing non-forest vegetation if this pixel (1) belongs to the non-forest vegetation in the reference map and (2) is labelled as 'change' by the algorithm. A pixel was considered as representing "disturbed" forest if (1) it belongs to disturbed forest in the reference map and (2) is labelled as 'change' by the algorithm. For the forest stratum, a pixel was considered "undisturbed forest"' if (1) it belongs to the forest stratum in the reference map and (2) is labelled as 'no change' by the algorithm, following the recommendation from (Olofsson et al., 2014).

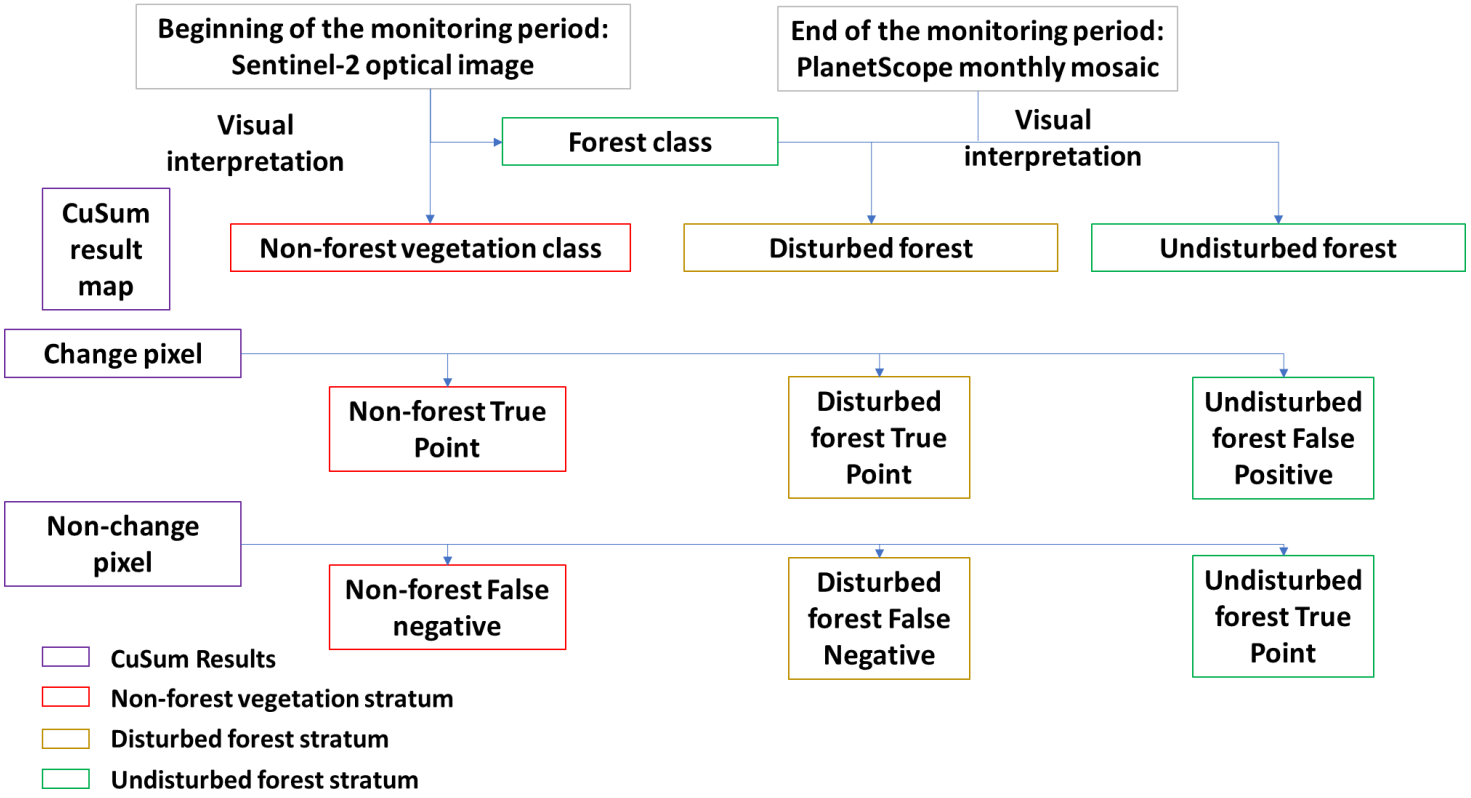

Figure V.4: Flowchart of the reference map production. Purple corresponds to the CuSum binary results, Red to the non-forest vegetation stratum, yellow-brown to the disturbed forest stratum, and green to the undisturbed forest stratum, all estimated from visual interpretation of the Sentinel-2 and PlanetScope mosaic.

5.2.4. Results

5.2.4.1. Backscatter time series

Times series of backscatter coefficients in the study area for two vegetation types (forest and non-forest) and for two cases 1) no change detected and 2) at least one change detected are presented in Figure V.5. Backscatter values over forest ranged from -8 to -4 dB in the VV polarization, and from -16 to -10 dB for the VH polarization. Backscatter values over non-forest vegetation ranged from -11 to -4 dB for the VV polarization and from -18 to -10 dB for the VH polarization. The time-series obtained over forest with no detected change and the ones obtained over the non-forest vegetation with no detected change are fairly similar, the signal being rather stable, centred at -6.5 dB for the VV polarization. For the VH polarization, the signal is centred on -13 dB for both forest and non-forest vegetation.

The detected change over forest in Figure V.5.a consists in a significant decrease in the VV signal (-5 to -10 dB in 08/2018), followed by a further decrease to -13 dB between 08/2018 and 12/2018, and by an increase to -9 dB. The detected change also results in a decrease in the VH signal, from -14 to -18 dB in 2 months, then a recovery to -16 dB.

Over the non-forest vegetation (Figure V.5.b and Figure V.5.d), the detected changes stem from a high variability of the signal. Compared to non-forest vegetation not showing a change, the signal is lower from 01/05/2018 to 05/09/2018, then higher for the rest of the study.

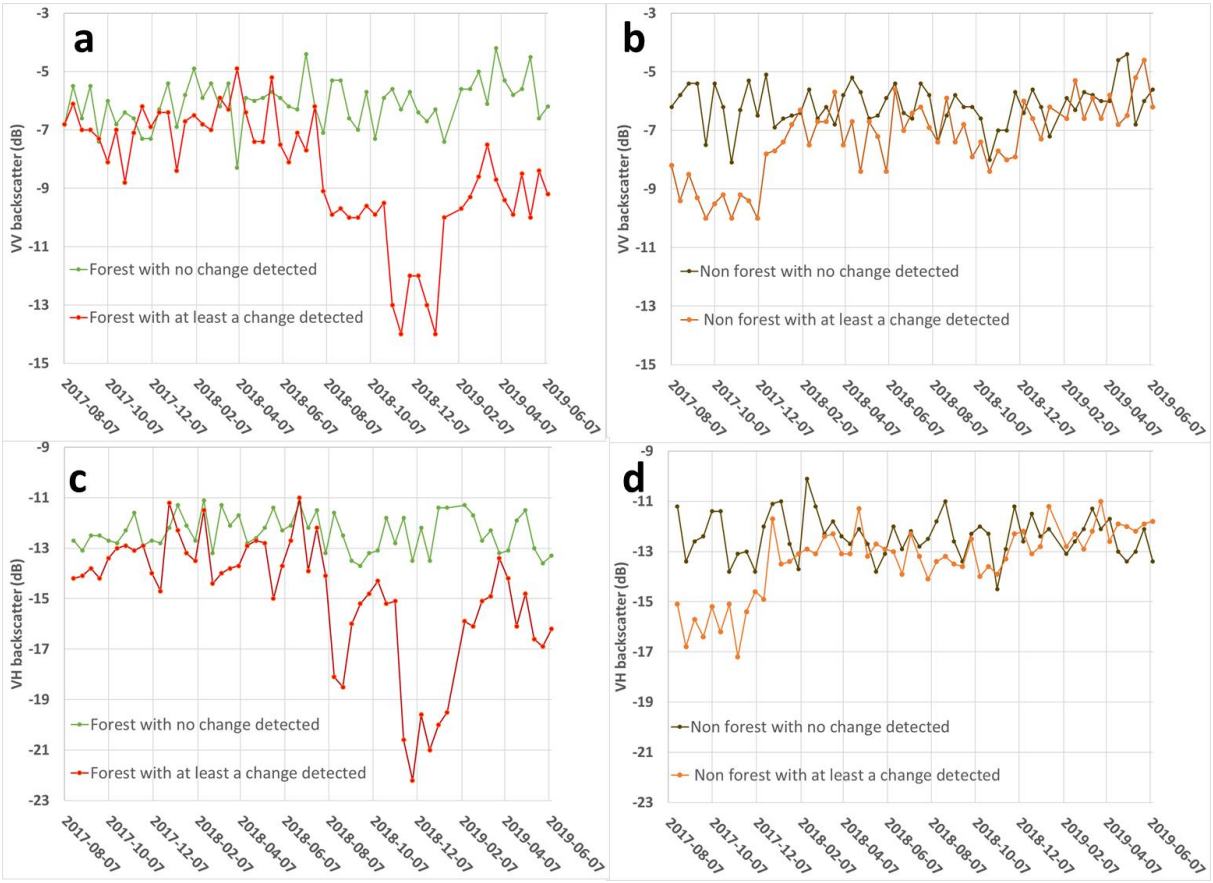

Figure V.5: Backscatter time series of (a) VV polarization in forest, (b) VV polarization in non-forest vegetation, (c) VH polarization in forest, (d) VH polarization in non-forest vegetation.

5.2.4.2. Relationship between the number of changes and the vegetation type

5.2.4.2.1. Number of changes as a function of polarization and T_c

The number of changes occurring over the Amazonian study area for both different polarizations and T_c is presented in Figure V.6. The number of changes decreases with increasing T_c values. This number is slightly higher for VV than for VH polarization and slightly lower for VH x VV combination. The VH 100, VH 95 and VV x VH 75 are the configurations presenting the highest difference between forest disturbance number of changes and non-forest vegetation number of changes. Overall, the number of changes is significantly higher (5 to 10 changes more) for the non-forest vegetation class than for the forest disturbance class for all polarizations used.

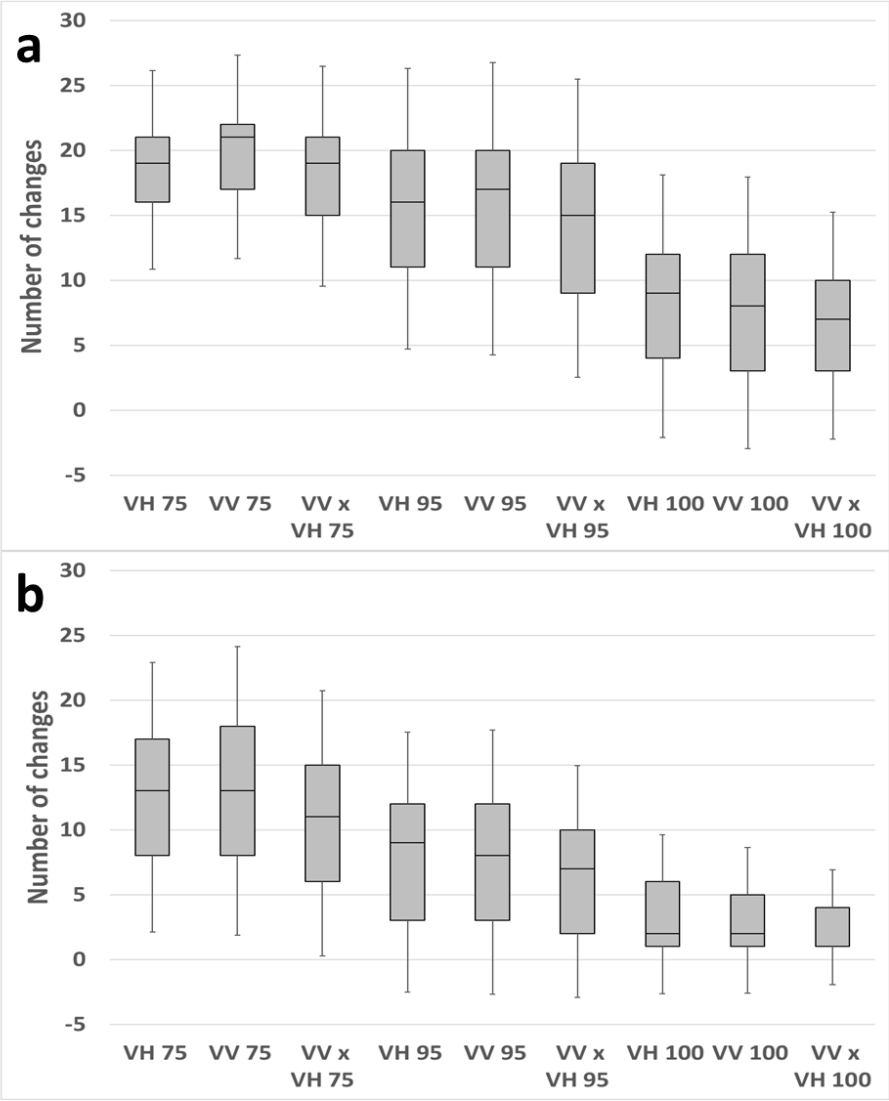

Figure V.6: Boxplot of (a) the number of changes of the pixels belonging to the non-forest vegetation class and (b) the number of changes belonging to the forest cover change class in the Amazon.

5.2.4.2.2. Relationship with the vegetation type

The number of changes per pixel widely varies over the study areas. Estimates of the number of changes over forest and non-forest areas were achieved using the CuSum over the forest/non-forest vegetation classes obtained in the reference map. In the study area, the relative percentage of area corresponding to non-forest vegetation increases with the number of changes per pixel in the VV and VH polarizations, 92% of the pixels presenting a number of changes ≥ 18 for VH 100 belonged to the non-forest vegetation class against 81% for VV 100. 86% of the pixels presenting a number of changes ≥ 19

changes for VH 95 belonged to the non-forest vegetation against 76% for VV 95 (Figure V.7.a and Figure V.7b). The number of changes obtained at VV x VH is lower and the distribution is very different from the former results. Indeed, the percentage of area classified as non-forest is lower than 50% at all boundaries for all T_c (Figure V.7.c).

Figure V.7.d presents the distribution of the number of changes at VH polarization for different T_c. This polarization was chosen as it exhibits the best determination of the non-forest areas (Figure V.7.b). Most pixels belong to the 1 – 3 changes range. A secondary maximum is observed for 6-9 and 18-20 changes for T_c = 100 and T_c = 95, respectively. This secondary maximum is used as the optimum number for the automation in the change detection approach. This phenomenon did not appear at T_c = 75, which is why the threshold selection was based on T_c = {100,95}.

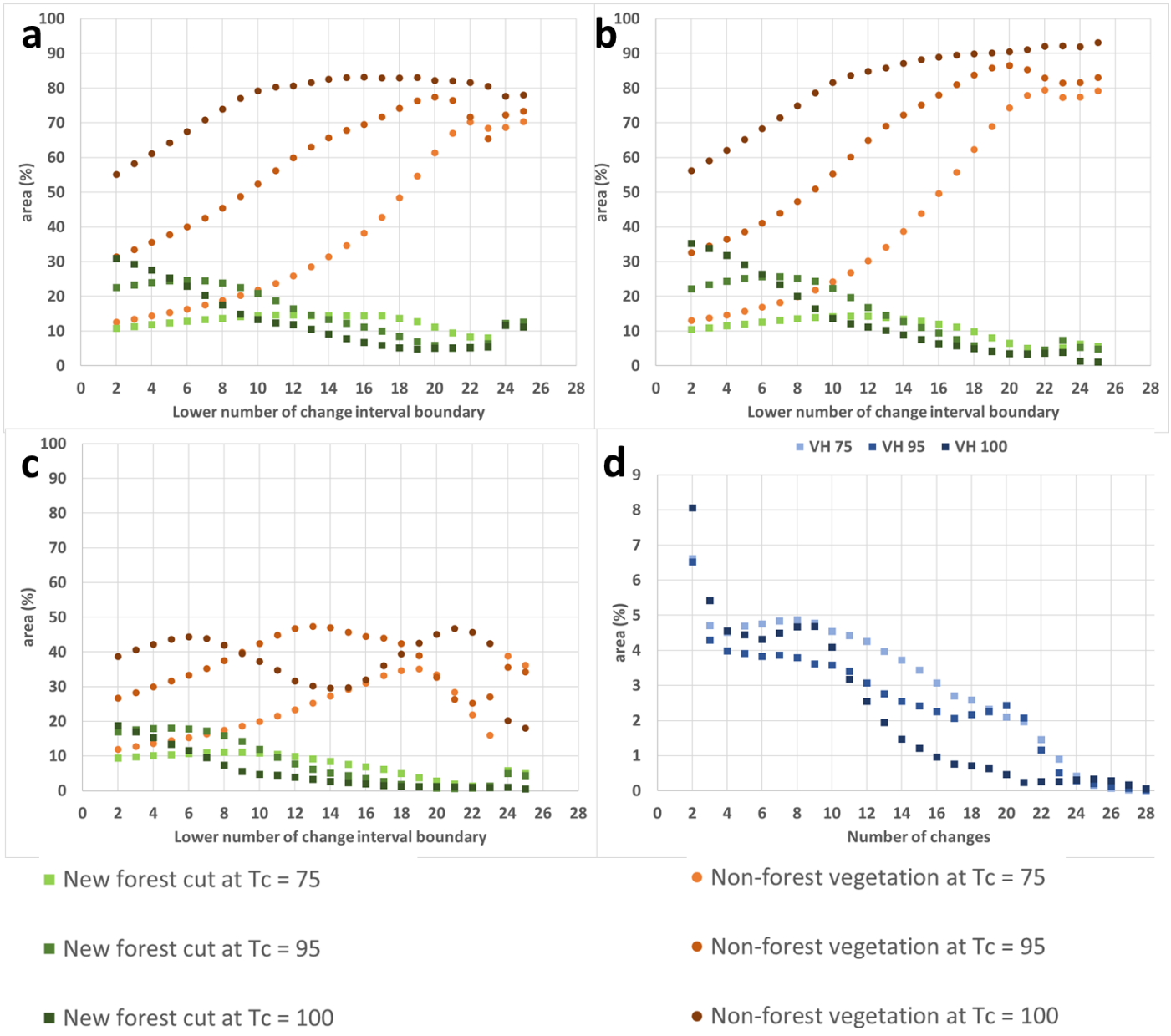

Figure V.7: Area (%) as a function of the minimum number of changes of the non-forest vegetation (brown to orange) and vegetation forest disturbance (green) areas at VV polarization (a), (b) the percentage area associated to the VH lower number of change boundary, (c) to the VV x VH lower number of change boundary in the Amazon study area and (d) the percentage of the total area detected as change for each number of changes.

5.2.4.3. Spatial visualization of the changes

In Figure V.8, results are presented with an increasing complexity in the processing, from the lower number of post-processing steps (raw cross-T_c) to the highest-end product (cross-T_c with rm_past and T_{nbc} application). The simple cross-T_c product detected both forest disturbances and non-forest vegetation classes accurately (Figure V.8.a). The number of changes is higher in the non-forest vegetation areas than in the forest affected by disturbances areas. There are very few changes detected outside these areas. In Figure V.8.b, the application of T_{nbc} reduced the number of pixels within all non-forest vegetation patches, but some pixels from the centres of forest disturbance areas were also removed. The pixels located in the corners of non-forest vegetation areas did not exhibit changes according to our method. In Figure V.8.c, the rm_past application successfully removed entire patches of non-forest vegetation. Few pixels located in the connection zone between forest disturbance and non-forest vegetation areas were also removed. Some patches of non-forest vegetation were not removed using this method.

In Figure V.8.d, the combination of the two additional post-processing steps allowed for those remaining non-forest vegetation areas to be removed. Visually, when comparing Figure V.8.b and Figure V.8.c to Figure V.8.d, the pixels removed by both methods are almost the same, meaning the two methods fulfil the same role with different characteristics. This will be later confirmed in subsection 5.2.4.4 using statistical information.

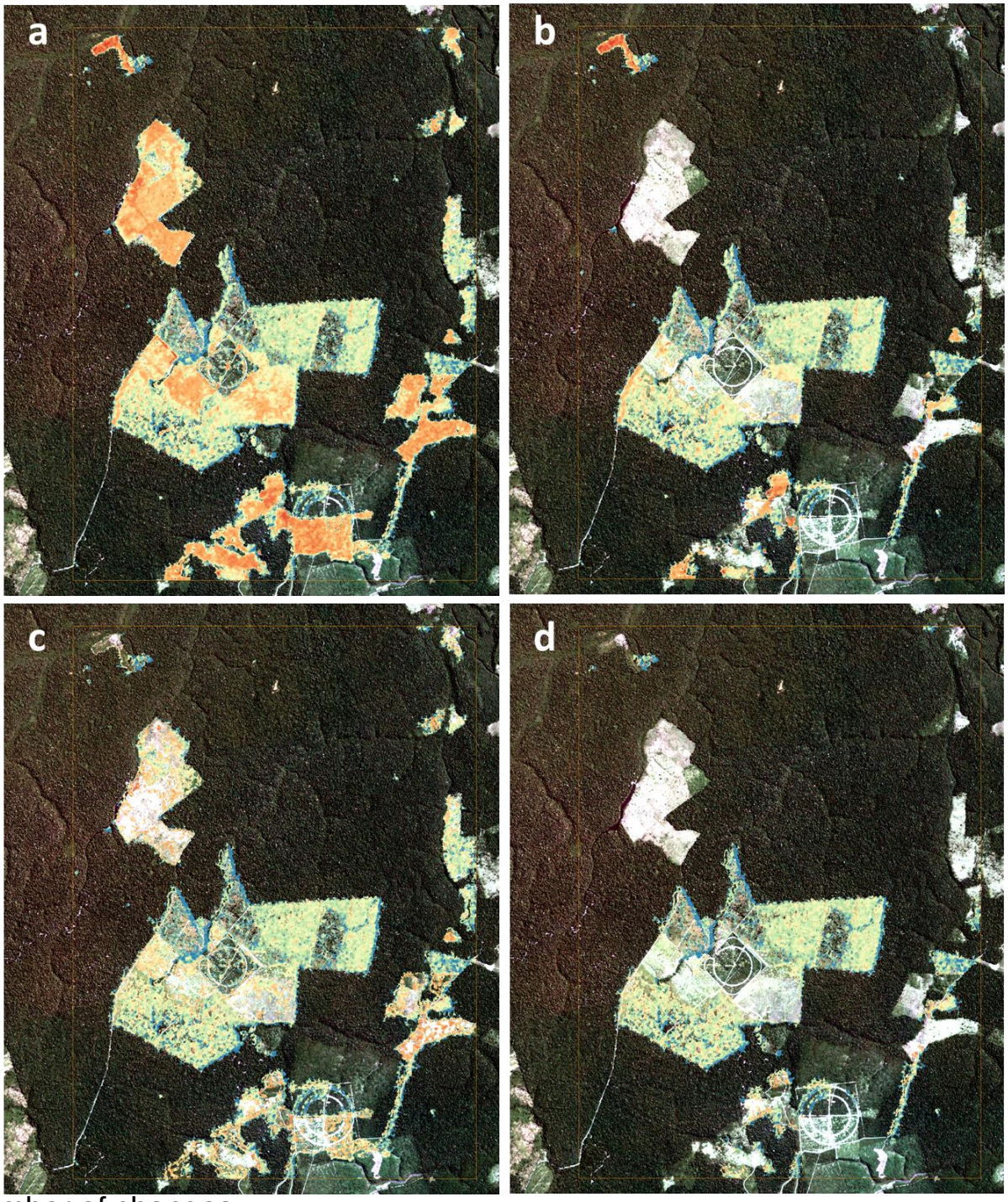

Figure V.8: Number of change result map of VV x VH 100_75 (a) algorithm, (b) algorithm after applying rm_hist, (c) algorithm after applying T_{nbc}, (d) algorithm after applying both rm_past and T_{nbc}.

5.2.4.4. Statistical results

In the study area, there are 31 disturbances confirmed by the reference map to be detected (*Table V.1*). An event is considered correctly detected if a CuSum result polygon intersects or contains the reference polygon. The rm_past T_{nbc} CuSum systematically detected more than 80% of these disturbances, on any polarization or combination used.

Parameters	Number of disturbances correctly detected	Percentage of disturbances correctly detected (%)
rm_past VV Tnbc 100_75	30	97
rm_past VH Tnbc 100_75	30	97
rm_past VV x VH Tnbc 100_75	25	81

Table V.1 : Statistics on the number of disturbances correctly detected using the VV, VH or VV x VH 100_75 rm_past – T_{nbc} parameters.

Table V.2 shows the area estimates resulting from the forest disturbance detected by the different versions of the CuSum post-processings developed in this study (with the application of rm_past, and / or T_{nbc}) compared to the reference map. The relative error in the estimation is computed from the False Positive errors (FP). The CuSum cross-T_c 100_75 applied on VV x VH data resulted in overestimation of the forest disturbance area, + 115% compared to the reference area. This high value results mostly of the FP area, as it composes 61.5% of the estimations. The application of T_{nbc} lowers the estimated area and the relative error, showing a value +50.8% higher than the reference area. This overestimation is half composed (50.5%) by the FP errors.

The application of rm_past reduces the estimation error to +10.4% of difference with the reference map area. The estimated area is 29.5% composed by the FP errors, compensating the False Negative (FN) errors. The VV x VH 100_75 rm_past is the algorithm providing the closest results to the reference forest disturbance derived from the reference map in terms of surface estimates of the deforestation. The application of both rm_past and T_{nbc} lowers the estimated area and the FP errors to an underestimation of -16.02% compared to the reference. The FP errors compose 18.19% of these estimations.

Algorithm	Estimated disturbed forest area (ha)	False Positive (ha)	False Negative (ha)	Relative error	Comparison with reference
Reference map	1020.9	0	0	0%	0%
VV x VH 100_75	2196.4	1351.4	175.9	61.5%	115.1%
VV x VH 100_75 rm_past	1127.2	332.3	226.0	29.5%	10.4%
VV x VH 100_75 T_{nbc}	1539.2	777.9	259.6	50.5%	50.8%
VV x VH 100_75 rm_past T_{nbc}	857.3	155.9	319.5	18.2%	-16%

Table V.2: Estimation of the area detected as forest disturbance. rm_past means with removal of past changes, T_{nbc} means with application of T_{nbc}. Red is considered as a weak result, orange as an acceptable result and green as a good result.

Figure V.9 shows the number of pixels correctly labelled as change (TP for True Positive), Falsely labelled as change (FP), Falsely labelled as not a change (FN) and correctly labelled as not a change (TN for True Negative). The TP numbers are high with the VV x VH cross-T_c algorithm (845.0 ha, Figure V.9.a), but decrease with the additional post-processing steps. The applying rm_past decreases the TP to 794.9 ha (Figure V.9.b), and the application of T_{nbc} decreases TP to 761.3 ha (Figure V.9.c). The application of both steps decreases TP to 701.4 ha, reducing the initial TP by 17.1% (Figure V.9.d). The number of FP is very high for VV x VH cross-T_c (2859.1 ha), but decreases to 1730.5 ha (39.5% decrease) by applying rm_past. The application of T_{nbc} decreases FP to 2278.5 ha (20.3% decrease). The application of both rm_past and T_{nbc} decreases FP to 1002.0 ha (65.0% decrease).

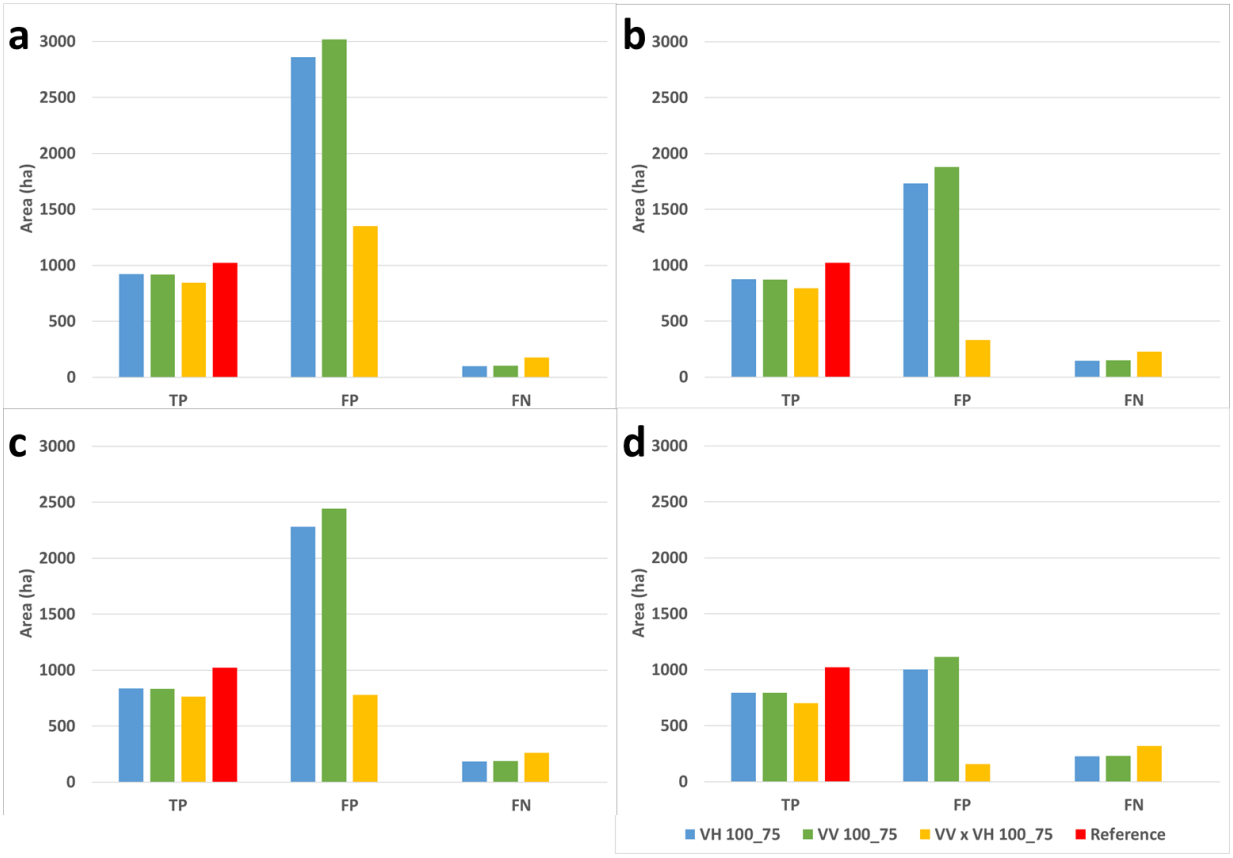

Figure V.9: Histograms of the TP, FP, FN area of (a) VV x VH 100_75, (b) VV x VH 100_75 with applied rm_past, (c) VV x VH 100_75 after applying Tnbc, (d) VV x VH 100_75 after applying both rm_past and Tnbc.

The Figure V.10 shows the statistics for the non-forest vegetation. Statistical results were obtained over non-forest vegetation: A precision of 0.48, an accuracy of 0.87, a recall of 0.90, a kappa coefficient of 0.56 and a F1-score of 0.63 for the VV x VH 100_75 are reached over non-forest vegetation (Figure V.10.a).

The application of rm_past (Figure V.10.b) decreases most statistics on non-forest vegetation. The precision decreases to 0.15 (-33%), the accuracy to 0.79 (-8%), the recall to 0.14 (-76%), the kappa coefficient to 0.03 (-53%), and the F1-score to 0.14 (-49%).

The application of T_{nbc} (Figure V.10.c) lowers the statistics up to 46% for the non-forest vegetation. The precision decreases to 0.34 (-14%), the accuracy to 0.82 (-5%), the recall to 0.44 (-46%), the kappa coefficient decreases to 0.29 (-27%) and the F1-score decreases to 0.38 (-25%).

The combined application of both rm_past and T_{nbc} (Figure V.10.d) lowers the statistics even more, with the precision decreasing to 0.04 (-44%), the accuracy decreased to 0.79 (-8%), the recall is lowered to 0.03 (-87%), the kappa coefficient to 0 (-56%) and the F1-score to 0.03 (-60%).

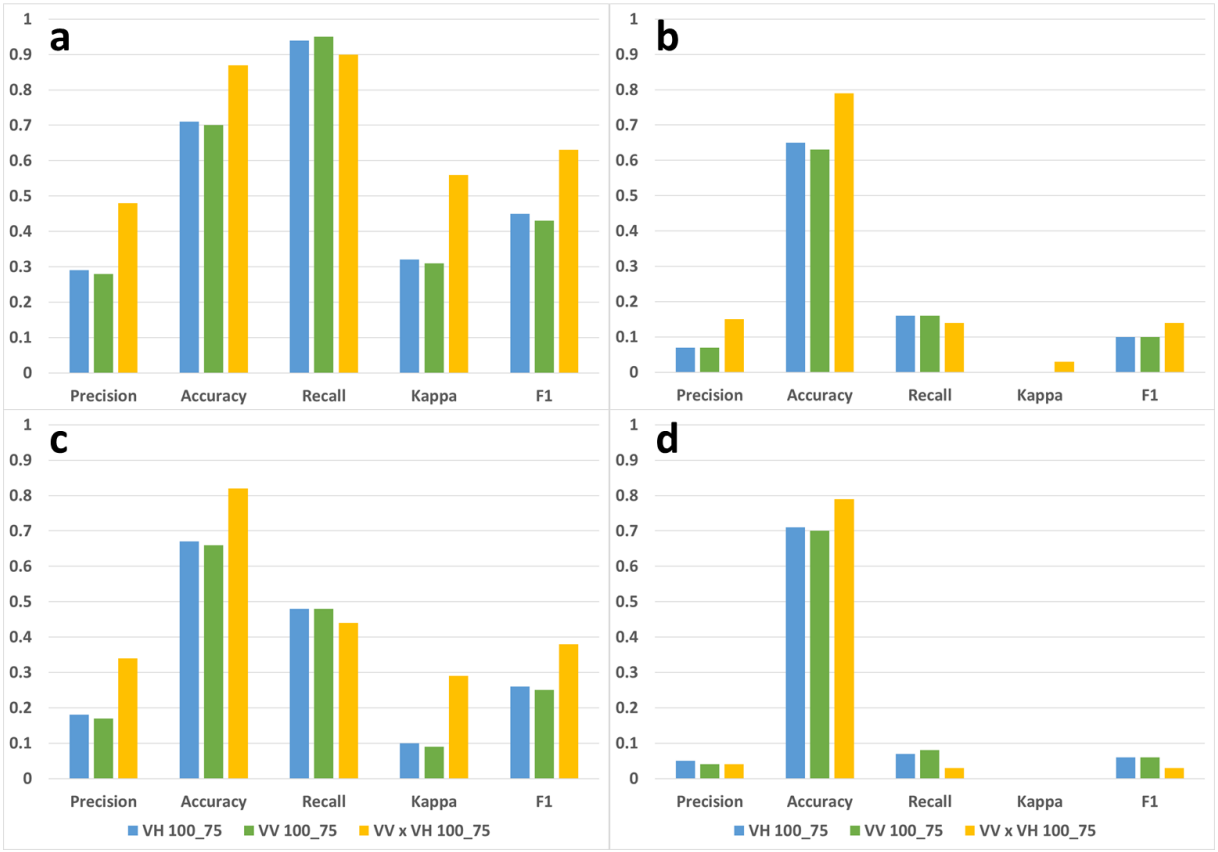

Figure V.10: Precision, Accuracy, Recall, Kappa coefficient, F1-score of the monitoring of non-forest vegetation using (a) cross-T_c products, (b) cross-T_c products after applying rm_past, (c) cross-T_c products after applying T_{nbc} [8,19], (d) cross-T_c products after applying T_{nbc} [8,19] and rm_past.

For the forest disturbance (Figure V.11), the statistics are lower than those obtained for the non-forest vegetation. The precision is lower (0.38). The accuracy is high (0.84), as the recall (0.82). The kappa coefficient is also fairly lower (0.44), as the F1-score (0.52).

After the application of rm_past, the precision increases to 0.70 (+32%), the accuracy to 0.94 (+10%). The recall decreases to 0.77 (-5%), but the Kappa coefficient and the F1-score increase respectively to 0.7 and 0.74 (+26% and +22%).

The application of T_{nbc} shows similar effects. The precision increases to 0.49, the accuracy to 0.89. The recall decreases to 0.74. The Kappa coefficient increases to 0.53 and the F1-score to 0.59.

The application of both post-processing steps increases the precision to 0.81 (+43%), the accuracy to 0.95 (+11%). The recall decreases to 0.68 (-14%). The kappa coefficient increases to 0.72 (+28%) and the F1-score to 0.74 (+22%).

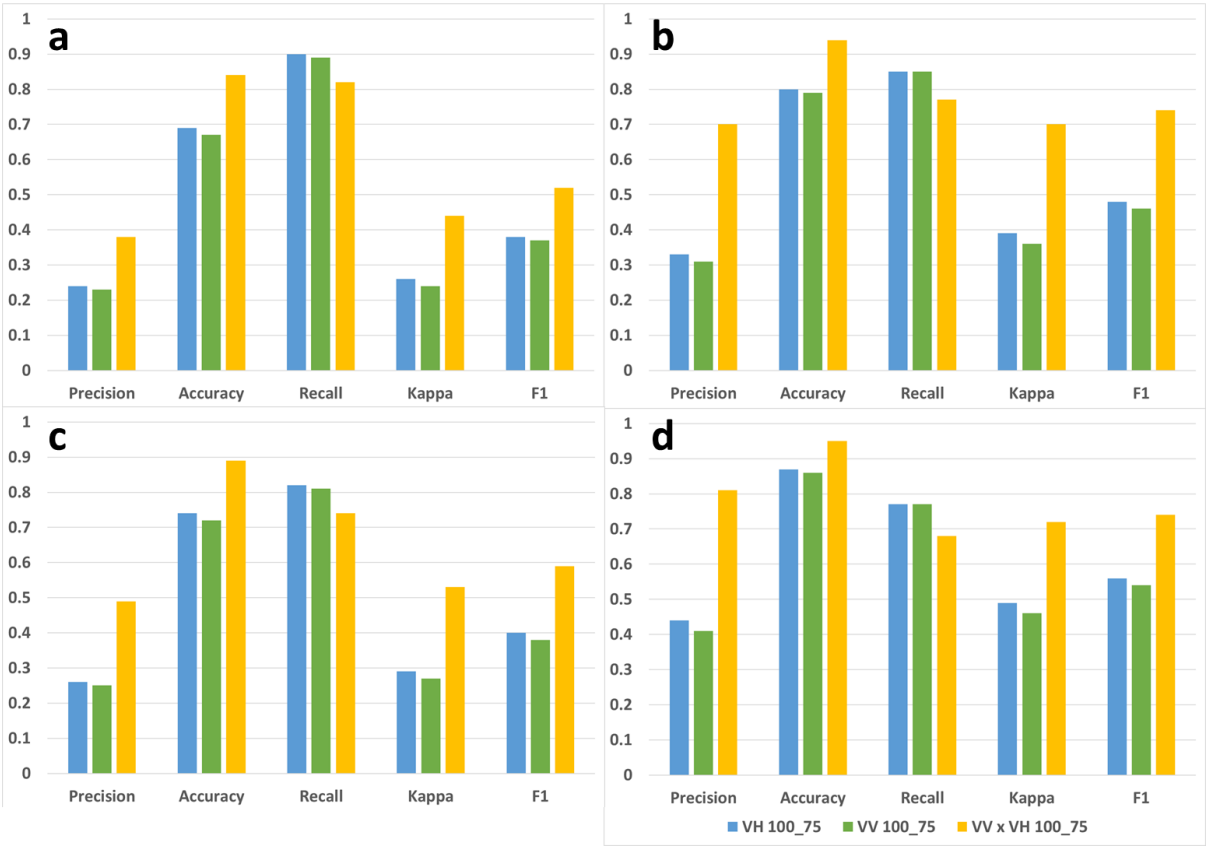

Figure V.11: Precision, Accuracy, Recall, Kappa coefficient, F1-score of the monitoring of forest disturbance using (a) cross-T_c products, (b) cross-T_c products after the rm_past, (c) cross-T_c products after applying T_{nbc} [8,19], (d) cross-T_c products after applying T_{nbc} [8,19] and rm_past.

5.2.4.5. Proposed new post-processing cascade

The upgrades to the CuSum cross-T_c algorithm consist in modifying the post-processing cascade with multiple steps (Figure V.12).

The first added step consists in the application of the single-change cross-T_c CuSum algorithm in a period past from the monitoring period to identify non-forest vegetation areas and past changes. The parameters for this algorithm are VV intersection VH, cross-T_c 100_75, MMU = 0.1 ha.

Then, the ReCuSum is started on the monitored period as simple T_c for VH, at T_c = 100 and T_c = 95. The maps of number of changes and the pixel population dynamics are analysed to produce a threshold T_{nbc}. Pixels showing a number of changes higher than this threshold in VH 100 or VH 95 are then considered as non-forest vegetation changes.

Finally, the ReCuSum is applied to the monitored period with the following parameters: VV intersection VH, cross-T_c 100_75, MMU = 0.03 ha, producing the main result map. The pixels considered as changes happening over non-forest vegetation from T_{nbc} are then removed from this image, along with past period changes / non-forest vegetation changes.

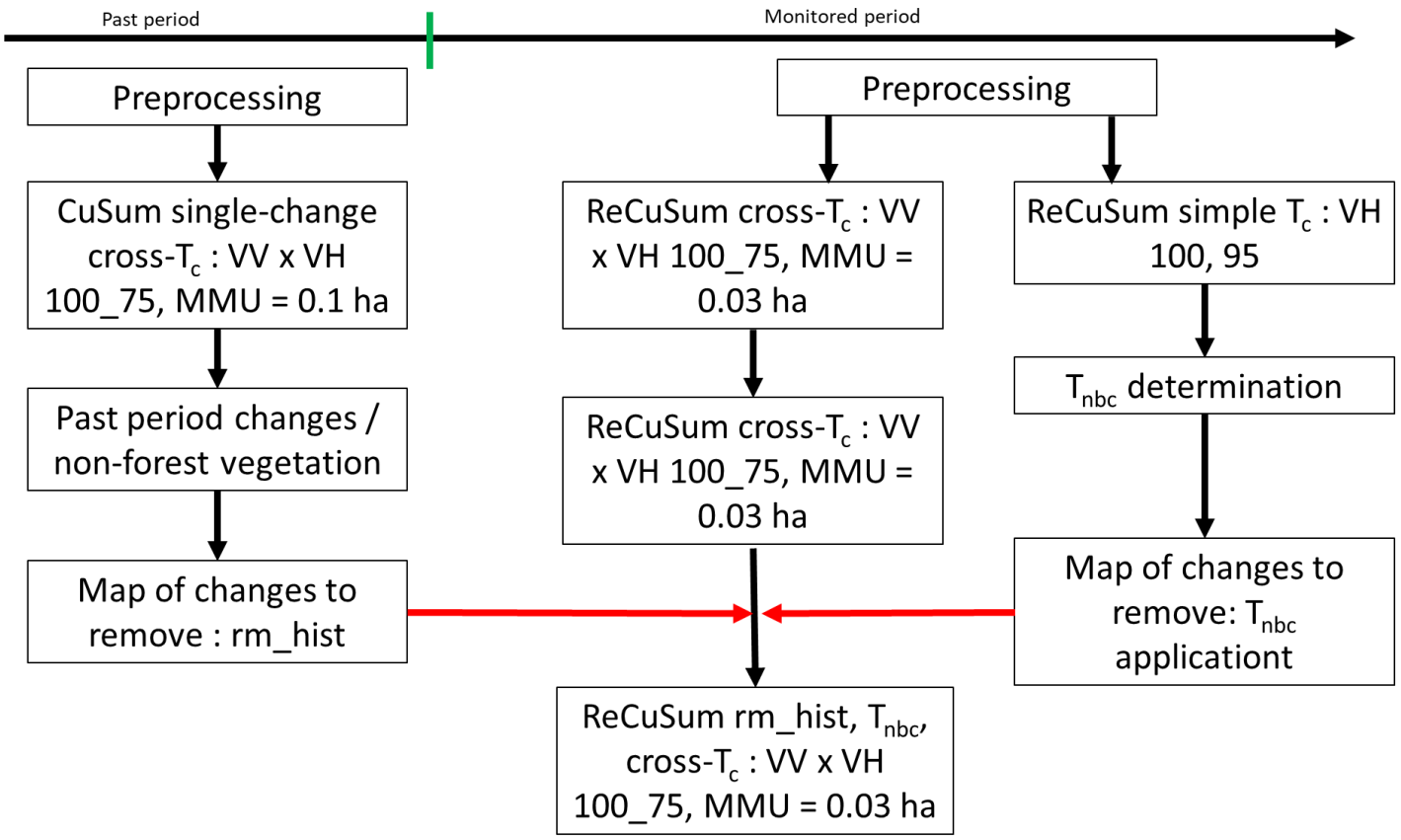

Figure V.12: New work process proposed for ReCuSum: computation of past changes and Tnbc.

5.2.5. Discussion

The ReCuSum results are similar to the CuSum simple detection results in terms of pure statistics and spatial assessments. The algorithm has the ability to detect the changes occurring in the tropical forest cover (Recall: 0.82 and F1-score: 0.52 for the VV x VH combination 100_75), but also to monitor the non-forest vegetation (Recall: 0.9 and F1-score: 0.63 for the VV x VH combination 100_75).

The number of changes obtained using the ReCuSum approach allows definition of an additional post-processing step, T_{nbc}, as a threshold based on the VH polarization at T_c = {100, 95} to mostly discriminate the forest disturbance from changes happening in non-forest vegetation areas. The application of this threshold decreases significantly the non-forest vegetation statistics, implying a decrease in the ability to detect changes in non-forest vegetation areas while reducing the false positives in the forest disturbance detection.

Visually, most pixels removed by the application of T_{nbc} belong to the non-forest vegetation class, but pixels in the patches borders still remain detected as change due to the large window used in the despeckling step (7x7, bilateral filter). Only the centres of the patches were successfully removed from the map. The forest disturbance areas were less impacted by T_{nbc}, but some patches had their centres removed at a smaller scale.

The use of T_{nbc} allows the discrimination of changes occurring in non-forest vegetation from changes happening in forested areas, as shown by the sharp decrease in the non-forest vegetation statistics after application. The thresholds used are based on the VH at T_c = {100,95}. The number of changes is higher in the centre of non-forest vegetation patches but also in the centre of areas affected by forest disturbance. The frequency distribution of the number of changes shows a rebound at VH polarization for T_c = 100 around 8 changes and at VH polarization for T_c = 95 around 18 changes. The threshold can be automatically determined using these distributions, but a user's visual assessment is expected to result to a more accurate threshold estimate. The use of this threshold decreases the relative error in the forest disturbance estimation from 67% to 50%. The relative error remains high due to the removal of pixels within the forest disturbances area.

The ability to monitor the non-forest vegetation areas along with the forest disturbance was used into another additional post-processing step. This ability allowed performing a pseudo-classification of the zone by applying the CuSum on a period prior to the monitoring period. The pixels found as 'change' during this period were removed from the monitoring period result maps. This additional step proved to

be efficient and should be used over the Amazon rainforest, as shown by the fair increase in precision, accuracy, Kappa coefficient and F1-score (respectively 32%, 10%, 26% and 22%). This step removed most of the changes located in the non-forest vegetation area (76% decrease in the area mapped as 'change happening on non-forest vegetation'). This result suggests that the CuSum results based on Sentinel-1 time-series are affected by the LULC and the stability of the signal. The application of rm_past decreased the relative error in the forest disturbance estimations from 67% to 29%. The estimations made using the CuSum different parameters are nearing the reference forest disturbance area estimation, being 10% higher than the reference forest disturbance area.

Another limit highlighted in this study is related to the CuSum approach in itself, as it needs at least a period of stability for the 'mean' to be accurate. In forest disturbance, a general short backscatter decrease is known to occur, even if hindered by changes either in soil moisture linked to rainfall or in roughness. The dates of change detected are delayed but the number of changes is accurate as the signal is mostly stable after a short period of regrowth. In a non-forest vegetation area showing multiple dates of change, the backscatter signal is not stable. It is often composed of a steep decrease followed by a long increase in backscatter coefficient due to regrowth. The application of the cumulative sum is then impacted because of the high disparity of the signal and its instable character. This phenomenon will create many dates of change as the values are continuously decreasing then continuously increasing, showing a time continuity. The dates of change detected will be at the beginning of the monitored period or at its end, and will recursively increase by one date. In such cases, the dates of detected change in non-forest vegetation areas are incorrect, but the number of changes resulting from this behaviour allows the pixels to be labelled as 'non-forest vegetation'. The application of a filter based on the standard deviation before applying the CuSum may remove the pixels showing these behaviours.

The application of both supplementary steps does not result in significant increases in the F1-score and kappa coefficient compared to the application of rm_past. This result is due to the effect of compensation: the decrease in the recall is compensated by the increase in precision (the decrease in false positives is compensated by an increase in false negatives). Pixel removal in both non-forest vegetation and forest disturbance areas leads to a 16% underestimation of the forest disturbance compared to the reference map. The map resulting from the application of both post-processing steps on VV x VH 100_75 is the most precise but shows the most omissions and an increased difference to the validation dataset compared to the map resulting from the application of rm_past on VV x VH 100_75 dataset.

5.2.6. Conclusion

The ReCuSum method, based on multiple iterations of the CuSum single-detection approach, demonstrated a strong potential for monitoring forest disturbance in tropical areas compared to a single iteration of the CuSum (single-detection) method. In these areas, a threshold based on the number of changes (T_{nbc}) can be set either automatically or semi-empirically (better discrimination) to discriminate between non-forest vegetation from forest disturbance using Sentinel-1 images, performing a pseudo-classification (changes occurring in non-forest vegetation against changes occurring in forested areas). In this study area, better results were obtained for T_{nbc} selection using VH polarization at T_c = {100,95}. Nevertheless, it is strongly recommended to visually assess the result map to help select the best T_{nbc} threshold minimizing the forest cover change detection loss.

This method can be used as an alternative when no forest benchmarks are available. As the CuSum (single change and multi change) ability to detect non-forest vegetation has been demonstrated in this study (precision of 48%, an accuracy of 0.87, a recall of 90%, a kappa coefficient of 0.56 and a F1-score of 0.63 have been obtained for the VV x VH combination at T_c = 100_75), the CuSum can be used to detect non-forest vegetation subject to disturbances and remove it in an area and past period before the wanted monitoring period, thus acting as a forest/non-forest benchmark. The active non-forest vegetation areas can be later classified to undisturbed non-forest vegetation in monitoring period, limiting the effectiveness as forest/non-forest benchmark. In forest cover change monitoring, combining the application of rm_past and T_{nbc} provides the best results with the VV x VH cross-T_c 100_75 combination (precision of 81%, an accuracy of 0.95, a recall of 68%, a kappa coefficient of 0.72 and a F1-score of 0.74 have been obtained for the VV x VH combination at T_c = 100_75). The application of rm_past in the VV x VH cross-T_c 100_75 dataset ensures the best estimations of forest cover change areas (overestimation of 10% compared to the reference forest cover change area).

5.2.7. References

Arikawa, Y. et al. (2014) 'ALOS-2 launch and early orbit operation result', in 2014 IEEE geoscience and remote sensing symposium. IEEE, pp. 3406–3409.

Ballère, M. et al. (2021) 'SAR data for tropical forest disturbance alerts in French Guiana: Benefit over optical imagery', Remote Sensing of Environment, 252. Available at: https://doi.org/10.1016/j.rse.2020.112159.

Bouvet, A. et al. (2018) 'Use of the SAR shadowing effect for deforestation detection with Sentinel-1 time series', Remote Sensing, 10(8), pp. 1–19. Available at: https://doi.org/10.3390/rs10081250.

Buchhorn, M. et al. (2020) 'Copernicus Global Land Service: Land Cover 100m: Collection 3: epoch 2015: Globe (Version V3.0.1)', Zenodo, pp. 1–14.

Contreras-Hermosilla, A. (2000) The underlying causes of forest decline. CIFOR Jakarta, Indonesia.

Creese, A., Washington, R. and Jones, R. (2019) 'Climate change in the Congo Basin: processes related to wetting in the December–February dry season', Climate Dynamics, 53(5–6), pp. 3583–3602. Available at: https://doi.org/10.1007/s00382-019-04728-x.

Diniz, C.G. et al. (2015) 'DETER-B: The New Amazon Near Real-Time Deforestation Detection System', IEEE Journal of Selected Topics in Applied Earth Observations and Remote Sensing, 8(7), pp. 3619–3628. Available at: https://doi.org/10.1109/JSTARS.2015.2437075.

Doblas, J. et al. (2020) 'Optimizing near real-time detection of deforestation on tropical rainforests using sentinel-1 data', Remote Sensing, 12(23), pp. 1–31. Available at: https://doi.org/10.3390/rs12233922.

Fan, L. et al. (2019) 'Satellite-observed pantropical carbon dynamics', Nature Plants, 5(9), pp. 944–951. Available at: https://doi.org/10.1038/s41477-019-0478-9.

Hamunyela, E. et al. (2020) 'Implementation of BFASTmonitor Algorithm on Google Earth Engine to support large-area and sub-annual change monitoring using earth observation data', Remote Sensing, 12(18). Available at: https://doi.org/10.3390/RS12182953.

Hamunyela, E., Herold, M. and Verbesselt, J. (2017) Space-time monitoring of tropical forest changes using observations from multiple satellites. Ph.D. Thesis, Wageningen University & Research, Laboratory of Geo-information Science and Remote Sensing, Wageningen, The Netherlands. Available at:

http://search.ebscohost.com/login.aspx?direct=true&db=edsbas&AN=edsbas.8D6F26D9&site=eds-live&scope=site.

Hansen, M.C. et al. (2013) 'High-resolution global maps of 21st-century forest cover change', Science, 342(6160), pp. 850–853. Available at: https://doi.org/10.1126/science.1244693.

Hansen, M.C. et al. (2016) 'Humid tropical forest disturbance alerts using Landsat data', Environmental Research Letters, 11(3). Available at: https://doi.org/10.1088/1748-9326/11/3/034008.

Hoekman, D. et al. (2020) 'Wide-area near-real-time monitoring of tropical forest degradation and deforestation using sentinel-1', Remote Sensing, 12(19), pp. 1–32. Available at: https://doi.org/10.3390/rs12193263.

Joshi, N. et al. (2015) 'Mapping dynamics of deforestation and forest degradation in tropical forests using radar satellite data', Environmental Research Letters, 10(3). Available at: https://doi.org/10.1088/1748-9326/10/3/034014.

Kleinschroth, F. et al. (2019) 'Road expansion and persistence in forests of the Congo Basin', Nature Sustainability, 2(7), pp. 628–634. Available at: https://doi.org/10.1038/s41893-019-0310-6.

Lescuyer, G. et al. (2011) The domestic market for smallscale chainsaw milling in Gabon: Present situation, opportunities and challenges. CIFOR.

Levy, R.C. et al. (2013) 'The Collection 6 MODIS aerosol products over land and ocean', Atmospheric Measurement Techniques, 6(11), pp. 2989–3034. Available at: https://doi.org/10.5194/amt-6-2989-2013.

Manogaran, G. and Lopez, D. (2018) 'Spatial cumulative sum algorithm with big data analytics for climate change detection', Computers and Electrical Engineering, 65, pp. 207–221. Available at: https://doi.org/10.1016/j.compeleceng.2017.04.006.

Martone, M. et al. (2018) 'The global forest/non-forest map from TanDEM-X interferometric SAR data', Remote Sensing of Environment, 205(August 2017), pp. 352–373. Available at: https://doi.org/10.1016/j.rse.2017.12.002.

Mistry, J. et al. (2021) 'Covid-19 impacts on Indigenous food sovereignty, livelihoods and biodiversity, Guyana', Report published by … [Preprint].

Nicolau, A.P. et al. (2021) 'Assessing SAR C-band data to effectively distinguish modified land uses in a heavily disturbed Amazon forest', International Journal of Applied Earth Observation and Geoinformation, 94(August 2020), p. 102214. Available at: https://doi.org/10.1016/j.jag.2020.102214.

Olofsson, P. et al. (2014) 'Good practices for estimating area and assessing accuracy of land change', Remote Sensing of Environment, 148, pp. 42–57. Available at: https://doi.org/10.1016/j.rse.2014.02.015.

Qin, Y. et al. (2021) 'Carbon loss from forest degradation exceeds that from deforestation in the Brazilian Amazon', Nature Climate Change, 11(5), pp. 442–448. Available at: https://doi.org/10.1038/s41558-021-01026-5.

Reiche, J. et al. (2018) 'Improving near-real time deforestation monitoring in tropical dry forests by combining dense Sentinel-1 time series with Landsat and ALOS-2 PALSAR-2', Remote Sensing of Environment, 204, pp. 147–161. Available at: https://doi.org/10.1016/j.rse.2017.10.034.

Reiche, J. et al. (2021) 'Forest disturbance alerts for the Congo Basin using Sentinel-1', Environmental Research Letters, 16(2), p. 024005. Available at: https://doi.org/10.1088/1748-9326/abd0a8.

Roy, D.P. et al. (2021) 'A global analysis of the temporal availability of PlanetScope high spatial resolution multi-spectral imagery', Remote Sensing of Environment, 264(June), p. 112586. Available at: https://doi.org/10.1016/j.rse.2021.112586.

Ruggiero, P.G.C. et al. (2019) 'Payment for ecosystem services programs in the Brazilian Atlantic Forest: Effective but not enough', Land Use Policy, 82, pp. 283–291. Available at: https://doi.org/10.1016/j.landusepol.2018.11.054.

Ruiz-Ramos, J. et al. (2020) 'Continuous forest monitoring using cumulative sums of sentinel-1 timeseries', Remote Sensing, 12(18). Available at: https://doi.org/10.3390/RS12183061.

Torres, R. et al. (2012) 'GMES Sentinel-1 mission', Remote Sensing of Environment, 120, pp. 9–24. Available at: https://doi.org/10.1016/j.rse.2011.05.028.

Turubanova, S. et al. (2018) 'Ongoing primary forest loss in Brazil, Democratic Republic of the Congo, and Indonesia', Environmental Research Letters, 13(7), pp. 2000–2010. Available at: https://doi.org/10.1088/1748-9326/aacd1c.

Umunay, P.M. et al. (2019) 'Selective logging emissions and potential emission reductions from reduced-impact logging in the Congo Basin', Forest Ecology and Management, 437, pp. 360–371.

Vargas, C., Montalban, J. and Leon, A.A. (2019) 'Early warning tropical forest loss alerts in peru using landsat', Environmental Research Communications, 1(12). Available at: https://doi.org/10.1088/2515-7620/ab4ec3.

Verhelst, K. et al. (2021) 'Improving forest baseline maps in tropical wetlands using gedi-based forest height information and sentinel-1', Forests, 12(10), pp. 1–16. Available at: https://doi.org/10.3390/f12101374.

Watanabe, M. et al. (2017) 'Development of early-stage deforestation detection algorithm (advanced) with PALSAR-2/ScanSAR for JICA-JAXA program (JJ-FAST)', in International Geoscience and Remote Sensing Symposium (IGARSS). Institute of Electrical and Electronics Engineers Inc., pp. 2446–2449. Available at: https://doi.org/10.1109/IGARSS.2017.8127487.

Watanabe, M. et al. (2018) 'Early-stage deforestation detection in the tropics with L-band SAR', IEEE Journal of Selected Topics in Applied Earth Observations and Remote Sensing, 11(6), pp. 2127–2133. Available at: https://doi.org/10.1109/JSTARS.2018.2810857.

Watanabe, M. et al. (2021) 'Refined algorithm for forest early warning system with ALOS-2/PALSAR-2 ScanSAR data in tropical forest regions', Remote Sensing of Environment, 265, p. 112643. Available at: https://doi.org/10.1016/j.rse.2021.112643.

Wheeler, D. et al. (2014) 'Satellite-based forest clearing detection in the Brazilian Amazon: FORMA, DETER, and PRODES', WRI Issue Brief, p. 24.

Wunder, S. (2015) 'Revisiting the concept of payments for environmental services', Ecological Economics, 117, pp. 234–243. Available at: https://doi.org/10.1016/j.ecolecon.2014.08.016.

Ygorra, B., Frappart, F., Wigneron, J., et al. (2021) 'Deforestation Monitoring Using Sentinel-L SAR Images in Humid Tropical Areas', in 2021 IEEE International Geoscience and Remote Sensing Symposium IGARSS, pp. 5957–5960. Available at: https://doi.org/10.1109/IGARSS47720.2021.9554698.

Ygorra, B., Frappart, F., Wigneron, J.P., et al. (2021) 'Monitoring loss of tropical forest cover from Sentinel-1 time-series: A CuSum-based approach', International Journal of Applied Earth Observation and Geoinformation, 103, p. 102532. Available at: https://doi.org/10.1016/j.jag.2021.102532.

Zhao, F. et al. (2022) 'Monthly mapping of forest harvesting using dense time series Sentinel-1 SAR imagery and deep learning', Remote Sensing of Environment, 269, p. 112822. Available at: https://doi.org/10.1016/j.rse.2021.112822.

5.3. Conference note: IGARSS 2022

Classification and deforestation monitoring using Sentinel-1 C-SAR images in a temperate exploited pine forest

Ygorra B.[1,2,3], Frappart F.[1], Wigneron J-P.[1], Moisy C.[1], [4]Pillot B, [5]Puiseux J., Riazanoff S.[2]

[1] INRAE, UMR1391 ISPA, 33140, Villenave d'Ornon, France

[2] VisioTerra,77420, Champs-sur-Marne, France

[3] University of Bordeaux, 33400, Talence, France

[4] Espace-DEV, IRD, University of Montpellier, 34093 Montpellier, France

[5]Direction Régionale de l'Alimentation, de l'Agriculture et de la Forêt

Abstract

Index Terms— CuSum, Sentinel-1, C-SAR, vegetation cover change, temperate forest, deforestation, classification

Earth Observation data is often used for land cover classification or change monitoring. It is rarely used for both goals in a single algorithm. The multi-change Cumulative Sum (CuSum) algorithm proposed in this study allows both classification and change monitoring in a single algorithm using Sentinel-1 C-SAR time series. The multi-change CuSum approach allowed to classify pixels belonging to the fused non-forest vegetation and bare soil classes apart from the pixels belonging to new cuts. The distinction of each class is better made using the two polarizations: VV is more accurate for detecting non-forest vegetation (Kappa coefficient of 0.62) and VH for detecting new cuts (Kappa coefficient of 0.65). The algorithm showed an accuracy up to 0.82.

5.3.1. Introduction

With the world population growth, the area occupied by forests has been diminishing at an alarming rate. Deforestation monitoring is performed using Earth Observations (EO) on a regional to global scale. Until recently, most global products were based on satellite optical images (Karra et al., 2021; Santoro et al., 2017). With the launch of Sentinel-1, SAR images have been increasingly used owing to the high spatial (#1 at 20 x5 m) and, above all, temporal (6 to 12 days) resolutions of these data (Bouvet et al., 2018; Deutscher et al., 2017; Dostálová et al., 2021; Haarpaintner and Hindberg, 2019; Hamunyela et al., 2017; Hirschmugl et al., 2017; Reiche et al., 2021; Ruiz-ramos et al., 2018; Ruiz-Ramos et al., 2020; Sr. et al., 2018; Ygorra *et al*., 2021b). Approaches used for deforestation monitoring are generally based on change detection method relying on a reference cover map stemming from a land cover classification. Very few methods achieve both the definition of the reference cover map and the detection of the changes. The Cumulative Sum algorithm is one of the numerous techniques developed for monitoring changes. This method is based on time series analysis. It is used to detect noticeable change in the average of a time-series (Manogaran and Lopez, 2018; Ygorra *et al*., 2021b). This method has been recently applied for the monitoring of temperate and tropical forests (Kellndorfer, 2019; Ruiz-ramos et al., 2018; Ruiz-Ramos et al., 2020; Ygorra *et al*., 2021a; Ygorra *et al*., 2021b). Applied to Sentinel-1 time-series in tropical forests, it was found to detect changes earlier than the reference date of cut. This technique was applied to detect only one change per pixel in the time-series of images (e.g., from forest to bare soil, in a 2-years monitoring). Here, we propose a new version of the algorithm to detect several changes in the time-series of images. In this study, we apply this new method to a time-series of Sentinel-1 SAR images acquired over Les Landes forest between 07/2016 and 06/2017.

5.3.2. Study area and datasets

5.3.2.1. Study area

The Les Landes pine forest study area is located in the Aquitaine region near the Arcachon Basin, in the southwest of France. The study area is mainly composed by Maritime Pine tree forests and wastelands. The study area is located between -1.231° and -1.092° E, 44.777° and 44.991° N and covers an area of 145 km² (Figure V.13).

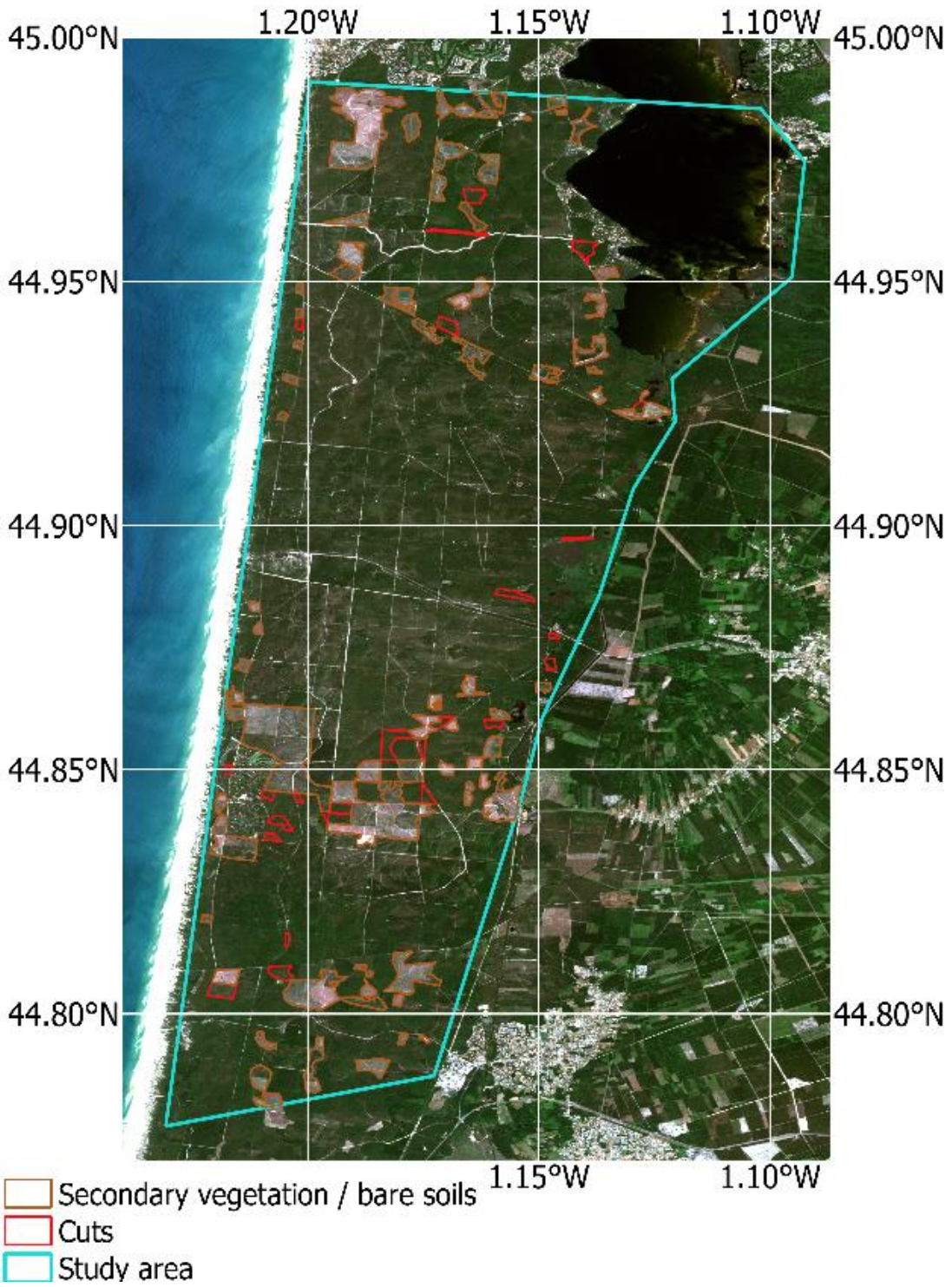

Figure V.13: Aquitaine study Site, located North from Arcachon Basin, RGB view of the Sentinel-2 image acquired 12/08/2016.

5.3.2.2 Satellite images

Three Earth Observation (EO) datasets were used in this study during the time period ranging from 21/07/2016 and 29/06/2017: Sentinel-1 Ground Range Detected (GRD) for the analysis, Sentinel-2 L2A at 10 m pixel resolution along with a change map from the French National Forest Office (ONF) for the validation. 148 Sentinel-1 IW GRD double polarization VV and VH images, two Sentinel-2 images acquired on 12/08/2016 and 18/06/2017 were provided by the European Space Agency (ESA) at *https://scihub.copernicus.eu*.

5.3.2.3. Methods

5.3.2.3.1. Preprocessing and processing

Sentinel-1 SAR images were pre-processed using the VtWeb preprocessing routine (*https://visioterra.org/VtWeb/*) consisting of the following steps: orbit correction, orthorectification, thermal noise removal, radiometric correction and terrain correction (see (Ygorra *et al*., 2021b) for more details). The PyRAT Toolbox's bilateral filter (Reigber et al., 2019) with a window of 7 by 7 pixels was then applied to reduce the speckle.

5.3.2.3.2. CuSum multi detection algorithm

The Cumulative Sum (CuSum) algorithm is a change point detection method often combined with a bootstrap analysis to identify the significant changes in a time-series (Manogaran and Lopez, 2018; Ygorra *et al*., 2021b). This method is based on a critical threshold (T_c) over which a change is considered valid. This method has been applied to remote sensing data in both tropical and temperate areas (Kellndorfer, 2019; Ruiz-ramos et al., 2018; Ygorra *et al.*, 2021; Ygorra *et al*., 2021b) as a single change detection method. The Cross-T_c was also applied in this study. The multi-detection version of the CuSum algorithm is composed by the repetition of the CuSum algorithm over different time periods. Once the CuSum detected a change, the multi-detection version splits the original time period into two distinct periods over which the CuSum single-change detection is run again. The iteration continues until no further valid date of change is found. In this study, the T_c chosen was 0.95. The minimal area unit of 300 m² was applied to form the cross-T_c 100_95 dataset.

5.3.2.4. Validation method

Sentinel-2 images were used to visually confirm the changes and clear cuts over the study area highlighted by the ONF change map composing the 'cut' class, along with determining the non-forest vegetation / bare soil areas at the start of the study period. Both visually defined

reference and the ONF land cover maps were used to compute the statistics derived from confusion matrix analysis: Accuracy, Precision, Recall, Cohen's Kappa coefficient and F1-score. The Random Sampling strategy was applied to ensure the classes are comparable in size. 23 277 pixels (232,77 ha) were randomly selected in each class (bare soils / non-forest vegetation, cut, other). The cut and bare soils / non-forest vegetation classes were studied independently as two different reference datasets were available.

5.3.3. Results

5.3.3.1. Forest / non-forest vegetation classification

The number of changes per pixel is an important variable in the class discrimination. As shown in Figure V.14, for the VV polarization, the pixels located in the small zones of cut appear to have less than 4 changes accounted for by the multi-change CuSum algorithm. Most pixels showing a number of change higher than 4 are located in the non-forest vegetation / bare soil class. There are also many changes detected in a mixed vegetation / opened forest zone.

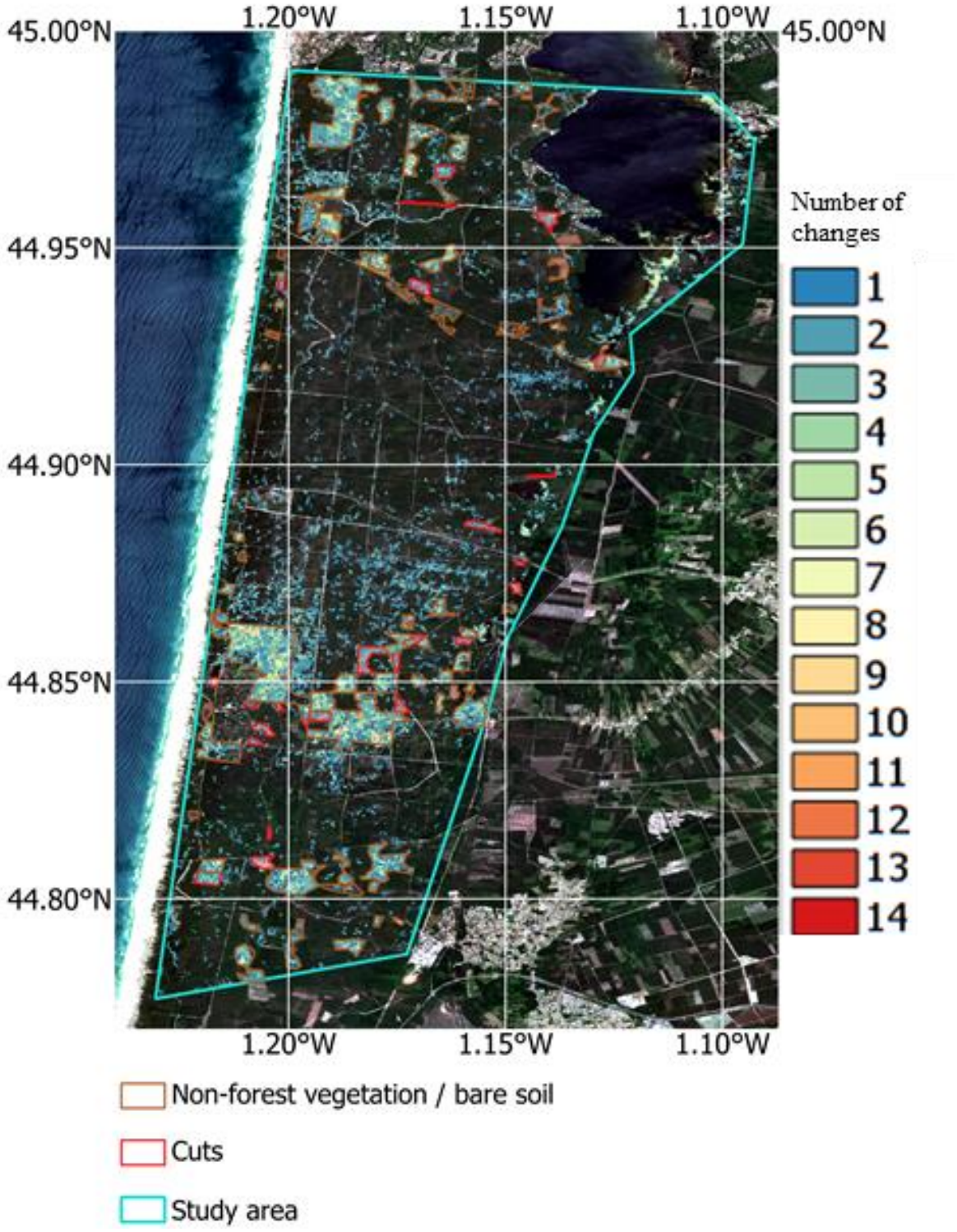

Figure V.14: VV 100_95 number of changes map on the Sentinel-2 image acquired 18/06/2017.

As shown in Figure V.15, the percentage of area associated with the lower boundary of the number of changes interval (e.g. if the lower limit is 5, the total area considered is represented by the pixels with 5 or more changes associated) increases with a higher boundary value, for the non-forest vegetation / bare soil class in both VV and VH presentations. More than 90% of the pixels presenting at least 8 changes are located in the soil / non-forest vegetation class in both the VV and VH change maps. In the cut class, the area corresponding to the number of changes interval decreases with the lower boundary of this interval. There are no pixels in the cut class showing 6 or more changes in the VV change maps and no pixels showing 8 or more changes in the VH change map.

The total area corresponding to each number of changes interval decreases for both classes in the VV intersect VH change map.

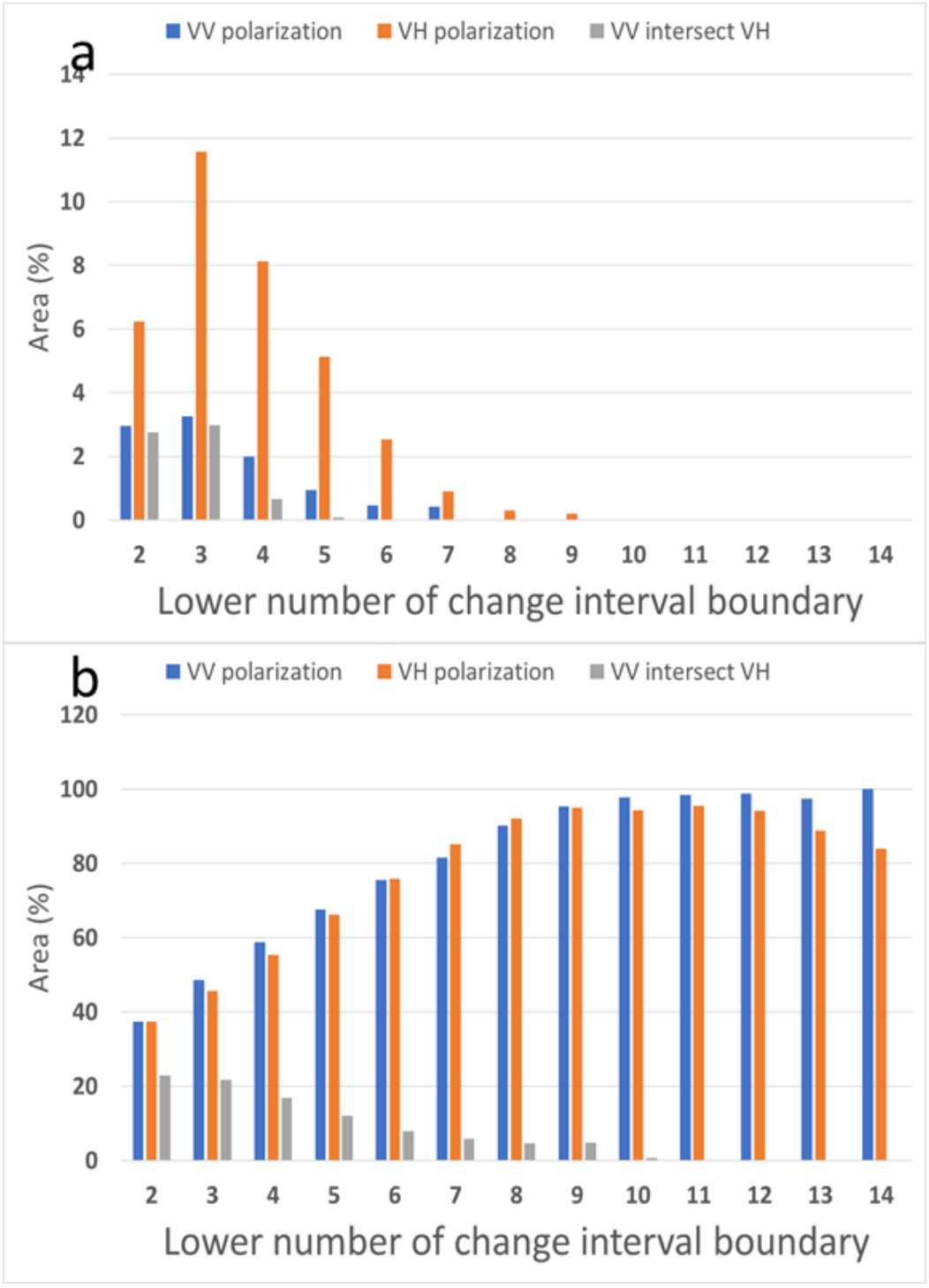

Figure V.15: (a) Histograms of the area percentage in function of the lower number of changes interval boundary (a) applied to the cut class and (b) applied to the bare soil / non-forest vegetation class.

5.3.3.2. Comparison against external datasets

As shown in Figure V.16, the different polarizations (VV, VH and their intersection) result in different statistics. The VV intersect VH recommended as the most precise combination according to (Ygorra et al., 2021b) shows the highest precision value for both classes (0.96 for the non-forest vegetation / bare soils and 0.87 for the cuts). The VH polarization shows the most consistent results in the cut class with high precision (0.81), accuracy (0.82), recall (0.85), Kappa coefficient (0.65) and F1-score (0.83). The most consistent results for the non-forest vegetation / bare soil class are obtained by the VV polarization, with a precision value of 0.87, an accuracy value of 0.81, a 0.73 recall value, a 0.62 kappa coefficient value and a 0.79 F1-score value.

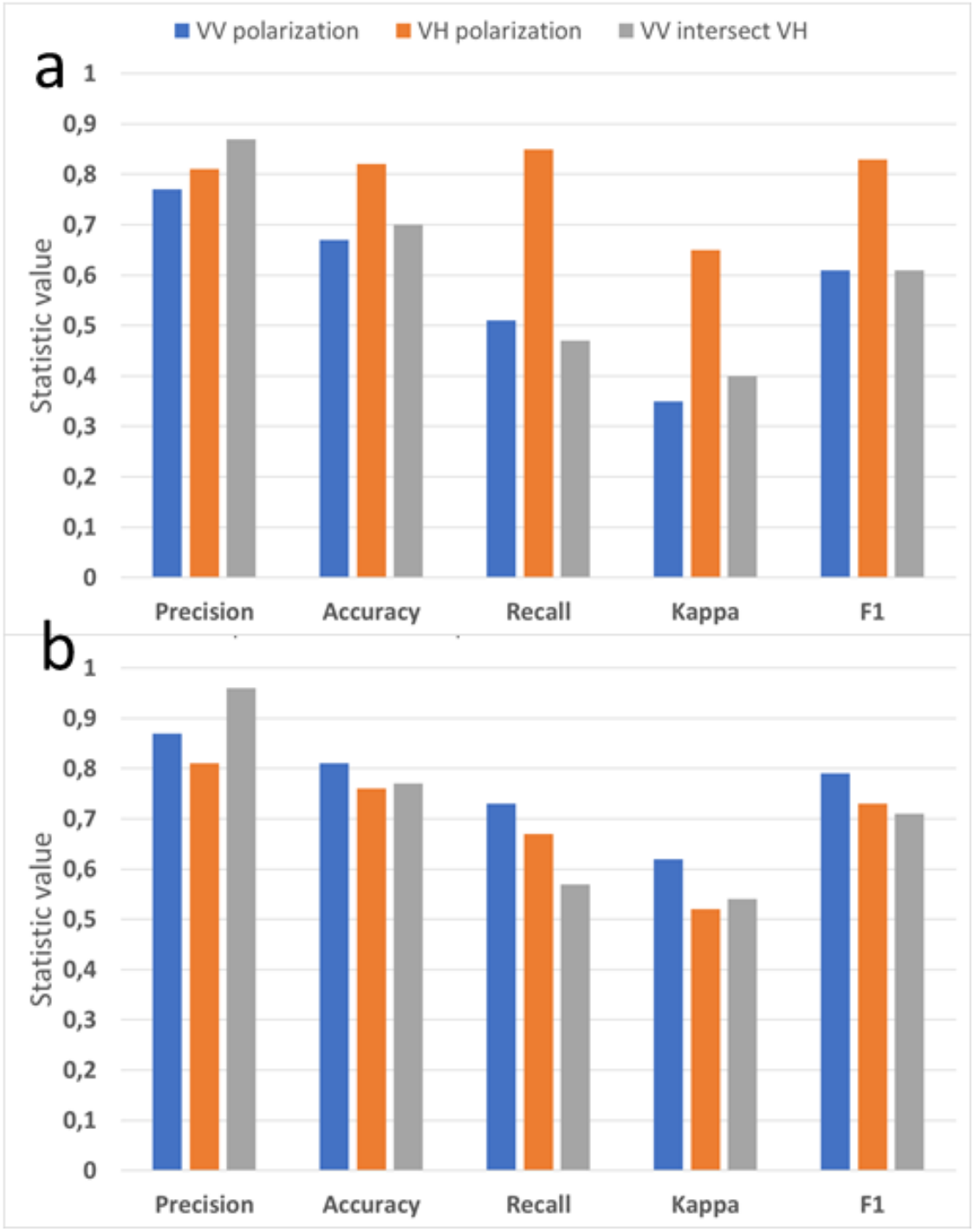

Figure V.16: (a) Histograms of the precision, accuracy, recall, Kappa and F1 statistics (a) of the cut class and (b) applied to the bare soil / non-forest vegetation class.

5.3.4. Discussion

The CuSum multi-detection is able to produce a series of dates of change on a single pixel. We explored the hypothesis that the number of changes is correlated to the dynamics of a cover in terms of backscatter coefficient. The results showed a correlation between the number of changes of a pixel and the class of the pixel. The pixels with a high number of changes are mostly located in the soil/ low vegetation class, and few to none are located in the cut class. Due to this characteristic, the CuSum multi-detection can be used to discriminate non-forest vegetation / bare soil from new cuts happening in forest. More than 90 % of the pixels showing a number of change greater or equal to 8 are located in the lower vegetation / bare soil class in both VV and VH result map.

The distinction between forest cuts and non-forest vegetation / bare soil classes is not possible using this method on the VV intersect VH dataset. Firstly? The purpose of the VV intersect VH dataset is to reduce the false positives, only keeping the changes showing a great amplitude affecting both VV and VH polarizations.

The CuSum seems to detect different events according to the polarization. The intersection of polarization means an event affected both polarizations, and should be considered as a great amplitude event. The VH polarization seems to better detect the cuts in temperate areas than the VV and the VV intersect VH polarizations, whereas the VV polarization seems to be able to detect changes on the non-forest / bare soils vegetations and thus classify it. The VV intersect VH should not be used to classify or to detect small changes in temperate areas.

5.3.5. Conclusion

The CuSum algorithm is able to detect changes in different covers (forest, bare soils, non-forest vegetation). Considering the covers dynamics in terms of radar backscatter, the multi-detection CuSum is able to differentiate the non-forest vegetation / bare soils from the new cuts on a forested area in temperate areas. The changes it detects can vary from a polarization to another. Further studies on the importance of the polarization in terms of physical determination of the change are needed.

5.3.6. References

[1] K. Karra, C. Kontgis, Z. Statman-Weil, J. C. Mazzariello, M. Mathis, and S. P. Brumby, “Global land use/land cover with Sentinel 2 and deep learning,” in 2021 IEEE International Geoscience and Remote Sensing Symposium IGARSS, 2021, pp. 4704–4707.

[2] M. Santoro et al., “Land Cover CCI: Product User Guide Version 2.0,” Clim. Chang. Initiat. Belgium Belgium, Leuven, 2017.

[3] A. Dostálová, M. Lang, J. Ivanovs, L. T. Waser, and W. Wagner, “European wide forest classification based on sentinel-1 data,” Remote Sens., vol. 13, no. 3, pp. 1–27, 2021, doi: 10.3390/rs13030337.

[4] S. N. Sr., A. Billey, and H. T.-O.-A. Jr., “Random forest classification using Sentinel-1 and Sentinel-2 series for vegetation monitoring in the Pays de Brest (France),” in Remote Sensing for Agriculture, Ecosystems, and Hydrology XX, 2018, vol. 10783, pp. 1–18, doi: 10.1117/12.2325546.

[5] J. Deutscher, K. Gutjahr, R. Perko, H. Raggam, M. Hirschmugl, and M. Schardt, “Humid tropical forest monitoring with multi-temporal L-, C- and X-band SAR data,” 2017 9th Int. Work. Anal. Multitemporal Remote Sens. Images, MultiTemp 2017, pp. 1–4, 2017, doi: 10.1109/Multi-Temp.2017.8035264.

[6] E. Hamunyela, M. Herold, and J. Verbesselt, “Space-time monitoring of tropical forest changes using observations from multiple satellites,” Ph.D. Thesis, Wageningen University & Research, Laboratory of Geo-information Science and Remote Sensing, Wageningen, The Netherlands, 2017.

[7] J. Ruiz-Ramos, A. Marino, C. Boardman, and J. Suarez, “Continuous forest monitoring using cumulative sums of sentinel-1 timeseries,” Remote Sens., vol. 12, no. 18, 2020, doi: 10.3390/RS12183061.

[8] J. Ruiz-ramos, A. Marino, and C. P. Boardman, “USING SENTINEL 1-SAR FOR MONITORING LONG TERM VARIATION IN BURNT FOREST AREAS Javier Ruiz-Ramos ; Armando Marino ; Carl P . Boardman,” IGARSS 2018 - 2018 IEEE Int. Geosci. Remote Sens. Symp., no. July 2017, pp. 4901–4904, 2018.

[9] A. Bouvet, S. Mermoz, M. Ballère, T. Koleck, and T. Le Toan, “Use of the SAR shadowing effect for deforestation detection with Sentinel-1 time series,” Remote Sens., vol. 10, no. 8, pp. 1–19, 2018, doi: 10.3390/rs10081250.

[10] B. Ygorra et al., “Deforestation Monitoring Using Sentinel-L SAR Images in Humid Tropical Areas,” in 2021 IEEE International Geoscience and Remote Sensing Symposium IGARSS, 2021, pp. 5957–5960, doi: 10.1109/IGARSS47720.2021.9554698.

[11] M. Hirschmugl, J. Deutscher, K. H. Gutjahr, C. Sobe, and M. Schardt, “Combined use of SAR and optical time series data for near real-time forest disturbance mapping,” 2017 9th Int. Work. Anal. Multitemporal Remote Sens. Images, MultiTemp 2017, pp. 0–3, 2017, doi: 10.1109/Multi-Temp.2017.8035208.

[12] J. Reiche et al., “Forest disturbance alerts for the Congo Basin using Sentinel-1,” Environ. Res. Lett., vol. 16, no. 2, p. 024005, 2021, doi: 10.1088/1748-9326/abd0a8.

[13] J. Haarpaintner and H. Hindberg, “Multi-temporal and multi-frequency sar analysis for forest land cover mapping of the Mai-Ndombe district (Democratic Republic of Congo),” Remote Sens., vol. 11, no. 24, 2019, doi: 10.3390/rs11242999.

[14] G. Manogaran and D. Lopez, “Spatial cumulative sum algorithm with big data analytics for climate change detection,” Comput. Electr. Eng., vol. 65, pp. 207–221, 2018, doi: 10.1016/j.compeleceng.2017.04.006.

[15] B. Ygorra et al., “Monitoring loss of tropical forest cover from Sentinel-1 time-series: A CuSum-based approach,” Int. J. Appl. Earth Obs. Geoinf., vol. 103, p. 102532, 2021, doi: https://doi.org/10.1016/j.jag.2021.102532.

[16] J. Kellndorfer, “Using SAR data for mapping deforestation and forest degradation,” in THE SAR HANDBOOK Comprehensive Methodologies for Forest Monitoring and Biomass Estimation, ServirGlobal : Huntsville, AL, 2019, pp. 65–79.

[17] A. Reigber, G. M. del Campo Becerra, and M. Jäger, “PyRAT: A Flexible SAR Postprocessing Toolbox,” 2019, [Online]. Available: https://elib.dlr.de/125869/.

5.4. Contribution to this work and perspective

Sentinel-1 and -2 data were available, with pre-processing already applied on the VtWeb platform. I developed the multi-detection, but the optimisation was entirely conducted by *B. Pillot*, Research Engineer IRD working for the Institute of Research for the Development (IRD) at the ESPACE-DEV UMR, enabling the CuSum to be used by many users through a Python package.

This study contributed to demonstrate the flexibility of the CuSum applied on time-series of Sentinel-1 images. Firstly, a non-forest mask can be established using CuSum cross-Tc over an earlier period. Then, the ReCuSum can be applied to the monitoring period to further discriminate forest cover changes from other changes.

This flexibility is also a strength of the CuSum, as all these algorithms can potentially be used on other types of remote sensed data. The intensity of the change can also be considered in order to further reduce false positives.

The development of this method concludes the first two parts of my PhD, which dealt with the offline versions of CuSum, to establish deforestation assessments over a given period of time. The best product available is the ReCuSum, but it is also the most expensive in terms of computational time and resources.

The third and final part of the PhD deals with the development of a NRT approach, as the ReCuSum is an offline method requiring long time-series as input.

CHAPTER VI.

DEVELOPMENT OF THE CUSUM CROSS-T_C AS AN NRT ALGORITHM

Table of contents

Chapter VI. Development of the CuSum cross-T_c as a Near-Real-Time algorithm

6.1. Introduction

This chapter presents the last part of my PhD and is related to its industrial goal. The industrial objective of my CIFRE contract was to develop a Near-Real-Time (NRT) algorithm to monitor changes in forest cover using Sentinel-1 data, with a focus on the tropical area. I developed the CuSum NRT version by applying the CuSum cross-T_c improvement from Chapter 4 to shorter time-series and remove changes belonging to non-forest by applying the mask developed in Chapter 5. The approach was tested in the same study area as in Chapter 5, in the Para state of the Brazilian Amazon. Before this chapter, the CuSum critical threshold (T_c) parameters were tested empirically for 5 thresholds in the Democratic Republic of the Congo region: 25, 50, 75, 95 and 100. Preliminary results from cross-T_c 100_75 and 100_95 indicated that the algorithm was more sensitive to speckle with a shorter time-series than the offline versions. This sensitivity was analysed thoroughly in this chapter. In order to check the potential of the NRT version, the algorithm was then compared with all state-of-the art NRT algorithms currently freely available on a site in Parà, near the site used in Chapter 5 and also used in the sensitivity analysis of the NRT version. The NRT version was then compared to the ReCuSum to evaluate potential changes to the performance.

In order to achieve an objective comparison of the performance in monitoring changes in forest cover between all algorithms, a large validation area was needed. Two Sentinel-2 images were used for this purpose along with a monthly PlanetScope mosaic to build a map referencing all changes in forest cover which occurred between those dates by visual inspection. The area of this map is approximately 6,855 km². An analysis of the effect of disturbance size on the algorithm's detection performance was conducted. Another analysis was conducted to compare the algorithm according to the Minimum Mapping Unit used, so that the comparison was objective and complete.

6.2. Publication

CuSum cross-T_c NRT development and comparison for tropical forest disturbance monitoring

Ygorra Bertrand[1,2,3], Frappart Frederic[1], Wigneron Jean-Pierre[1], Moisy Christophe[1], Catry Thibault[4], Pillot Benjamin[4], Kharlanova Anna[4], Riazanoff Serge[2]

[1] INRAE, UMR1391 ISPA, 33140, Villenave d'Ornon, France

[2] VisioTerra,77420, Champs-sur-Marne, France

[3] Université de Bordeaux, 33400, Talence, France

[4] ESPACE-DEV, Univ Montpellier, IRD, Univ Antilles, Univ Guyane, Univ Réunion, Montpellier, France

Corresponding author: Ygorra Bertrand, bertrand.ygorra@gmail.com.

6.2.1. Introduction

Tropical forests, which play a critical role in the global climate regulation by recycling between ~2.1Gt $CO_2.y^{-1}$ (Federici et al., 2015) and 7.0 Gt $CO_2.y^{-1}$ (Harris *et al.*, 2021) are being damaged at increasing rates. They are endangered by deforestation, climate change and increasing anthropogenic pressure (Creese et al., 2019; Gatti et al., 2021). Recent studies showed that tropical rainforests are both a sink and a source in the carbon cycle with an overall neutral budget (Fan et al., 2019). Increased global awareness of climate change and degradation of tropical forests has not decreased deforestation rates. According to the Global Forest Review published by the World Resources Institute (WRI) in Washington, DC, USA, in 2021, the annual loss of tree cover has increased continuously since the beginning of the monitoring by (Hansen et al., 2013), in the year 2000, reaching 12 million hectares in 2020. In Amazonia, the forest losses in carbon stocks are driven by multiple factors, including legal or illegal selective logging causing

degradations, or cuts to fulfil the needs of local populations in terms of agriculture (Creese et al., 2019; Kleinschroth et al., 2019; Lescuyer et al., 2011; Qin et al., 2021; Umunay et al., 2019).

Remote sensing has been identified as a major tool for monitoring deforestation (Lynch et al., 2013). Several operational systems operating in near-real-time were developed to monitor deforestation in tropical areas. In the Brazilian Amazon, PRODES has been issuing alerts 1988, joined by Near-Real-Time Deforestation Detection System (DETER) since 2004 (Assunção et al., 2017). These systems are basing their detection on multispectral data. These monitoring systems have been improved over time and are still operational to this date (Diniz et al., 2015).The limitation of such optical systems lies in the constant cloud cover over Brazilian Amazon regions (Weisse et al., 2019). In certain parts of the Brazilian Amazon, mean cloud cover can reach up to 74% (Doblas et al., 2020; Weisse et al., 2019), delaying the detections in monitoring systems based on optical sensors.

The potential of base surveillance systems on Synthetic Aperture Radar (SAR) has been demonstrated (Joshi et al., 2015) as active sensors are less sensitive to the presence of water in the atmosphere. Several automatic Near-Real-Time (NRT) forest monitoring systems have since been developed, including JJ-FAST (Watanabe et al., 2021, 2018, 2017) using L-band SAR images from Phased-Array L-band Synthetic Aperture Radar-2 (PALSAR-2, Arikawa *et al.*, 2014) and RAdar for Detection Deforestation alerts (Reiche et al., 2021) using C-band SAR images from Sentinel-1 (Torres et al., 2012). More recently, a new version of the DETER system, known as DETER-Radar (DETER-R), is using Sentinel-1 images for detecting changes in forest cover (Doblas et al., 2022). Sentinel-1 are also used by the Tropisco project to identify the shadow effect caused by tree cuts in the SAR images which to detect the boundaries of the deforested areas (Ballère et al., 2021; Bouvet et al., 2018; Mermoz et al., 2021).

The Cumulative Sum (CuSum, (Manogaran and Lopez, 2018; Mistry et al., 2021; Ruiz-Ramos et al., 2020; Ygorra et al., 2021b; Ygorra et al., 2021a) applied to Sentinel-1 images was recently identified as an efficient tool for deforestation monitoring (Manogaran and Lopez, 2018; Mistry et al., 2021; Ruiz-Ramos et al., 2020; B Ygorra et al., 2021b, 2021a)). The objective of this study is to develop a near-real-time version of the CuSum cross-T_c. In this study, the calibration of the NRT version of the CuSum algorithm is presented. It consists in determining the best choice for the number of images before the monitored date, the number of images after the monitored date (delay), the high T_c value and the low T_c value in terms of F1-score on a small study area located in the Brazilian Amazonia. Then, the performances of the CuSum NRT method are compared with the ReCuSum performances.

6.2.2. Study areas and data

6.2.2.1. Study areas

The study areas consist of two sites located in the State of Parà, in the Amazon rainforest in Brazil (Figure VI.1). The first site was used to calibrate and validate the parameter configurations of CuSum cross-T_c Near-Real-Time. The ReCuSum and the CuSum NRT were compared using this area. This site is a small area of 97.2 km² for an improved calibration speed. This site will be later referred as 'Test site'. The second site will be used for the comparison between the different NRT algorithms. It is a large site of 6,855.4 km². This site will be later referred as 'Main site'.

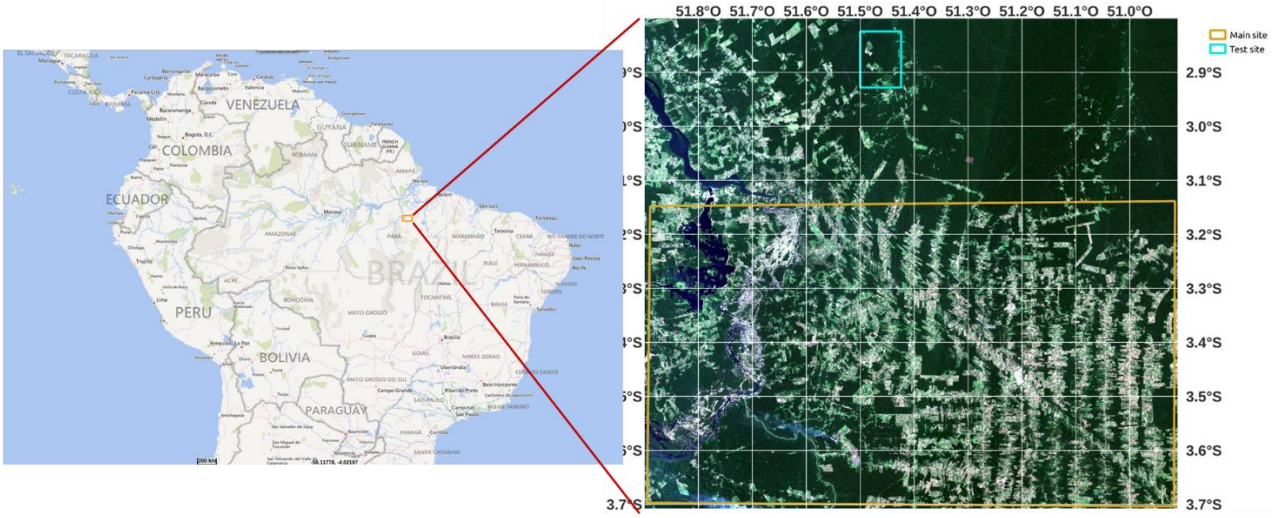

Figure VI.1: Main site (yellow rectangle) and Test site (cyan rectangle) of the study area in the Amazon Forest, State of Para, Brazil. The background is a RGB - Natural colours Sentinel-2 image acquired on 28/07/2017.

6.2.2.2. Data

6.2.2.2.1. Sentinel-1

RADD, DETER-R and CuSum-NRT alerts are based on time-series of Sentinel-1 C-band SAR images. The revisit period of the satellite is 12 days over the study area.

The data used in this study for the CuSum NRT corresponds to the Multi-Look Detected (GRD) products. They were acquired in Interferometric Wide-Swath (IW) mode at VV and VH polarizations. The resulting pixel size is 5 m x 20 m. The images were made available by ESA at *https://scihub.copernicus.eu* and downloaded using VtWeb (*https://visioterra.org/VtWeb/*). The downloaded images were pre-processed, including orbit correction, thermal noise removal, terrain

correction, speckle removal and raincell-contaminated images removal (Ygorra *et al.*, 2021b). The resolution of the output pixels is 9.55 m².

A total of 82 images were available on the Test site between 29/09/2016 and 01/07/2019. These images were divided into two periods. 26 images were employed for defining a non-forest mask using CuSum cross-T_c as described in Ygorra *et al.*, submitted 2023**,** over the 29/09/2016 – 01/08/2017 period.

56 images were then used in the CuSum – NRT version monitoring during the 01/08/2017 – 01/07/2019 period.

A total of 115 images are available between 01/01/2018 and 01/01/2022 over the Main site. The non-forest mask definition was based on 58 images over the 01/01/2018 – 01/01/2020 period.

6.2.2.2.2. Sentinel-2

6.2.2.2.3. PlanetScope monthly mosaic

The level 3B products from PlanetScope Ortho-Scene, derived from the multi-spectral images acquired by the CubeSat constellation, were used to produce monthly mosaics. They consist in 4-band Surface Reflectance (SR) images, orthorectified and scaled with a 5m pixel resolution (Red: 605 – 695 nm, Green: 515 – 595 nm, Blue: 450 – 515 nm, Near-InfraRed: 740 – 900 nm).

They are made available through the NICFI program (https://www.planet.com/nicfi/). Two PlanetScope monthly mosaics were accessed on the study area respectively in June and December 2019.

6.2.3. Methods

6.2.3.1. Reference map composition

The calibration and validation phases were achieved on two different study areas (referred as Test and Main sites) on different periods of time. The calibration of the CuSum NRT over the Test site was performed between 01/08/2017 and 01/07/2019 due to the availability of a Sentinel-2 image and a PlanetScope mosaic to perform the visual interpretation of forest cover changes (Figure VI.2). The interpretation was made on RGB colour compositions. According to this map, a total of 10.2 km² of forested areas showed a change in cover during the time period.

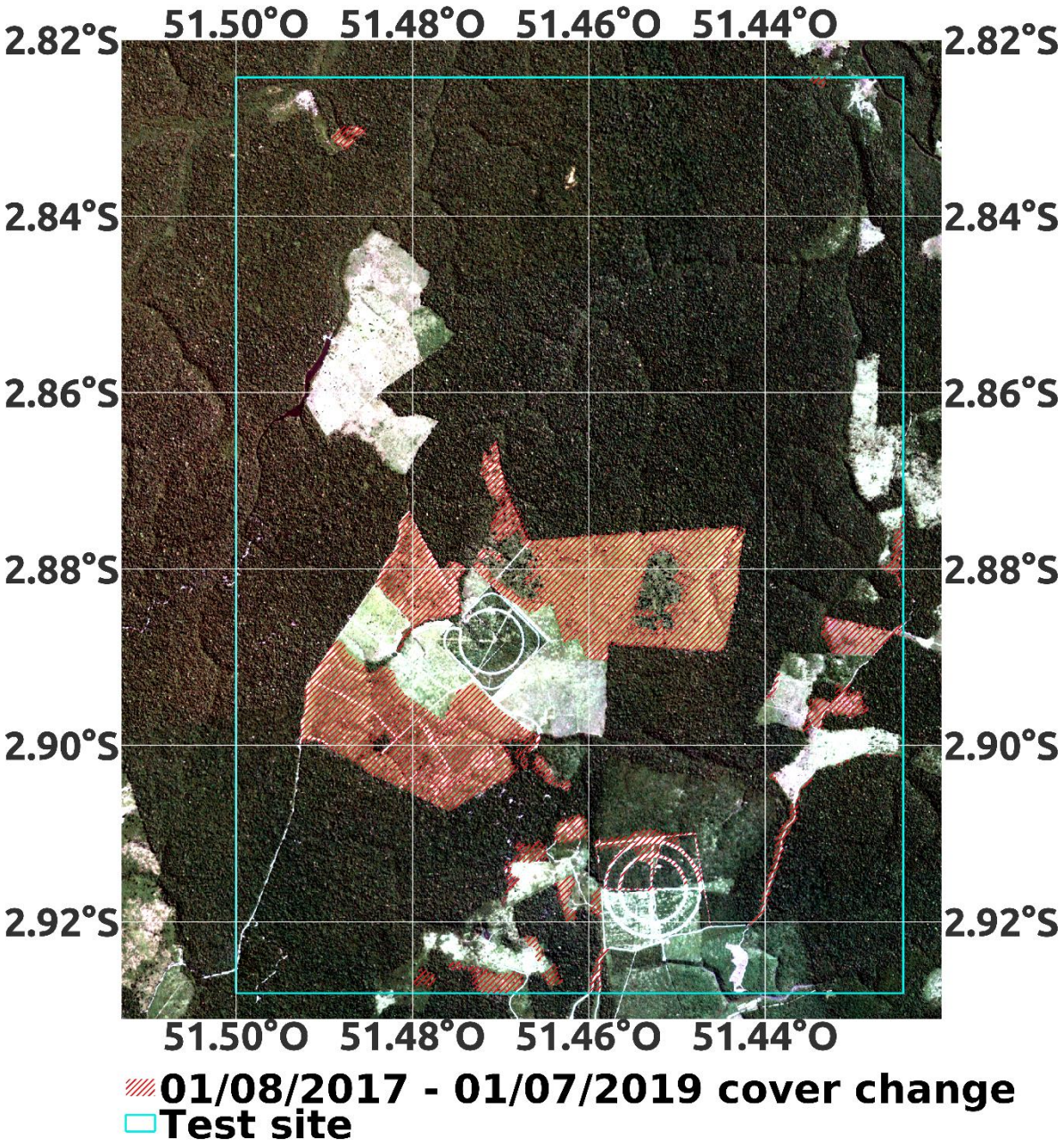

Figure VI.2: Over the Test site (blue rectangle), forest cover changes (red hatches) were identified between 01/08/2017 and 01/07/2019 through visual inspection. They are superimposed on the PlanetScope monthly mosaic of 06/2019.

For the same reason (i.e., the availability of the multi-spectral images), the reference map of the Main site was created through visual interpretation of Sentinel-2 images and a monthly PlanetScope mosaic. Several reference maps were produced, using (1) Sentinel-2 acquired between 23/06/2019 and 11/08/2021 and (2) monthly PlanetScope mosaic acquired in 12/2019.

First, the forest cover changes were identified using the two Sentinel-2 images, producing the 01/07/2019 – 01/08/2021 reference map. Then, changes that occurred before 12/2019 (identified using the monthly PlanetScope mosaic) were removed to form the 01/01/2020 – 01/08/2021 reference dataset. This latter operation was achieved due to the common availability period of all the NRT products used in the comparison.

The difference in spatial resolution between monthly PlanetScope mosaic and Sentinel-2 images did not affect the manual delimitation of the changes removed from the 01/07/2019 – 01/08/2021 dataset as they were manually removed.

The 01/01/2020 – 01/08/2021 forest cover change reference map was used on the Main site for the algorithm comparison (Figure VI.3). Approximately 223.5 km² of the Main site forested areas showed a cover change during this period. Changes found after the end of the monitoring period for algorithms (01/08/2021) and before 11/08/2021, date of the end of the reference dataset, were considered negligible. This assumption is likely to be responsible for a small increase in false negatives.

Two classes were considered: forest changes and not-a-forest-change (including forest non-change, non-forest non-change and changes occurring on other different land covers). The ‘Not-a-forest-change’ class was considered as the reference for True Negatives and False Positives.

With such an area (6,855.4 km²) to visually interpret, the reference map itself may be lacking some detections, most under the MMU of the algorithms. The missed forest cover change may increase the number of False Positives of the algorithm and should be accounted for in the interpretation.

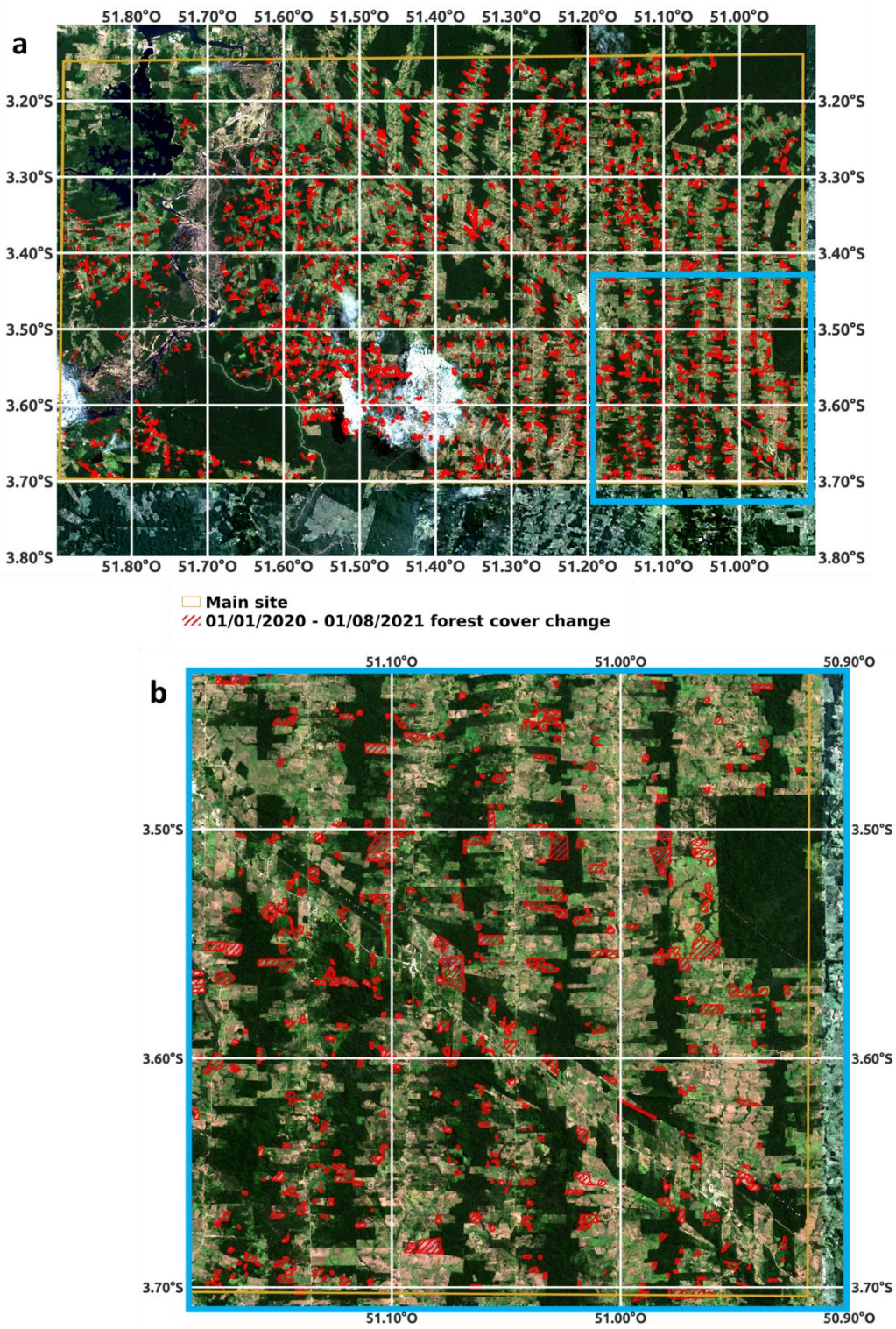

Figure VI.3: Main site 01/01/2020 – 01/08/2021 forest cover change reference map. (a) whole site and (b) a zoom to illustrate. View: Natural colours of Sentinel-2 image acquired 11/08/2021.

6.2.3.2. NRT CuSum

6.2.3.2.1. NRT CuSum sensitivity analysis

The NRT CuSum has been developed based on the CuSum cross-T_c. The CuSum cross-T_c analyses long time-series in order to find a change with different critical thresholds (T_c) and then spatially recombines higher T_c polygons of detected change with lower T_c polygons of detected change. The NRT version of the algorithm works on smaller time-series, with varying length.

CuSum NRT input parameters differ from the ReCuSum and the CuSum single-change cross-T_c. The post-processing cascade is similar to the CuSum single-change cross-T_c not including T_{nbc} the threshold based on the number of changes applied to the ReCuSum. The additional input parameters consist in the number of images considered in the time-series before the monitored image and the number of images considered after the monitored image, forming the length of the time-series. The parameters 'Low T_c' and 'High T_c' of the spatial recombination were also analysed. The sensitivity analysis was achieved over the Test site to determine the best cross-T_c thresholds as well as the best number of images to take into account before and after the monitored date.

6.2.3.2.2. Sensitivity analysis validation parameter

The input parameters possibilities were analysed using Monte-Carlo's method. All parameters' configurations within the boundaries shown in Table VI.1 were computed. The maps of changes obtained were then analysed using the Test site reference map. This is the same reference map as in Ygorra *et al.,* 2023 in the Amazon Basin. The statistic used to analyse and to compare the results is the F1-score, as it is less affected by the population of pixels imbalance between change pixels and non-change pixels.

	High T_c	Low T_c	Number of images before	Number of images after
Range	96 – 100	80 – 95	6 – 12	0 – 6

Table VI.1: Parameters of the CuSum NRT.

6.2.3.3. ReCuSum

The ReCuSum method was used in this study to estimate deforestation for the area and period considered. The method is further described in Ygorra *et al.,* 2023**.** It involves the iterative application of the CuSum cross-T_c, thus changing the 'single breakpoint' feature of the CuSum to 'multiple breakpoints'. The 'multiple breakpoints' feature is obtained by splitting the time-series

into two parts at the first breakpoint, then running the CuSum independently on each time-series. The input parameters used were: 1) MMU of 300 m², 2) cross-T_c of 100_75 and 3) T_{nbc} (threshold based on the number of changes) of 8 for VH at T_c = 100 and 19 at T_c = 75.

The removal of previous changes was also applied in order to eliminate changes that occur on non-forested areas, with a MMU of 1000 m², a cross-T_c of 100_75. The ReCuSum was applied to both Main and Test sites.

6.2.3.4. Validation statistics

The different NRT datasets were compared using the Main site forest cover change reference map. The comparison between CuSum-NRT and ReCuSum was performed using the Test site forest cover change reference map. Confusion matrix statistics such as False Positives (FP), False negatives (FN), True positives (TP) and True negatives (TN) were computed and analysed. Using these variables as input, the kappa coefficient, recall, precision, accuracy and F1-score were computed. The classes 'Forest Change' and 'Not-a-Forest-Change' are unbalanced, the latter being wider. This imbalance led to a necessity to interpret these variables altogether (Olofsson et al., 2014).

6.2.3.5. Comparison between CuSum NRT and ReCuSum

On both Test and Main sites, the CuSum cross-T_c NRT was used as a simulation over a period to establish a deforestation assessment. The ReCuSum was also used over this whole period to establish a similar deforestation assessment. The two obtained maps of changes were compared to the reference map, obtaining the aforementioned statistics. The two results were compared in terms of statistics.

6.2.4. Results

6.2.4.1. CuSum cross-T_c NRT sensitivity analysis

6.2.4.1.1. Low T_c and high T_c combination analysis

The results were analysed sequentially. Firstly, the F1-scores were analysed in function of the cross-T_c combination values of low T_c with high T_c (Figure VI.4). On Figure VI.4, it is possible to see that the VV and the VH polarisation results are systematically lower than the VV x VH results. For these two polarisations, a higher value of low T_c increases slightly the results by 0.05. The value of high T_c does not seem to significantly change the resulting F1-score compared to the low T_c value.

The VV x VH results show the best F1-score value, up to 0.70. An increased low T_c value does not systematically result in an increased F1-score, as a low T_c higher than 92 results in a lower maximum F1-score value (0.69 for low T_c = 93, 0.68 for 94 and 0.67 for 95). The highest F1-score at each low T_c value are obtained using a high T_c value of 100. A higher T_c value does not systematically result in a higher F1-score value, as the number of images before/after the monitoring date may influence the F1-score. Only values showing a F1-score > 0.60 were kept for the analysis of the optimal number of changes before / after for deforestation monitoring purposes.

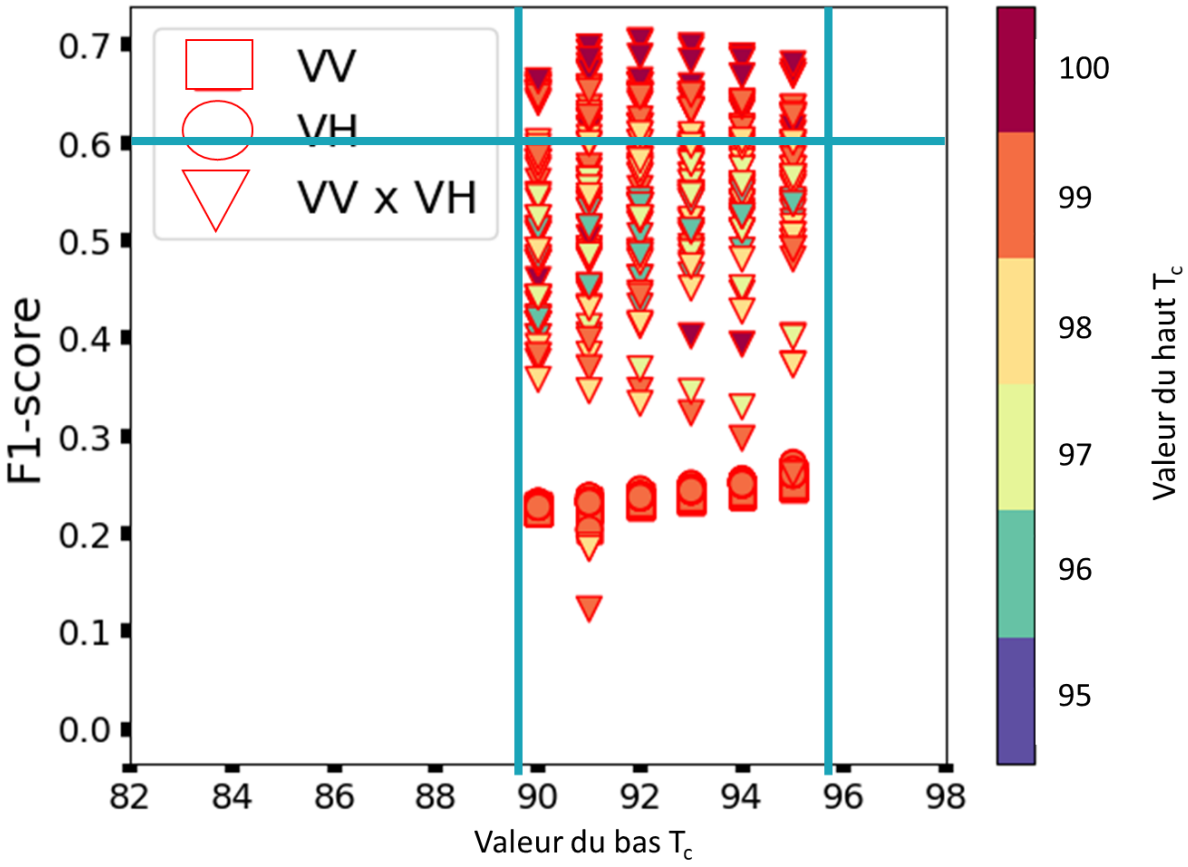

Figure VI.4: Graph of the F1-score obtained according to the polarisation, low T_c and high T_c values set in the parameters.

6.2.4.1.2. Analysis of the number of dates before / after targeted S1 image

The results aforementioned were further analysed to determine the influence of the number of images before / after the date targeted used to form the time-series (Figure VI.5). The number of images taken before the monitoring date to form the time series were analysed from 8 to 11

images. The maximum F1-score value was reached at 11 images before, this value decreasing for 10 and 9 images taken before. The F1-score value further decreases at 8 images.

The number of images taken 'after' the monitoring date (delay) was also analysed. Results show an optimum obtained at 3 images taken after the monitoring date.

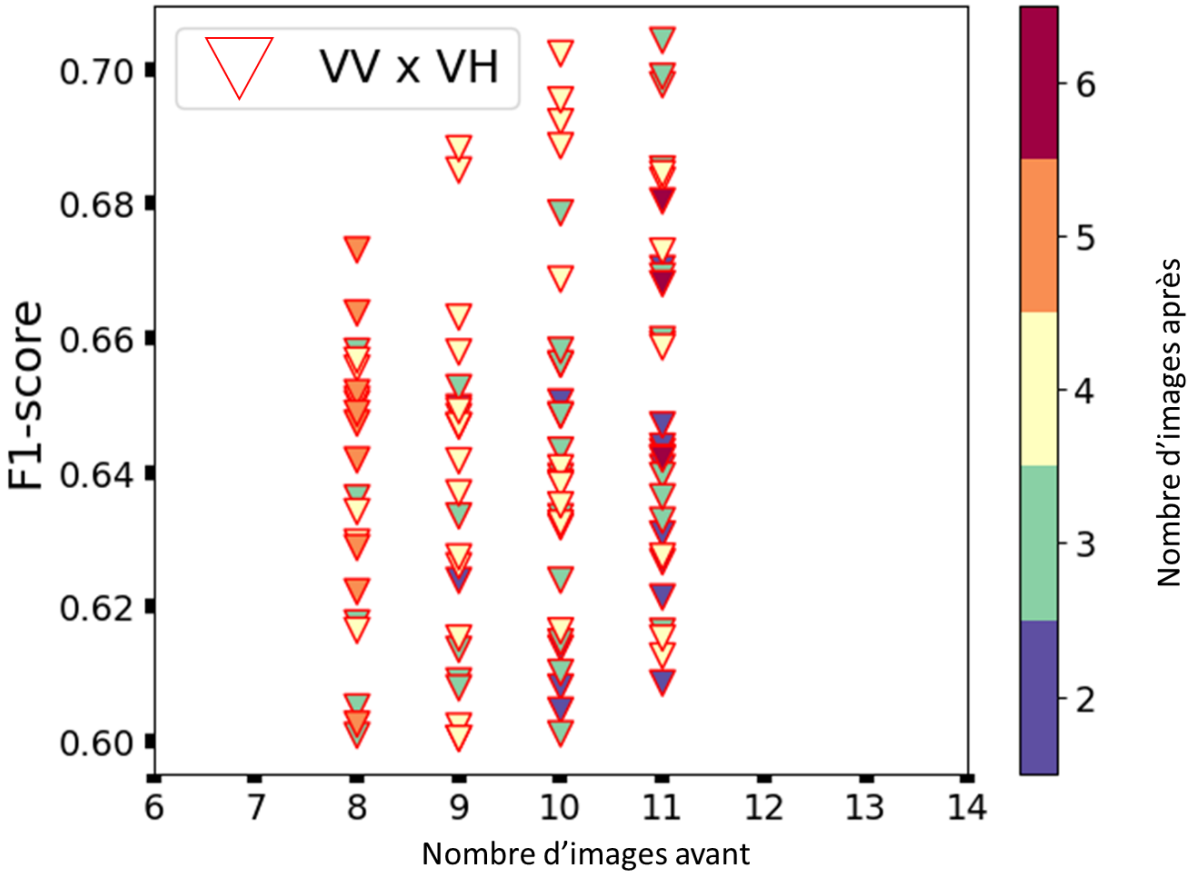

Figure VI.5: Graph of the F1-score obtained according to the values of number of images before / after the monitored date set in the parameters.

The parameters used in the NRT CuSum for this study were T_c high = 100, T_c low = 92, number of images considered in the time series before the monitored date = 11 and number of images considered in the time series after the monitored date = 3.

6.2.4.2. CuSum inter-comparison: NRT vs ReCuSum (Test site)

The ReCuSum and CuSum cross-T_c NRT were compared at the Test site. The ReCuSum is the upgraded offline version of the CuSum cross-T_c used to produce forest cover change

assessment over an extended period of time. On the Test site, the ReCuSum showed 701 ha TP for 319 ha FN compared to 731 ha TP and 290 ha FN for the NRT version.

The ReCuSum showed a precision value of 0.81, meaning that 81% of the alerts are validated changes in forest cover against 68 % for the NRT version (Table VI.2: Precision, Recall, Accuracy, F1-score and Kappa coefficient values obtained by comparing ReCuSum and CuSum NRT to the disturbance reference map.. The recall value is 68%: the ReCuSum detected 68% of the total forest cover change area to detect against 71 for the NRT version.

The Kappa coefficient value is 0.72 for the ReCuSum compared to 0.66 for the NRT version. The f1-score value is 0.74 for the ReCuSum against 0.70 for the NRT version.

	Precision (%)	Recall (%)	Accuracy (%)	F1-score	Kappa coefficient
ReCuSum 100_75	81	68	95	0.74	0.72
CuSum NRT 100_92	68	72	93	0.71	0.67

Table VI.2: Precision, Recall, Accuracy, F1-score and Kappa coefficient values obtained by comparing ReCuSum and CuSum NRT to the disturbance reference map.

6.2.5. Discussion

In this article, the CuSum cross-T_c NRT was developed and analysed. The VV, VH and VV x VH results were compared. The VV x VH map provided the best results as mentioned in (Ygorra *et al*, 2021a; Ygorra *et al*., 2021b; Ygorra et al., 2022; Ygorra *et al*, 2023). The T_c thresholds used in offline-versions were chosen in a semi-empiric way and no detailed parameter analysis was done. Both low and high T_c combinations were analysed in order to define the optimal T_c parameters for cross-T_c in NRT version. A greater value of high T_c translated into a higher f1-score. This could be interpreted as the basis for recombination needing to be as robust as possible. Low T_c analysis is more complex, as lower values lead to wider polygons of change and more connexions between polygons. The pure number of polygons also decreases, along with the number of False Negatives. A lower value also increases the number of False Positives and True Positives. A higher low T_c value reduces the polygons' width and increases the number of polygons by splitting some polygons apart. This also results in a higher FN value against a lower FP and TP values. The switching threshold between more TP against more FP seems to be at T_c

= 92, as the f1-score of low T_c < 92 or > 92 decreases. This threshold was calibrated for Brazilian Amazon forest cover change and should not be applied as 'best' in all tropical forests, even though it would work to some extent. A different climate, soil exploitation or degradation could easily alter the low T_c 'best' value for NRT cross-T_c to 90-94.

Previously, we wrote that a higher number of images considered 'after' the monitoring date resulted in a lower f1-score. Previous and unpublished results on CuSum cross-T_c offline versions showed that a longer time-series (Two years versus one year) resulted in more accurate results. The opposition between NRT and offline versions could be explained by several factors. First, the number of images before a change should be considered, as there seems to be a balance between the before / after numbers of images to successfully monitor a change. This behaviour was also seen in the offline version in the form of difficulties to detect changes occurring near the beginning / end of the time-series. Second, the stability of the time-series, shorter in NRT than in offline, may be impacted by the regrowth phenomenon. This phenomenon would result in a higher number of false positives, thus a lower f1-score value. A higher number of images taken after the monitored date would lead to a greater regrowth and a lower f1-score.

Finally, the CuSum NRT was compared to ReCuSum. The results showed a small f1-score difference between the two versions. This means that the CuSum NRT is as capable as the ReCuSum to monitor changes. This statement could be explained as ephemeral changes may not be correctly detected by the ReCuSum due to the stability of the time-series, as opposed to the shorter NRT time-series version. Thus, ReCuSum may miss the appearance and disappearance of small roads due to the regrowth of the canopy. The opposite phenomenon can also occur, as a progressive forest cover change and modification of the SAR backscatter can be seen on the offline version and not on the NRT version. The change can be too slow compared to the length of the NRT time-series and would be dismissed by the bootstrap analysis.

6.2.6. Conclusion

This study presented the development of the CuSum cross-T_c near real time version, as well as the sensitivity analysis of its input parameters. The CuSum cross-T_c NRT was designed to monitor disturbances in forest cover even during prolonged periods of cloud cover in tropical forests, the main limit of the optical systems. The NRT version was then compared to the original ReCuSum to identify the differences in detection performance. The NRT was 4% less effective than the ReCuSum, resulting in a f1-score value of 0.71 compared to 0.74 for the ReCuSum. The sensitivity analysis was conducted using Monte-Carlo's method and revealed that the CuSum-

NRT was very sensitive to the low T_c parameter. The best low and high T_c to form the cross-T_c spatial recombination were determined in this study to be 92 and 100, respectively. As for the detection delay, the analysis determined that the NRT version needed 3 images after a change to better detect it (highest f1-score). More images considered after a change led to a decline in f1-scores. The number of images to take before a change into the time-series is correlated to the number of images taken after a change. Too few images would create an unstable time-series that is more prone to false positives, whereas too many images would hinder the detection of small changes, as well as getting near to the offline time-series in terms of length. In this study, considering all 11 images in the time-series before a change gave the better f1-score.

A possible upgrade to the CuSum-NRT version would be to implement a Bayesian update system after the first detection with increasing probabilities of being a real change.

Research should be conducted on multi-scale detection and fusion. Algorithms currently working at high resolution should be also implemented on aggregated images with degraded resolution in order to alter the scale of the detections.

6.2.7. References

Arikawa, Y. et al. (2014) 'ALOS-2 launch and early orbit operation result', in 2014 IEEE geoscience and remote sensing symposium. IEEE, pp. 3406–3409.

Assunção, J., Gandour, C. and Rocha, R. (2017) 'DETERring deforestation in the Amazon: environmental monitoring and law enforcement'.

Ballère, M. et al. (2021) 'SAR data for tropical forest disturbance alerts in French Guiana: Benefit over optical imagery', Remote Sensing of Environment, 252. Available at: https://doi.org/10.1016/j.rse.2020.112159.

Bouvet, A. et al. (2018) 'Use of the SAR shadowing effect for deforestation detection with Sentinel-1 time series', Remote Sensing, 10(8), pp. 1–19. Available at: https://doi.org/10.3390/rs10081250.

Bunting, P. et al. (2022) 'Global Mangrove Extent Change 1996–2020: Global Mangrove Watch Version 3.0', Remote Sensing, 14(15), p. 3657. Available at: https://doi.org/10.3390/rs14153657.

Creese, A., Washington, R. and Jones, R. (2019) 'Climate change in the Congo Basin: processes related to wetting in the December–February dry season', Climate Dynamics, 53(5–6), pp. 3583–3602. Available at: https://doi.org/10.1007/s00382-019-04728-x.

Diniz, C.G. et al. (2015) 'DETER-B: The New Amazon Near Real-Time Deforestation Detection System', IEEE Journal of Selected Topics in Applied Earth Observations and Remote Sensing, 8(7), pp. 3619–3628. Available at: https://doi.org/10.1109/JSTARS.2015.2437075.

Doblas, J. et al. (2020) 'Optimizing near real-time detection of deforestation on tropical rainforests using sentinel-1 data', Remote Sensing, 12(23), pp. 1–31. Available at: https://doi.org/10.3390/rs12233922.

Doblas, J. et al. (2022) 'DETER-R: An Operational Near-Real Time Tropical Forest Disturbance Warning System Based on Sentinel-1 Time Series Analysis', Remote Sensing, 14(15), p. 3658. Available at: https://doi.org/10.3390/rs14153658.

Fan, L. et al. (2019) 'Satellite-observed pantropical carbon dynamics', Nature Plants, 5(9), pp. 944–951. Available at: https://doi.org/10.1038/s41477-019-0478-9.

Federici, S. et al. (2015) 'New estimates of CO2 forest emissions and removals: 1990-2015', Forest Ecology and Management, 352(September), pp. 89–98. Available at: https://doi.org/10.1016/j.foreco.2015.04.022.

Gatti, L.V. et al. (2021) 'Amazonia as a carbon source linked to deforestation and climate change', Nature, 595(7867), pp. 388–393.

Hamunyela, E. et al. (2020) 'Implementation of BFASTmonitor Algorithm on Google Earth Engine to support large-area and sub-annual change monitoring using earth observation data', Remote Sensing, 12(18). Available at: https://doi.org/10.3390/RS12182953.

Hansen, M.C. et al. (2013) 'High-resolution global maps of 21st-century forest cover change', Science, 342(6160), pp. 850–853. Available at: https://doi.org/10.1126/science.1244693.

Hansen, M.C. et al. (2016) 'Humid tropical forest disturbance alerts using Landsat data', Environmental Research Letters, 11(3). Available at: https://doi.org/10.1088/1748-9326/11/3/034008.

Harris, N.L. et al. (2021) 'Global maps of twenty-first century forest carbon fluxes', Nature Climate Change, 11(3), pp. 234–240. Available at: https://doi.org/10.1038/s41558-020-00976-6.

Joshi, N. et al. (2015) 'Mapping dynamics of deforestation and forest degradation in tropical forests using radar satellite data', Environmental Research Letters, 10(3). Available at: https://doi.org/10.1088/1748-9326/10/3/034014.

Kleinschroth, F. et al. (2019) 'Road expansion and persistence in forests of the Congo Basin', Nature Sustainability, 2(7), pp. 628–634. Available at: https://doi.org/10.1038/s41893-019-0310-6.

Lescuyer, G. et al. (2011) The domestic market for smallscale chainsaw milling in Gabon: Present situation, opportunities and challenges. CIFOR.

Manogaran, G. and Lopez, D. (2018) 'Spatial cumulative sum algorithm with big data analytics for climate change detection', Computers and Electrical Engineering, 65, pp. 207–221. Available at: https://doi.org/10.1016/j.compeleceng.2017.04.006.

Mermoz, S. et al. (2021) 'Continuous Detection of Forest Loss in Vietnam, Laos, and Cambodia Using Sentinel-1 Data', Remote Sensing, 13(23), p. 4877. Available at: https://doi.org/10.3390/rs13234877.

Mistry, J. et al. (2021) 'Covid-19 impacts on Indigenous food sovereignty, livelihoods and biodiversity, Guyana', Report published by … [Preprint].

Olofsson, P. et al. (2014) 'Good practices for estimating area and assessing accuracy of land change', Remote Sensing of Environment, 148, pp. 42–57. Available at: https://doi.org/10.1016/j.rse.2014.02.015.

Qin, Y. et al. (2021) 'Carbon loss from forest degradation exceeds that from deforestation in the Brazilian Amazon', Nature Climate Change, 11(5), pp. 442–448. Available at: https://doi.org/10.1038/s41558-021-01026-5.

Reiche, J. et al. (2021) 'Forest disturbance alerts for the Congo Basin using Sentinel-1', Environmental Research Letters, 16(2), p. 024005. Available at: https://doi.org/10.1088/1748-9326/abd0a8.

Ruiz-Ramos, J. et al. (2020) 'Continuous forest monitoring using cumulative sums of sentinel-1 timeseries', Remote Sensing, 12(18). Available at: https://doi.org/10.3390/RS12183061.

Torres, R. et al. (2012) 'GMES Sentinel-1 mission', Remote Sensing of Environment, 120, pp. 9–24. Available at: https://doi.org/10.1016/j.rse.2011.05.028.

Turubanova, S. et al. (2018) 'Ongoing primary forest loss in Brazil, Democratic Republic of the Congo, and Indonesia', Environmental Research Letters, 13(7), pp. 2000–2010. Available at: https://doi.org/10.1088/1748-9326/aacd1c.

Umunay, P.M. et al. (2019) 'Selective logging emissions and potential emission reductions from reduced-impact logging in the Congo Basin', Forest Ecology and Management, 437, pp. 360–371.

Watanabe, M. et al. (2017) 'Development of early-stage deforestation detection algorithm (advanced) with PALSAR-2/ScanSAR for JICA-JAXA program (JJ-FAST)', in International Geoscience and Remote Sensing Symposium (IGARSS). Institute of Electrical and Electronics Engineers Inc., pp. 2446–2449. Available at: https://doi.org/10.1109/IGARSS.2017.8127487.

Watanabe, M. et al. (2018) 'Early-stage deforestation detection in the tropics with L-band SAR', IEEE Journal of Selected Topics in Applied Earth Observations and Remote Sensing, 11(6), pp. 2127–2133. Available at: https://doi.org/10.1109/JSTARS.2018.2810857.

Watanabe, M. et al. (2021) 'Refined algorithm for forest early warning system with ALOS-2/PALSAR-2 ScanSAR data in tropical forest regions', Remote Sensing of Environment, 265, p. 112643. Available at: https://doi.org/10.1016/j.rse.2021.112643.

Weisse, M. et al. (2019) 'Use of Near-Real-Time Deforestation Alerts'.

Ygorra, B., Frappart, F., Wigneron, J., et al. (2021) 'Deforestation Monitoring Using Sentinel-L SAR Images in Humid Tropical Areas', in 2021 IEEE International Geoscience and Remote Sensing Symposium IGARSS, pp. 5957–5960. Available at: https://doi.org/10.1109/IGARSS47720.2021.9554698.

Ygorra, B., Frappart, F., Wigneron, J.P., et al. (2021) 'Monitoring loss of tropical forest cover from Sentinel-1 time-series: A CuSum-based approach', International Journal of Applied Earth Observation and Geoinformation, 103, p. 102532. Available at: https://doi.org/10.1016/j.jag.2021.102532.

Ygorra, B. et al. (2022) 'Classification and Deforestation Monitoring Using Sentinel-1 C-SAR Images in a Temperate Exploited Pine Forest', in IGARSS 2022-2022 IEEE International Geoscience and Remote Sensing Symposium. IEEE, pp. 691–694.

Ygorra B., Frappart F.,. Wigneron J.P.,. Moisy C.,. Catry T.,. Pillot B.,. Kharlanova A. Riazanoff, S. (2023) 'ReCuSum, a polyvalent method to monitor tropical forest disturbances', International Society for Photogrammetry and Remote Sensing, in press.

6.3. Contribution and perspectives

This study demonstrated that the NRT version of the CuSum was very sensitive to the low T_c used in the cross-T_c spatial recombination. The importance of the number of images in the length of the time-series before / after a change was also significant. This study also showed that the NRT version produced similar results to the ReCuSum version, with a minimal difference of 0.04 in f1-score.

The results obtained from the comparison between RADD, DETER-R, DETER-B, PRODES, JJ-FAST and CuSum-NRT will be later added to this chapter in the manuscript.

CHAPTER VII.

CONCLUSION AND PERSPECTIVES

Table of contents

Chapters VII. Conclusion and perspectives

7.1. Conclusion

My PhD thesis work focused on the development of a new approach to monitor changes in tropical forest cover using Sentinel-1 C-band SAR data (Torres et al., 2012). This was a requirement from VisioTerra for a future use of my developments in a NRT deforestation system. Two different types of change detection algorithms were developed: offline breakpoint algorithms requiring long time-series, and Near-Real-Time (NRT, online) algorithm requiring shorter time-series. I first worked on the analysis of the potential of the Cumulative Sum algorithm (CuSum, (Kellndorfer, 2019; Manogaran and Lopez, 2018; Ruiz-Ramos et al., 2020) for such application, estimating its performance in terms of the detection of changes in the forest cover. This method is based on the estimation of a confidence level (CL) by applying a bootstrap analysis to the time-series, to validate the estimated breakpoint. The Critical Threshold (T_c) is the main input parameter based on the value of the confidence level. All pixels showing a CL < T_c are removed. The CuSum was first tested in the forest concession of *Alibuku*, in the Democratic Republic of the Congo. The results showed that a high T_c value resulted in many false negatives and few false positives, opposite of a low T_c value that resulted in few false negatives but many false positives.

Next, I improved the original CuSum, which was only based on the temporal dimension, by conducting a spatial recombination of high T_c with low T_c result maps of change, called cross-T_c. This recombination keeps the low-T_c polygons which show at least one intersection with a high-T_c polygon. This step allowed to remove the low-T_c polygons constituting the false positives, and to keep only those that have a robust base of high-T_c. The base CuSum is a single-breakpoint algorithm. The continuity of my work consisted of changing the single-breakpoint nature of the algorithm to multiple-breakpoint and build better estimates of disturbance in the forest canopy. Finally, I developed a NRT version of the CuSum cross-T_c and compared its detection performance with other operational NRT algorithms developed by (Diniz et al., 2015; Doblas et al., 2022; Hansen et al., 2013; Reiche et al., 2021; Wheeler et al., 2014) on a study area of 6,855 km² located in the Brazilian Amazon. The results will be presented during the defence and added later to the manuscript.

In the first tested area, the forest concession *Alibuku* in Democratic Republic of the Congo, each polarisation was tested and the intersection of the results maps from both VV and VH polarisations was evaluated. The CuSum cross-T_c 100_75 provided the best results with the VV x VH intersection map of results (Kappa coefficient: 0.59, Precision: 0.77, Accuracy: 0.91, Recall: 0.55). Another major finding was revealed during this study, as the date of change data hinted

that the algorithm was detecting degradation before actual deforestation. These degradations may be invisible to optical sensors as it can happen beneath the canopy (Reiche et al., 2021). Small degradations opening the canopy may also be undetectable between two available optical images as the fast regrowth happening in these biomes may have closed the canopy gap (Reiche et al., 2021). The major drawback of this approach was the limitation of the single-breakpoint algorithm. The status of a pixel did not change over time once it was detected as 'change' or 'not change'. In order to solve that issue, ReCuSum was developed.

To overcome the single-breakpoint limitations of the CuSum cross-T_c, I developed the ReCuSum, a multiple-breakpoints detection algorithm and tested it in a study area near the study zone used for the algorithm comparison, located in the Brazilian Amazon. It is based on a recursive iteration of the CuSum cross-T_c, splitting time-series into two independent time-series at the validated date of change. A key finding of this study was that the CuSum cross-T_c was capable to detect accurately non-forest vegetation (90% recall, 0.63 f1-score). I applied it to create a non-forest vegetation mask to remove changes found on these areas, calling this step rm_hist (remove_history). The ReCuSum map of number of changes could also be used to differentiate changes occurring on forested areas from changes occurring on non-forested vegetation areas. This was achieved by applying a threshold based on the number of changes in the VH at T_c 100 and VH at T_c 95 maps of number of changes, called T_{nbc}. The ReCuSum achieved a precision of 81%, a recall of 68% and a f1-score of 0.74 for the VV x VH combination at cross-T_c 100_75. The application of both T_{nbc} and rm_hist led to an average 16% underestimation of the disturbances in forest cover, whereas the application of only rm_hist resulted in an average 10% overestimation of disturbances in forest cover. The application of T_{nbc} greatly decreases the number of false positives at the cost of false negatives. The ReCuSum showed a limitation due to the instability of time-series showing transitional regrowth, leading to an abnormal number of detected changes. In order to eliminate this artefact, increasing the length of the time-series would work, as a stability period would be present after the transition periods. Thus, the ReCuSum method was found unsuitable for near-real-time monitoring because it provided better results using longer time-series. Long time-series are needed to better differentiate between changes in non-forest vegetation and changes in forested areas.

I based the development of the NRT version of the CuSum on the cross-T_c version. The mask step described above was added to the cross-T_c version for NRT monitoring. I conducted the Monte-Carlo's analysis on the T_c parameters as well as the number of images to consider before a change / after a change. The best results were obtained using cross-T_c 100_92 with 11 images

before a change and 3 images after, with a 0.70 f1-score. The algorithm was found to be highly sensitive to the low T_c value at this length of time-series. The series being shorter, it is more unstable, leading to higher low T_c value being more accurate. The comparison of the results obtained by this method with the ReCuSum results, it is possible to see an overall similar F1-score (0.74 for ReCuSum, 0.71 for CuSum-NRT). The CuSum-NRT has more false positives than ReCuSum, but detects more of the disturbed area (0.72 Recall for CuSum-NRT against 0.68 for ReCuSum).

7.2. Perspectives

7.2.1. Understanding C-SAR response to forest degradations

During this PhD, we obtained forest disturbance detection maps using the CuSum-based algorithms and reference maps made through visual interpretation. Sometimes, there were detections with coherent structure and localisation in the CuSum result map that did not appear in the reference map. These detections were too coherent to be simply dismissed as false positives. Sometimes, the images used to form the reference map are very spaced in time and can miss small degradation events (Reiche et al., 2021). As we lacked in-situ evidence that the detected disturbances were true degradations, we considered these changes as false positives, with the hypothesis that such events are degradations. The C-SAR based algorithms can monitor forest degradations unseen by optical means, meaning the reference maps made through visual interpretation will always lack some disturbances.

Radar backscatter values seem to decrease in both degradation and deforestation event. But as highlighted in Chapter IV, degradation events are more detected using the VH polarisation than using the VV polarisation. The opposite occurs for the VV polarisation: clear-cut deforestation events are more detected using it than using the VH polarisation. These results mean that clear-cut deforestation and degradation affect differently the backscatter. As the VH polarisation is more linked with volume changes and the VV polarisation with surface changes (Kellndorfer, 2019), we can make the following hypothesis:

- Degradation events affect the penetration of C-band by creating gaps in the canopy, reducing the volume backscatter but affecting less the surface backscatter
- Clear-cut events affect more the surface backscatter, transitioning from ‘forest canopy’ surface backscatter to ‘Rough transitioning soil’ surface backscatter.

7.2.2. Fusion of operational methods based on Sentinel-1

Currently, there are multiple algorithms based on Sentinel-1 images analysis working operationally on the Brazilian Amazon. Those algorithms work separately and are freely available. As they rely on different methods for the analysis, each produces different results. The nature of the detection should be analysed with in-situ data to understand the strength and weaknesses of each algorithm in the categories of detection: forest clear-cut for agricultural use, illegal mining operation, degradation by selective logging, ... The algorithms could be complementary in the different categories, thus, the fusion of the results from these algorithms should be conducted.

This fusion would result in a map of probability of detection, with each algorithm weighting in the probability system according to their overall precision.

7.2.3. On CuSum utility

7.2.3.1. CuSum for forest monitoring: upgrades

In this PhD thesis, we showed the potential of the CuSum based on Sentinel-1 data in terms of forest disturbance monitoring. We found some post-processing steps enhancing the results, such as the cross-T_c spatial recombination to reduce the number of false positives of lower T_c values and reduce the number of false negatives of high T_c values. The CuSum cross-T_c is an algorithm based on time-series of images, as it uses information from the space dimension.

Thus, CuSum cross-T_c is an algorithm applicable to all time-series of images. It is not applicable only to Sentinel-1 VV and VH data. Further tests should be performed on the polarisation ratio $\frac{\sigma^0_{VV}}{\sigma^0_{VH}}$, the Normalised Difference Index NDI applied on Sentinel-1 data $\frac{\sigma^0_{VV} - \sigma^0_{VH}}{\sigma^0_{VV} + \sigma^0_{VH}}$.

Further testing should be also done on the potential of the cross-T_c CuSum to detect forest disturbances based on L-band SAR data and on HH, HV polarisations.

The CuSum cross-T_c should also be tried on different optical indexes and bands, such as the Normalized Difference Vegetation Index (NDVI), or on the thermal InfraRed, known to be sensitive to vegetation changes. Algorithms based on the fusion of optical and SAR data have already been developed and tested (Hamunyela et al., 2017; Reiche et al., 2018a). In the aforementioned study, the fusion increased the statistics compared to only optical or SAR inputs, along with the temporal resolution, reducing the detection delays.

In the case of the CuSum cross-T_c, the crossing of these results may further enhance the quality of the results, but at the cost of computational time.

7.2.3.2. CuSum application to inundation monitoring

Other results, highlighted in Ygorra *et al.*, 2022, demonstrated the possibility of using the CuSum cross-T_c on Sentinel-1 images to monitor ephemeral lakes and inundations. This hypothesis is backed by similar results seen in the Amazon region, as changes were systematically detected in the river bends. These events were detected at the same time in different locations of the river. Inundations can impact the soil moisture durably, leading to a persistent change in the C-band backscatter that would be detected by the CuSum. These results should be confirmed and further tested, to qualify the sensitivity level of the CuSum to moisture changes.

7.2.3.3. CuSum for agricultural use?

The high number of changes in ReCuSum's non-forest change class can be attributed to vegetation regrowth. In the case of monitoring forest disturbances, we dismissed such pixels as false positives. Further research with in-situ data should be conducted to determine the nature of the correlation between the number of changes found and the regrowth. There are several explanations possible, as the CuSum needs at least part of the time-series to be stable. The first hypothesis is that the number of changes in the case of regrowth is an artefact caused by the backscatter time-series values ever increasing, not letting a period to be stable long enough. This hypothesis can be checked by increasing the length of the time-series to reach the 'plateau' of saturation. Another explanation would be the cyclic character of agriculture with fast regrowth in tropical regions. The capabilities of the CuSum in terms of agricultural use should be assessed with strong in-situ data on a long period.

References

Achard, F. et al. (2007) 'Pan-tropical monitoring of deforestation', Environmental Research Letters, 2(4), p. 045022. Available at: https://doi.org/10.1088/1748-9326/2/4/045022.

Almeida-Filho, R. et al. (2005) 'Evaluation and perspectives of using multitemporal L-band SAR data to monitor deforestation in the Brazilian Amazo/spl circ/nia', IEEE Geoscience and Remote Sensing Letters, 2(4), pp. 409–412. Available at: https://doi.org/10.1109/LGRS.2005.856679.

Almeida-Filho, R. et al. (2009) 'Using dual-polarized ALOS PALSAR data for detecting new fronts of deforestation in the Brazilian Amazônia', International Journal of Remote Sensing, 30(14), pp. 3735–3743. Available at: https://doi.org/10.1080/01431160902777175.

Alpers, W. and Melsheimer, C. (2004) 'Rainfall', Synthetic Aperture Radar marine user's manual, pp. 355–371.

Andersen, H.-E., Reutebuch, S.E. and McGaughey, R.J. (2006) 'Active remote sensing', in Computer applications in sustainable forest management. Springer, pp. 43–66.

Antropov, O. et al. (2016) 'Mapping forest disturbance using long time series of Sentinel-1 data: Case studies over boreal and tropical forests', in 2016 IEEE International Geoscience and Remote Sensing Symposium (IGARSS), pp. 3906–3909. Available at: https://doi.org/10.1109/IGARSS.2016.7730014.

Arikawa, Y. et al. (2014) 'ALOS-2 launch and early orbit operation result', in 2014 IEEE geoscience and remote sensing symposium. IEEE, pp. 3406–3409.

Assunção, J., Gandour, C. and Rocha, R. (2017) 'DETERring deforestation in the Amazon: environmental monitoring and law enforcement'.

Avtar, R. et al. (2012) 'Characterization of forests and deforestation in Cambodia using ALOS/PALSAR observation', Geocarto International, 27(2), pp. 119–137. Available at: https://doi.org/10.1080/10106049.2011.626081.

Ballère, M., Bouvet, A., Mermoz, S., Le Toan, T., Koleck, T., Bedeau, C., André, M., Forestier, E., Frison, P.-L., et al. (2021) 'SAR data for tropical forest disturbance alerts in French Guiana: Benefit over optical imagery', Remote Sensing of Environment, 252, p. 112159. Available at: https://doi.org/10.1016/j.rse.2020.112159.

Balzter, H. (2001) 'Forest mapping and monitoring with interferometric synthetic aperture radar (InSAR)', Progress in Physical Geography: Earth and Environment, 25(2), pp. 159–177. Available at: https://doi.org/10.1177/030913330102500201.

Bamler, R. and Hartl, P. (1998) 'Synthetic aperture radar interferometry', Inverse Problems, 14(4), pp. R1–R54. Available at: https://doi.org/10.1088/0266-5611/14/4/001.

Belenguer-Plomer, M.A., Chuvieco, E. and Tanase, M.A. (2019) 'Temporal decorrelation of c-band backscatter coefficient in mediterranean burned areas', Remote Sensing, 11(22), pp. 1–19. Available at: https://doi.org/10.3390/rs11222661.

Bouvet, A. et al. (2018) 'Use of the SAR shadowing effect for deforestation detection with Sentinel-1 time series', Remote Sensing, 10(8), pp. 1–19. Available at: https://doi.org/10.3390/rs10081250.

Brodu, N. (2018) 'Low-rankness transfer for denoising Sentinel-1 SAR images', 9th International Symposium on Signal, Image, Video and Communications, ISIVC 2018 - Proceedings, pp. 106–111. Available at: https://doi.org/10.1109/ISIVC.2018.8709210.

Buchhorn, M. et al. (2020) 'Copernicus Global Land Service: Land Cover 100m: Collection 3: epoch 2015: Globe (Version V3.0.1)', Zenodo, pp. 1–14.

Bujor, F.T. et al. (2001) 'Data fusion approach for change detection in multi-temporal ERS-SAR images', in IGARSS 2001. Scanning the Present and Resolving the Future. Proceedings. IEEE 2001 International Geoscience and Remote Sensing Symposium (Cat. No.01CH37217). IGARSS 2001. Scanning the Present and Resolving the Future. Proceedings. IEEE 2001 International Geoscience and Remote Sensing Symposium (Cat. No.01CH37217), pp. 2590–2592 vol.6. Available at: https://doi.org/10.1109/IGARSS.2001.978098.

Bullock, E.L. et al. (2020) 'Satellite-based estimates reveal widespread forest degradation in the Amazon', Global Change Biology, 26(5), pp. 2956–2969.

Bunting, P. et al. (2022) 'Global Mangrove Extent Change 1996–2020: Global Mangrove Watch Version 3.0', Remote Sensing, 14(15), p. 3657. Available at: https://doi.org/10.3390/rs14153657.

da C.F. Yanasse, C. et al. (1997) 'Exploratory study of the relationship between tropical forest regeneration stages and SIR-C L and C data', Remote Sensing of Environment, 59(2), pp. 180–190. Available at: https://doi.org/10.1016/S0034-4257(96)00149-6.

Coelho, L.P. (2013) 'Mahotas: Open source software for scriptable computer vision', Journal of Open Research Software, 1(1), p. e3. Available at: https://doi.org/10.5334/jors.ac.

Contreras-Hermosilla, A. (2000) The underlying causes of forest decline. CIFOR Jakarta, Indonesia.

Creese, A., Washington, R. and Jones, R. (2019) 'Climate change in the Congo Basin: processes related to wetting in the December–February dry season', Climate Dynamics, 53(5–6), pp. 3583–3602. Available at: https://doi.org/10.1007/s00382-019-04728-x.

DeFries, R.S. et al. (2002) 'Carbon emissions from tropical deforestation and regrowth based on satellite observations for the 1980s and 1990s', Proceedings of the National Academy of Sciences, 99(22), pp. 14256–14261. Available at: https://doi.org/10.1073/pnas.182560099.

Deutscher, J. et al. (2017) 'Humid tropical forest monitoring with multi-temporal L-, C- and X-band SAR data', 2017 9th International Workshop on the Analysis of Multitemporal Remote Sensing Images, MultiTemp 2017, pp. 1–4. Available at: https://doi.org/10.1109/Multi-Temp.2017.8035264.

Diniz, C.G. et al. (2015) 'DETER-B: The New Amazon Near Real-Time Deforestation Detection System', IEEE Journal of Selected Topics in Applied Earth Observations and Remote Sensing, 8(7), pp. 3619–3628. Available at: https://doi.org/10.1109/JSTARS.2015.2437075.

Doblas, J., Shimabukuro, Y., Sant'anna, S., et al. (2020) 'Optimizing near real-time detection of deforestation on tropical rainforests using sentinel-1 data', Remote Sensing, 12(23), pp. 1–31. Available at: https://doi.org/10.3390/rs12233922.

Doblas, J. et al. (2022) 'DETER-R: An Operational Near-Real Time Tropical Forest Disturbance Warning System Based on Sentinel-1 Time Series Analysis', Remote Sensing, 14(15), p. 3658. Available at: https://doi.org/10.3390/rs14153658.

Dostálová, A. et al. (2021) 'European wide forest classification based on sentinel-1 data', Remote Sensing, 13(3), pp. 1–27. Available at: https://doi.org/10.3390/rs13030337.

Durieux, A.M.S. et al. (2020) 'BUDD: Multi-modal Bayesian Updating Deforestation Detections', in IGARSS 2020 - 2020 IEEE International Geoscience and Remote Sensing Symposium. IGARSS 2020 - 2020 IEEE International Geoscience and Remote Sensing Symposium, pp. 6638–6641. Available at: https://doi.org/10.1109/IGARSS39084.2020.9323938.

Durieux, A.M.S. et al. (2021) 'Expanding SAR-based probabilistic deforestation detections using deep learning', in Applications of Machine Learning 2021. Applications of Machine Learning 2021, SPIE, pp. 24–31. Available at: https://doi.org/10.1117/12.2594031.

Duveiller, G. et al. (2008) 'Deforestation in Central Africa: Estimates at regional, national and landscape levels by advanced processing of systematically-distributed Landsat extracts',

Remote Sensing of Environment, 112(5), pp. 1969–1981. Available at: https://doi.org/10.1016/j.rse.2007.07.026.

Elachi, C. (1988) 'Spaceborne radar remote sensing: applications and techniques', New York [Preprint].

Fan, L. et al. (2019) 'Satellite-observed pantropical carbon dynamics', Nature Plants, 5(9), pp. 944–951. Available at: https://doi.org/10.1038/s41477-019-0478-9.

Federici, S. et al. (2015) 'New estimates of CO2 forest emissions and removals: 1990-2015', Forest Ecology and Management, 352(September), pp. 89–98. Available at: https://doi.org/10.1016/j.foreco.2015.04.022.

Feng, Y. et al. (2022) 'Doubling of annual forest carbon loss over the tropics during the early twenty-first century', Nature Sustainability, 5(5), pp. 444–451. Available at: https://doi.org/10.1038/s41893-022-00854-3.

Filipponi, F. (2019) 'Sentinel-1 GRD Preprocessing Workflow', p. 4.

Flores, A. et al. (2019) 'SAR Handbook: Comprehensive Methodologies for Forest Monitoring and Biomass Estimation', THE SAR HANDBOOK Comprehensive Methodologies for Forest Monitoring and Biomass Estimation, pp. 1–307. Available at: https://doi.org/10.25966/nr2c-s697.

Fransson, J.E.S. et al. (2007) 'Detection of forest changes using ALOS PALSAR satellite images', in 2007 IEEE International Geoscience and Remote Sensing Symposium. 2007 IEEE International Geoscience and Remote Sensing Symposium, pp. 2330–2333. Available at: https://doi.org/10.1109/IGARSS.2007.4423308.

Frost, V.S. et al. (1982) 'A model for radar images and its application to adaptive digital filtering of multiplicative noise', IEEE Transactions on pattern analysis and machine intelligence, (2), pp. 157–166.

Gatti, L.V. et al. (2021) 'Amazonia as a carbon source linked to deforestation and climate change', Nature, 595(7867), pp. 388–393.

Gaveau, D.L.A., Balzter, H. and Plummer, S. (2003) 'Forest woody biomass classification with satellite-based radar coherence over 900 000 km2 in Central Siberia', Forest Ecology and Management, 174(1), pp. 65–75. Available at: https://doi.org/10.1016/S0378-1127(02)00028-2.

Giordano, S. (2015) Démélange d'images radar polarimétrique par séparation thématique de sources. PhD Thesis. Paris Est.

Goodman, J.W. (1975) 'Statistical properties of laser speckle patterns', in Laser speckle and related phenomena. Springer, pp. 9–75.

Gower, S.T. (2003) 'Patterns and Mechanisms of the Forest Carbon Cycle'. Available at: https://minds.wisconsin.edu/handle/1793/34242 (Accessed: 30 August 2022).

Grace, J., Mitchard, E. and Gloor, E. (2014) 'Perturbations in the carbon budget of the tropics', Global Change Biology, 20(10), pp. 3238–3255. Available at: https://doi.org/10.1111/gcb.12600.

Green, R.M. (1998) 'Relationships between polarimetric SAR backscatter and forest canopy and sub-canopy biophysical properties', International Journal of Remote Sensing, 19(12), pp. 2395–2412. Available at: https://doi.org/10.1080/014311698214794.

Grover, K.D. and Quegan, S. (1995) 'ERS-1 observations and potential for use in tropical forest monitoring', in 1995 International Geoscience and Remote Sensing Symposium, IGARSS '95. Quantitative Remote Sensing for Science and Applications. 1995 International Geoscience and Remote Sensing Symposium, IGARSS '95. Quantitative Remote Sensing for Science and Applications, pp. 1210–1212 vol.2. Available at: https://doi.org/10.1109/IGARSS.1995.521186.

Haarpaintner, J. and Hindberg, H. (2019) 'Multi-temporal and multi-frequency sar analysis for forest land cover mapping of the Mai-Ndombe district (Democratic Republic of Congo)', Remote Sensing, 11(24). Available at: https://doi.org/10.3390/rs11242999.

Hamunyela, E. et al. (2020) 'Implementation of BFASTmonitor Algorithm on Google Earth Engine to support large-area and sub-annual change monitoring using earth observation data', Remote Sensing, 12(18). Available at: https://doi.org/10.3390/RS12182953.

Hamunyela, E., Herold, M. and Verbesselt, J. (2017) Space-time monitoring of tropical forest changes using observations from multiple satellites. Ph.D. Thesis, Wageningen University & Research, Laboratory of Geo-information Science and Remote Sensing, Wageningen, The Netherlands. Available at: http://search.ebscohost.com/login.aspx?direct=true&db=edsbas&AN=edsbas.8D6F26D9&site=eds-live&scope=site.

Hamunyela, E., Verbesselt, J. and Herold, M. (2016) 'Using spatial context to improve early detection of deforestation from Landsat time series', Remote Sensing of Environment, 172, pp. 126–138. Available at: https://doi.org/10.1016/j.rse.2015.11.006.

Hansen, M.C. et al. (2008) 'A method for integrating MODIS and Landsat data for systematic monitoring of forest cover and change in the Congo Basin', Remote Sensing of Environment, 112(5), pp. 2495–2513. Available at: https://doi.org/10.1016/j.rse.2007.11.012.

Hansen, M.C. et al. (2013) 'High-resolution global maps of 21st-century forest cover change', Science, 342(6160), pp. 850–853. Available at: https://doi.org/10.1126/science.1244693.

Hansen, M.C. et al. (2016) 'Humid tropical forest disturbance alerts using Landsat data', Environmental Research Letters, 11(3). Available at: https://doi.org/10.1088/1748-9326/11/3/034008.

Hanssen, R.F. (2001) Radar interferometry: data interpretation and error analysis. Springer Science & Business Media.

Haralick, Robert M., Shanmugam, K. and Dinstein, I. (1973) 'Textural Features for Image Classification', IEEE Transactions on Systems, Man, and Cybernetics, SMC-3(6), pp. 610–621. Available at: https://doi.org/10.1109/TSMC.1973.4309314.

Haralick, Robert M, Shanmugam, K. and Dinstein, I.H. (1973) 'Textural features for image classification', IEEE Transactions on systems, man, and cybernetics, (6), pp. 610–621.

Harris, N.L. et al. (2021) 'Global maps of twenty-first century forest carbon fluxes', Nature Climate Change, 11(3), pp. 234–240. Available at: https://doi.org/10.1038/s41558-020-00976-6.

Hirschmugl, M. et al. (2017) 'Combined use of SAR and optical time series data for near real-time forest disturbance mapping', 2017 9th International Workshop on the Analysis of Multitemporal Remote Sensing Images, MultiTemp 2017, pp. 0–3. Available at: https://doi.org/10.1109/Multi-Temp.2017.8035208.

Hoang, N.T. and Kanemoto, K. (2021) 'Mapping the deforestation footprint of nations reveals growing threat to tropical forests', Nature Ecology & Evolution, 5(6), pp. 845–853. Available at: https://doi.org/10.1038/s41559-021-01417-z.

Hoekman, D. (2000) 'Monitoring tropical forests using synthetic aperture radar', in INDREX (Indonesian Radar Experiment) Final Results Workshop, p. 11.

Hoekman, D. et al. (2020) 'Wide-area near-real-time monitoring of tropical forest degradation and deforestation using sentinel-1', Remote Sensing, 12(19), pp. 1–32. Available at: https://doi.org/10.3390/rs12193263.

Houghton, R.A. et al. (2012) 'Carbon emissions from land use and land-cover change', Biogeosciences, 9(12), pp. 5125–5142. Available at: https://doi.org/10.5194/bg-9-5125-2012.

Igarashi, T. et al. (2003) 'Preliminary study on data sets of ADEOS-II and ALOS dedicated to terrestrial carbon observation', Advances in Space Research, 32(11), pp. 2147–2152. Available at: https://doi.org/10.1016/S0273-1177(03)90536-9.

Joshi, N. et al. (2015) 'Mapping dynamics of deforestation and forest degradation in tropical forests using radar satellite data', Environmental Research Letters, 10(3). Available at: https://doi.org/10.1088/1748-9326/10/3/034014.

Karra, K. et al. (2021) 'Global land use/land cover with Sentinel 2 and deep learning', in 2021 IEEE International Geoscience and Remote Sensing Symposium IGARSS, pp. 4704–4707.

Keil, M., Scales, D. and Winter, R. (1995) 'Investigation of forest areas in Germany and Brazil using SAR data of the SIR-C/X-SAR and other SAR missions', in 1995 International Geoscience and Remote Sensing Symposium, IGARSS '95. Quantitative Remote Sensing for Science and Applications. 1995 International Geoscience and Remote Sensing Symposium, IGARSS '95. Quantitative Remote Sensing for Science and Applications, pp. 997–999 vol.2. Available at: https://doi.org/10.1109/IGARSS.1995.521119.

Kellndorfer, J. (2019) 'Using SAR data for mapping deforestation and forest degradation', in THE SAR HANDBOOK Comprehensive Methodologies for Forest Monitoring and Biomass Estimation. ServirGlobal : Huntsville, AL, pp. 65–79.

Kim, Y. and van Zyl, J.J. (2009) 'A Time-Series Approach to Estimate Soil Moisture Using Polarimetric Radar Data', IEEE Transactions on Geoscience and Remote Sensing, 47(8), pp. 2519–2527. Available at: https://doi.org/10.1109/TGRS.2009.2014944.

Kleinschroth, F. et al. (2019) 'Road expansion and persistence in forests of the Congo Basin', Nature Sustainability, 2(7), pp. 628–634. Available at: https://doi.org/10.1038/s41893-019-0310-6.

Kondo, M. et al. (2022) 'Chapter 7 - State of science in carbon budget assessments for temperate forests and grasslands', in B. Poulter et al. (eds) Balancing Greenhouse Gas Budgets. Elsevier, pp. 237–270. Available at: https://doi.org/10.1016/B978-0-12-814952-2.00011-3.

Kuan, D.T. et al. (1985) 'Adaptive noise smoothing filter for images with signal-dependent noise', IEEE transactions on pattern analysis and machine intelligence, (2), pp. 165–177.

Kucera, J., Barbosa, P. and Strobl, P. (2007) 'Cumulative Sum Charts - A Novel Technique for Processing Daily Time Series of MODIS Data for Burnt Area Mapping in Portugal', in 2007 International Workshop on the Analysis of Multi-temporal Remote Sensing Images, pp. 1–6. Available at: https://doi.org/10.1109/MULTITEMP.2007.4293051.

Kuntz, S. and Siegert, F. (1999) 'Monitoring of deforestation and land use in Indonesia with multitemporal ERS data', International Journal of Remote Sensing, 20(14), pp. 2835–2853. Available at: https://doi.org/10.1080/014311699211822.

Kupidura, P. (2016) 'COMPARISON OF FILTERS DEDICATED TO SPECKLE SUPPRESSION IN SAR IMAGES', ISPRS - International Archives of the Photogrammetry, Remote Sensing and Spatial Information Sciences, XLI-B7, pp. 269–276. Available at: https://doi.org/10.5194/isprsarchives-XLI-B7-269-2016.

Kuplich, T.M. (2006) 'Classifying regenerating forest stages in Amazônia using remotely sensed images and a neural network', Forest Ecology and Management, 234(1), pp. 1–9. Available at: https://doi.org/10.1016/j.foreco.2006.05.066.

Lardeux, C. (2008) Apport des données radar polarimétriques pour la cartographie en milieu tropical. PhD Thesis. Université Paris-Est.

Lawrence, W. et al. (1995) 'Utilization of SAR and optical remote sensing data for habitat conservation in the tropical forest of Brazil', in 1995 International Geoscience and Remote Sensing Symposium, IGARSS '95. Quantitative Remote Sensing for Science and Applications. 1995 International Geoscience and Remote Sensing Symposium, IGARSS '95. Quantitative Remote Sensing for Science and Applications, pp. 1480–1482 vol.2. Available at: https://doi.org/10.1109/IGARSS.1995.521786.

Le Toan, T. et al. (1992) 'Relating forest biomass to SAR data', IEEE Transactions on Geoscience and Remote Sensing, 30(2), pp. 403–411. Available at: https://doi.org/10.1109/36.134089.

Le Toan, T. et al. (2004) 'Relating Radar Remote Sensing of Biomass to Modelling of Forest Carbon Budgets', Climatic Change, 67(2), pp. 379–402. Available at: https://doi.org/10.1007/s10584-004-3155-5.

Lee, J.-S. (1980) 'Digital image enhancement and noise filtering by use of local statistics', IEEE transactions on pattern analysis and machine intelligence, (2), pp. 165–168.

Lescuyer, G. et al. (2011) The domestic market for smallscale chainsaw milling in Gabon: Present situation, opportunities and challenges. CIFOR.

Levy, R.C. et al. (2013) 'The Collection 6 MODIS aerosol products over land and ocean', Atmospheric Measurement Techniques, 6(11), pp. 2989–3034. Available at: https://doi.org/10.5194/amt-6-2989-2013.

Lievens, H. et al. (2017) 'Assimilation of global radar backscatter and radiometer brightness temperature observations to improve soil moisture and land evaporation estimates', Remote

Sensing of Environment, 189, pp. 194–210. Available at: https://doi.org/10.1016/j.rse.2016.11.022.

Longepe, N. et al. (2011) 'Assessment of ALOS PALSAR 50 m Orthorectified FBD Data for Regional Land Cover Classification by Support Vector Machines', IEEE Transactions on Geoscience and Remote Sensing, 49(6), pp. 2135–2150. Available at: https://doi.org/10.1109/TGRS.2010.2102041.

Lucas, R. et al. (2011) 'An Evaluation of the ALOS PALSAR L-Band Backscatter—Above Ground Biomass Relationship Queensland, Australia: Impacts of Surface Moisture Condition and Vegetation Structure', Selected Topics in Applied Earth Observations and Remote Sensing, IEEE Journal of, 3, pp. 576–593. Available at: https://doi.org/10.1109/JSTARS.2010.2086436.

Lucas, R.M. et al. (2007) 'The potential of L-band SAR for quantifying mangrove characteristics and change: case studies from the tropics', Aquatic Conservation: Marine and Freshwater Ecosystems, 17(3), pp. 245–264. Available at: https://doi.org/10.1002/aqc.833.

Lynch, J. et al. (2013) 'Choose satellites to monitor deforestation', Nature, 496(7445), pp. 293–294. Available at: https://doi.org/10.1038/496293a.

Maıtre, H. (2001) 'Traitement des images de RSO', Hermès [Preprint].

Manogaran, G. and Lopez, D. (2018) 'Spatial cumulative sum algorithm with big data analytics for climate change detection', Computers and Electrical Engineering, 65, pp. 207–221. Available at: https://doi.org/10.1016/j.compeleceng.2017.04.006.

Margono, B.A. et al. (2012) 'Mapping and monitoring deforestation and forest degradation in Sumatra (Indonesia) using Landsat time series data sets from 1990 to 2010', Environmental Research Letters, 7(3), p. 034010. Available at: https://doi.org/10.1088/1748-9326/7/3/034010.

Martone, M. et al. (2018) 'The global forest/non-forest map from TanDEM-X interferometric SAR data', Remote Sensing of Environment, 205(August 2017), pp. 352–373. Available at: https://doi.org/10.1016/j.rse.2017.12.002.

Marzano, F.S., Mori, S. and Weinman, J.A. (2010) 'Evidence of Rainfall Signatures on X-Band Synthetic Aperture Radar Imagery Over Land', IEEE Transactions on Geoscience and Remote Sensing, 48(2), pp. 950–964. Available at: https://doi.org/10.1109/TGRS.2009.2034843.

Massonnet, D. and Souyris, J.-C. (2008) Imaging with synthetic aperture radar. EPFL press.

Melshelmer, C., Alpers, W. and Gade, M. (1996) 'Investigation of multifrequency/multipolarization radar signatures of rain cells, derived from SIR-C/X-SAR data', in IGARSS '96. 1996 International Geoscience and Remote Sensing Symposium. IGARSS '96. 1996 International Geoscience and Remote Sensing Symposium, pp. 1370–1372 vol.2. Available at: https://doi.org/10.1109/IGARSS.1996.516666.

Mermoz, S. et al. (2021) 'Continuous Detection of Forest Loss in Vietnam, Laos, and Cambodia Using Sentinel-1 Data', Remote Sensing, 13(23), p. 4877. Available at: https://doi.org/10.3390/rs13234877.

Metternicht, G. et al. (2010) 'Remote Sensing of Land Degradation: Experiences from Latin America and the Caribbean', Journal of Environmental Quality, 39(1), pp. 42–61. Available at: https://doi.org/10.2134/jeq2009.0127.

Milne, A.K. et al. (2012) 'Sensor capabilities for deforestation and forest degradation', in 2012 IEEE International Geoscience and Remote Sensing Symposium. 2012 IEEE International Geoscience and Remote Sensing Symposium, pp. 3154–3157. Available at: https://doi.org/10.1109/IGARSS.2012.6350756.

Mistry, J. et al. (2021) 'Covid-19 impacts on Indigenous food sovereignty, livelihoods and biodiversity, Guyana', Report published by … [Preprint].

Mitchard, E.T.A. (2018) 'The tropical forest carbon cycle and climate change', Nature, 559(7715), pp. 527–534. Available at: https://doi.org/10.1038/s41586-018-0300-2.

Morton, D.C. et al. (2005) 'Rapid Assessment of Annual Deforestation in the Brazilian Amazon Using MODIS Data', Earth Interactions, 9(8), pp. 1–22. Available at: https://doi.org/10.1175/EI139.1.

Nelson, R. and Holben, B. (1986) 'Identifying deforestation in Brazil using multiresolution satellite data', International Journal of Remote Sensing, 7(3), pp. 429–448. Available at: https://doi.org/10.1080/01431168608954696.

NELSON, R., HORNING, N. and STONE, T.A. (1987) 'Determining the rate of forest conversion in Mato Grosso, Brazil, using Landsat MSS and AVHRR data', International Journal of Remote Sensing, 8(12), pp. 1767–1784. Available at: https://doi.org/10.1080/01431168708954815.

Neumann, M., Ferro-Famil, L. and Reigber, A. (2010) 'Estimation of Forest Structure, Ground, and Canopy Layer Characteristics From Multibaseline Polarimetric Interferometric SAR Data', IEEE Transactions on Geoscience and Remote Sensing, 48(3), pp. 1086–1104. Available at: https://doi.org/10.1109/TGRS.2009.2031101.

Nicolau, A.P. et al. (2021) 'Assessing SAR C-band data to effectively distinguish modified land uses in a heavily disturbed Amazon forest', International Journal of Applied Earth Observation and Geoinformation, 94(August 2020), p. 102214. Available at: https://doi.org/10.1016/j.jag.2020.102214.

Numbisi, F.N. and Van Coillie, F. (2020) 'Does sentinel-1A backscatter capture the spatial variability in canopy gaps of tropical agroforests? A proof-of-concept in cocoa landscapes in Cameroon', Remote Sensing, 12(24), pp. 1–29. Available at: https://doi.org/10.3390/rs12244163.

Nunes, L.J.R. et al. (2020) 'Forest contribution to climate change mitigation: Management oriented to carbon capture and storage', Climate, 8(2). Available at: https://doi.org/10.3390/cli8020021.

Olofsson, P. et al. (2014) 'Good practices for estimating area and assessing accuracy of land change', Remote Sensing of Environment, 148, pp. 42–57. Available at: https://doi.org/10.1016/j.rse.2014.02.015.

Park, J.-W., Korosov, A. and Babiker, M. (2017) 'Efficient thermal noise removal of Sentinel-1 image and its impacts on sea ice applications', in EGU General Assembly Conference Abstracts, p. 12613.

Piantanida, R. and Miranda, N. (2017) 'Thermal Denoising of Products Generated by the S-1 IPF'.

Podest, E. and Saatchi, S. (2002) 'Application of multiscale texture in classifying JERS-1 radar data over tropical vegetation', International Journal of Remote Sensing, 23(7), pp. 1487–1506. Available at: https://doi.org/10.1080/01431160110093000.

Potapov, P. et al. (2020) 'Landsat analysis ready data for global land cover and land cover change mapping', Remote Sensing, 12(3). Available at: https://doi.org/10.3390/rs12030426.

Potapov, P.V. et al. (2014) 'National satellite-based humid tropical forest change assessment in Peru in support of REDD$\mathplus$ implementation', Environmental Research Letters, 9(12), p. 124012. Available at: https://doi.org/10.1088/1748-9326/9/12/124012.

Qin, Y. et al. (2021) 'Carbon loss from forest degradation exceeds that from deforestation in the Brazilian Amazon', Nature Climate Change, 11(5), pp. 442–448. Available at: https://doi.org/10.1038/s41558-021-01026-5.

Quegan, S. et al. (2000) 'Multitemporal ERS SAR analysis applied to forest mapping', IEEE Transactions on Geoscience and Remote Sensing, 38(2), pp. 741–753.

Ranson, K.J. et al. (2003) 'Disturbance recognition in the boreal forest using radar and Landsat-7', Canadian Journal of Remote Sensing, 29(2), pp. 271–285. Available at: https://doi.org/10.5589/m02-096.

Ranson, Kj. and Sun, G. (1994a) 'Mapping biomass of a northern forest using multifrequency SAR data', IEEE Transactions on Geoscience and Remote Sensing, 32(2), pp. 388–396.

Ranson, K.J. and Sun, G. (1994b) 'Northern forest classification using temporal multifrequency and multipolarimetric SAR images', Remote Sensing of Environment, 47(2), pp. 142–153. Available at: https://doi.org/10.1016/0034-4257(94)90151-1.

Ranson, K.J. and Sun, G. (2000) 'Effects of environmental conditions on boreal forest classification and biomass estimates with SAR', IEEE Transactions on Geoscience and Remote Sensing, 38(3), pp. 1242–1252. Available at: https://doi.org/10.1109/36.843016.

Reiche, J. et al. (2015) 'A Bayesian Approach to Combine Landsat and ALOS PALSAR Time Series for Near Real-Time Deforestation Detection', Remote Sensing, 7(5), pp. 4973–4996. Available at: https://doi.org/10.3390/rs70504973.

Reiche, J., Verhoeven, R., et al. (2018) 'Characterizing Tropical Forest Cover Loss Using Dense Sentinel-1 Data and Active Fire Alerts', Remote Sensing, 10(5), p. 777. Available at: https://doi.org/10.3390/rs10050777.

Reiche, J., Hamunyela, E., et al. (2018) 'Improving near-real time deforestation monitoring in tropical dry forests by combining dense Sentinel-1 time series with Landsat and ALOS-2 PALSAR-2', Remote Sensing of Environment, 204, pp. 147–161. Available at: https://doi.org/10.1016/j.rse.2017.10.034.

Reiche, J., Mullissa, A., Slagter, B., Gou, Y., Tsendbazar, N.E., et al. (2021) 'Forest disturbance alerts for the Congo Basin using Sentinel-1', Environmental Research Letters, 16(2), p. 024005. Available at: https://doi.org/10.1088/1748-9326/abd0a8.

Reigber, A., del Campo Becerra, G.M. and Jäger, M. (2019) 'PyRAT: A Flexible SAR Postprocessing Toolbox', in ESA POLinSAR Workshop.

Ribbes, F. et al. (1997) 'Deforestation monitoring in tropical regions using multitemporal ERS/JERS SAR and INSAR data', in IGARSS'97. 1997 IEEE International Geoscience and Remote Sensing Symposium Proceedings. Remote Sensing - A Scientific Vision for Sustainable Development. IGARSS'97. 1997 IEEE International Geoscience and Remote Sensing Symposium Proceedings. Remote Sensing - A Scientific Vision for Sustainable Development, pp. 1560–1562 vol.4. Available at: https://doi.org/10.1109/IGARSS.1997.608944.

Rignot, E., Salas, W.A. and Skole, D.L. (1997) 'Mapping deforestation and secondary growth in Rondonia, Brazil, using imaging radar and thematic mapper data', Remote Sensing of Environment, 59(2), pp. 167–179. Available at: https://doi.org/10.1016/S0034-4257(96)00150-2.

Rignot, E., Williams, C. and Viereck, L. (1994) 'Radar Estimates of Aboveground Biomass in Boreal Forests of Interior Alaska', IEEE Transactions on Geoscience and Remote Sensing, 32(5), pp. 1117–1124. Available at: https://doi.org/10.1109/36.312903.

Rignot, E.J.M. (2000) 'Effect of Faraday rotation on L-band interferometric and polarimetric synthetic-aperture radar data', IEEE Transactions on Geoscience and Remote Sensing, 38(1), pp. 383–390. Available at: https://doi.org/10.1109/36.823934.

Robert M. Haralick, K. Shanmugam, I.D. (1973) 'Textural Features for Image Classification'.

Romshoo, S.A., Shimada, M. and Igarashi, T. (2002) 'Peatland ecosystem characterization employing L-band SAR', in IEEE International Geoscience and Remote Sensing Symposium. IEEE International Geoscience and Remote Sensing Symposium, pp. 1795–1797 vol.3. Available at: https://doi.org/10.1109/IGARSS.2002.1026257.

Rosenqvist, Å. et al. (2003) 'A review of remote sensing technology in support of the Kyoto Protocol', Environmental Science & Policy, 6(5), pp. 441–455. Available at: https://doi.org/10.1016/S1462-9011(03)00070-4.

Roy, D.P. et al. (2021) 'A global analysis of the temporal availability of PlanetScope high spatial resolution multi-spectral imagery', Remote Sensing of Environment, 264(June), p. 112586. Available at: https://doi.org/10.1016/j.rse.2021.112586.

Rüetschi, M., Small, D. and Waser, L.T. (2019) 'Rapid detection of windthrows using Sentinel-1 C-band SAR data', Remote Sensing, 11(2), pp. 1–23. Available at: https://doi.org/10.3390/rs11020115.

Ruggiero, P.G.C. et al. (2019) 'Payment for ecosystem services programs in the Brazilian Atlantic Forest: Effective but not enough', Land Use Policy, 82, pp. 283–291. Available at: https://doi.org/10.1016/j.landusepol.2018.11.054.

Ruiz-Ramos, J. et al. (2020) 'Continuous forest monitoring using cumulative sums of sentinel-1 timeseries', Remote Sensing, 12(18). Available at: https://doi.org/10.3390/RS12183061.

Ruiz-ramos, J., Marino, A. and Boardman, C.P. (201a) 'USING SENTINEL 1-SAR FOR MONITORING LONG TERM VARIATION IN BURNT FOREST AREAS Javier Ruiz-Ramos ; Armando Marino ; Carl P . Boardman', IGARSS 2018 - 2018 IEEE International Geoscience and Remote Sensing Symposium, (July 2017), pp. 4901–4904.

Saatchi, S.S. et al. (2000) 'Mapping land cover types in the Amazon Basin using 1 km JERS-1 mosaic', International Journal of Remote Sensing, 21(6–7), pp. 1201–1234. Available at: https://doi.org/10.1080/014311600210146.

Saatchi, S.S. et al. (2007) 'Distribution of aboveground live biomass in the Amazon basin', Global Change Biology, 13(4), pp. 816–837. Available at: https://doi.org/10.1111/j.1365-2486.2007.01323.x.

Saatchi, S.S., Soares, J.V. and Alves, D.S. (1997) 'Mapping deforestation and land use in amazon rainforest by using SIR-C imagery', Remote Sensing of Environment, 59(2), pp. 191–202. Available at: https://doi.org/10.1016/S0034-4257(96)00153-8.

Salas, W.A. and Skole, D. (1998) 'Remote sensing of land cover change: secondary growth dynamics in Rondonia, Brazil', in IGARSS '98. Sensing and Managing the Environment. 1998 IEEE International Geoscience and Remote Sensing. Symposium Proceedings. (Cat. No.98CH36174). IGARSS '98. Sensing and Managing the Environment. 1998 IEEE International Geoscience and Remote Sensing. Symposium Proceedings. (Cat. No.98CH36174), pp. 2515–2517 vol.5. Available at: https://doi.org/10.1109/IGARSS.1998.702263.

Santoro, M. et al. (2010) 'Clear-Cut Detection in Swedish Boreal Forest Using Multi-Temporal ALOS PALSAR Backscatter Data', IEEE Journal of Selected Topics in Applied Earth Observations and Remote Sensing, 3(4), pp. 618–631. Available at: https://doi.org/10.1109/JSTARS.2010.2048201.

Santoro, M. et al. (2017) 'Land Cover CCI: Product User Guide Version 2.0', Climate Change Initiative Belgium: Belgium, Leuven [Preprint].

Santoro, M. and Schmullius, C. (2004) 'Investigations on ARD monitoring in Siberian forest using spaceborne SAR', in IGARSS 2004. 2004 IEEE International Geoscience and Remote Sensing Symposium. IGARSS 2004. 2004 IEEE International Geoscience and Remote Sensing Symposium, pp. 1029–1032 vol.2. Available at: https://doi.org/10.1109/IGARSS.2004.1368586.

Servello, E.L., Kuplich, T.M. and Edemir Shimabukuro, Y. (2010) 'Tropical land cover change detection with polarimetric SAR data', in 2010 IEEE International Geoscience and Remote Sensing Symposium. 2010 IEEE International Geoscience and Remote Sensing Symposium, pp. 1477–1480. Available at: https://doi.org/10.1109/IGARSS.2010.5653215.

Shimabukuro, Y.E. et al. (2007) 'Quantifying optical and SAR image relationships for tropical landscape features in the Amazônia', International Journal of Remote Sensing, 28(17), pp. 3831–3840. Available at: https://doi.org/10.1080/01431160701236829.

Skole, D. and Tucker, C. (1993) 'Tropical Deforestation and Habitat Fragmentation in the Amazon: Satellite Data from 1978 to 1988', Science, 260(5116), pp. 1905–1910. Available at: https://doi.org/10.1126/science.260.5116.1905.

Small, D. (2011) 'Flattening gamma: Radiometric terrain correction for SAR imagery', IEEE Transactions on Geoscience and Remote Sensing, 49(8), pp. 3081–3093. Available at: https://doi.org/10.1109/TGRS.2011.2120616.

Souyris, J.-C. et al. (1996) 'Use of polarisation synthesis for deforestation studies based on SIR-C/XSAR data analysis', in IGARSS '96. 1996 International Geoscience and Remote Sensing Symposium. IGARSS '96. 1996 International Geoscience and Remote Sensing Symposium, pp. 836–838 vol.2. Available at: https://doi.org/10.1109/IGARSS.1996.516493.

Souza, C.M. et al. (2013) 'Ten-year landsat classification of deforestation and forest degradation in the brazilian amazon', Remote Sensing, 5(11), pp. 5493–5513. Available at: https://doi.org/10.3390/rs5115493.

Sr., S.N., Billey, A. and Jr., H.T.-O.-A. (2018) 'Random forest classification using Sentinel-1 and Sentinel-2 series for vegetation monitoring in the Pays de Brest (France)', in C.M.U. Neale and A. Maltese (eds) Remote Sensing for Agriculture, Ecosystems, and Hydrology XX. SPIE, pp. 1–18. Available at: https://doi.org/10.1117/12.2325546.

Suga, Y. and Takeuchi, S. (2000) 'Application of JERS-1 InSAR for monitoring deforestation of tropical rain forest', in IGARSS 2000. IEEE 2000 International Geoscience and Remote Sensing Symposium. Taking the Pulse of the Planet: The Role of Remote Sensing in Managing the Environment. Proceedings (Cat. No.00CH37120). IGARSS 2000. IEEE 2000 International Geoscience and Remote Sensing Symposium. Taking the Pulse of the Planet: The Role of Remote Sensing in Managing the Environment. Proceedings (Cat. No.00CH37120), pp. 432–434 vol.1. Available at: https://doi.org/10.1109/IGARSS.2000.860555.

Takeuchi, S. et al. (2000) 'Monitoring of new plantation development in tropical rain forests using JERS-1 SAR data', Advances in Space Research, 26(7), pp. 1151–1154. Available at: https://doi.org/10.1016/S0273-1177(99)01134-5.

Takeuchi, S., Suga, Y. and Yoshimura, M. (2001) 'A comparative study of coherence information by L-band and C-band SAR for detecting deforestation in tropical rain forest', in IGARSS 2001. Scanning the Present and Resolving the Future. Proceedings. IEEE 2001

International Geoscience and Remote Sensing Symposium (Cat. No.01CH37217). IGARSS 2001. Scanning the Present and Resolving the Future. Proceedings. IEEE 2001 International Geoscience and Remote Sensing Symposium (Cat. No.01CH37217), pp. 2259–2261 vol.5. Available at: https://doi.org/10.1109/IGARSS.2001.977968.

Takeuchi, S, Suga, Y. and Yoshimura, M. (2001) 'A comparative study of coherence information by L-band and C-band SAR for detecting deforestation in tropical rain forest', in IGARSS 2001. Scanning the Present and Resolving the Future. Proceedings. IEEE 2001 International Geoscience and Remote Sensing Symposium (Cat. No.01CH37217), pp. 2259–2261 vol.5. Available at: https://doi.org/10.1109/IGARSS.2001.977968.

Takeuchi, S. and Yamada, S. (2002) 'Monitoring of forest fire damage by using JERS-1 InSAR', in IEEE International Geoscience and Remote Sensing Symposium. IEEE International Geoscience and Remote Sensing Symposium, pp. 3290–3292 vol.6. Available at: https://doi.org/10.1109/IGARSS.2002.1027159.

Tanase, M.A. et al. (2010) 'TerraSAR-X Data for Burn Severity Evaluation in Mediterranean Forests on Sloped Terrain', IEEE Transactions on Geoscience and Remote Sensing, 48(2), pp. 917–929. Available at: https://doi.org/10.1109/TGRS.2009.2025943.

Tanase, M.A., Kennedy, R. and Aponte, C. (2015) 'Radar Burn Ratio for fire severity estimation at canopy level: An example for temperate forests', Remote Sensing of Environment, 170, pp. 14–31. Available at: https://doi.org/10.1016/j.rse.2015.08.025.

Tansey, K.J. et al. (2004) 'Classification of forest volume resources using ERS tandem coherence and JERS backscatter data', International Journal of Remote Sensing, 25(4), pp. 751–768. Available at: https://doi.org/10.1080/0143116031000149970.

Thiel, C. et al. (2006) 'Radar remote sensing for the delineation of forest cover maps and the detection of deforestation', Forestry: An International Journal of Forest Research, 79(5), pp. 589–597. Available at: https://doi.org/10.1093/forestry/cpl036.

Tomasi, C. and Manduchi, R. (1998) 'Bilateral filtering for gray and color images', Proceedings of the IEEE International Conference on Computer Vision, pp. 839–846. Available at: https://doi.org/10.1109/iccv.1998.710815.

Torres, R. et al. (2012) 'GMES Sentinel-1 mission', Remote Sensing of Environment, 120, pp. 9–24. Available at: https://doi.org/10.1016/j.rse.2011.05.028.

Treuhaft, R. et al. (2015) 'Tropical-Forest Biomass Estimation at X-Band From the Spaceborne TanDEM-X Interferometer', IEEE Geoscience and Remote Sensing Letters, 12(2), pp. 239–243. Available at: https://doi.org/10.1109/LGRS.2014.2334140.

Treuhaft, R.N. et al. (2009) 'Vegetation profiles in tropical forests from multibaseline interferometric synthetic aperture radar, field, and lidar measurements', Journal of Geophysical Research: Atmospheres, 114(D23). Available at: https://doi.org/10.1029/2008JD011674.

Turubanova, S. et al. (2018) 'Ongoing primary forest loss in Brazil, Democratic Republic of the Congo, and Indonesia', Environmental Research Letters, 13(7), pp. 2000–2010. Available at: https://doi.org/10.1088/1748-9326/aacd1c.

Tyukavina, A. et al. (2018) 'Congo Basin forest loss dominated by increasing smallholder clearing', Science Advances, 4(11). Available at: https://doi.org/10.1126/sciadv.aat2993.

Ulaby, F.T. et al. (2014) Microwave radar and radiometric remote sensing. University of Michigan Press Ann Arbor, MI, USA (5).

Umunay, P.M. et al. (2019) 'Selective logging emissions and potential emission reductions from reduced-impact logging in the Congo Basin', Forest Ecology and Management, 437, pp. 360–371.

Valeriano, D.M. et al. (2004) 'Monitoring tropical forest from space: the PRODES digital project', International Archives of Photogrammetry Remote Sensing and Spatial Information Sciences, 35, pp. 272–274.

Vargas, C., Montalban, J. and Leon, A.A. (2019) 'Early warning tropical forest loss alerts in peru using landsat', Environmental Research Communications, 1(12). Available at: https://doi.org/10.1088/2515-7620/ab4ec3.

Verhelst, K. et al. (2021) 'Improving forest baseline maps in tropical wetlands using gedi-based forest height information and sentinel-1', Forests, 12(10), pp. 1–16. Available at: https://doi.org/10.3390/f12101374.

Wagner, W. et al. (2003) 'Large-scale mapping of boreal forest in SIBERIA using ERS tandem coherence and JERS backscatter data', Remote Sensing of Environment, 85(2), pp. 125–144. Available at: https://doi.org/10.1016/S0034-4257(02)00198-0.

Watanabe, M. et al. (2017) 'Development of early-stage deforestation detection algorithm (advanced) with PALSAR-2/ScanSAR for JICA-JAXA program (JJ-FAST)', in International Geoscience and Remote Sensing Symposium (IGARSS). Institute of Electrical and Electronics Engineers Inc., pp. 2446–2449. Available at: https://doi.org/10.1109/IGARSS.2017.8127487.

Watanabe, M. et al. (2018) 'Early-stage deforestation detection in the tropics with L-band SAR', IEEE Journal of Selected Topics in Applied Earth Observations and Remote Sensing, 11(6), pp. 2127–2133. Available at: https://doi.org/10.1109/JSTARS.2018.2810857.

Watanabe, M., Koyama, Christian N., et al. (2021) 'Refined algorithm for forest early warning system with ALOS-2/PALSAR-2 ScanSAR data in tropical forest regions', Remote Sensing of Environment, 265, p. 112643. Available at: https://doi.org/10.1016/j.rse.2021.112643.

Weisse, M. et al. (2019) 'Use of Near-Real-Time Deforestation Alerts'.

Wheeler, D. et al. (2014) 'Satellite-based forest clearing detection in the Brazilian Amazon: FORMA, DETER, and PRODES', WRI Issue Brief, p. 24.

Whittle, M. et al. (2012) 'Detection of tropical deforestation using ALOS-PALSAR: A Sumatran case study', Remote Sensing of Environment, 124, pp. 83–98. Available at: https://doi.org/10.1016/j.rse.2012.04.027.

Wigneron, J.P. et al. (2020) 'Tropical forests did not recover from the strong 2015–2016 El Niño event', Science Advances, 6(6), pp. 1–11. Available at: https://doi.org/10.1126/sciadv.aay4603.

Wunder, S. (2015) 'Revisiting the concept of payments for environmental services', Ecological Economics, 117, pp. 234–243. Available at: https://doi.org/10.1016/j.ecolecon.2014.08.016.

Ygorra, B., Frappart, F., Wigneron, J–P., et al. (2021a) 'Deforestation Monitoring Using Sentinel-1 SAR Images in Humid Tropical Areas', in 2021 IEEE International Geoscience and Remote Sensing Symposium IGARSS. 2021 IEEE International Geoscience and Remote Sensing Symposium IGARSS, pp. 5957–5960. Available at: https://doi.org/10.1109/IGARSS47720.2021.9554698.

Ygorra, B, Frappart, F., Wigneron, J P, et al. (2021b) 'Monitoring loss of tropical forest cover from Sentinel-1 time-series: A CuSum-based approach', International Journal of Applied Earth Observation and Geoinformation, 103, p. 102532. Available at: https://doi.org/10.1016/j.jag.2021.102532.

Ygorra, B. et al. (2022) 'Classification and Deforestation Monitoring Using Sentinel-1 C-SAR Images in a Temperate Exploited Pine Forest', in IGARSS 2022-2022 IEEE International Geoscience and Remote Sensing Symposium. IEEE, pp. 691–694.

Ygorra B., Frappart F, Wigneron J.P.,. Moisy C.,. Catry T.,. Pillot B.,. Kharlanova A., Riazanoff, S. (2023) 'ReCuSum, a polyvalent method to monitor tropical forest disturbances', International Society for Photogrammetry and Remote Sensing, in press.

Zhang, F. et al. (2011) 'Polarimetric Signature and the Temporal Variation Analysis for Deforestation Mapping in Southwest China', p. 5.

Zhao, F. et al. (2022) ‘Monthly mapping of forest harvesting using dense time series Sentinel-1 SAR imagery and deep learning’, Remote Sensing of Environment, 269, p. 112822. Available at: https://doi.org/10.1016/j.rse.2021.112822.

Annexes

Explicative schema of the Cross-T_c computation

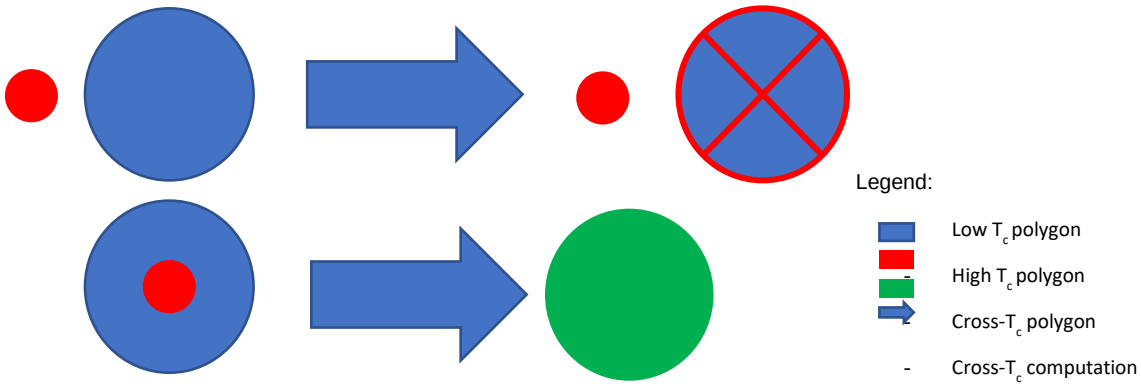

Applied to the VH with T_c = 0.75 dataset

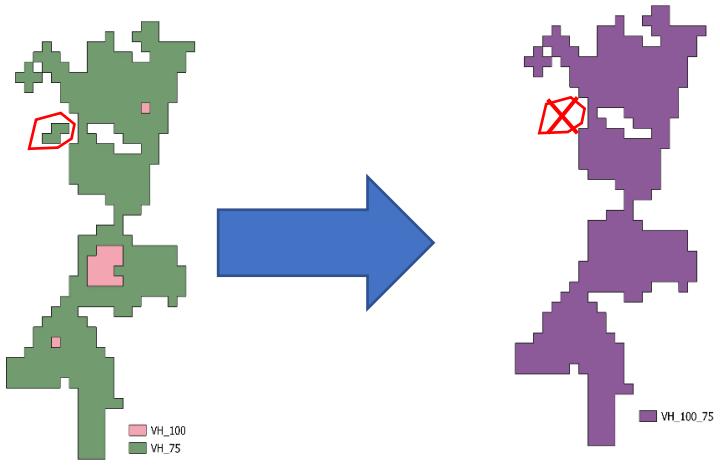

Annexe 1: Explicative schema of the Cross-T_c computation.

Time period monitored	Cut area (m²)	Change area detected in time (m²)	Change area detected early (m²)	Change area detected early (%)	Change area detected late (m²)	Change area detected late (%)
2018/01/06 - 2018/02/02	52700	22100	0	0,00%	30600	58,06%
2018/02/02 - 2018/03/17	56700	30000	4400	7,76%	22300	39,33%
2018/03/17 - 2018/04/19	5600	800	3000	53,57%	1800	32,14%
2018/04/19 - 2018/06/15	29400	23300	1900	6,46%	4200	14,29%
2018/06/15 - 2018/08/17	18200	13000	2700	14,84%	2500	13,74%
2018/08/17 - 2018/09/10	3400	0	1500	44,12%	1900	55,88%
2018/09/10 - 2018/11/08	110700	60500	22400	20,23%	27800	25,11%
2018/11/08 - 2018/12/19	565400	214300	324100	57,32%	27000	4,78%
2018/12/19 - 2019/01/06	386000	143300	229500	59,46%	13200	3,42%
2019/01/06 - 2019/01/22	359200	88500	260300	72,47%	10400	2,90%
2019/01/22 - 2019/02/02	193200	24100	163500	84,63%	5600	2,90%
2019/02/02 - 2019/03/03	484400	93600	384800	79,44%	6000	1,24%
2019/03/03 - 2019/03/31	108900	11000	97500	89,53%	400	0,37%
2019/03/31 - 2019/05/03	11100	100	10200	91,89%	800	7,21%
2019/05/03 - 2019/08/06	70600	23100	47100	66,71%	400	0,57%
2019/08/06 - 2019/11/10	46200	28700	17500	37,88%	0	0,00%

2019/11/10 - 2019/11/26	112000	6100	105900	94,55%	0	0,00%
Total	2613700	782500	1676300	64,14%	154900	5,93%

Annexe 2: Table of the detection time of the change.

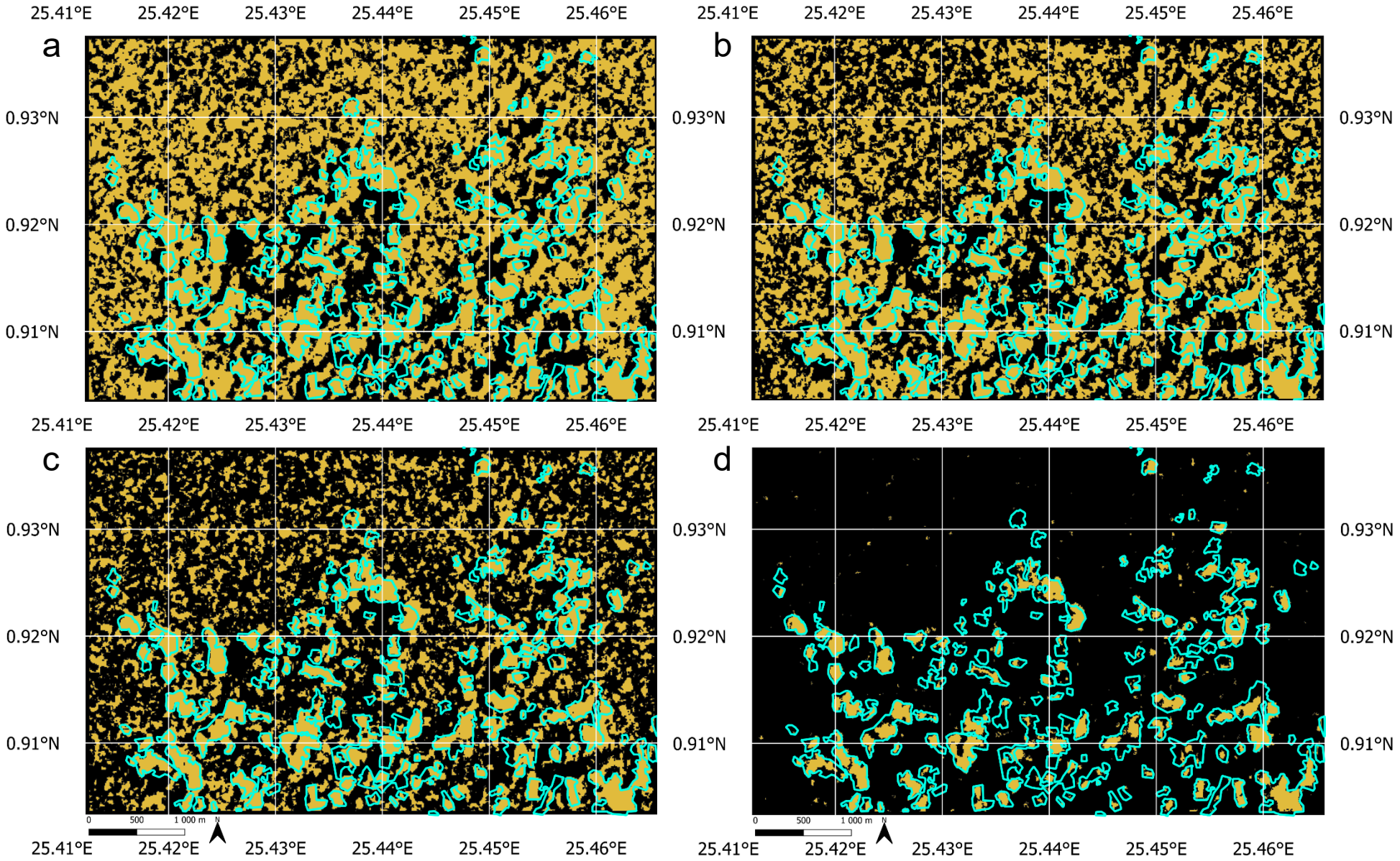

Annexe 3 : Map of the results of the CuSum based on VV union VH with T_c = (a) 0.25, (b) 0.50, (c) 0.75 and (d) 1.00.

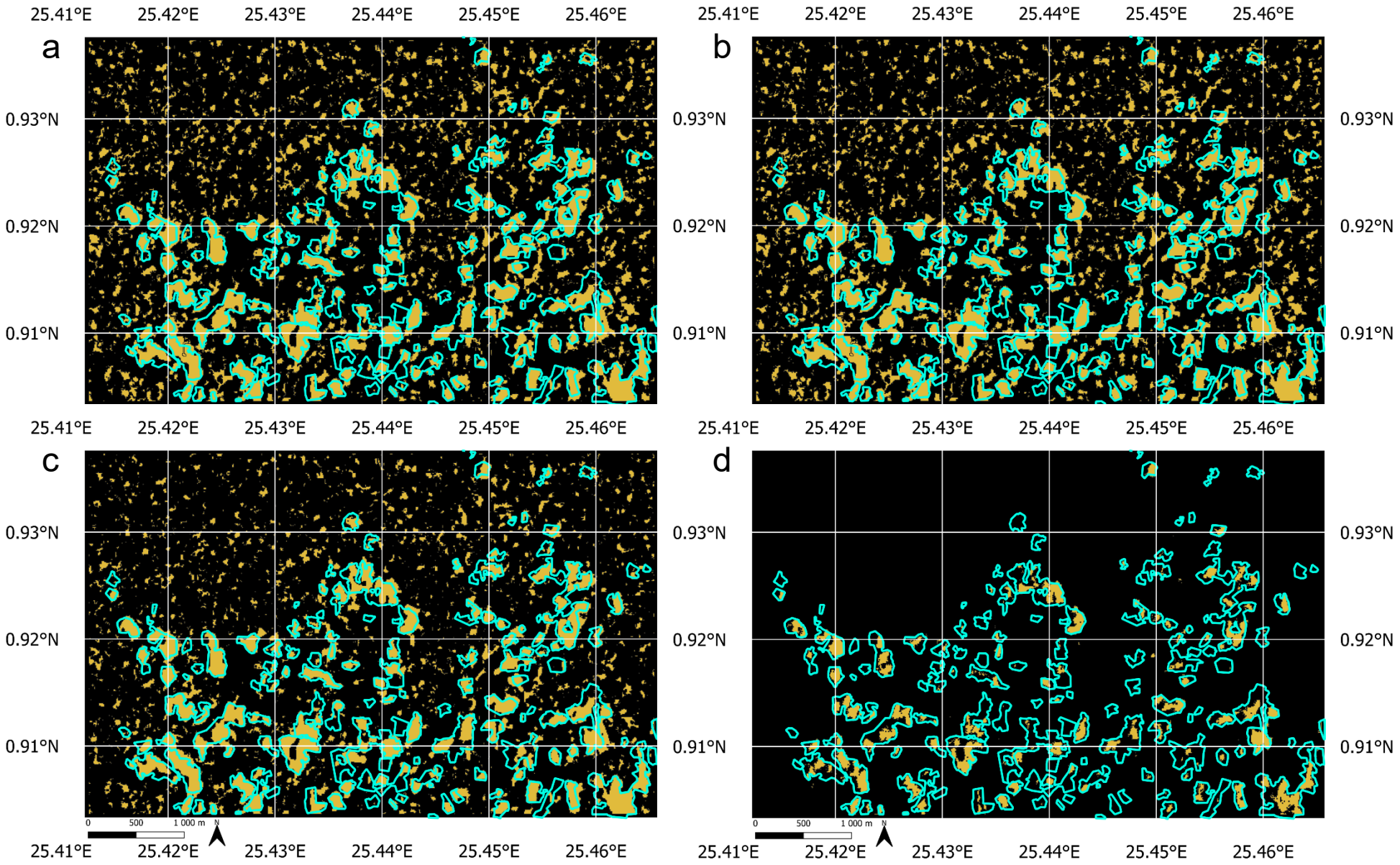

Annexe 4 : Map of the results of the CuSum based on VV intersect VH with T_c = (a) 0.25, (b) 0.50, (c) 0.75 and (d) 1.00.

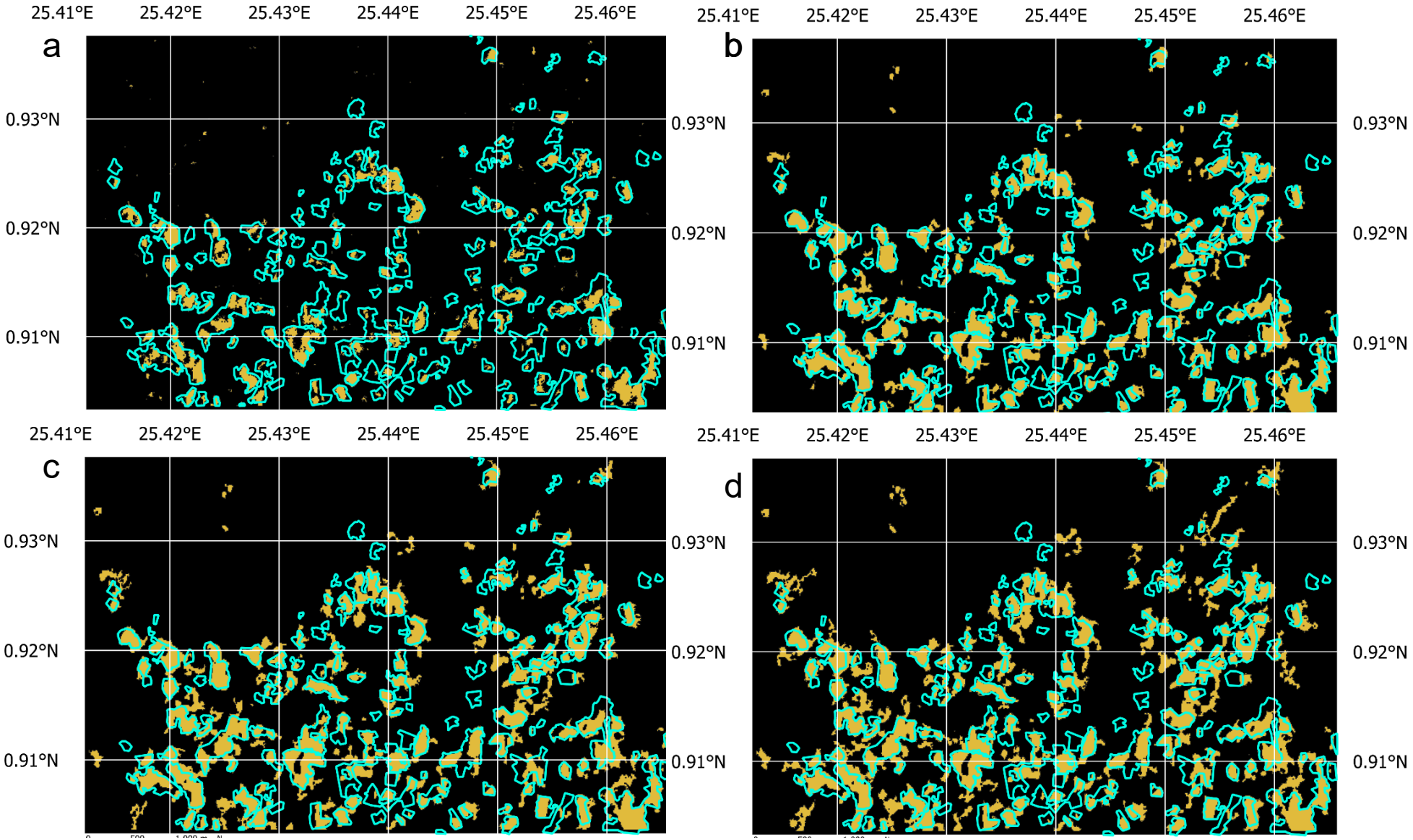

Annexe 5 : Map of the results of the CuSum based on VV intersect VH with (a) Tc = 1.00, (b) cross-T_c 100_75, (c) cross-T_c 100_50 and (d) cross-T_c 100_25.

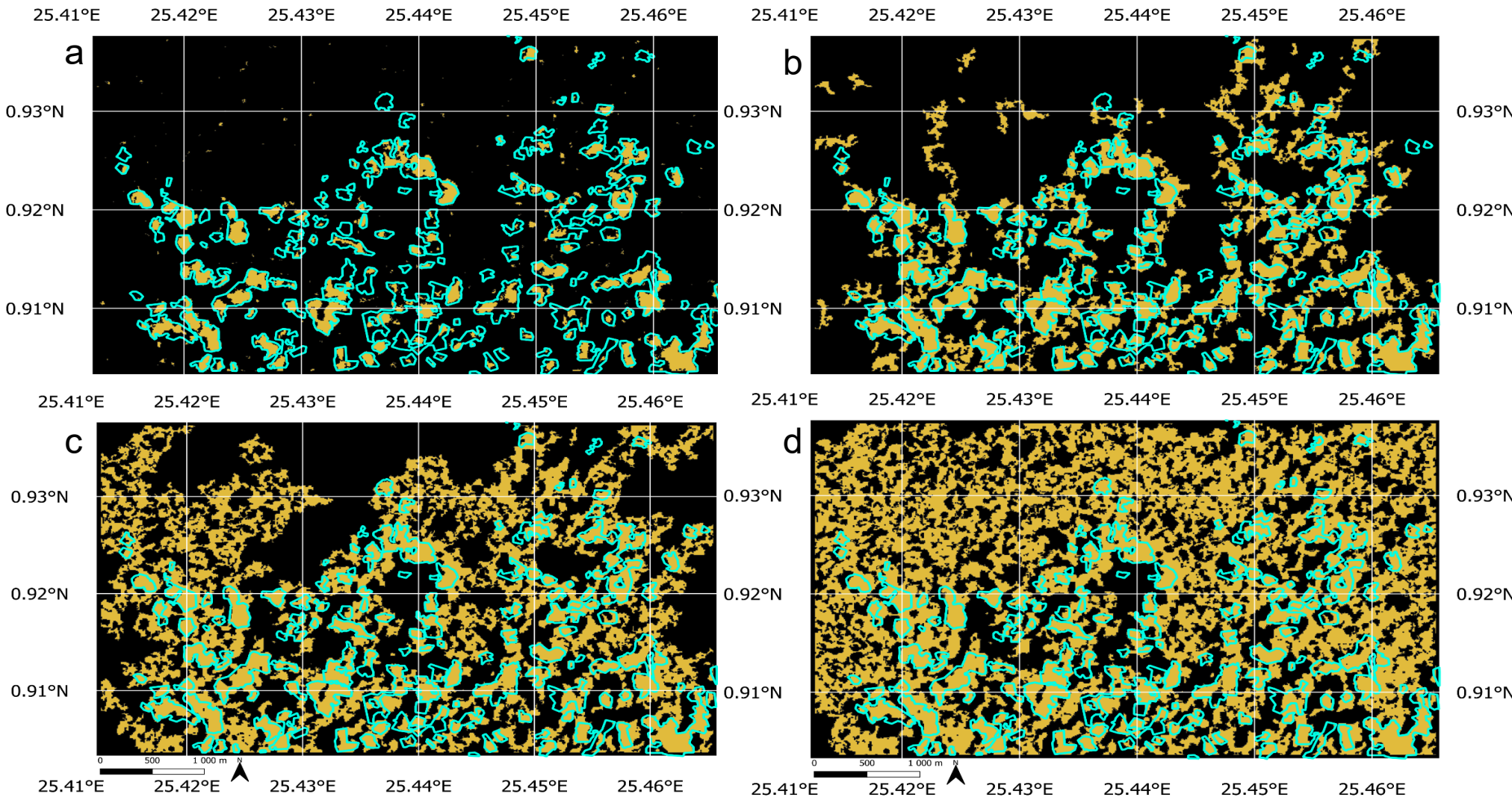

Annexe 6 : Map of the results of the CuSum based on VV union VH with (a) T_c = 1.00, (b) cross-T_c 100_75, (c) cross-T_c 100_50 and (d) cross-T_c 100_25.